NUMERICAL STUDY OF MIXING OF DIFFERENT NEWTONIAN AND NON-NEWTONIAN FLUIDS IN STIRRED TANK

A dissertation

Submitted in partial fulfilment of the

Requirements for the award of the Degree of

Doctor of Philosophy

In

Chemical Engineering

By

Akhilesh Prabhakar Khapre

(Roll No.: 510CH102)

Under the supervision of

Dr. Basudeb Munshi

Department of Chemical Engineering
National Institute of Technology
Rourkela, Odisha, India – 769008
2015

NATIONAL INSTITUTE OF TECHNOLOGY
ROURKELA ODISHA, INDIA – 769008

Certificate

This is to certify that the dissertation report entitled**, “*Numerical Study of Mixing of Different Newtonian and non-Newtonian Fluids in Stirred Tank*”,** is a bonafide record of independent research work done by ***Akhilesh Prabhakar Khapre,*** Roll No. ***510CH102,*** under my supervision and submitted to National Institute of Technology Rourkela in the partial fulfillment for the award of the Degree of ***Doctor of Philosophy*** in Chemical Engineering.

Date:

Dr. BASUDEB MUNSHI
Associate Professor
Department of Chemical Engineering
National Institute of Technology, Rourkela

Acknowledgments

I would like to express my profound and heartfelt gratitude to my supervisor Dr. Basudeb Munshi for his invaluable supervision and endless encouragement throughout this work. His able knowledge and expert guidance with unswerving patience fathered my work at every stage. Without his warm affection and support, the fulfillment of the task would have been very difficult.

I express my sincere thanks to Prof. P. Rath, Head, Chemical Engineering Department and members of Doctoral Scrutiny Committee (DSC) Prof. M. Kundu, Prof. H.M. Jena, Prof. J. Srinivas, Prof. P. Chowdhury and all the faculty members of Chemical Engineering Department for their suggestions and constructive criticism during the preparation of the thesis.

I am very much thankful to my friends Lallan Singh, Gaurav Sir, Sachin Sir, Rajib Sir, Yogesh, Sambhurisha, Arvind, Sangram and Saroj for their cordial support, valuable information and guidance, which helped me in completing this task through various stages.

Last but not the least, thank to my loving parents and brother for incredible love, support and the believing me unconditionally.

I am grateful to the Almighty for guiding me through these years and achieving whatever I have achieved till date.

Akhilesh Prabhakar Khapre

Abstract

Mixing has the most common occurrence in process industries like chemical, food and polymer and plays a significant part in overall success of the processes. Stirred tanks are commonly used for mixing various types of Newtonian and non-Newtonian liquids. Impeller is the movable part and is used as the rotating device in stirred tank systems for achieving mixing. An impeller while it rotates imparts shear force in the vicinity along the peripheral zone. Literature is rich with information on various experimental and theoretical findings on the hydrodynamics and mixing behaviour of Newtonian fluids in stirred tank systems. However, with non-Newtonian fluids, limited published literature is available on the hydrodynamic behaviour of the mixing process in stirred vessels. A few available experimental works in literatures successfully explained the mixing process in a non-Newtonian system using Rushton turbine (impeller commonly used in industry). But unavailability of the theoretical prediction of the same is basically explains the motivation behind the study on the mixing of non-Newtonian fluids in stirred tank with Rushton turbine.

For mixing highly viscous liquids, helical ribbon impellers are most suited. In this thesis work, it was aimed to study the computational aspects of the hydrodynamic performance of helical ribbon impeller in a highly viscous non-Newtonian system and comparing the results with helical screw ribbon impeller through computational fluid dynamics (CFD) simulation. Entropy generation minimization study is an integral part of this thesis work. Mostly, the earlier works involve use of analytical expressions from basics of mass, energy and entropy balance which has got certain limitations because of many assumptions. Here, we aimed for a detailed numerical study on the same. Also, the understanding of residence time distribution (RTD) study in a stirred tank system gives an idea on the distribution of flow structure. Although, this particular aspect has been studied by various research groups, however, some of the experimental data are not compared with numerical findings for validation. In this work it was aimed to predict RTD numerically especially by using swept volume of the impeller into consideration.

A computational fluid dynamics study using Ansys Fluent was carried out to determine the mixing performance of a tank stirred with Rushton turbine. The predicted profiles of the velocity components were validated with literature data. The non-parametric Spearman’s rank order test was used to find the interaction of velocity profiles with the impeller Reynolds number and flow behavior index. The characteristic performance parameters such as power number and flow number of the impeller were predicted. The variations of entropy generation due to only viscous dissipation with Reynolds number, tank geometry, etc. were calculated for the isothermal tank. The entropy generation minimization (EGM) approach was used to optimize the performance of the non-isothermal continuous stirred tank with respect to the system parameters like inlet Reynolds number, impeller speed, and impeller clearance and impeller blade width.

The numerical study of the stirred tank with helical ribbon (HR) and helical ribbon with screw (HRS) impellers was carried out successfully. The CFD models were successfully validated with the experimental power number given in literature. The power constant for Newtonian fluid (K_p) and non-Newtonian fluid ($K_p(n)$) were calculated and compared successfully with the literature data. The Metzner Otto or geometry constant, K_s were computed following four different methods and the best one was identified by predicting successfully the generalized power curve. The flow numbers of HRS impeller were predicted for wide range of impeller Reynolds number. The non-dimensional mixing times were varied in scattered way with impeller Reynolds number, and the dispersive flow away from the impeller shaft was observed. The entropy generations were increased with the impeller Reynolds number, and an empirical model of entropy generation with impeller Reynolds number was developed. The non-isothermal stirred tank with HR and HRS impellers were optimized employing the entropy generation minimization technique.

The hydrodynamic and the residence time distribution (RTD) behavior of the viscous Newtonian fluid was studied using a tracer age distribution function, $I(\theta)$. The experimental tracer age distribution functions were predicted by CFD tools using tracer injection and swept volume methods. The predicted results were found in good agreement with the literature data. The mixing behaviour was changed from dispersion to ideal mixing state with increasing the tank Reynolds number and impeller rotations. The mixing performance parameters like holdback, segregation, number of ideal continuous stirred tank in series equivalent to single actual continuous stirred tank were also calculated to identify the necessary flow parameters and their magnitude to obtain the ideal flow distribution in the tank.

Keywords: Mixing, Rushton turbine, Helical ribbon impeller, Shear thinning fluids, Newtonian fluid, Flow number, Power number, Power constant, Entropy generation minimization, Impeller geometry constant, mixing time, Residence time distribution.

CONTENTS

LIST OF FIGURES

LIST OF TABLES

NOMENCLATURE

a	Length of the impeller blade (m)
A_{in}	Inlet cross-sectional area (m^2)
b	Impeller blade width (m)
Be	Bejan Number ($Be = \frac{S_{gen,HT}}{S_{gen,Total}}$)
C_i	Impeller off bottom clearance (m)
$C(t)$	Concentration of a tracer at an outlet from the reactor at the moment t (mole/L)
C_0^+	Concentration of a tracer fed into the reactor after a step-wise change (mole/L)
C_0^-	Initial concentration of a tracer in the reactor (mole/L)
d	Inlet and outlet diameter of pipe (m)
D	Tank diameter (m)
D_i	Impeller diameter (m)
h	Height of helical ribbon impeller (m)
H	Tank height (m)
$I(\theta)$	Internal age distribution function
K	Consistency index (kg s^{n-2}/ m)
K_{eff}	Effective thermal conductivity (W/(m^2 K))
K_p	Power constant for Newtonian fluid
K_p (n)	Power constant for non-Newtonian fluid
K_s	Impeller geometry constant
n	Flow behavior index

N	Impeller rotational speed (rps or rpm)
N_p	Power number ($N_P = \dfrac{P}{\rho N^3 D_i^5}$)
N_q	Flow number ($N_q = \dfrac{Q}{N D_i^3}$)
P	Power input (W)
Q	Impeller pumping capacity (m^3/min)
r	Radial distance (m)
Re	Impeller Reynolds number ($Re = \dfrac{\rho N D_i^2}{\mu}$ or $Re = \dfrac{\rho N^{2\text{-}n} D_i^2}{K \cdot k_s^{n-1}}$)
Re_t	Tank Reynolds number ($Re_t = \dfrac{4V^* \rho}{\pi D \mu}$)
Re_{in}	Inlet Reynolds number ($Re_{in} = \dfrac{Re_t}{d/D} = \dfrac{4V^* \rho}{\pi d \mu}$)
R_i	Impeller radius (m)
R	Tank radius (m)
s	Specific entropy (J/kg K)
S^*	Dimensionless Entropy generation ($S^* = \dfrac{S_{gen,Total} \cdot D^2}{\lambda}$)
s/D_i	Pitch ratio of helical ribbon impeller
$S_{gen,HT}$	Entropy generation rate due to temperature gradient per unit volume (W/K m^3)
$S_{gen,\overline{HT}}$	Entropy generation due to mean heat transfer per unit volume (W/K m^3)
$S_{gen,HT'}$	Entropy generation due to fluctuating temperature gradient per unit volume (W/K m^3)
$S_{gen,VD}$	Entropy generation rate due to fluid viscous dissipation per unit volume (W/K m^3)

$S_{gen,VD'}$	Entropy generation due to fluctuating viscous dissipation per unit volume (W/K m^3)
$S_{gen,\overline{VD}}$	Entropy generation due to mean viscous dissipation per unit volume (W/K m^3)
$S_{gen,Total}$	Total entropy generation rate per unit volume (W/K m^3)
S_s	Screw pitch ratio
T	Temperature (K)
t	Time (min or sec)
t_m	Mixing time (sec)
u_{in}	Inlet velocity, (m/sec)
V	Liquid volume inside tank (m^3)
V^*	Inlet volumetric flow rate, (l/h or m^3/sec)
V_{tip}	Impeller tip velocity (m/s)
W	Width of helical ribbon impeller blade (m)
W_b	Baffles width (m)
W_s	Width of screw blade (m)

Greek Letters

α	Thermal diffusivity (m^2/s)
α_t	Turbulent thermal diffusivity (m^2/s)
α_{DME}	Dispersive mixing efficiency ($\alpha_{DME} = \dfrac{\lVert\dot{\gamma}\rVert}{\lVert\dot{\gamma}\rVert + \lVert\omega\rVert}$)
μ	Viscosity (Pa s or cP)
η	Apparent viscosity (Pa s)
μ_{eff}	Effective viscosity (Pa s)

ρ	Density (kg/m^3)
φ_v	Viscous dissipation function (s^2)
k	Turbulent kinetic energy (m^2/s^2)
ε	Dissipation due to turbulence kinetic energy (m^2/s^3)
λ	Thermal conductivity (W/(mK))
Φ_v	Viscous dissipation function (s^2)
φ_v	Mean viscous dissipation due to mean velocity components
$\dot{\gamma}$	Shear rate (s^{-1})
$\dot{\gamma}_{eff}$	Effective shear rate (s^{-1})
$\bar{\bar{\tau}}$	Stress tensor (kgm^{-1}s^{-2})
τ	Holdup time of liquid in tank (min)
θ	Dimensionless time ($\theta = t/\tau$)
σ	Variance of the residence time distribution
ω	Vorticity tensor (s^{-1})

Abbreviations

CFD	Computational Fluid Dynamics
CMC	Carboxymethyl cellulose
CSTR	Continuous Stirred Tank Reactor
EGM	Entropy Generation Minimization
HR	Helical Ribbon
HRS	Helical Ribbon Screw
RMS	Root Mean Square

rpm	Revolutions per minute
RTD	Residence Time Distribution
STR	Stirred Tank Reactor
XG	Xanthan gum

CHAPTER 1

INTRODUCTION TO HYDRODYNAMIC AND MIXING BEHAVIOR OF STIRRED TANK

1.1 INTRODUCTION

Mixing plays an important role in the process industries like chemical, food and polymer industries. It is one of the oldest operations in process industries (Bonvillani et al., 2006). Stirred tanks are commonly used for mixing single or multi-phase systems e.g. blending of miscible liquids, dispersing of gases into a liquid and dispersing immiscible liquids into another liquid. The mixing in stirred tank also promotes heat and mass transfer. To obtain a high yield of a product, reactants should come into an intimate contact with each other in the reactor. Many uses of stirred/agitated tanks are found in the mineral and metallurgical industries e.g. leaching, crystallizers, mixer-settlers, etc.

The working fluids in the mixer may be Newtonian or non-Newtonian fluid. Foods such as yogurt, sauces and soups, and emulsions like paint and latex show non-Newtonian characteristics. The mixing of high viscous fluid is limited in laminar zone, but in the industry, the turbulent mixing is not uncommon especially for low viscous fluids. In many occasions, the working liquid starts as Newtonian fluid, but with time, the rheological behavior of the liquid changes to non-Newtonian. It may occur either because of chemical reactions or because of formation of emulsions. The changing of rheologically different liquid may affect the product quality.

The impeller is used as rotating device in the stirred tank for mixing the fluid. It imparts a shear force on the nearby fluid which moves along the impeller. The moving fluid transfers momentum outwardly to the stagnant fluids. The geometry of the impeller affects the flow pattern in the stirred fluids. Depending on the geometry and flow patterns created there are different types of the impeller. Among them Rushton Turbine, Propeller, Cross-beam, Frame, Blade, Anchor, Pitched blade, MIG, INTER MIG, and helical ribbon impeller are a few. In the present work Rushton turbine and helical ribbon impeller, as shown in Figure 1.1, are used.

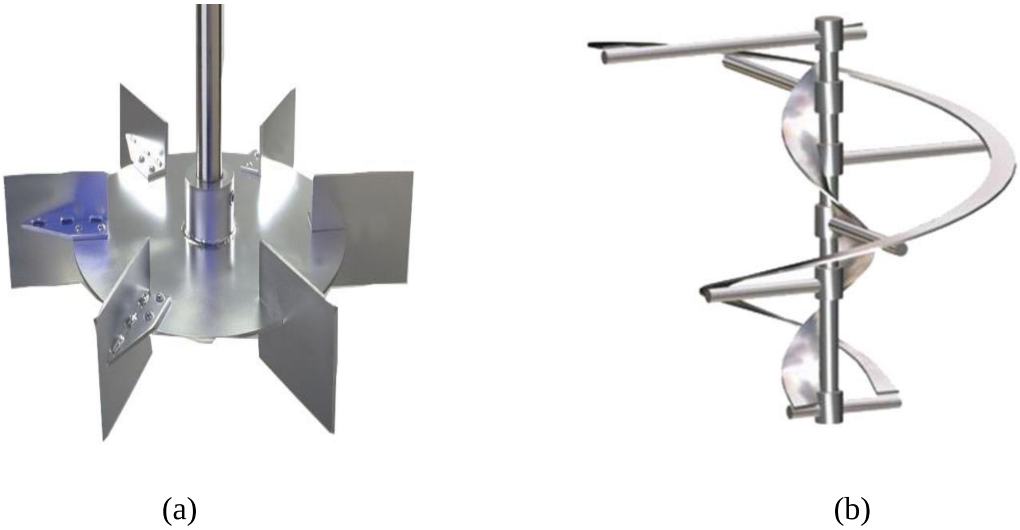
(a) (b)

Figure 1.1 (a) Rushton turbine, (b) Helical ribbon with screw (Harnby et al., 1992).

Rushton turbine is a radial flow impeller. It is used for intense mixing specially for low viscous liquid. The Rushton turbine (Figure 1.1(a)) is constructed with six vertical blades on the disk. The helical ribbon stirrer (Figure 1.1(b)) is a close clearance stirrer and is mostly used for mixing of high viscous liquids. It is operated at very slow speed. The selection of impeller depends on the required flow pattern, power consumptions and viscosity of fluids. The general flow patterns of the above two impellers are shown in Figure 1.2.

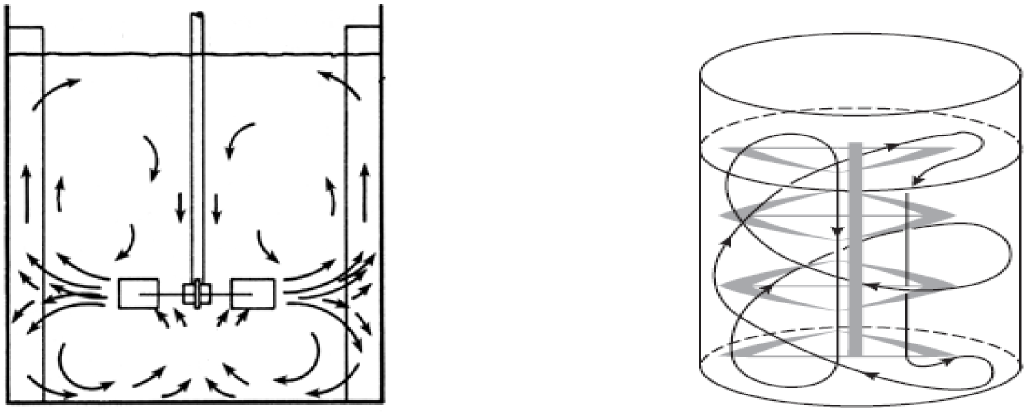
(a) (b)

Figure 1.2 Flow pattern around, (a) Rushton turbine, (b) Helical ribbon impeller (Harnby et al., 1992).

For radial flow Rushton turbine the discharge of fluid is radially out from the blade towards the tank wall (Ochieng et al., 2008; Driss et al., 2014). The flow splits at the tank wall, and approximately 50% of the fluid circulates towards the surface while the rest to the bottom. It creates two circulations flows around the impeller shown in Figure 1.2(a). The helical ribbon impeller pumps the fluid in the axial direction (Ameur et al. 2012; Zhang et al. 2014). The flow produced by the helical ribbon, shown in Figure 1.2(b), confined in the inside and outside regions of the blade, while the flow between the wall and bulk liquid is mainly circular in nature. The large shear strain developed between impeller and tank wall helps to generate axial flow. The screw used with helical ribbon impeller produces strong axial movement inside the tank.

Rushton turbine is a radial flow impeller and is used to mix low viscous fluid at high Reynolds number. On other hand the axial flow helical ribbon impeller is used to mix very high viscous fluid where Reynolds number is necessarily kept low. Thus Rushton turbine and helical ribbon impellers are two poles impeller and made us interested to study.

1.2 IMPORTANT ASPECTS OF MIXING PROCESS

The following aspects of the mixing process are very important (Chhabra and Richardson, 2008):

- Mechanisms of mixing
- Scale-up of stirred vessels
- Power number
- Flow number
- Residence Time Distribution (RTD)
- Mixing time

1.2.1 Mechanisms of Mixing

The homogenization of liquids (Busciglio et al., 2014; Bao et al., 2015) occurs due to molecular diffusion in laminar mixing. In turbulent mixing, the inertial force imparted by the impeller to the surrounding liquid helps to form eddies. Mixing by eddy diffusion is faster and, therefore, turbulent mixing occurs more rapidly than laminar mixing.

1.2.2 Scale-up of Stirred Vessels

To have the same flow structures, the geometrical, kinematic and dynamic similarity and identical boundary conditions are to be maintained in two different size systems. The power used by the agitator can be related to the geometrical and mechanical arrangement of the mixer. Many dimensionless numbers like Reynolds, Froude and Weber numbers are important for scale up of the mixing processes. Froude number becomes important when significant vortex formation occurs.

1.2.3 Power Number

Power consumption is the most important design parameter of the stirred tank (Wu, 2009 & 2010a; Xie et al., 2014). It represents the rate of energy dissipation within the liquid. The non-dimensional Power number, N_p, includes the power consumption, speed of the impeller and effective viscosity terms. The dependency of Power number on the impeller Reynolds number, *Re* can be presented graphically called Power curve. For a given stirred tank and impeller, there should be a unique curve. A typical power curve is shown in Figure 1.3. It can be seen that at low values of the Reynolds number, less than about 10, a laminar region exists and here the flow is dominated by viscous forces. The slope of the power curve (on log-log scale) is –1 indicating

$$N_p = \frac{K_p}{Re} \qquad 1.1$$

where, K_p is a constant called power constant. It depends only on the system geometry. The range of a laminar zone can be extended to a higher Reynolds number with decreasing the value of flow index of non-Newtonian fluids. The impeller Reynolds number is defined by

$$Re = \frac{\rho N D_i^2}{\mu_a} \qquad 1.2$$

where ρ is the density of the liquid, N is the rotation of the impeller, D_i is the diameter of the impeller and μ_a is apparent viscosity. For Newtonian fluid μ_a is the dynamic viscosity. At high Reynolds numbers, greater than about 10^4, the power number is essentially constant. In the transition zone, a non-simple mathematical relation between power number and Reynolds number exists.

1.2.4 Flow Number

Flow number is, N_q is another important parameter which calculates the discharge capacity of the impeller (Wu, 2009 & 2010a; Delafosse et al., 2014). It is defined as

$$N_q = \frac{Q}{ND_i^3} \tag{1.3}$$

where, Q is the volumetric flow rate of fluid passing through an area adjoining the impeller with a height equal to that of the impeller blade. The N_q increases with the impeller Reynolds number and becomes constant at higher Re (Lamberto et al., 1999; Hall, 2005).

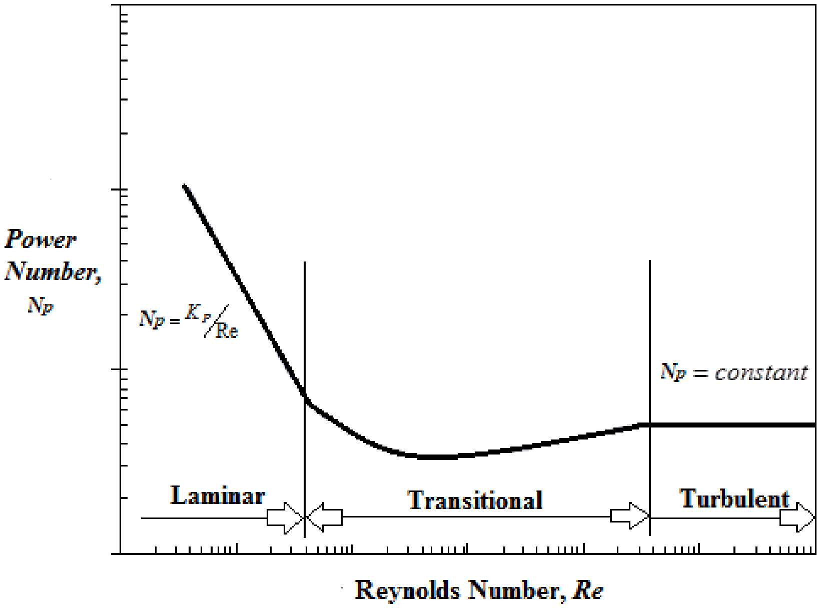

Figure 1.3 General characteristics of power curve.

1.2.5 Residence Time Distribution (RTD)

The knowledge of the liquid RTD in the stirred tank is important to identify the mixing characteristics that occur in the tank (Liu, 2012; Dagadu et al. 2014). RTD finds the duration of the various elements passed in the tank and it also measures the extent of back mixing in the tank (Fogler, 1999). The desired flow pattern inside the tank can be achieved using RTD tools and hence, this tool can be used for process scale up. Experimentally, RTD is determined by injecting a tracer into the tank and then measuring the tracer concentration at the exit as a function of time. The selected tracer should be nonreactive, easily detectable, should have the same physical properties as of tank liquid, and should be completely soluble in the mixture (Fogler, 1999).

1.2.6 Mixing Time

Mixing time is the time needed to produce a mixture or a product of pre-determined quality, (Chhabra and Richardson, 2008; Delafosse et al., 2014). The mixing time is measured as the interval between the tracer injection time and the time when the contents of the vessel have reached the required degree of homogeneity (95 or 99% of the final value). It is graphically shown in Figure 1.4. The mixing time primarily depends on the geometry of the impeller, rheology of working fluids, etc. It also depends on the tracer injection method and the location of the detector.

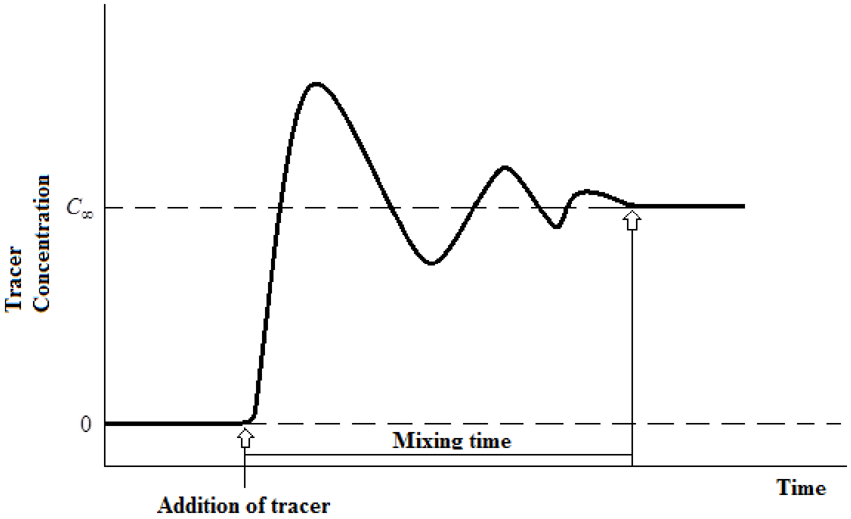

Figure 1.4 Mixing time measurement using tracer concentration.

1.3 ENTROPY GENERATION MINIMIZATION

The analysis of the second law of thermodynamics i.e. finding entropy generation of thermal and chemical processes is very important (Awad and Muzychka, 2012; Adham et al., 2014). The entropy generation in a flow system with heating facility is associated with major energy losses due to heat transfer and fluid friction irreversibility (Kahraman and Yurusoy, 2008). If entropy generation is decreased, the destruction of available exergy decreased and the destruction is minimal at the minimum entropy generation point. Thus, to improve the performance of any heat transfer and fluid flow process, the entropy generation minimization is considered as an effective tool (El Haj Assad and Oztop, 2012). At the minimum entropy generation, the utilization of the supplied energy is a maximum for a particular system.

1.4 ORIGIN OF THE WORK

Rushton turbine is a widely used radial impeller to mix low viscous Newtonian and non-Newtonian fluids. The advantage of it is to use at very high speed so that the turbulent state can be reached very quickly. For high viscous fluids, the Rushton turbine creates cavern around the impeller and the speed of the impeller may result in the formation of large amount of heat (Solomon et al., 1981; Pakzad et al., 2008). Thus, ultimately the mixing efficiency of high viscous fluids with Rushton turbine is very less. There is abundant research work available on the hydrodynamic and mixing behavior of stirred tank with Newtonian fluid. Both the experimental and theoretical works are included there. But the meagre amounts of hydrodynamics data of non-Newtonian liquids in stirred vessels are available in the literature (Venneker et al., 2010). Venneker et al. (2010) have reported excellent experimental work on the turbulent velocity fields of both Newtonian and non-Newtonian fluids. The work has motivated us to predict their experimental data by CFD model equations.

The helical ribbon impeller is always used for the mixing operation and particularly for the highly viscous liquid. As a consequence, it appears important to study this impeller and to make a comparison with the helical screw ribbon impeller through a CFD simulation. In mixing studies, the Metzner-Otto relation, namely, the effective shear rate for non-Newtonian fluid is directly proportional to the speed of the impeller and the proportionality constant K_s is independent of fluid property (Metzner and Otto, 1957). Some researchers have validated this relation (Chavan and Ulbrecht, 1973) and else have found contradictory results. Hall and Godfrey (1970), Rieger and Novak (1973), Nagata (1975) have observed the only geometry dependent K_s whereas Yap et al. (1979) and Delaplace et al. (2006) have found dependency of K_s on the power law index. So, it is necessary to re-examine the Metzner-Otto hypothesis numerically for the given experimental condition available in the open literature (Brito-De La Fuente et al., 1997). Further for helical ribbon with screw (HRS) impeller, the flow number is not yet available in the literature. The mixing study of stirred tank with HRS is also untouched, and the quantitative estimation of power number is also limited to laminar zone. Therefore, the present work has responded to these shortcomings of the previous works.

Several applications of the entropy generation minimization (EGM) are found in the literature in designing many heat transfer devices. Only a very few works are carried out in the area of entropy generation minimization of continuous stirred tank (Naterer and Adeyinka, 2009; Driss et al., 2012). Those work used only analytical equations for mass, energy and entropy. EGM is theoretically sound technique to optimize any non-isothermal flow processes. These have motivated us to apply EGM technique for designing non-isothermal stirred tank. The entropy generations are calculated using the computed velocity and temperature gradients by CFD models.

The RTD study gives an idea on the distribution of flow structure in a stirred tank. It can find the distribution of stagnant and mixed zones inside the tank. Regarding this many experimental and theoretical works already have been done (Arratia et al., 2004; Xiao-chang et al., 2008; Liu, 2012; Vite-Martinez et al., 2014). A long back, Burghardt and Lipowska (1972) and Lipowska (1974) have determined experimental RTD of the stirred tank in the presence and absence of impellers and baffles. Lipowska (1974) used a unique method based on the swept volume of impeller calculating the RTD, and Burghardt and Lipowska (1972) used a tracer injection method in their experimental work. No one yet predicted RTD numerically by calculating the swept volume of the impeller. Also, excellent work of Burghardt and Lipowska (1972) are not used to validate the CFD models yet. These have encouraged us to simulate the stirred tank for predicting the experimental RTD data of Burghardt and Lipowska (1972) and Lipowska (1974). The validated models are further used to design a non-ideal stirred tank reactor.

1.5 OBJECTIVE OF THE PRESENT RESEARCH PROJECT

Numerical studies of the stirred tank mixing process, optimum designing and parametric study of the mixing performance are carried out in the present work. The specific objectives of the present research work are

- ❖ Numerical study of the mixing performance of stirred tank with Rushton turbine impeller
    - ✓ Prediction of interaction of Reynolds number and flow behavior index with the

  velocity profiles using non-parametric test.

  - ✓ Prediction of flow number, power number, mixing time and dispersive mixing efficiency using the validated CFD models.
  - ✓ Prediction of entropy generation and optimization of the non-isothermal continuous stirred tank using entropy generation minimization method.

- ❖ Numerical study of the mixing performance of stirred tank with helical ribbon impeller
  - ✓ Prediction of power constant, K_p, and impeller geometry constant, K_s, for different types of helical ribbon screw impeller.
  - ✓ Prediction of generalized power consumption curve with the computed K_s.
  - ✓ Prediction of power number and flow number up to transition zone.
  - ✓ Prediction of entropy generation and optimization of the non-isothermal stirred tank using entropy generation minimization method.
- ❖ Numerical study of the mixing performance of stirred tank with residence time distribution (RTD) method
  - ✓ Prediction of the effect of the tank Reynolds number, rotations of impeller, and viscosity of working fluids on the RTD of the stirred tank.
  - ✓ Prediction of the distributions of the mean residence time, variance, holdback and segregation of the stirred tank.

1.6 ORGANIZATION OF THE THESIS

The thesis has been divided into six chapters. The first chapter presents a brief introduction to a mixing process in stirred tank with Rushton turbine and helical ribbon impeller as the agitator. The motivation for the present work is presented. The chapter also includes the objective of the present work. **Chapter 2** presents an extensive survey of the literature on many aspects of the mixing process. It also discusses various design parameters and also experimental and numerical design method of mixing process in stirred tank. The background of residence time distribution is also presented.

Chapter 3 demonstrates the modelling and simulation study of the performance stirred tank with Rushton turbine impeller. It includes the prediction of experimental hydrodynamic behavior of the stirred tank available in the open literature. The mixing study in terms of the characteristics mixing parameters like power number, flow number and mixing time also have been demonstrated. The optimum design of the non-isothermal reactor by EGM technique also described here.

Chapter 4 describes the modelling and simulation study of the performance of stirred tank with the helical ribbon and helical ribbon with screw impeller. The performance of the mixing process is shown in terms of mixing parameters like power number, flow number, and mixing time. The geometry constant, Ks has been calculated. The optimum design of the non-isothermal stirred tank in the presence of helical ribbon and helical ribbon with screw impeller has been carried out in this chapter.

Chapter 5 describes the prediction of RTD by both swept volume method and tracer injection method. The CFD predicted RTD is used to design the non-ideal stirred tank just by finding the parameters like holdback, segregation, etc.

Finally, **Chapter 6** includes some concluding remarks and the scope of future work.

CHAPTER 2

LITERATURE REVIEW

The batch and continuous stirred tank is widely used in chemical and its allied industries for mixing purposes. The mixing process is essential due to its profound influence on the blending, transport and reaction phenomena, power consumption and operating efficiency (Yeoh et al., 2005). The flow pattern in the tank is the key parameter in the mixing process. The fluid movement inside the tank is achieved by the impeller. On the basis of the direction of flow, impellers are classified into two broad categories (i) radial flow impellers (ii) axial flow impellers (shown in Figure 2.1). The radial flow impeller is mainly used for producing turbulence while the axial flow impeller is used for generating convection. Radial flow impellers are more suited for applications such as gas-liquid, liquid-liquid and other multiphase dispersions. Axial flow impellers are used for blending, heat transfer and solid suspension.

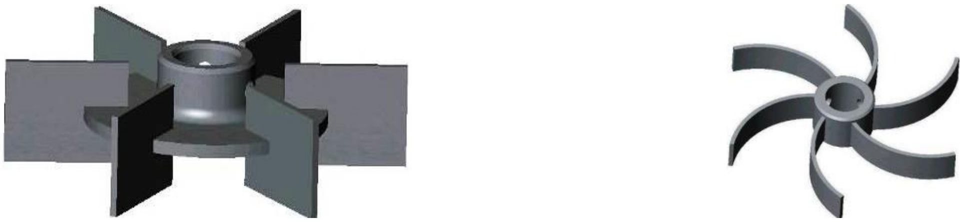

(a) Rushton Turbine

(b) Spiral Turbine

(c) Spiral Turbine Propeller

(d) Pitched blade turbine

Figure 2.1 Radial flow impeller: (a) Rushton turbine, (b) Spiral turbine; Axial flow impeller: (c) Spiral Turbine Propeller, (d) Pitched blade turbine (Harnby et al., 1992).

The axial impeller discharges fluid mainly axially, parallel to the impeller shaft. The fluid is pumped by the impeller, normally towards the bottom of the tank. The flow makes a turn at the bottom side of the tank, then moves along the bottom and rises near the tank wall. From Figure 2.2(a), it becomes clear that the flow radially enters at the tip of the impeller blade. For radial impellers, the discharge of fluid is radially out from the blade towards the tank wall. The flow splits at the tank wall, and approximately 50% of the fluid circulates towards the surface while the rest to the bottom. It creates two regions of low mean velocity as shown in Figure 2.2(b).

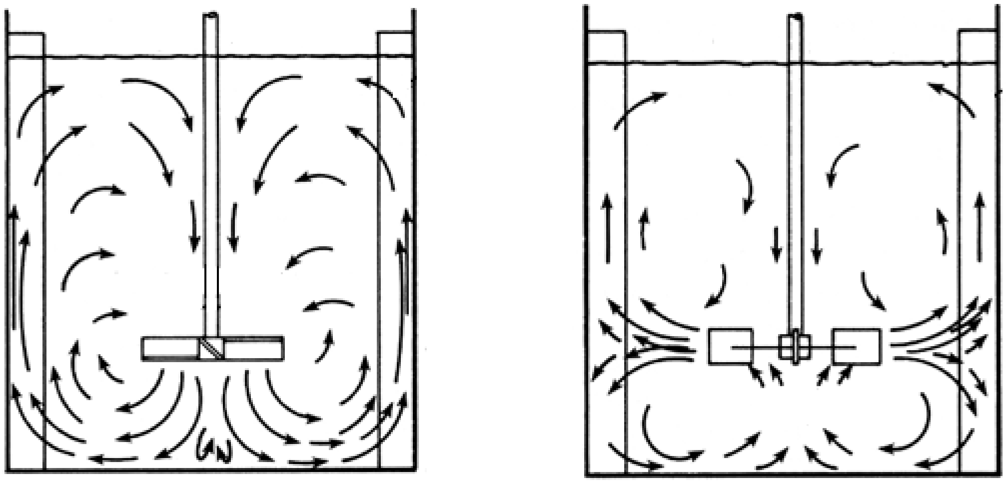

(a) (b)

Figure 2.2 (a) Flow pattern produced by axial impeller; (b) Flow pattern produced by radial impeller (Harnby et al., 1992).

For high viscous liquid, the close clearance impeller, such as anchor impeller, gate-type impeller, helical ribbon impeller, etc. is often used for the mixing (Figure 2.3). The anchor and gate-type impeller are slowly rotating, large surface area impeller, with small tank wall clearance. Hence, the anchor impeller does not produce strong top-to-bottom fluid movement. However, the helical ribbon impeller, which pumps the fluid in the axial direction, used to overcome the drawback of an anchor impeller. The flow produced by the helical ribbon impeller confined in the inside and outside regions of the blade while the flow between the wall and the bulk liquid is mainly circular in nature. Sometimes, the screw is used with helical ribbon impeller to promote strong axial movement inside the tank.

Residence time distribution (RTD) of a reactor is also a characteristic of the mixing that occurs in the chemical reactor. The RTD gives information about how long the various elements have been in the reactor. It provides a quantitative measure of the degree of backmixing within a system. Thus, the knowledge of the RTD is important (Fogler, 1999) for accurate modeling of the system and to design reactor to have a desired flow pattern in the tank. Another important issue about the use of RTD is that it does thorough comparison between systems with different configurations and represents a tool in successful process scale-up.


(a) (b)

Figure 2.3 Close clearance impeller; (a) Anchor impeller, (b) Helical ribbon impeller.

The efficiency of heat and mass transfer in a stirred tank reactor (STR) depends largely on the extent of mixing. The optimum designing of STR is a challenging task to achieve the required mixing of the reactants. Many researchers carried out it by solving the standard process model equations based on the first law of thermodynamics along with the conventional or latest optimization techniques (Powell and Hill, 2008; Petrov and Tzonkov, 2009; Chaibakhsh et al., 2010; Chen and Wang, 2010; Song et al., 2010; Vaneshani and Jazayeri-Rad, 2011; Sivapathasekaran and Sen, 2013; Aghbolaghy and Karimi, 2014). The objectives of all these optimization techniques are either to minimize the cost or to obtain the optimal operating condition to control the product quality. The application of the second law of thermodynamics with entropy generation minimization (EGM) approach is a useful technique to achieve the optimum conditions (Alebrahim and Bejan, 1999; Zimparov and Penchev, 2003; Balaji et al., 2007; Jankowski, 2009; Guo et al., 2010). In general, the mathematical models of stirred tank include all three transport equations: momentum, mass and energy. The finite temperature gradient in a heat transfer process and a frictional loss in the flow process increase the entropy generation at the cost of work potential of the system. Thus, the destruction of available energy decreases with decreasing entropy generation and it is minimal at the minimum entropy generation point. Nowadays, the energy is one of the most concerned issues. At the minimum entropy generation, the use of supplied energy is a maximum for the particular system.

To know the background of the present work, the literature survey is carried out giving emphasis on the followings.

- Concept of Newtonian and non-Newtonian Fluids
- Mixing in stirred tank with Rushton turbine
- Mixing in stirred tank with helical ribbon impeller
- Determination of geometry constant, K_s
- Entropy generation optimization
- Ideal and non-ideal reactors
- Residence time distribution (RTD) analysis

2.1 CONCEPT OF NEWTONIAN AND NON-NEWTONIAN FLUIDS

For Newtonian fluid shear stress is directly proportional to the local shear rate. Mathematically it is written as (Chhabra and Richardson, 2008)

$$\tau = \mu\left(-\frac{dV}{dy}\right) = \mu\dot{\gamma} \qquad 2.1$$

where τ is the shear stress, μ is a proportionality constant known as viscosity and $\frac{dV}{dy}$ is the derivative of velocity component.

A non-Newtonian fluid is a fluid in which the shear stress is not linearly proportional to shear rate. There are different types of non-Newtonian fluids depending on the relation between shear stress and shear rate such as Dilatant fluid, pseudoplastic fluid, Bingham plastic and yield-pseudoplastic fluid. The flow behavior curve is shown in Figure 2.4.

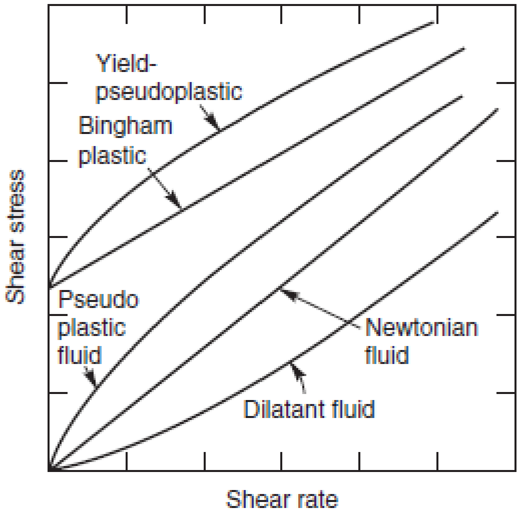

Figure 2.4 Flow behavior curve (Chhabra and Richardson, 2008).

2.1.1 Pseudoplastic Fluid (Shear Thinning Fluid)

Pseudoplastic (shear thinning) fluid is characterized by an apparent viscosity which decreases with increasing shear rate. Hence this fluid is also known as shear thinning fluid. Many mathematical expressions of varying complexity and form have been proposed in the literature to model shear thinning characteristics. Only a few selected and widely used viscosity models are given here.

1. The power law

The relationship between shear stress and shear rate for a shear thinning fluid can often be approximated by a straight line on logarithmic plot. Mathematically it can be expressed as (Chhabra and Richardson, 2008)

$$\tau = K(\dot{\gamma})^n \qquad 2.2$$

in which K and n are the fluid consistency coefficient and the flow behavior index, respectively.

So the apparent viscosity for the power-law fluid is

$$\mu = K(\dot{\gamma})^{n-1} \qquad 2.3$$

For $n < 1$, the fluid exhibits shear-thinning properties, $n = 1$, the fluid shows Newtonian behavior and for $n > 1$, the fluid shows shear-thickening behavior.

2. ***The Carreau viscosity equation***

When there are significant deviations from the power-law model at very high and very low shear rates, it is necessary to use a model which incorporates the limiting values of viscosities μ_0 and μ_∞. The model was developed by Carreau (1972).

$$\frac{\mu - \mu_\infty}{\mu_0 - \mu_\infty} = \{1 + (\lambda\dot{\gamma})^2\}^{(n-1)/2} \qquad 2.4$$

where n (< 1) and λ are two curve-fitting parameters. This model predicts Newtonian fluid behavior $\mu = \mu_0$ when either $n = 1$ or $\lambda = 0$ or both.

3. ***The Cross viscosity equation***

Cross (1965) proposed a four parameter model for viscosity and is written as:

$$\frac{\mu - \mu_\infty}{\mu_0 - \mu_\infty} = \frac{1}{1 + k(\dot{\gamma})^n} \qquad 2.5$$

In Equation 2.5, n (< 1) and k are two fitting parameters whereas μ_0 and μ_∞ are the limiting values of the apparent viscosity at low and high shear rates, respectively.

2.2 MIXING IN STIRRED TANK WITH RUSHTON TURBINE

Van Der Molen and Van Maanen (1978) used a laser Doppler velocimetry (LDV) equipped with a frequency shift to measure the turbulent flow in a stirred tank with Rushton turbine. Water (Newtonian fluid) was used as the working fluid. They found that the turbulent energy near the impeller is very sensitive to the geometry of the impeller. Benayad et al. (1985) measured the velocity fluctuations in the discharge flow of the Rushton turbine with a laser Doppler anemometer (LDA). They observed the occurrence of an isotropic homogeneous turbulence far from the impeller region.

Yianneskis et al. (1987) studied experimentally the steady and unsteady flow characteristics in a stirred tank with Rushton turbine. They showed that the flow stream from the impeller discharged at an angle of the impeller blade. They also revealed that the vortices were formed above and below the impeller, and the size of vortices depends on the impeller clearance from the bottom tank wall.

Costes and Couderc (1988) analyzed the hydrodynamic characteristics of six-blade Rushton turbine in two different volumetric tanks filled with the water. They found that the velocity profiles in non-dimensional form are independent of the tank size and the impeller rotational speeds i.e. independent of the Reynolds number.

Bujalski et al. (1987) obtained power numbers for a wide Reynolds number range of Rushton turbines using water as the working fluid. They carried out experiments in six different fully baffled tanks. They showed that for Reynolds numbers $> 2 \times 10^4$, the average peak power number is dependent on the impeller disc thickness to impeller diameter and the tank diameter ratios.

Tiljander et al. (1997) characterized a high flow impeller, a Rushton turbine and a pitched blade turbine, by measuring local mean and fluctuating velocities with the LDV technique. They carried out experiments in turbulent flow regime with water as working fluid. They found that the flow rate at constant impeller rotations increased in the order of high flow impeller, Rushton turbine and pitched blade turbine and the order of turbulence intensities were, high flow impeller, pitched blade turbine, Rushton turbine.

Cheng et al. (1997) experimentally measured 2D velocity flow fields in a standard tank for different impeller speeds using PIV. They observed a spatial variation of flow characteristics such as vortex formation near the impeller. They also developed the technique to derive turbulence dissipation rate and energy intensities, local velocity gradient and Kolmogorov microscale for raw PIV data. They used PIV data to calculate vorticity, which could not be obtained by more traditional measurement techniques, such as LDV.

Lee and Yianneskis (1998) experimentally investigated the structure of the flow in a tank filled with distilled water and stirred by a Rushton turbine in turbulent regime. They determined the time and length scales of turbulence to estimate the dissipation rate of turbulence energy. They found that the levels of turbulence energy and dissipation were high near the turbine and decreased rapidly with increasing distance from the turbine blades. They also observed that close to the impeller blades, the turbulence in the impeller stream is mostly anisotropic.

Montante et al. (1999) investigated the effects of the impeller clearance and rotational speed on the flow patterns in the water filled tank equipped with the Rushton turbine. They found that at impeller clearances around 1/5th of the diameter of the tank, the characteristic double loop flow pattern changed to a single loop flow pattern with the impeller discharge stream direction becoming partially axial and slightly inclined to the horizontal. They also observed that the inclination of impeller discharge flow varied with radial distance from the impeller and the angular position between the blades.

Escudie and Line (2003) analyzed the hydrodynamics generated by a Rushton turbine using PIV in a water filled tank in turbulent flow regime. They collected the data like the mean velocity, the periodically induced stress, and the Reynolds stress. They used these data to recognize and measure the transfer of turbulent kinetic energy between mean flow, fluctuating flow, and turbulence and then estimated the dissipation rate of turbulent kinetic energy from the balance of turbulent kinetic energy.

Jahangiri (2005) measured mean and fluctuating tangential and radial velocity components using a two-component LDA for a typical Rushton turbine impeller in the lower transition region ($35 < Re < 1800$). The working fluids were different concentrations of polyacrylamide solutions which behaved as non-Newtonian fluid. He found that the dimensionless radial and tangential velocities are almost independent of the impeller speed.

Lamberto et al. (1999) characterized the laminar flow structure of glycerine inside an unbaffled stirred tank generated by a 6-blade radial flow impeller using flow visualization experiments, particle imaging velocimetry experiments, and computational fluid dynamics (CFD) simulations. They found that the circulation flow is approximately four times the pumping capacity of the impeller.

Torrez and Andre (1999) numerically investigated the mixing of yield stress fluids in the laminar region tank stirred by Rushton turbine using CFD package, Fluent. They studied the effect of impeller rotations and position on the local average shear rate. They found that, near the impeller, the shear rate is higher and it is proportional to the impeller rotations. They also predicted the power number, power constant and Metzner-Otto constant for the yield stress fluids.

Ranade et al. (2001) studied the existence of trailing vortices behind the blades of a standard Rushton turbine with PIV technique in the water filled tank. Further, they carried out the CFD simulation with snapshot approach and compared the predicted results with the PIV results. They also predicted the flow number and compared with literature data.

Yeoh et al. (2005) simulated the mixing of an inert scalar in a tank stirred by a Rushton impeller using the large eddy simulation (LES) technique. They found that a substantial amount of scalar trapped in a region between two vertical baffles. They recorded scalar concentrations at numerous points inside the domain and showed the occurrence of different mixing patterns across the tank.

Montante et al. (2006) investigated the effect of shaft eccentricity on the hydrodynamics of unbaffled Rushton turbine stirred tank filled with water. They measured the velocity vectors in horizontal and vertical planes through the PIV technique. They used the PIV results to perform the RANS-based CFD simulation.

Javed et al. (2006) simulated a batch mixing in a baffled water vessel agitated by the Rushton turbine. They used sliding mesh technique in Fluent software. They predicted the tracer concentration distribution of an inert tracer at different locations in the tank with time.

Bombac et al. (2007) presented an experimental analysis of power consumption in mixing and dispersing of air into a shear thinning CMC solution in a vessel stirred with a Rushton turbine. They used the Metzner-Otto method to calculate relation between power and Reynolds number. In aerated stirred tank, they found that, at higher impeller speeds and gas flow rates, the power consumption of the impeller reduced.

Yapici et al. (2008) numerically predicted the turbulent flow field in a water filled tank generated by Rushton turbine impeller using large eddy simulation. They further studied the effects of impeller clearance and disc thickness on the power number and found that the power number decreased with decreasing clearance and increasing disc thickness.

Zadghaffari et al. (2008) computed and validated the mixing time, pumping number and power number in a stirred tank agitated by 6-blade Rushton turbine in the turbulent flow field. They used the LES and the sliding mesh approach in the simulation work.

Ochieng et al. (2008) carried out mixing studies in stirred tank at low clearance. They showed that at a small impeller clearance, the Rushton turbine generates a flow field that changed from the typical two circulation loops to a single circulation loop pattern like an axial impeller. They also carried out experiments and simulation by adding a draft tube in the tank to improve axial velocity and were able to achieve significant improvement in mixing performance.

Zadghaffari et al. (2008) numerically and experimentally investigated the flow field, pumping capacity and mixing time in a fully baffled stirred vessel with dual six-blade Rushton turbines. The operating liquid was water, and a Rhodamine-590 was used as tracer for mixing study. The LES and sliding mesh method was used for the numerical predictions.

Venneker et al. (2010) did an experimental work on the hydrodynamics of shear thinning liquids such as the aqueous solution of carboxymethyl cellulose and xanthan gum in a stirred tank. They found all the time average velocity components at the impeller disk level of the stirred tank. They noted the condition for Reynolds number similarity when the velocities became independent of Reynolds number. They also found the effects of Reynolds number and flow behavior index on the flow filed.

Wu (2009, 2010a) performed CFD simulations study of mixing in an anaerobic digesters. The turbulent flow mixing was modelled by employing the realizable k-ε model. The predicted power and flow numbers of the impeller were validated with the experimental data.

Zhipeng et al. (2011) investigated the single-loop flow fields in Rushton turbine stirred tanks with clearance, 0.15 times the tank diameter, by using PIV experiments and LES methods. The stirred tank was operated in turbulent regime with water as the working fluid. They found that the Reynolds number had a little effect on the mean flow and the single loop flow pattern changed into a double loop one if the diameter of impeller increased from 1/3 to 1/2 times the tank diameter.

Wang et al. (2013) investigated experimentally and numerically the mixing of viscous Newtonian fluids (glycerol) in Rushton turbine stirred tank with different inclined shaft and offset impeller configurations. They used decolourization visualization method in their experimental study. They found that the angle of inclination had the significant effect on the mixing time, as the larger inclination destroyed the dead zone. They also found that the increased shaft angle reduced the specific energy required for complete homogenization. From simulations results, they showed that both liquid blending and particle dispersion enhanced by using inclined-shaft systems.

Driss et al. (2014) studied experimentally the turbulent flow induced by the Rushton turbine inside a baffled stirred tank. They used 2D PIV technique to determine vector field’s plots and contours of time-averaged radial and axial components of velocities in the impeller stream.

Molnar et al. (2014) experimentally and numerically studied the flow field, mixing time, and power number in stirred tank agitated by four different Rushton turbines varying in number of blades from three to six. They used ethylene-glycol as the working fluid. They showed that the mixing time is dependent on the impeller blade number and rotational speed. They predicted the power number for all the impellers to compare the mixing efficiency.

Delafosse et al. (2014) predicted the hydrodynamics behavior of bioreactors with biological reactions using the combination of CFD simulation and compartment model. They used a velocity flow field obtained by CFD to find the flow rates between two adjacent compartments. The mixing time obtained by this method is compared and found a good accuracy with experimental results.

Xie et al. (2014) experimentally measured the power consumption of different concentration of xanthan gum solution under the transitional flow regime in stirred tank. Impellers used in various combinations can be distinguished as two categories: small-diameter impeller, which include Rushton turbine, hollow blade turbine and wide-blade hydrofoil impeller and large-diameter including ellipse gate impeller, intermig and double helical ribbon. They observed that to gain the same power input for impeller combinations, the rotating speed of small-diameter impeller combinations has to be increased as the concentration of xanthan gum increases while it has to be decreased for large-diameter impeller combinations.

Sossa-Echeverria and Taghipour (2015) numerically investigated the flow generated by the axial flow impeller installed on the side of tank which is filled with shear thinning non-Newtonian fluid. They carried out the simulations in the range of laminar to transition flow regime and compared successfully numerically obtained velocity vectors field results with PIV experiments. They also showed the effects of impeller blade angle and rheological characteristics on the velocity components, location of recirculation loops and the power requirement.

2.3 MIXING IN STIRRED TANK WITH HELICAL RIBBON IMPELLER

In the field of viscous Newtonian and non-Newtonian mixing, helical ribbon impellers are considered to be among the most efficient systems used to homogenize such complex substances. Like many other impellers, helical ribbon impellers are designed either empirically or based on experimental power draw correlations. These relationships derived from dimensional analysis and flow analogies (Brito-De La Fuente et al., 1997).

Chavan and Ulbrecht (1972) developed a generalized model to correlate the power consumption of the helical ribbon impeller for Newtonian, as well as non-Newtonian shear thinning fluids. They examined the correlation for Newtonian and shear thinning fluids with available literature data for a broad range of geometrical parameters. In 1973, they reported generalized power correlations for a variety of close clearance helical impellers, i.e. helical screw impellers with a draft tube, helical ribbon impellers, and combined ribbon-screw impellers.

Takahashi et al. (1984) carried out experimental measurements of power consumption for pseudoplastic fluids in laminar zone using helical ribbon impeller as stirrer. They proposed an empirical correlation of power consumption for helical ribbon impeller based on the three geometrical parameters, clearance between blades and wall, impeller pitch, and blade width.

Shamlou and Edwards (1985) reported the power input measurement for helical ribbon impeller for viscous Newtonian and non-Newtonian fluids. They provided correlations based on different impeller geometry parameters, particularly in the small Reynolds number region.

Carreau et al. (1993) investigated the power drawn for the mixing of viscous Newtonian and non-Newtonian fluids using a different helical ribbon impeller. They calculated the effective shear rate from the torque of the impeller and compared with the effective shear rate determined from Metzner-Otto method. They also reported that the power consumption increased with increase in fluid elasticity and showed that the power curve for viscoelastic fluids deviated from the generalized Newtonian power curve in the laminar region.

Netusil and Rieger (1993) measured the power consumption of screw and helical ribbon impeller in pseudoplastic fluids in the creeping flow regime. They performed experiments with different geometrical configuration, such as screw with a draught tube, off centered screw and helical impeller with different pitch ratio. They suggested a correlation to calculate the values of the

Metzner-Otto coefficient, K_s and found that K_s increased with the decrease in the flow behavior index, n.

Cheng and Carreau (1994) investigated the power requirement in an aerated mixing of various Newtonian, shear thinning inelastic, viscoelastic and non-shear thinning elastic fluids with helical ribbon impeller in the laminar and transition flow regimes. They reported that the power requirement for the non-shear thinning elastic fluids was higher in aerated fluids than in unaerated fluids. For the shear thinning inelastic fluids, they observed a decrease in power consumption.

Espinosa-Solares et al. (1997) measured power consumption for a dual coaxial mixer composed of a Rushton turbine and a helical ribbon in laminar conditions for Newtonian and non-Newtonian shear thinning fluids. For the non-Newtonian fluids, they showed that, at a particular Reynolds number, the power consumption decreased as the shear thinning behavior increased. They obtained a dimensionless and unique representation of the power consumption data by shifting the non-Newtonian power consumption results to the Newtonian curve.

Brito-De La Fuente et al. (1997) experimentally carried out mixing in batch stirred tank with helical ribbon and helical ribbon screw impellers. They used different shear thinning fluids with power law index varied from 0.14 to 0.65. They showed that the power consumption of fluids decreased as the flow behavior index decreased. They compared predicted K_s with the Metzner and Otto method and found good agreement. They found that K_s is function of the flow behavior index especially for high shear thinning fluids. They reported that the power consumption increased with decrease in the blade pitch ratio or increase in blade width ratio. They also concluded that K_s is independent of both blade pitch and blade width ratio.

Tanguy et al. (1997) investigated experimentally and numerically the performance of mixing of Newtonian and non-Newtonian shear thinning fluids in a tank stirred with dual impeller agitator composed of a disc turbine and a helical ribbon impeller. They showed that the dual impeller mixer outperformed the standard helical ribbon in terms of axial circulation. They developed a generalized power curve for the dual impeller mixer.

De la Villeon et al. (1998) numerically studied the mixing performance of different helical ribbon impeller in shear thinning fluids. They considered single helical ribbon impeller, double helical ribbon impeller, and double helical ribbon impeller with the central screw for the finite element simulation. They measured mixing efficiency using the dispersion of tracer, length stretch values, and dispersive mixing efficiency coefficients. From simulated results, they found that the double helical ribbon impeller is more efficient than single helical ribbon impeller and double helical ribbon impeller with the central screw.

Bertrand et al. (1999) numerically found the power drawn in viscoelastic fluids with helical ribbon impeller. They solved the governing fluid flow equation using finite element method combined with the Lagrangian method for the treatment of nonlinear equation. They predicted a rise in power drawn with the increase in the elasticity.

Delaplace et al. (2000) determined the Metzner-Otto constant, K_s for the helical impeller from PARAVISC mixing system for shear thinning and shear thickening fluid. For shear thinning fluid, they showed that K_s vary weakly with the fluid flow behavior index. While for shear thickening fluid, they reported a complex relation between K_s and the fluid flow behavior index because of the partial solidification of fluid around the impeller blade.

Aubin et al. (2000) simulated laminar mixing of Newtonian and non-Newtonian fluid in a tank stirred by a helical screw agitator with and without a draft tube. They predicted power number and the circulation number and determined impeller geometry constant for the geometry with and without the draft tube. They obtained Metzner and Otto constant, $K_s = 16.23$. From simulation data, they confirmed that power number constant was inversely proportional to Reynolds number and was dependent on the flow behavior index. They also found that the circulation number was unaffected by the Reynolds number but dependent on the tank geometry and properties of the fluids.

Yao et al. (2001) numerically analyzed the local and total dispersive mixing performance of MAXBLEND and double helical ribbons impellers. They found that MAXBLEND had an excellent local dispersive mixing performance than the double helical ribbon impeller, even though it induced a good total circulation throughout the stirring tank.

Dieulot et al. (2002) investigated the mixing of highly viscous Newtonian fluids in a tank using a helical ribbon impeller fitted with an anchor. They used a tracer injection method to find the degree of homogeneity in the tank. They showed that the use of time-dependent rotational speed during the mixing process saved the energy.

Shekhar and Jayanti (2003) performed CFD simulations of high viscous pseudoplastic fluids in laminar zone in a tank with helical ribbon impeller. They determined K_s using the circumference-average shear rate around the impeller and found K_s as dependent on geometrical parameters, but independent of the flow behavior index.

Perse and Zumer (2004) studied the mixing phenomenon of high viscous Newtonian and non-Newtonian fluids stirred with a single helical ribbon impeller. They measured torque to obtain power curve and to determine the viscosity of fluids at different impeller speeds. They showed that the torque depends on the impeller speed and the flow behavior index. They determined K_s for non-Newtonian fluids and showed that K_s were function of the flow behavior index.

Ihejirika and Ein-Mozaffari (2007) simulated the flow field generated in a tank by a helical ribbon impeller using a pseudoplastic fluid with yield stress in the laminar region. They used Ultrasonic Doppler velocimetry (UDV) to measure xanthan gum velocity. They calculated power consumption and mixing time from the predicted flow field. They found that the torque and power characteristics remained the same for upward and downward pumping impeller, but the mixing times were considerably longer for the downward pumping mode.

Chhabra et al. (2007) presented experimental and CFD study of the mixing times for viscous Newtonian and non-Newtonian viscoelastic fluids agitated with a Paravisc helical ribbon impeller (Ekato). They used an advanced imaging method to measure the mixing time in the tank. They observed significant differences in the mixing times for viscous Newtonian and non-Newtonian fluids.

Zhang et al. (2008) simulated a non-Newtonian flow field generated in the laminar region by a double helical ribbon impeller to calculate Metzner-Otto constant, K_s. They used three different methods to calculate Metzner-Otto constant; the slope method, the circumference-average shear rate around the impeller and the area-weighted average viscosity around the impeller. They found that all three methods predicted well the Metzner-Otto constant.

Tsui and Hu (2008) computationally investigated the mixing performance of a stirred tank with a screw impeller and with or without a draught tube. They used multiple reference frames and unstructured grid methodology for the simulation. They predicted the performance of the impeller in terms of circulation number, power number, and non-dimensional mixing energy.

Rahimi et al. (2010) performed experimental and CFD studies on mixing characteristics of modified helical ribbon impeller in a viscous fluid. They calculated several parameters like axial flow number, axial circulation time and power consumption, and showed that the modified impeller had the highest performance in terms of axial flow number and axial circulation time.

Tsui and Hu (2011) did numerical study on the mixing in the tank stirred by a helical ribbon impeller. They adopted the multi-reference frame model for the rotation of the impeller. They optimized the impeller geometry considering the parameters like blade pitch, the blade width, and the clearance between the blade and the surrounding wall. They reported that after optimization of the impeller geometry, the mixing time and the power consumption was reduced.

Sanjuan-Galindo et al. (2011) compared the mixing performance of three different helical ribbon impeller geometries. They gave particular emphasis on the improvement of pumping capabilities of helical ribbon impellers as it exhibited poor bottom pumping properties. They selected a standard bottom, an anchor type bottom and a paddle type bottom as the base design. They used 3D finite-element simulation technique to investigate the hydrodynamics and mixing performance using various distributive and dispersive criteria. They showed that the helical ribbon with a paddle type bottom operating in a down pumping mode offered the best performance.

Driss et al. (2011) numerical investigated the mixing performance of double helical ribbon and double helical screw ribbon impellers in stirred tank. They showed that the predicted velocity flow field was more active in the double helical screw ribbon impeller. They also showed that the effectiveness of the viscous dissipation and the pumping flow was more significant in the double helical screw ribbon impeller.

Ameur et al. (2012) simulated the mixing of shear thinning fluids in an unbaffled and flat bottomed tank with simple and double helical ribbon impeller. They predicted the effect of the impeller rotations, fluid properties, impeller size and impeller off bottom clearance on the flow fields and power consumption. They compared the predicted results of the two impellers and found that the double helical ribbon impeller gave best performance when placed in the middle of the tank, with moderate blade size and operating at *Re* > 20.

Bao et al. (2015) experimentally investigated the power consumption and mixing time in an elliptical bottom stirred tank with different coaxial mixers. Syrup and CMC solution as Newtonian and non-Newtonian fluid respectively were used for the experiments. Four different coaxial mixers combinations of 2-blade hydrofoil, Pfaudler impeller as inner one, and anchor or helical ribbon as outer one were used. They showed that Pfaudler-helical ribbon mixer had the lowest mixing time among four mixers for the same power input.

2.4 DETERMINATION OF GEOMETRY CONSTANT, K_S

Metzner and Otto (1957) assumed K_s to be a constant for a particular impeller geometry and also independent of liquid rheology. But for helical ribbon and helical ribbon screw impeller, there were some conflicting results exist in the literature towards the dependency of K_s on the flow behavior index *n*. Such as, Hall and Godfrey (1970), Rieger and Novak (1973), Nagata (1975), Sawinski et al. (1976), Chowdhury and Tiwari (1979), Kuriyama et al. (1983) and Shamlou and Edwards (1985) all concluded that K_s is only function of impeller geometry. However, Bourne and Bulter (1969), Chavan and Ulbrecht (1973), Yap et al. (1979), Carreau et al. (1993), Brito-De La Fuente et al. (1997) and Delaplace et al. (2006) had reported that K_s varies both with the impeller geometry and the flow behavior index, *n* of non-Newtonian fluids. In last four decades, many researchers developed correlation for K_s. Three different approaches were used to develop these correlations. In the first approach, the flow was assumed to be Couette type, and the helical ribbon impeller was replaced by an equivalent diameter cylinder having same torque experienced by the impeller (Bourne and Bulter, 1969; Chavan and Ulbrecht, 1973; Carreau et al., 1993). The developed analytical expression of K_s appeared dependent on the flow behavior index. Some researcher (Brito-De la Fuente et al., 1990) found it weakly dependent on the flow behavior index. The second approach used the concept of drag flow on rotating impeller and cylinder (Yap et al., 1979; Patterson et al., 1979). The third approach was based on the experimental prediction of K_s (Sawinski et al., 1976; Kuriyama et al., 1983; Shamlou and Edwards, 1985). It did not provide any dependency of K_s on impeller geometry and the liquid rheology. All these approaches made good idealisation of complex flow behavior, but none of these models explained functional dependency of K_s on impeller geometry and flow behavior index. Recently, Delaplace et al. (2006) developed an analytical model based on the Couette flow analogy to predict power consumption of helical and helical screw ribbon impeller. They claimed their model predicts better than the previously developed models. In recent years, the developments in computational fluid dynamics (CFD) techniques lead researchers to use CFD models as a substitute for experiment to obtain the detail view of flow field for a given set of mixing equipment. Some researchers carried out CFD simulations of mixing process with helical and helical ribbon impellers to understand their mixing characteristics (Tanguy et al., 1992; Driss et al., 2011; Rahimi et al., 2010; Tusi and Hu, 2011; De la Villeon et al., 1998; Yao et al., 2001). Shekhar and Jayanti (2003) performed CFD simulation of laminar mixing of high viscous pseudoplastic fluids to verify an assumed linear relationship between shear rate and the rotational speed of impeller (Metzner-Otto concept). Zhang et al. (2008) found K_s of non-Newtonian flow generated in the laminar region by a double helical ribbon impeller. They used three different methods to calculate the effective viscosity and in turn K_s. Method included: the slope method, the circumference-average shear rate around the impeller and the effective shear rate and the area-weighted average shear rate around the impeller. Zhang et al. (2008) concluded that all the three methods predicted well the Metzner-Otto constant. The details on the K_s determination methods are discussed below:

The methods for determination of K_s are given below:

Method 1:

Rieger and Novak (1973) proposed the analytical expression to determine impeller constant, K_s, as follows

$$K_s = \left(\frac{K_p(n)}{K_p} \right)^{1/(n-1)} \qquad 2.6$$

This method is also known as direct calculation of K_s.

The above equation can also be written as

$$\ln K_p(n) = \ln K_p - (1-n)\ln K_s \qquad 2.7$$

The K_s value can be obtained as the slope of the straight line from plot $K_p(n)$ versus (1-n) on log-log plot. This method is known as slope method.

Method 2:

Shekhar and Jayanti (2003) numerically examined the Metzner-Otto concept. They had drawn the radial profile of the circumferential averaged shear rate at mid-height of the vessel. The maximum shear rates were found from the graph for each impeller rotations. Taking this to be the effective shear rate near the impeller, its variation with speed of rotations was plotted and from slope of this plot K_s were calculated.

Method 3:

Chhabra and Richardson (2008) discussed the K_s determination method which was first established by Metzner and Otto (1957). The experimental evaluation of K_s is as follows:

(i) The Power number (N_p) was determined for a particular N.

(ii) The corresponding impeller Reynolds number, Re was obtained from the appropriate power curve (relating to an identical geometry) for a Newtonian liquid.

(iii) The apparent viscosity was computed from Re.

(iv) The corresponding shear rate was obtained, either directly from a flow curve or by use of an appropriate fluid model such as the power-law model.

(v) The value of K_s was calculated for a particular impeller configuration using $\dot{\gamma}_{eff} = K_s N$.

This procedure can be repeated for different values of N and an average value of K_s can be estimated.

2.5 ENTROPY GENERATION MINIMIZATION (EGM)

Many fluid flows and heat transfer devices are optimized using EGM technique. It was first proposed by McClintock (1951) who did the optimum design of fluid passages of a heat exchanger. Later, an abundant work in the area of EGM was carried out, and most of the works were analytical in nature. Bejan (1979) examined the entropy generation in the convective heat transfer process. He further carried out the entropy generation analysis of numbers of fundamental applications and showed that the minimization of entropy generation increased the efficiency of the system (Bejan, 1995). After that, the entropy generation minimization was used by many researchers for the purpose of analysis and optimization of systems such as fluid flow system, heat exchanger design, fins design, power plant design (Figure 2.5).

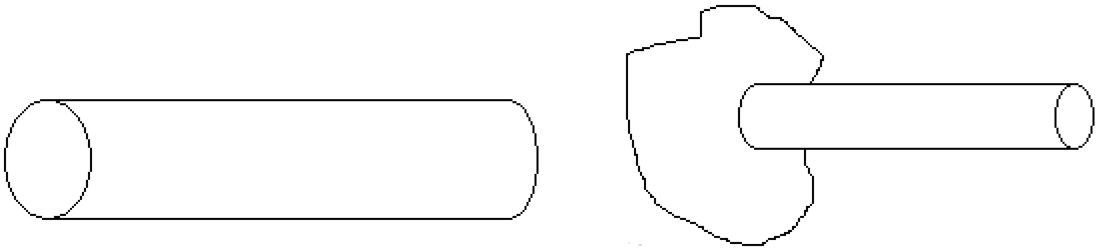

(a) Pipe flow

(b) Fins

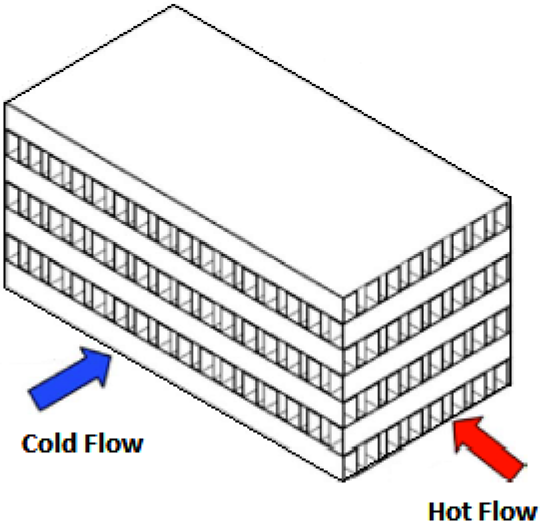

(c) Heat exchanger (Ahmadi et al., 2011)

Figure 2.5 Different types of systems optimized using entropy generation minimization.

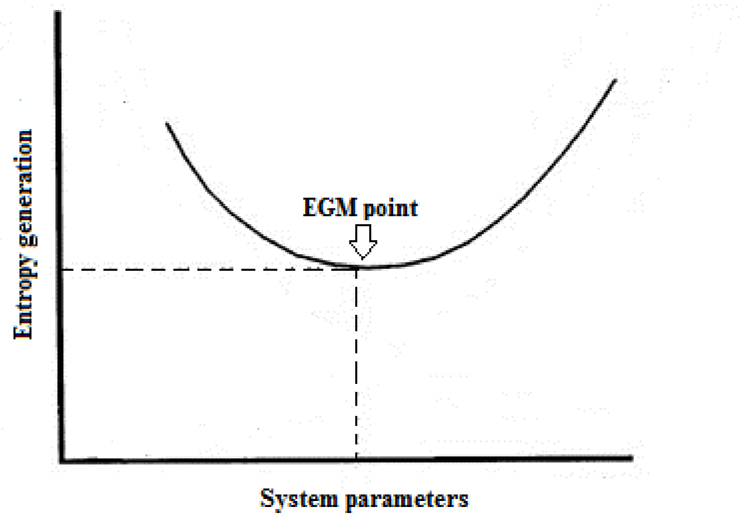

Figure 2.6 Entropy generation minimization curve.

A hypothetical EGM diagram is shown in Figure 2.6. The total entropy generation of the system is minimized with respect to system parameters. The thermal entropy generation decreases and viscous dissipation entropy increases with increasing the system parameters. A trade of point is isolated where entropy generation is the minimum.

Sahin and Mansour (2003) studied the entropy generation numerically in a circular pipe with uniform wall heat flux. Engine oil, water and Freon used as the working fluid. They observed that the entropy generation rate was higher near the wall and sharply decreased along the radius.

Kock and Herwig (2004) analyzed the entropy production of an incompressible turbulent shear flow of Newtonian fluids. They developed four entropy production terms based on asymptotic wall functions and incorporated into a CFD code.

Basha et al. (2007) performed a computational study on a turbulent flow and heat transfer in a rotating rectangular channel. They computed entropy generation due to heat transfer and fluid friction. Sciubba (2010) performed the multi-variable optimization of the bifurcation of the branch of a pipe using the entropy generation minimization. The selected parameters for the optimization were the aspect ratio of the domain, diameter ratio of branches and the length of the secondary branch. Sahin (2014) used the Log Mean Temperature method at which the convection heat transfer and fluid flow properties are determined to evaluate the total entropy generation in a laminar flow duct. He showed that for both uniform wall heat flux and wall temperature boundary conditions, the approximate Log Mean Temperature method provided considerably accurate values of the total rate of entropy generation in a duct. Hassan et al. (2013) theoretically studied the effects of heat transfer and fluid flow in mini and micro-channels on entropy generation in a laminar flow regime. They found that the use of highly viscous alumina-water nanofluid was not desirable under a laminar flow regime in microchannels.

Adham et al. (2014) used the effective combination of the entropy generation minimization and Genetic algorithm to examine the performance of a rectangular microchannel heat sink under laminar and turbulent flow regime. They investigated the effects of parameters like the channel aspect ratio, fin spacing ratio, Reynolds number and different materials on the overall performance of the system.

The viscosity of fluid accounts the presence of frictional loss, i.e., viscous dissipation in the flow system. Thus, the viscosity of fluid significantly influences the entropy generation. Sahin (2002) used temperature dependent viscosity of the fluid to determine the heat transfer coefficient and fluid friction factor in the pipe at constant heat flux. He found a strong effect of the variation of viscosity on entropy generation. Galanis and Rashidi (2012) used power law fluid to study the heat and mass transfer in circular and parallel plate ducts. An analytical solution of a velocity, temperature and concentration used to evaluate the local entropy generation rate.

Naterer and Adeyinka (2009) studied the entropy generation of laminar fluid flow in a tank induced by a magnetic stirrer experimentally. They calculated entropy production rates using the measured hydrodynamics data and found the highest entropy production rates near the stirrer. Manzi and Carrazzoni (2008) optimized a continuous stirred tank reactor (CSTR) in the presence of a typical irreversible, exothermic and first order chemical reaction. They found that entropy generation is minimal when inlet temperature of the reactant was equal to the reaction temperature. Manzi et al. (2009) worked on the direct method of entropy minimization to produce propylene glycol inside a CSTR. They used chemical process model equations in their work. Driss et al. (2012) studied the hydrodynamics and mixing performance of a stirred tank numerically to show the influence of multiple Rushton turbine arrangements. They found the highest viscous dissipation rate near the impeller blade tip. However, they did not study the entropy generation minimization of the stirred tank system.

2.6 IDEAL AND NON-IDEAL REACTORS

Ideal reactors have three ideal flow patterns as shown in Figure 2.7. Real reactors should approach these ideals as closely as possible.

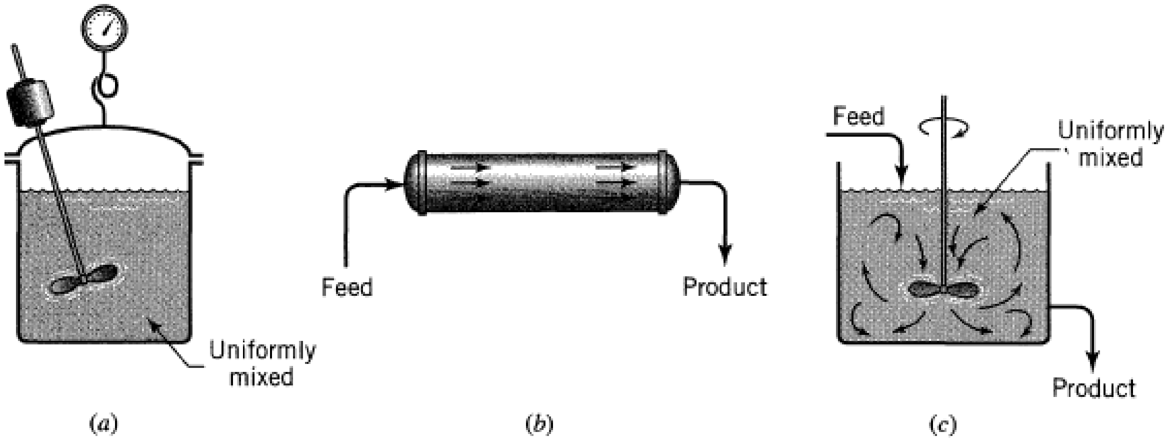

Figure 2.7 Three types of ideal reactors: (a) batch reactor, (b) plug flow reactor, and (c) mixed flow reactor (Levenspiel, 1999).

In the ideal batch reactor, of Figure 2.7(a) the reactants are initially charged into a container, are well mixed, and are left to react for a certain period. At any instant the composition throughout the reactor is uniform.

The flow reactor as shown in Figure 2.7(b) is known as the plug flow and piston flow reactor. There may be lateral mixing of fluid in a plug flow reactor; but, there should be no mixing or diffusion along the flow path. The residence time in the reactor must be the same for all elements of fluid.

The other ideal steady-state flow reactor shown in Figure 2.7(c) is called the mixed reactor or continuous stirred tank reactor (CSTR). It is a reactor in which the contents are well stirred and uniform throughout, and the exit concentration is the same as the fluid within the reactor.

Most of the stirred processes in the industries are non-ideal. The flow patterns in real reactors shown in Figure 2.8 do not conform exactly to those postulated for ideal plug flow and continuous stirred tank reactors. The deviation from the ideal flow patterns may be because of channeling of fluid, recycling of fluid, or the creation of stagnant regions in the vessel.

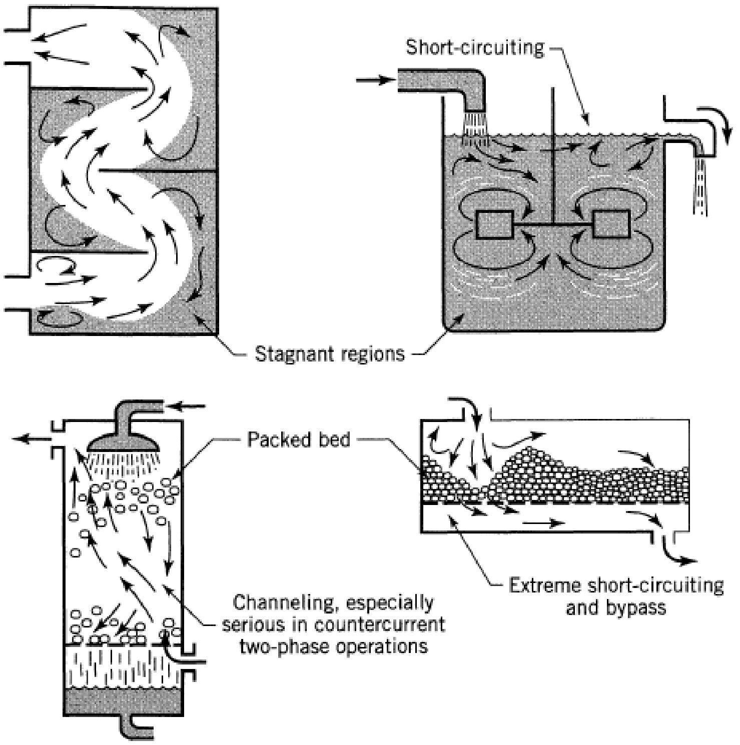

Figure 2.8 Non-ideal flow patterns which may exist in process equipment (Levenspiel, 1999).

2.7 RESIDENCE TIME DISTRIBUTION (RTD) ANALYSIS

The RTD determined experimentally by injecting a tracer, into the reactor at some time $t = 0$ and then measuring the tracer concentration, *C*, at the exit with time. The tracer must have the same physical properties as of reactor liquid, and should be completely soluble in the mixture (Fogler, 1999). The tracer can be injected as pulse input and step input. For pulse injection the residence time distribution function is defined as

$$E(t) = \frac{C(t)}{\int_0^{\infty} C(t)dt} \qquad 2.8$$

where $C(t)$ is the tracer concentration at the exit of the reactor.

In case step tracer experiment, the response function, $F(t)$ is

$$F(t) = \frac{C_{out}}{C_0} \qquad 2.9$$

The relation between the RTD function $E(t)$ and $F(t)$ is

$$E(t)=\frac{dF(t)}{dt}=\frac{d}{dt}\left[\frac{C(t)}{C_0}\right]_{step} \qquad 2.10$$

The significance of $F(t)$ and C-diagrams were explained by Danckwerts (1953) and these are shown in Figures 2.9 and 2.10 respectively. Where the volumetric flow rate in the feed is v, the total liquid holdups in the reactor is V, and Q is the total amount of tracer injected in the reactor within a very short duration.

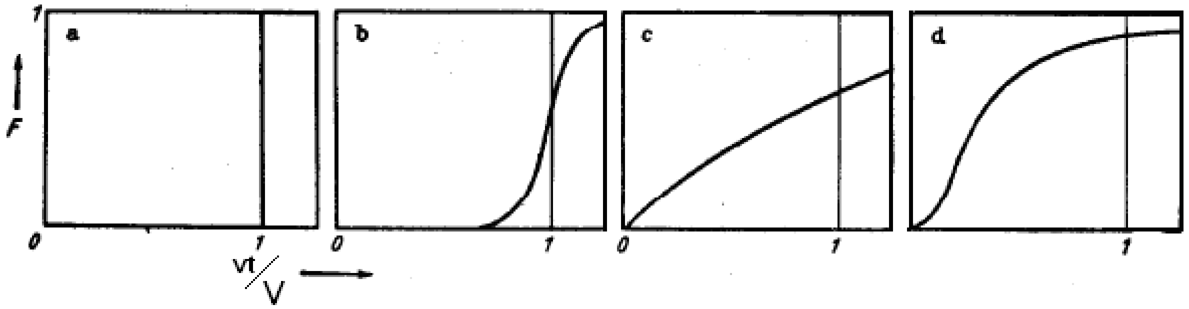

Figure 2.9 F-diagrams, (a) Piston Flow, (b) Piston flow with some longitudinal mixing, (c) Complete mixing, (d) Dead water (Danckwerts, 1953).

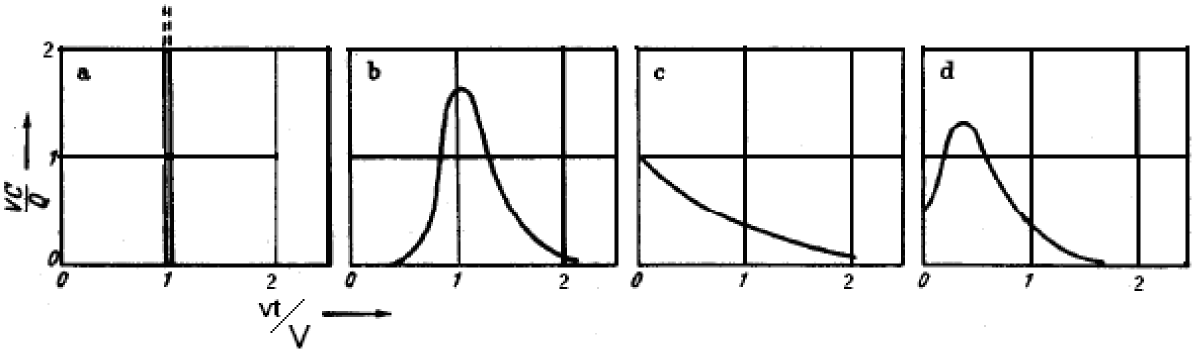

Figure 2.10 C-diagrams, (a) Piston Flow, (b) Piston flow with some longitudinal mixing, (c) Complete mixing, (d) Dead water (Danckwerts, 1953).

The Perfect piston flow shown in Figure 2.9(a) never occurs with low viscous Newtonian fluids. Figure 2.9(b) illustrates the departure from piston flow caused by longitudinal mixing. Figure 2.9(c) represents the condition for perfect mixing; the equation of the curve is:

$$F(t)=1-e^{-V^{*}t/V} \qquad 2.11$$

Figure 2.9(d) shows the presence of dead water in the system. Similar kind of phenomena occurs for pulse injection experiment, and it is shown in Figure 2.10. Danckwerts (1953) defined a term called holdback. It is defined as the average spending time of the fluid inside the reactor compared to the hydraulic residence time, $\tau = V/V^*$. Mathematically, it is

$$H = \frac{1}{\tau}\int_0^\tau F(t)dt \qquad 2.12$$

H varies from 0 for piston-flow to 1 when most of the space in the vessel is dead water. For completely mixed flow (Figure 2.9(c)), $H = 1/e$. A high holdback means that much of the reactant passes rapidly through the vessel by a short-circuit route.

The efficiency of mixing in a vessel can be given by a single quantity, S , called "segregation" (Danckwerts, 1953). The size of shaded are $(A_1 + A_2)$ in Figure 2.11(a) measures the degree of departure from perfect mixing. Mathematically segregation, S is

$$S = \int_0^\tau \left(F(t) - F_{impeffect}(t)\right)dt \qquad 2.13$$

If there is dead water in a system, the position of the curve may be inverted shown in Figure 2.11(b) with segregation, S as negative. S varies from $+1/e$ for piston flow to values approaching –1 when most of space in the system is dead water.

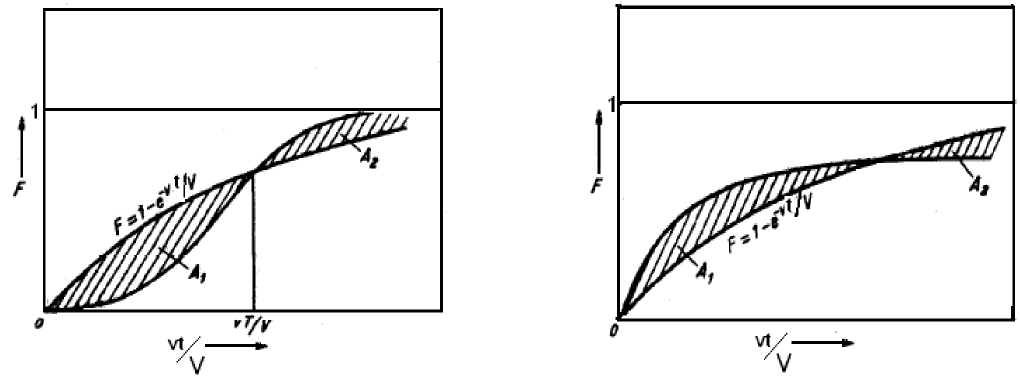

(a) (b)

Figure 2.11 (a) Perfect and imperfect mixing (b) Perfect and imperfect mixing with dead volume (Danckwerts, 1953).

Van de Vusse (1962) developed a mathematical model for stirred tank reactor (STR) taking the effect of loop flow rate and functions in term of RTD. He derived the expressions for the conversion of a first-order reaction, the spread in residence times and the distribution function for the continuous STR.

Levenspiel and Turner (1970) worked on the effect of the methods of injection and measurement of the tracer on the RTD when the fluid velocity was not uniform through the injection and measurement planes.

Burghardt and Lipowska (1972) investigated the RTD of the stirred tank reactor using an internal age distribution function. They used water and high viscosity liquids for the experiments. They determined the conditions in which the liquid was ideally mixed by the inlet flow energy only. They also found the requirement of stirrer rotations to achieve the ideal mixing state in the tank. Further, Lipowska (1974) continued the work of Burghardt and Lipowska (1972) for determining the ideal mixing conditions using different diameters of stirred tank and inlet tube.

Trivedi and Vasudeva (1974) determined the experimental RTD at low Reynolds number for helical coils. They found that under the conditions of negligible molecular diffusion and curvature ratio of coil, a significant change in RTD occurs.

Turner (1982) pointed out that if molecular diffusion and chemical reaction were significant, the concept of residence times itself became blurred. For different species in the steady flow through a given system, the observed residence time distribution might found to depend upon the different diffusion coefficients and thus, the one tracer did not give the answer for all species.

Saravanathamizhan et al. (2008) studied the residence time distribution of electrolyte in a continuous stirred electrochemical reactor. They analyzed the flow behavior of electrolyte using the pulse tracer technique. They observed that the residence time distribution increased with the increase in the flow ratio between active and dead zones.

Patwardhan (2001) predicted the residence time distribution in stirred tank equipped with the pitched blade impeller. He found the RTD and exit age distribution function with the help of the concentration profile of the tracer in the tank. He compared the predicted RTD with the experimental measurement and found good agreement.

Cozewith and Squire (2000) studied the composition distribution of functional groups in polymerization reactions. They showed that the breadth of the composition distribution of the functional groups was equal to the width of the RTD.

Arratia et al. (2004) worked on finding the presence of segregated and chaotic regions inside a CSTR with acid/base reaction mechanism and fluorescent techniques. They examined the effect of inlet/outlet stream position and Reynolds number on the dynamics of the mixing processes. They observed that at a given and constant inlet/outlet flow rate, the mixing efficiency decreased at a higher agitation speed.

The RTD of the horizontal stirred bed reactor for polypropylene production was investigated experimentally by Dittrich and Mutsersb (2007) in a cold-flow horizontal mixing apparatus. They compared the experimental data with the RTD of a cascade of continuous stirred tank reactors (CSTRs) with equal volumes. They showed that the number of CSTRs in a series necessary for simulating the experimental pulse-response curves increased with rising throughput and decreasing residence time.

Sahle-Demessie (2003) simulated the annular cylindrical photocatalytic reactor using Fluent 6.2 software. They used laminar incompressible fluid flow model along with particles tracking mechanism for developing RTD. The effect of the speed and type of fan on the RTD was also found. They observed that axial or mixed flow fans were better for reducing backmixing than that obtained in the case of radial fans.

Choi et al. (2004) conducted both the experimental and numerical study on RTD of a CSTR. They compared the experimental results for the baffled tank with computational fluid dynamics predictions of the RTD using the $k-\varepsilon$ model for transitional flow regime in the tank. They found the qualitative features of the predicted RTD similar to those measured experimentally. They accurately predicted the mean residence times as well as the variances of the residence time in the transition flow regime. They examined the effect of impeller speed on the mean residence time and variance.

Xiao-chang et al. (2009) studied RTD of a tubular shaped continuous stirred reactor using number of tee type impeller supported on a coaxial shaft. They performed both the experimental work and simulation analysis. They injected a tracer as a pulse input. They observed that the tubular reactor with a stirrer could improve the flow pattern by contracting the RTD curve, reducing mean residence time and evading back mixing.

Liu (2012) studied the residence time distribution in the continuous flow stirred tank reactor with age distribution. He investigated numerically the effect of inlet and outlet locations, flow rates, the ratio of mean residence time to the batch mixing time on the mixing performance of a continuous flow stirred tank reactor with probability distributions of age and the spatial distribution of mean age inside and at the exit of the reactors.

Busciglio et al. (2014) studied mixing time of free surface unbaffled stirred tank using planar laser induced fluorescence (PLIF) technique. They carried out experiments with different impeller geometries and impeller rotations. From the results, they confirmed that the mixing time in unbaffled tank is larger than the baffled tank. They also found as the free surface vortex approached the impeller, the mixing efficiency approximately became equal to baffled tank.

Vite-Martinez et al. (2014) numerically analyzed the mixing operation in batch stirred tank to distribute rapidly and homogeneously reagents. They calculated the distribution of the tracer concentration inside the stirred tank by solving the RANS equations and Realizable κ-ε turbulence model. They analyzed the flow pattern and reagents distribution in tank using tracer response curves. For optimizing the injection points of reagents in tank, they performed several simulations and obtained tracer concentration curves at different positions.

CHAPTER 3

NUMERICAL STUDY OF NEWTONIAN AND SHEAR THINNING FLUID IN STIRRED TANK WITH RUSHTON TURBINE

3.1 INTRODUCTION

Proper mixing in stirred tank is very important in process industries. The required torque for achieving the satisfactory mixing becomes very high for highly viscous non-Newtonian fluid. It may lead to the destruction of mixing system (Dular et al., 2006). Even for the low viscous non-Newtonian fluids, the study of mixing in the presence of Rushton turbine is restricted to laminar and transition regimes (Nouri and Whitelaw, 1990 and Ameur and Bouzit, 2012). The hydrodynamics behavior of the non-Newtonian fluid in the turbulent zone is seldom studied. Venneker et al. (2010) reported Laser Doppler Anemometry (LDA) measurements of the turbulent velocity fields of both Newtonian and non-Newtonian fluids in stirred tank agitated by a Rushton turbine. Entropy generation is an important parameter for studying the mixing process. Only a few works on the entropy generation study in stirred tanks are available in literature (Manzi et al. 2009; Naterer and Adeyinka, 2009; Driss et al. 2012). The application of the second law of thermodynamics with entropy generation minimisation (EGM) approach is a useful technique to achieve the optimum conditions (Alebrahim and Bejan, 1999; Zimparov and Penchev, 2003; Balaji et al., 2007; Jankowski, 2009; Guo et al., 2010). At the minimum entropy generation, the utilization of supplied energy is the maximum. There are two ways to determine the EGM: deterministic approach and heuristic approach. The deterministic approach needs the development of analytical expressions of entropy generations as a function of system parameter. The deterministic approach fails for the complicated problems, which can be solved better by the heuristic approach. In heuristic approach, the calculations of the entropy generation minimizations are carried out using computational fluid dynamics (CFD) tools.

The thorough literature survey showed that the very least amount of theoretical study of the non-Newtonian fluid flow behavior in stirred tank with radial impeller is carried out. To the best of my knowledge, no one has predicted the excellent work of Venneker et al. (2010) to study the hydrodynamic behavior of the non-Newtonian fluid in turbulent zone. The effect of the system parameters like the flow index of fluid, the size of the impeller blade, impeller clearance and the rotational speed of the impeller on the entropy production of the stirred tank are not studied previously. The heuristic approach was already applied to design heat exchangers and fluid flow systems using EGM method. It was also found that there were few works carried out in the area of EGM to optimize the stirred tank (Manzi and Carrazzoni, 2008; Manzi et al., 2009; Driss et al., 2012) but those works used only analytical equations for mass, energy and entropy. So, there is a scope to use CFD tools to optimize the complicated non-isothermal continuous stirred tank using EGM technique.

Therefore, the present chapter aims to discuss number of issues which include the validation of the experimental hydrodynamics data available in the open literature (Van der Molen and Van Maanen, 1978; Wu and Patterson, 1989; Dyster et al., 1993; Lunden, 1995; Venneker et. al., 2010). Besides these, the present work has used CFD models to predict and analyse many important observations of Venneker et al. (2010) of both the Newtonian and non-Newtonian fluids. The mixing time of the batch stirred tank agitated by Rushton turbine is studied here. This chapter also focuses on the numerical analysis of entropy production in the isothermal stirred tank and non-isothermal continuous stirred tank due to the change of the system parameters. The EGM analysis is carried out in the present study with a heuristic approach to optimise the performance of the continuous stirred tank. The commercial CFD code, Ansys Fluent, is used to simulate the models of the stirred tank. The identification of optimal design of the continuous stirred tank is found by the EGM technique with respect to system parameters such as inlet Reynolds number, impeller speed, impeller clearance and impeller blade width.

3.2 SYSTEM SPECIFICATION

The system configuration as given in Venneker et al. (2010) is shown in Figure 3.1. It represents a flat bottom baffled stirred tank with the Rushton turbine to agitate the Newtonian and non-Newtonian fluid. The diameter of the tank (D) is 0.627 m. The liquid is filled up to level H which is equal to the tank diameter D. Six blades Rushton turbine impeller with diameter $D_i = D/3$ is mounted at an off bottom clearance of $C_i = D_i$. Four baffles are placed along the wall of the tank at 90° interval having width, W_b, equal to $D/10$. At the points P_1 to P_4 in the figure, concentrations of the tracer will be collected with time to finding out the mixing time of the tank.

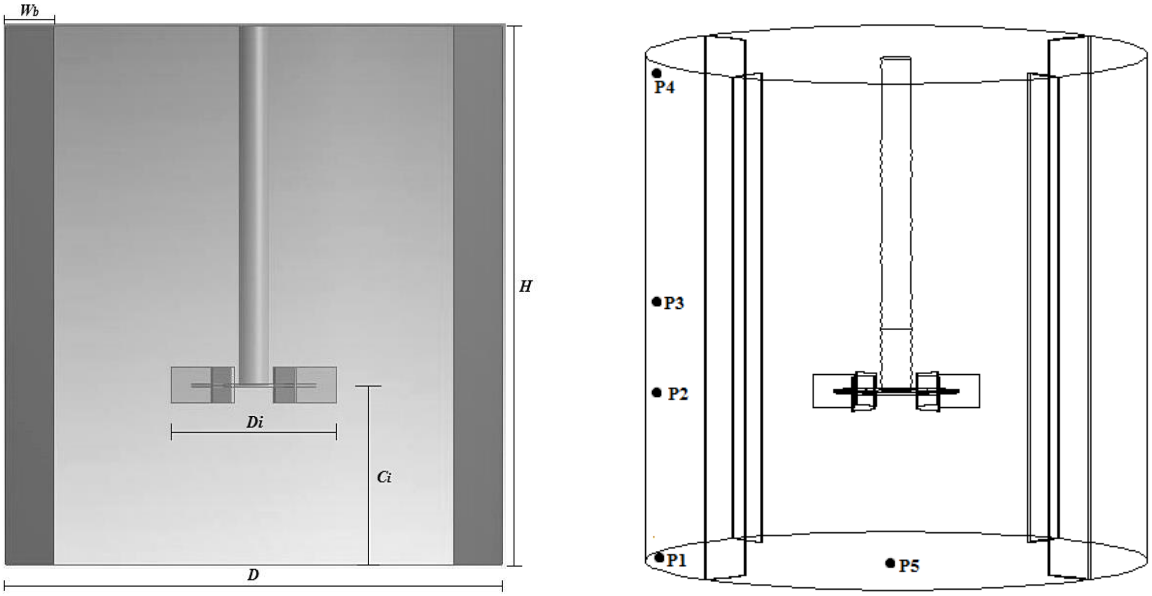

(a) (b)

Figure 3.1 (a) Geometry of the stirred tank (Venneker et al., 2010), (b) P_1 (0.313, 0.05), P_2 (0.313, 0.209), P_3 (0.313, 0.3135) and P_4 (0.313, 0.62) are tracer measuring points in (r, z) coordinate and P_5 is the tracer injection point.

Water (Newtonian fluid) and Carboxymethyl cellulose (CMC) and Xanthan gum (XG) solution in water (non-Newtonian shear thinning fluids) are used as the working fluid. The rheological parameters of the fluids are given in Table 3.1 where K is the consistency index and n is the flow behavior index.

Table 3.1 Rheological properties of the working fluids (Venneker et al., 2010)

Solution	wt. %	$K \times 10^{-3}$ (kg s^{n-2} m^{-1})	n (-)
Water	-	1.0	1.00
CMC	0.1	13.2	0.85
XG-1	0.045	9.5	0.80
XG-2	0.08	34.0	0.64

(CMC – Carboxymethyl cellulose and XG - Xanthangum)

3.3 GOVERNING EQUATIONS

The present numerical study includes the equation of continuity, equation of motion, and the turbulent kinetic energy and rate of its dissipation along with some closer equation for viscosity, Reynolds number, etc. The commercial software, Ansys Fluent, which uses a control volume technique to discretize the conservation equations (Patankar, 1980), is used to solve the conservation of mass and momentum along with the other equations and generate flow fields.

The governing equation of continuity, momentum and temperature are as follows (Ansys Fluent 13: Theory guide, 2011),

$$\frac{\partial \rho}{\partial t}+\nabla\cdot\left(\rho\vec{v}\right)=0 \qquad 3.1$$

$$\frac{\partial}{\partial t}\left(\rho\vec{v}\right)+\nabla\cdot\left(\rho\vec{v}\vec{v}\right)=-\nabla P+\nabla\cdot\left(\bar{\bar{\tau}}\right)+\rho\vec{g} \qquad 3.2$$

$$\rho C_P\frac{\partial T}{\partial t}+\rho C_P\nabla\left(\vec{v}T\right)=K_{eff}\cdot\nabla^2 T-\Phi_v \qquad 3.3$$

where $\vec{v}$ is velocity vector, T is temperature, P is the static pressure, $\bar{\bar{\tau}}$ is the stress tensor, $\vec{g}$ is the gravitational body force, K_{eff} is an effective thermal conductivity, C_P is the heat capacity of the liquid at constant pressure and Φ_v is the viscous dissipation function. The stress tensor $\bar{\bar{\tau}}$ is expressed as

$$\bar{\bar{\tau}}=\eta\left[\left(\nabla\vec{v}+\nabla\vec{v}^T\right)-\frac{2}{3}\nabla.\vec{v}I\right] \qquad 3.4$$

where η is the apparent viscosity, I is the unit tensor.

The temporal and spatial distributions of the concentration of the tracer are calculated by solving the species transport equation, which is

$$\frac{\partial}{\partial t}\left(\rho\omega_k\right)+\frac{\partial}{\partial x_j}\left(\rho u_j\omega_k\right)=\frac{\partial}{\partial x_j}\left(\rho D_{eff}\frac{\partial\omega_k}{\partial x_j}\right) \qquad 3.5$$

where ω_k is the mass fraction of k^{th} species, D_{eff} is the effective diffusivity of the species in the liquid mixture. Assuming the used tracer is KCl and the effective diffusivity is taken as 1.95×10^{-9} m^2/s (Harned and Nuttall, 1949)

The turbulent flow, which is induced by the Rushton turbine, is modelled by realizable *k*-*ε* turbulence model. The transport equations of turbulence kinetic energy, *k*, and its rate of dissipation, *ε*, are (Ansys Fluent 13: Theory guide, 2011),

$$\nabla\cdot(\rho k\vec{v}) = \nabla\cdot\left[\left(\mu+\frac{\mu_t}{\sigma_k}\right)\nabla\cdot k\right]+G_k-\rho\varepsilon \qquad 3.6$$

and

$$\nabla\cdot(\rho \varepsilon\vec{v}) = \nabla\cdot\left[\left(\mu+\frac{\mu_t}{\sigma_\varepsilon}\right)\nabla\cdot \varepsilon\right]+C_2\rho\frac{\varepsilon^2}{k+\sqrt{\nu\varepsilon}} \qquad 3.7$$

in which C_2 is constant. σ_k and σ_ε are the turbulent Prandtl numbers for *k* and *ε* respectively. The following values are used for the constants (Ansys Fluent 13: Theory guide, 2011),

$$C_2 = 1.92,\ \sigma_k = 1.0,\ \sigma_\varepsilon = 1.2 \qquad 3.8$$

In equation 3.5, G_k represents the generation of turbulence kinetic energy due to mean velocity gradients and calculated as

$$G_k = -\rho\overline{u_i^{'}u_j^{'}}\frac{\partial u_j}{\partial x_i} \qquad 3.9$$

The turbulent or eddy viscosity, μ_t, is computed by combining *k* and *ε* as follows (Ansys Fluent 13: Theory guide, 2011),

$$\mu_t = \rho C_\mu\frac{k^2}{\varepsilon} = \mu_t S^2 \qquad 3.10$$

where *S* is the modulus of the mean rate of strain tensor,

$$S = \sqrt{2S_{ij}S_{ij}} \ \text{ and } \ S_{ij} = \frac{1}{2}\left(\frac{\partial u_j}{\partial x_i}+\frac{\partial u_i}{\partial x_j}\right) \qquad 3.11$$

The variable C_μ is a calculated as (Ansys Fluent 13: Theory guide, 2011),

$$C_{\mu} = \frac{1}{A_0 + A_s \frac{kU^*}{\varepsilon}} \qquad 3.12$$

where $U^* = \sqrt{S_{ij} S_{ij} + \bar{\Omega}_{ij} \bar{\Omega}_{ij}}$ 3.13

and $\bar{\Omega}_{ij} = \Omega_{ij} - 2\varepsilon_{ijk}\omega_k$ 3.14

where $\bar{\Omega}_{ij}$ is the mean rate of rotation of tensor viewed in a moving reference frame with angular velocity ω_k. The model constants A_0 and A_s are given as (Ansys Fluent 13: Theory guide, 2011),

$A_0 = 4.04$ and $A_s = \sqrt{6}\,cos\,\varphi$ 3.15

where

$$\varphi = \frac{1}{3} cos^{-1}\left(\sqrt{6}W\right),\ W = \frac{S_{ij} S_{jk} S_{ki}}{\bar{S}^3},\ \bar{S} = \sqrt{S_{ij} S_{ij}}\ . \qquad 3.16$$

For a Newtonian fluid, the impeller Reynolds number for the stirred tank is given by

$$Re = \frac{\rho N D_i^2}{\mu} \qquad 3.17$$

where N is the rotational speed of the impeller and ρ is the density of the fluid.

For non-Newtonian fluid, the power law is used to model viscosity, is given as

$$\eta = K \cdot \dot{\gamma}^{n-1} \qquad 3.18$$

in which η is apparent viscosity, K is consistency index and n is the flow behavior index.

The impeller Reynolds number for shear thinning fluid is calculated using the Metzner-Otto method (Metzner and Otto, 1957)

$$Re = \frac{\rho N^{2-n} D_i^2}{K \cdot k_s^{n-1}} \qquad 3.19$$

where k_s is Metzner-Otto constant with $k_s = 11.5$.

The power number of impeller is calculated by

$$N_P = \frac{P}{\rho N^3 D_i^5} \tag{3.20}$$

where, P is the power input, which is calculated from the torque, Γ, applied on the impeller shaft. Mathematically calculated as

$$P = 2\pi N \cdot \Gamma \tag{3.21}$$

Another important parameter for studying the hydrodynamic behavior of stirred tank is flow number of impeller and it is determined using an equation

$$N_q = \frac{Q}{N D_i^3} \tag{3.22}$$

where Q is volumetric discharge from impeller blade.

For non-isothermal condition, the temperature and shear rate dependent viscosity is given as (Ansys Fluent 13: User's Guide, 2011)

$$\eta = K \cdot \dot{\gamma}^{n-1} \cdot H(T) \tag{3.23}$$

H(T) is the temperature dependent part in the viscosity expression and is given in Equation 3.24, (Ansys Fluent 13: User's Guide, 2011)

$$H(T) = \exp\left[\beta\left(\frac{1}{T - T_0} - \frac{1}{T_\beta - T_0}\right)\right] \tag{3.24}$$

where β is the ratio of molar activation energy to the universal gas constant. The value of β is 2324.5 K (Converti et al., 1999). The reference temperature T_β is taken as 288.15 K. T_0 is the minimum temperature shift and taken as zero in the present work.

The transport equation for entropy is (Kock and Herwig, 2004)

$$\frac{\partial}{\partial t}(\rho s) + \nabla(\rho s \vec{v}) = div\left(\frac{\vec{q}}{T}\right) + \frac{\Phi}{T} + \frac{\Phi_\theta}{T^2} \tag{3.25}$$

where s is the specific entropy and T is temperature. The last two terms on the right side are related to entropy generation: first term represents the entropy generation due to viscous dissipation and second term describes the entropy generation due to heat transfer by finite temperature gradient. The above equation is applicable for both laminar and turbulent flow state. In turbulent state, according to Reynolds averaged Navier-Stokes approach, the instantaneous entropy is decomposed into mean and fluctuation term. The time averaged equation of entropy is written as

$$\frac{\partial}{\partial t}(\rho\bar{s})+\nabla(\rho\bar{s}\bar{v})=\overline{div(\vec{q}/T)}-\nabla\left(\rho\overline{u's'}\right)+\overline{\Phi/T}+\overline{\Phi_\theta/T^2} \tag{3.26}$$

$\overline{\Phi/T}$ describes the entropy generation due to viscous dissipation and it has two parts: mean viscous dissipation ($S_{gen,\overline{VD}}$) and turbulent viscous dissipation ($S_{gen,VD'}$). Thus,

$$\overline{\Phi/T}=S_{gen,VD}=S_{gen,\overline{VD}}+S_{gen,VD'} \tag{3.27}$$

In terms of mean velocity and velocity fluctuation gradients, these can be written as

$$\begin{aligned}S_{gen,\overline{VD}}=\frac{\mu_{eff}}{\bar{T}}&\left[2\left\{\left(\frac{\partial\bar{u}}{\partial r}\right)^2+\frac{1}{r^2}\left(\frac{\partial\bar{v}}{\partial\theta}+\bar{u}\right)^2+\left(\frac{\partial\bar{w}}{\partial z}\right)^2\right\}\right]+\left(\frac{\partial\bar{v}}{\partial z}+\frac{1}{r}\frac{\partial\bar{w}}{\partial\theta}\right)^2\\&+\left(\frac{\partial\bar{w}}{\partial r}+\frac{\partial\bar{u}}{\partial z}\right)^2+\left[\frac{1}{r}\frac{\partial\bar{u}}{\partial\theta}+r\frac{\partial}{\partial r}\left(\frac{\bar{v}}{r}\right)\right]^2\end{aligned} \tag{3.28}$$

$$\begin{aligned}S_{gen,VD'}=\frac{\mu_{eff}}{\bar{T}}&\left[2\left\{\overline{\left(\frac{\partial u'}{\partial r}\right)^2}+\overline{\frac{1}{r^2}\left(\frac{\partial v'}{\partial\theta}+u'\right)^2}+\overline{\left(\frac{\partial w'}{\partial z}\right)^2}\right\}\right]+\overline{\left(\frac{\partial v'}{\partial z}+\frac{1}{r}\frac{\partial w'}{\partial\theta}\right)^2}\\&+\overline{\left(\frac{\partial w'}{\partial r}+\frac{\partial u'}{\partial z}\right)^2}+\overline{\left[\frac{1}{r}\frac{\partial u'}{\partial\theta}+r\frac{\partial}{\partial r}\left(\frac{v'}{r}\right)\right]^2}\end{aligned} \tag{3.29}$$

where μ_{eff} is the effective viscosity of fluid.

The term $\overline{\Phi_\theta/T^2}$ in Equation 3.26 is the entropy generation due to heat transfer irreversibility. It also has two parts: entropy generation due to gradient of mean temperature ($S_{gen,\overline{HT}}$) and gradient of fluctuating temperature ($S_{gen,HT'}$). Thus

$$\overline{\Phi_\theta/T^2}=S_{gen,HT}=S_{gen,\overline{HT}}+S_{gen,HT'} \tag{3.30}$$

In terms of mean temperature and temperature fluctuation gradients, these can be written as

$$S_{gen,\overline{HT}} = \frac{K_{eff}}{\overline{T}^2}\left[\left(\frac{\partial\overline{T}}{\partial r}\right)^2 + \left(\frac{1}{r}\frac{\partial\overline{T}}{\partial\theta}\right)^2 + \left(\frac{\partial\overline{T}}{\partial z}\right)^2\right] \qquad 3.31$$

$$S_{gen,HT'} = \frac{K_{eff}}{\overline{T}^2}\left[\overline{\left(\frac{\partial T'}{\partial r}\right)^2} + \overline{\left(\frac{1}{r}\frac{\partial T'}{\partial\theta}\right)^2} + \overline{\left(\frac{\partial T'}{\partial z}\right)^2}\right] \qquad 3.32$$

where K_{eff} is the effective thermal conductivity.

The solution of turbulent momentum, k-ε model equation and energy equation makes the mean velocities and temperatures available. Therefore, both $S_{gen,\overline{VD}}$ and $S_{gen,\overline{HT}}$ can be determined directly. But the remaining two terms are unknown and need additional equations. The equations are given below (Kock and Herwig, 2004; 2005; Herwig and Kock 2007).

$$S_{gen,VD'} = \frac{\rho\varepsilon}{\overline{T}} \qquad 3.33$$

$$S_{gen,HT'} = \frac{\alpha_t}{\alpha} S_{gen,\overline{HT}} \qquad 3.34$$

where α_t is the turbulent thermal diffusivity and α is thermal diffusivity of fluid.

From Equations 3.26, 3.27 and 3.30, the total entropy generation due to both the heat transfer irreversibility and fluid viscous dissipation can be written as

$$S_{gen,Total} = S_{gen,HT} + S_{gen,VD} = S_{gen,\overline{HT}} + S_{gen,HT'} + S_{gen,\overline{VD}} + S_{gen,VD'} \qquad 3.35$$

Further, the total entropy generation can be written in dimensionless form as (Yilbas et al., 1999, Basha et al., 2007)

$$S^* = \frac{S_{gen,Total} \cdot D^2}{\lambda} \qquad 3.36$$

where λ is the thermal conductivity of the fluid.

To know the relative contribution of entropy generation due to viscous dissipation and heat transfer irreversibility on the total entropy generation, the Bejan number, *Be*, is defined as follows (Ko and Wu, 2009).

$$Be = \frac{S_{gen,HT}}{S_{gen,Total}} \tag{3.37}$$

Bejan number ranges from 0 to 1. When *Be* = 1, the irreversibility is because of the heat transfer only, and for *Be* = 0, the irreversibility occurs only by the fluid viscous dissipation.

But for isothermal condition, the entropy production due to temperature gradient, i.e., heat transfer is zero. Because of turbulence, the dissipation term is decomposed into two terms namely, mean and fluctuating viscous dissipation terms (Cebeci and Bradshaw, 1984). So the total entropy generation equation becomes,

$$S_{gen,Total} = S_{gen,VD} = S_{gen,\overline{VD}} + S_{gen,VD'} = \frac{\mu_{eff}\,\varphi_v}{T} + \frac{\rho\varepsilon}{T} \tag{3.38}$$

where μ_{eff} is the effective viscosity, T is the temperature of system and φ_v is the mean viscous dissipation due to mean velocity components which is given as

$$\varphi_v = 2\left[\left(\frac{\partial u}{\partial r}\right)^2 + \left(\frac{\partial v}{r\partial\theta} + \frac{u}{r}\right)^2 + \left(\frac{\partial w}{\partial z}\right)^2\right] + \left[\frac{\partial v}{\partial r} - \frac{v}{r} + \frac{\partial u}{r\partial\theta}\right]^2 + \left[\frac{\partial w}{r\partial\theta} + \frac{\partial v}{\partial z}\right]^2 + \left[\frac{\partial u}{\partial z} + \frac{\partial w}{\partial r}\right]^2 \tag{3.39}$$

and $\rho\varepsilon$ is fluctuating dissipation due to fluctuating velocity components, given as

$$\rho\varepsilon = 2\left[\overline{\left(\frac{\partial u'}{\partial r}\right)^2} + \overline{\left(\frac{\partial v'}{r\partial\theta} + \frac{u'}{r}\right)^2} + \overline{\left(\frac{\partial w'}{\partial z}\right)^2}\right] + \overline{\left[\frac{\partial v'}{\partial r} - \frac{v'}{r} + \frac{\partial u'}{r\partial\theta}\right]^2} + \overline{\left[\frac{\partial w'}{r\partial\theta} + \frac{\partial v'}{\partial z}\right]^2} + \overline{\left[\frac{\partial u'}{\partial z} + \frac{\partial w'}{\partial r}\right]^2} \tag{3.40}$$

But previous literature (Kock and Herwig, 2003, 2004 and 2005) suggests that the ε term in above equation cannot be determined exactly, hence it is replaced with ε-model equation of k-ε turbulence model.

3.4 NUMERICAL METHODOLOGY AND BOUNDARY CONDITIONS

The geometry of the physical system is prepared in Ansys Workbench. It is meshed then with mesh modeler (Figure 3.2). Mesh independence tests are performed with mesh sizes ranging from 900000 to 1500000 control volumes. The calculated velocities for each selected mesh are compared with the water velocities given in Venneker et al. (2010) and respective calculated RMS errors (Equation 3.41) are given in Table 3.2. Results show that the mesh containing

1200000 elements provides the same average RMS error to those obtained with 1500000 elements. Therefore, the 1200000 mesh element is used for further simulation study.

$$RMS = \sqrt{\frac{\sum_{i=1}^{m}\left(V_{Water} - V_{non-newtonian}\right)^2}{m}} \qquad 3.41$$

where V_{water} and $V_{non\text{-}Newtonian}$ are the water (Newtonian) and non-Newtonian fluid velocities, and *m* is the number of data points.

Steady state multiple reference frame commonly known as MRF is used to model rotating impeller. In this approach, a rotating frame is used for rotating components, whereas a stationary frame is used for stationary components. In the rotating frame, the impeller is kept stationary. While, the tank wall and baffles are at rest in stationary frame. The flow characteristic equations inside rotating components are solved using a rotating frame while the stationary components used stationary frame to solve the same equations. Both the frames are connected using interface over which a flow properties such as velocity, pressure etc. are exchanged. A rotating boundary condition is applied to the shaft which is outside the rotating frame and the no-slip boundary condition is applied on the wall of the tank and baffles.

SIMPLE (Semi-Implicit Method for Pressure Linked Equations) algorithm is used to couple pressure and velocity terms. The non-Newtonian fluid viscosity is modeled using non-Newtonian Power Law model (Equation 3.18). All transport equations are discretized using second order upwind difference scheme. The convergence criterion for all transport equation is set to 10^{-5}. The computations are carried out using a 3.2 GHz Intel Core i5 CPU having 4 GB RAM. The computational time was about 7-8 hours.

Table 3.2 Mesh size and RMS error

Mesh Size	RMS error (in %)			
	Axial velocity	Radial velocity	Tangential velocity	Average error
900000	2.99	3.26	6.2	4.15
1200000	3.05	2.05	5.41	3.50
1500000	3.1	2.10	5.42	3.50

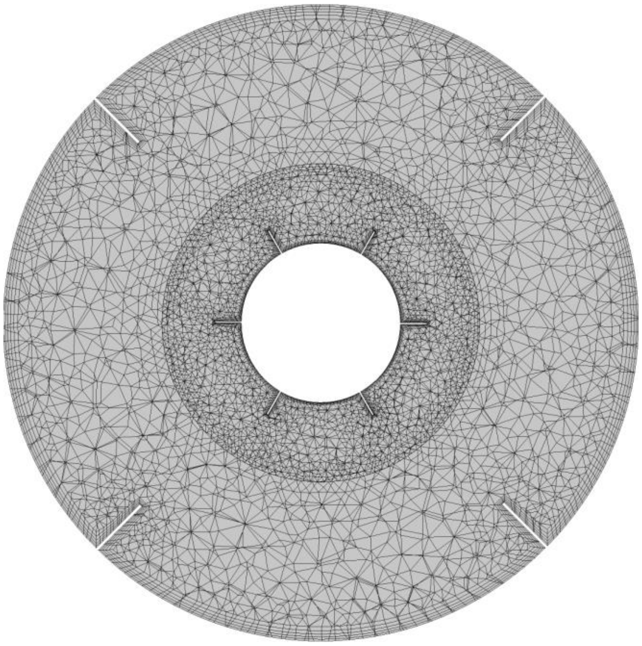

Figure 3.2 Computational mesh (tetrahedral mesh).

3.5 RESULTS AND DISCUSSION

3.5.1 Validation of CFD Models

The CFD models are required to be validated before simulation study. To achieve it, the present simulated velocities of water at the impeller Reynolds number, $Re = 1.305 \times 10^5$ are compared with the experimental data (Van der Molen and Van Maanen, 1978; Wu and Patterson, 1989; Dyster et al., 1993; Lunden, 1995; Venneker et al., 2010). It is shown in Figure 3.3. The velocity data are made dimensionless by impeller tip velocity, $V_{tip} = \pi N D_i$ and collected at impeller disk level along the non-dimensional radial distance, r/R_i, where r is radial distance and R_i is radius of the impeller. The trend of the figure proves qualitative satisfactory validation of the CFD models. The validation is quantified by the RMS error factor given in Table 3.2. It shows that for 1200000 and higher mesh sizes the RMS error becomes negligible. Thus, the CFD models are validated both qualitatively and quantitatively, and can be used for the further simulation study.

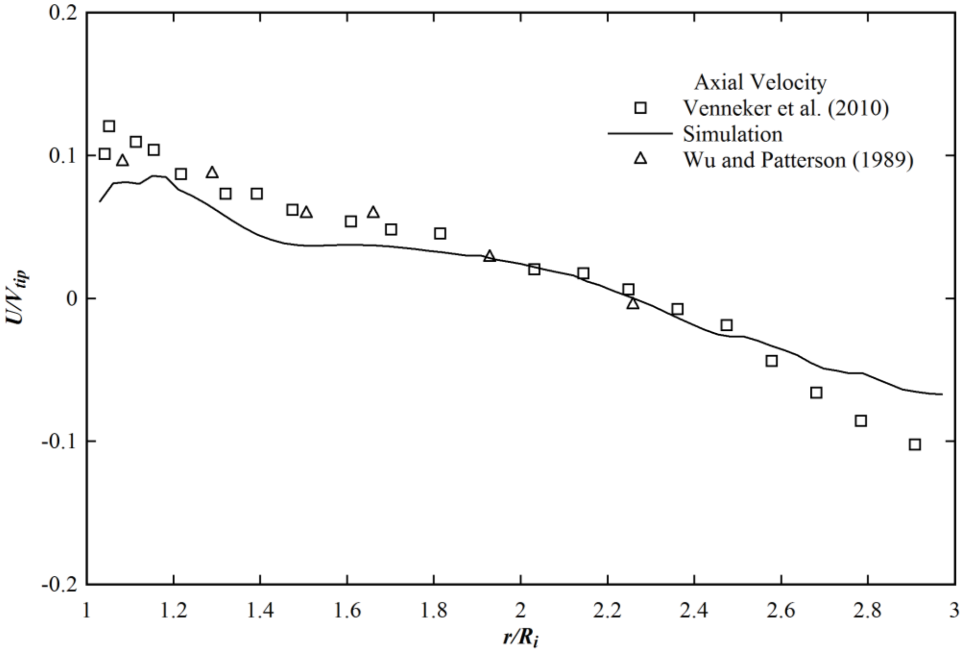
Axial Velocity
Venneker et al. (2010)
Simulation
Wu and Patterson (1989)
U/V_{tip}
r/R_i
0.2
0.1
0
-0.1
-0.2
1
1.2
1.4
1.6
1.8
2
2.2
2.4
2.6
2.8
3

(a)

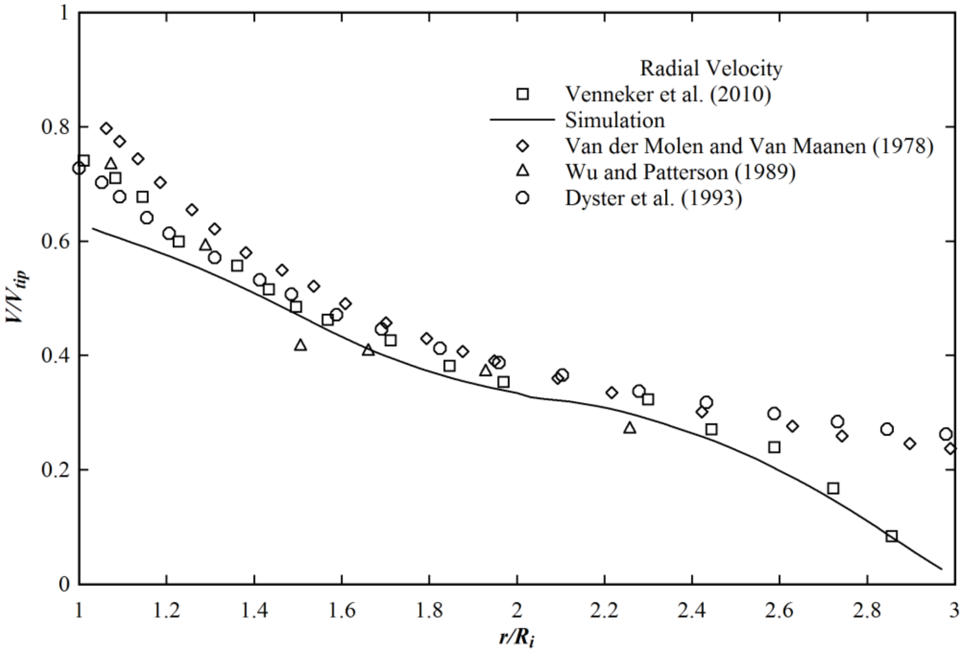
Radial Velocity
Venneker et al. (2010)
Simulation
Van der Molen and Van Maanen (1978)
Wu and Patterson (1989)
Dyster et al. (1993)
V/V_{tip}
r/R_i
1
0.8
0.6
0.4
0.2
0
1
1.2
1.4
1.6
1.8
2
2.2
2.4
2.6
2.8
3

(b)

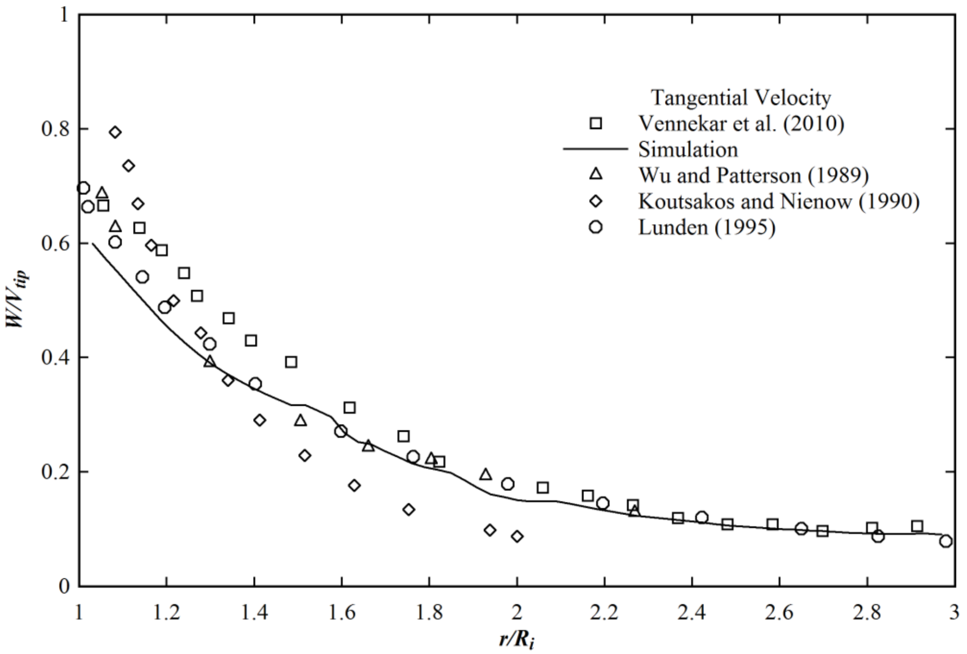

(c)

Figure 3.3 Comparison of predicted velocity profile with literature data for water at *Re* = 1.305 x 10^5; (a) Axial velocity, (b) Radial velocity, (c) Tangential velocity.

To predict the effect of impeller Reynolds number, *Re* on the velocity profiles given in Venneker et al. (2010), the velocities of CMC solution are calculated and depicted in Figure 3.4 at different *Re*. Both the literature and predicted data show that the axial velocity passes through the maxima near the impeller blade (Figure 3.4(a)). At around r/R_i = 2.3, the experimental axial velocity profile changes the direction of flow which is closely predicted by simulation data. The change of direction of axial velocity is found independent of Reynolds number. The figure shows that the simulated data can predict well the experimental data except near the impeller blade and tank wall. The effect of *Re* on the radial velocity distribution is shown in Figure 3.4(b). The accuracy of prediction becomes better with impeller Reynolds number and also with radial distance. The velocity profile approaches toward the water fit line at higher impeller Reynolds number. Similarly, the effect of impeller Reynolds number on the tangential velocity is shown in Figure 3.4(c). It shows that there is a deviation of predicted velocity from the experimental data up to non-dimensional radial position 1.6; however, onward an excellent agreement between these two is observed.

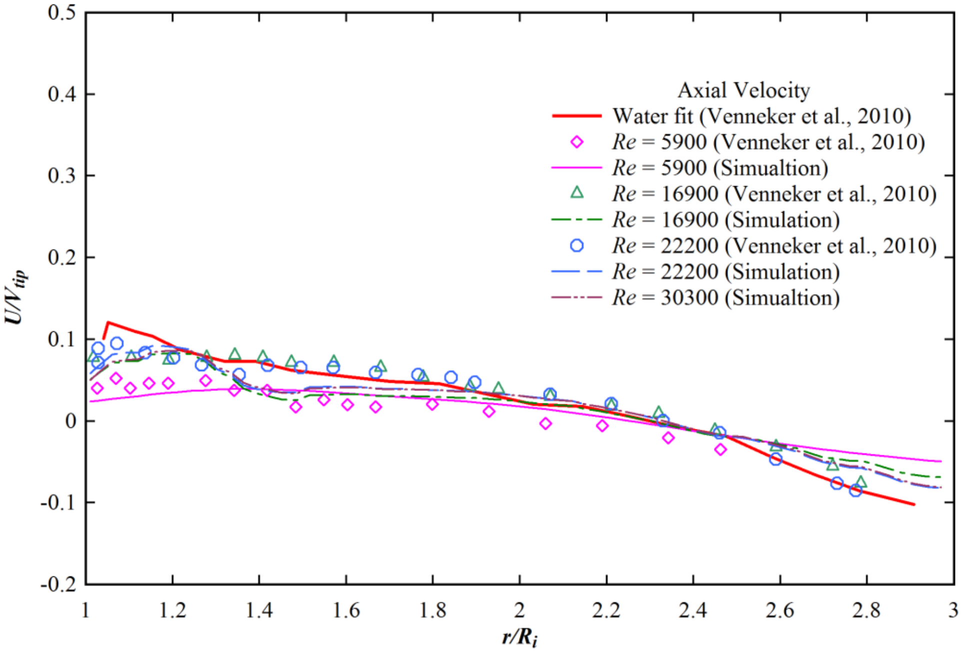
Axial Velocity
Water fit (Venneker et al., 2010)
Re = 5900 (Venneker et al., 2010)
Re = 5900 (Simualtion)
Re = 16900 (Venneker et al., 2010)
Re = 16900 (Simulation)
Re = 22200 (Venneker et al., 2010)
Re = 22200 (Simulation)
Re = 30300 (Simualtion)
U/V_tip
r/R_i
0.5
0.4
0.3
0.2
0.1
0
-0.1
-0.2
1
1.2
1.4
1.6
1.8
2
2.2
2.4
2.6
2.8
3

(a)

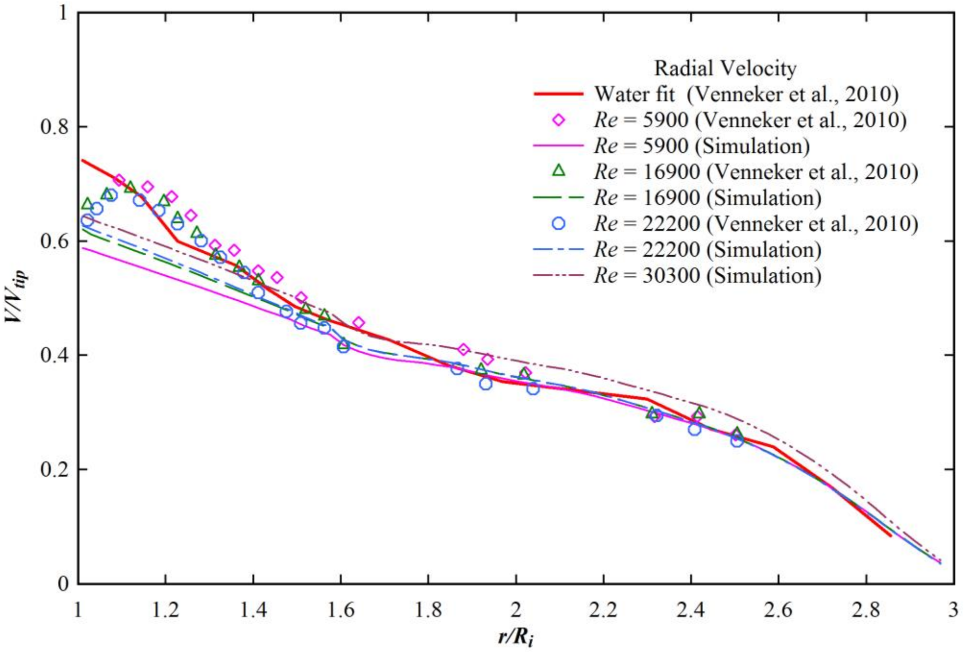
Radial Velocity
Water fit (Venneker et al., 2010)
Re = 5900 (Venneker et al., 2010)
Re = 5900 (Simulation)
Re = 16900 (Venneker et al., 2010)
Re = 16900 (Simulation)
Re = 22200 (Venneker et al., 2010)
Re = 22200 (Simulation)
Re = 30300 (Simulation)
V/V_tip
r/R_i
1
0.8
0.6
0.4
0.2
0
1
1.2
1.4
1.6
1.8
2
2.2
2.4
2.6
2.8
3

(b)

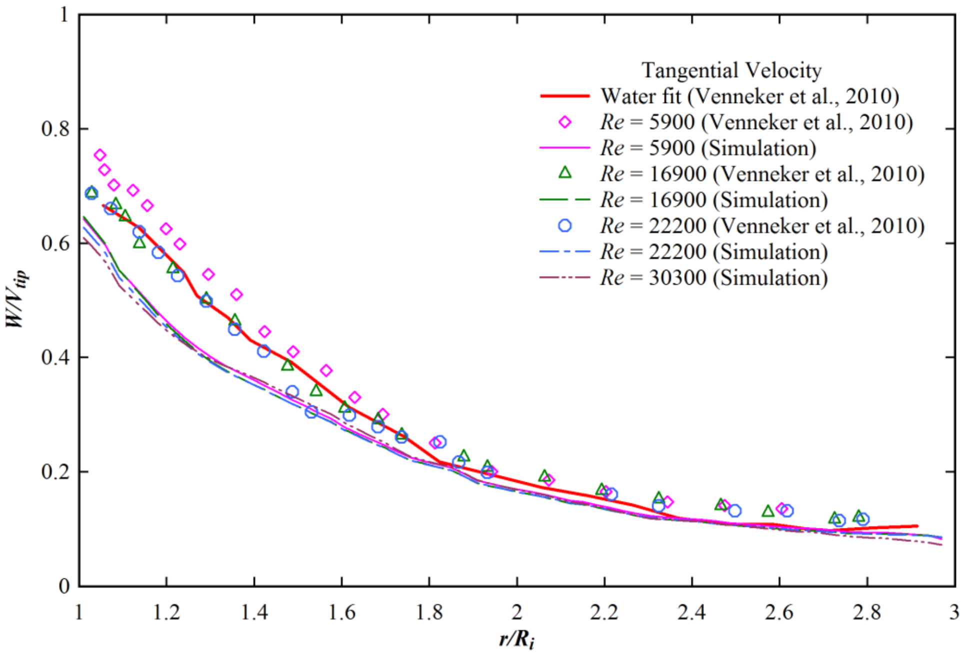

(c)

Figure 3.4 Comparison of velocity profile of shear thinning solution, CMC, at different *Re* with literature data (a) Axial velocity, (b) Radial velocity, (c) Tangential velocity.

For non-Newtonian fluid, the change of the flow behavior index, *n*, changes the consistency index, *K*. Both of these affect the impeller Reynolds number. Hence, it is difficult to find the exclusive effect of *n* on the hydrodynamic behavior of the non-Newtonian fluid. Since experimental data of velocity profiles at different *n* are available in Venneker et al. (2010), the computed velocity profiles are compared with the experimental (Venneker et al., 2010) data at different *n*.

The CMC solution ($n = 0.85$) is simulated at $Re = 22200$ and the Xanthan gum solution with *n*, 0.80 and 0.64, are simulated at Reynolds number, 33700 and 13800, respectively. The velocity profile for the water is computed and compared with the experimental data at $Re = 135000$. Figure 3.5(a) shows that the simulated axial velocities are close to the experimental data for all non-Newtonian fluids. A discrepancy for water velocity at higher radial distance occurs due to stronger bottom circulation loop. The computed radial component velocities are compared with experimental data for *n* equal to 0.85 and 0.80, and due to non-availability of experimental data, only simulated data are presented in Figure 3.5(b) for $n = 0.64$. The figure shows that the simulated data can predict the trend of the experimental data, especially at a little distance away from the impeller surface. The distribution of the radial velocity is found to be dependent on the flow index of the non-Newtonian fluid. Venneker et al. (2010) observed a sharper decay of velocity for radial distance larger than $r/R_i = 1.2$, however, they were uncertain about this trend and explained this as the shortage of experimental data. The present computational results in Figure 3.5(b) also have the same trend of the experimental data, and thus it can be concluded that the experimental data of Venneker et al. (2010) is accurate. Similarly, in Figure 3.5(c), the simulated tangential velocities are found to be under-predicted near the impeller blade region. But as we move away from the impeller region, the prediction becomes excellent. Another important finding in the figure is that the simulated tangential velocities are less dependent on the flow behavior index than the radial and axial component velocities.

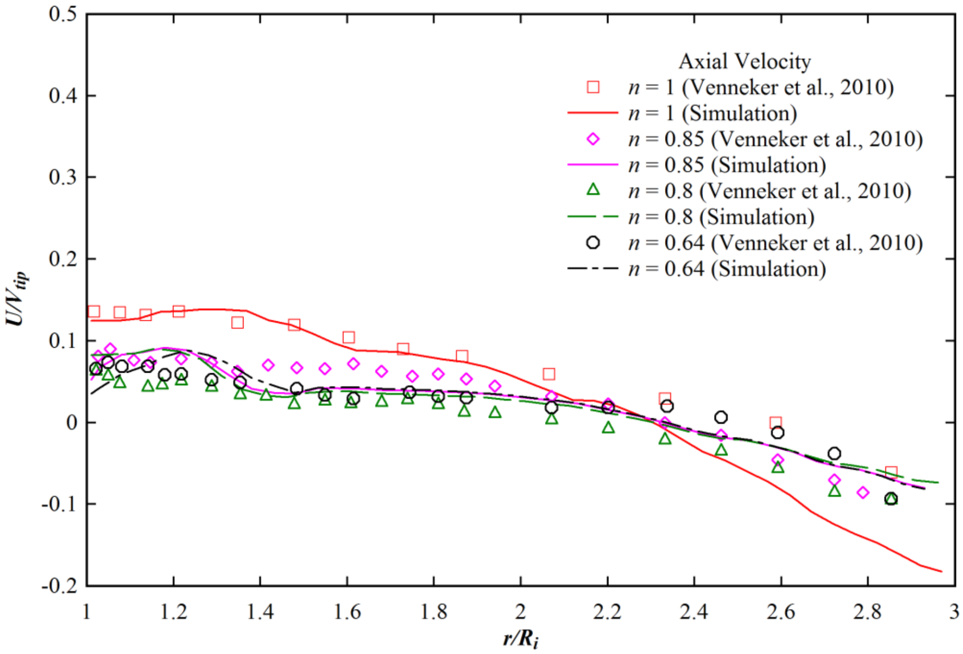

(a)

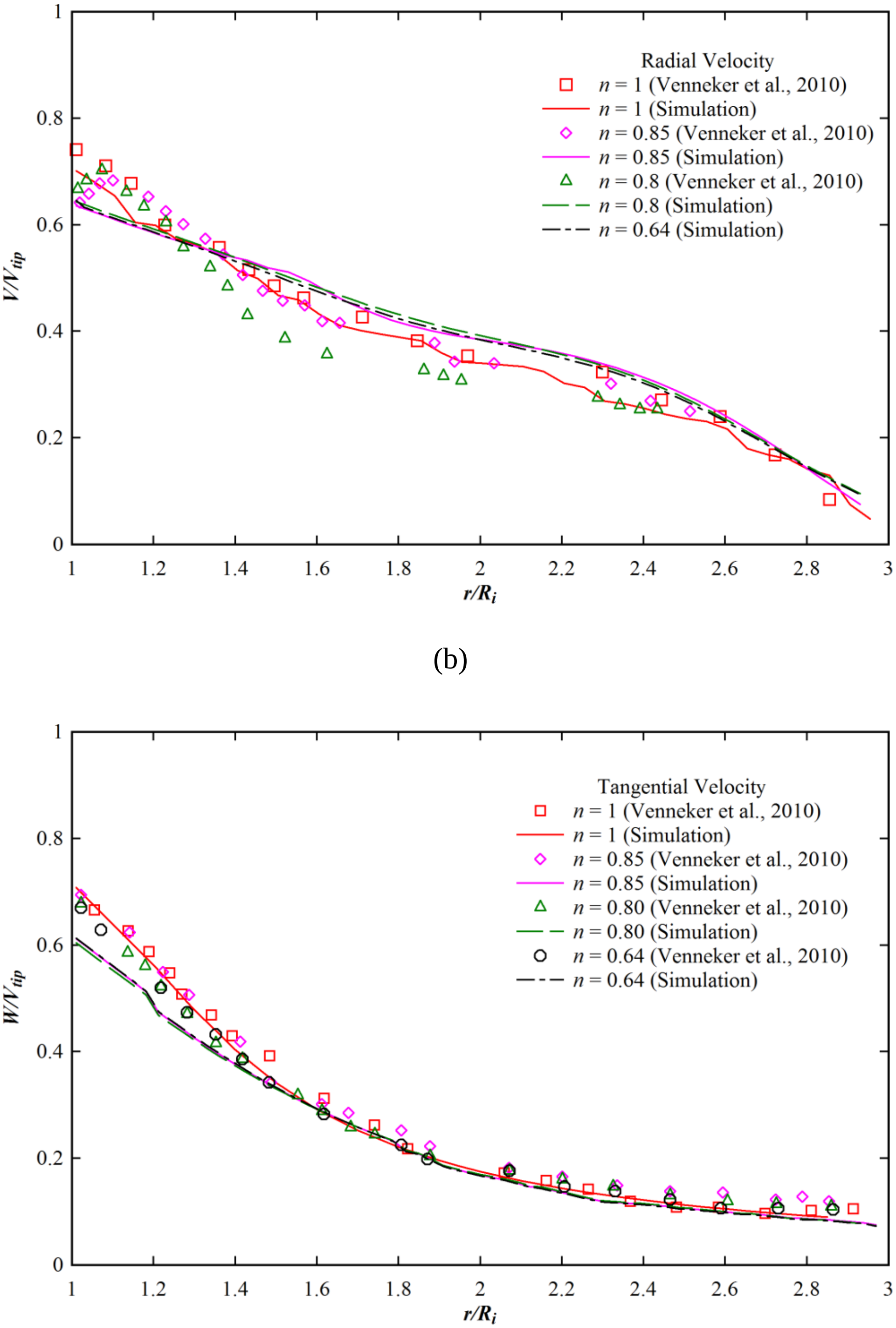

(b)

(c)

Figure 3.5 Comparison of velocity profiles of shear thinning fluid at different flow index (*n*) with literature data (a) Axial velocity, (b) Radial velocity, (c) Tangential velocity.

3.5.2 Prediction of Discharge Velocity Profiles

Figure 3.6 shows the discharge profile of all three velocity components along the impeller surface, *z**. Where *z** is the normalized position of the impeller blade in the axial direction. The experimental axial discharge velocities (Venneker et al., 2010) are dependent on the flow index number, *n*, whereas the numerical values show independence on *n*. Also, the magnitude of CFD predicted velocity components shows either or both under- or/and over-prediction with literature values. The variation of the width of the radial and tangential discharge velocities given in the literature is the function of *n*, but the computed values of these are unaffected by the flow behavior index, *n*. The peak point of radial and tangential discharge velocities is respectively under-predicted and satisfactorily predicted. The axial discharge velocity profile is showing zigzag pattern with *z**. Although, the CFD models cannot predict exactly the axial discharge velocity, the trend of it proved the qualitative prediction capability of the models. One important observation can be made from an axial discharge velocity profile is that the location of the peak points of both the experimental and predicted data are qualitatively same.

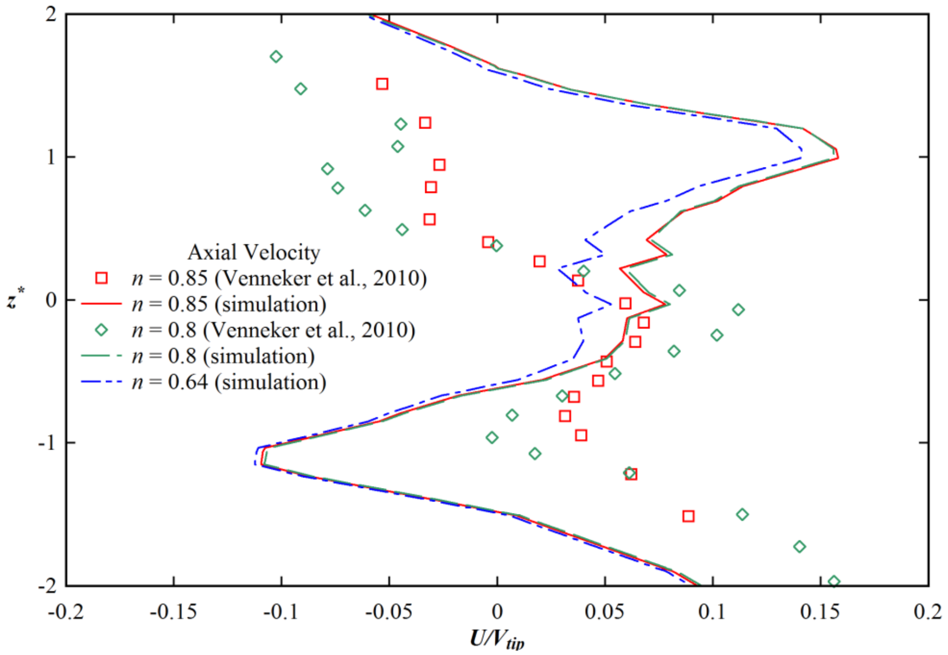

(a)

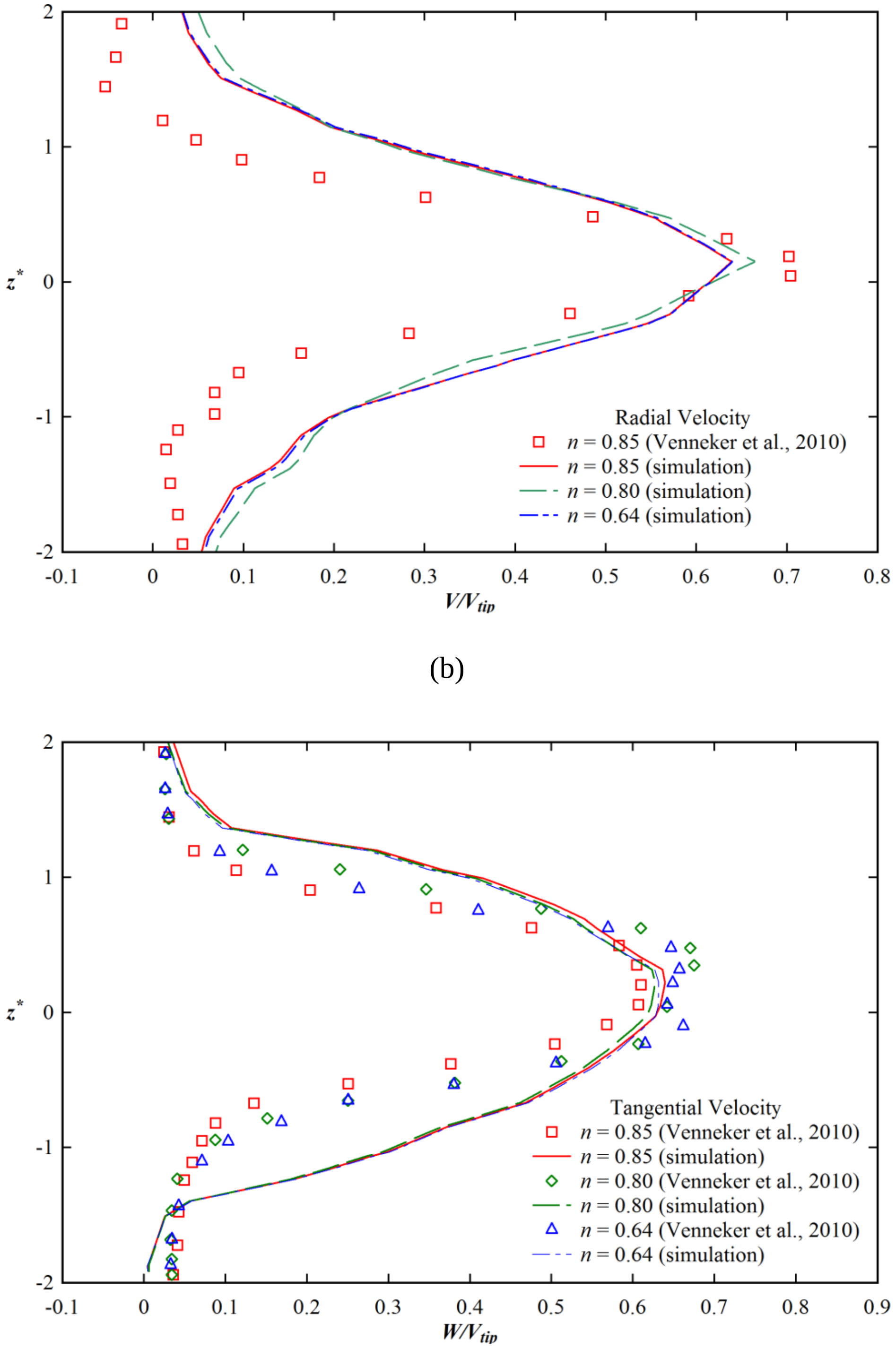

(b)

(c)

Figure 3.6 Comparison of the discharge velocity profiles from impeller blade (a) Axial velocity, (b) Radial velocity, (c) Tangential velocity.

3.5.3 Prediction of Interaction of *Re* and *n* on the Velocity Profile and Discharge Profile

In general, the velocity profiles of non-Newtonian fluids are the function of Reynolds number and fluid flow index. Venneker et al. (2010) has studied the interaction of velocity profile with *Re* and *n*. They used three selected parameters for axial velocity profile: U_1 (the dimensionless axial velocity at the impeller blade tip, $r/R_i = 1$), R_0 (the dimensionless radius at which the axial velocity profile changes the flow direction), and U_{wall} (the extrapolated axial velocity at the tank wall), for radial velocity profile: V_1 (the dimensionless radial velocity at the impeller blade tip) and for tangential velocity: W_1 (the dimensionless tangential velocity at the impeller blade tip) and W_{wall} (the extrapolated tangential velocity at the tank wall). The dependency of these selected variables on the impeller Reynolds number and flow behavior index can be monotonic, i.e., with the increase or decrease in *Re* or flow behavior index, the variables should increase or decrease, respectively. They used Spearman’s rank-order correlation coefficient technique (Sheskin, 2004) to determine the presence of interaction between the selected variables and *Re* and *n*. The present study also uses the same statistical method to predict/evaluate the interaction between the theoretically calculated velocity profiles and *Re* and *n*. In addition to the selected variables as used by Venneker et al. (2010) some more variables like $U_{1.5}$ (axial velocity at $r/R_i = 1.5$), $V_{1.5}$ (radial velocity at $r/R_i = 1.5$), $V_{2.4}$ (radial velocity at $r/R_i = 2.4$), $W_{1.5}$ and $W_{2.4}$ are also used in the present study. The Spearman's rank-order correlation is the nonparametric form of the Pearson product-moment correlation. Spearman's correlation coefficient, r_s, measures the strength of association between two variables by using variable rank order. It is calculated by the following equation

$$r_s = 1 - \frac{6\sum p_i^2}{p(p^2 - 1)} \qquad 3.42$$

In which p_i is the difference in paired rank of the variables and p is the number of paired variables. If there are tied ranks then the formula is,

$$r_s = \frac{\sum (x_i - \bar{x})(y_i - \bar{y})}{\sqrt{\sum (x_i - \bar{x})^2 \sum (y_i - \bar{y})^2}} \qquad 3.43$$

where i is paired score, x_i and y_i are the ranks of paired variables, while $\bar{x}$ and $\bar{y}$ are the average ranks of all paired variables. The absolute value of r_s represents the strength of association between the two variables. The significance of the nonzero value of r_s is evaluated by employing student's t distribution test. The value of t is computed by,

$$t = \frac{r_s \sqrt{p-2}}{\sqrt{1-r_s^2}} \tag{3.44}$$

According to the Spearman's rank-order theory, if computed t from Equation 3.44 is more than the critical value of student's t-distribution table reports, $t_{0.05}$ (at the one-tailed 95% significance level), there is a positive interaction between the selected parameter and Reynolds number or flow index. In Table 3.3, the values determined for interaction between computed velocity profiles and *Re* and *n* are illustrated and also compared with the Venneker et al. (2010) observation. It shows the same kind of observation except on U_{wall} where present work does not find any effect of *Re* whereas Venneker et al. (2010) did and on W_{wall} where present work finds a positive effect of *n* but Venneker et al. (2010) did not. The non-parametric test results of discharge profiles are presented in Table 3.4. In the table, the subscripts along the variables represent the axial position. The table shows many differences between the prediction of the present simulated results and Venneker et al. (2010) observation on the effect of *Re* and *n* on the selected parameters of the discharge profiles.

Table 3.3 Non-parametric test results for velocity profiles

Velocity	Parameters	$t_{0.05}$	t_{Re}	t_n	Significant *Re* (predicted)	Significant *Re* (Venneker et al., 2010)	Significant *n* (predicted)	Significant *n* (Venneker et al., 2010)
Axial	U_1	1.96	2.0	0.194	yes	yes	no	no
	$U_{1.5}$	2.353	0.532	0.751	no	-	no	-
	U_{wall}	2.353	0.544	1.566	no	yes	no	no
	R_0	2.353	0.544	1.566	no	no	no	no
Radial	$V1$	2.353	1.697	2.177	no	no	no	no
	$V1.5$	2.353	1.697	2.177	no	-	no	-
	$V2.4$	2.353	1.299	2.177	no	-	no	-
	$Vwall$	2.353	0.544	1.566	no	-	no	-

Tangential	*W1*	2.353	1.0	2.1775	no	no	no	no
	W1.5	2.353	0.353	3.464	no	-	yes	-
	W2.4	2.353	0.0	0.755	no	-	no	-
	Wwall	2.353	0.174	3.464	no	no	yes	no

Table 3.4 Non-parametric test results for discharge velocity profiles

Velocity	Parameters	$t_{0.05}$	t_{Re}	t_n	Significant *Re* (Predicted)	Significant *Re* (Venneker et al., 2010)	Significant *n* (Predicted)	Significant *n* (Venneker et al., 2010)
Axial	U_{-2}	2.353	1.697	-2.177	no	yes	no	no
	U_{-1}	2.353	-0.755	3.464	no	no	yes	no
	U_0	2.353	1.697	-2.177	no	yes	no	yes
	U_{+1}	2.353	1.697	-2.177	no	yes	no	yes
	U_{+2}	2.353	0.353	-2.177	no	yes	no	yes
radial	$V_{@z^*=z0}$	2.353	1.697	0.616	no	no	no	no
	$z^*_{@z=0}$	2.353	1.566	0.447	no	no	no	no
	$width_{@Vz=02}$	2.353	1.697	-2.177	no	yes	no	yes
tangential	$z^*_{@z=z0}$	2.353	1.074	0.534	no	no	no	no
	$width_{@w=0.2}$	2.353	-0.647	3.464	no	no	yes	yes
	$z^*=0$	2.353	0.174	-1.566	no	no	no	no

3.5.4 Prediction of Flow Number

The flow number, N_q, proportionate to the pumping capacity of the impeller is an important parameter for testing the performance of the mixing process in the stirred tank. Venneker et al. (2010) found flow number of non-Newtonian fluid over a small range of Reynolds number, $10^3 < Re < 7\text{x}10^4$, and also compared with Dyster et al. (1993) who had found it experimentally only for Newtonian fluid for laminar to turbulent flow state ($2 < Re < 3\text{x}10^4$). The computed flow number in the present work is shown in Figure 3.7 ($1.0 < Re < 6.0 \text{ x } 10^4$). The figure shows that the computed flow number for shear thinning fluids follow the flow number of Venneker et al. (2010) for non-Newtonian fluid, and they are also coming in between Dyster et al. (1993) and Koutsakos and Nienow (1990) where experimental flow numbers were found for shear thinning fluid with some viscoelastic behavior. The closeness of computed flow numbers to the Dyster et al. (1993) happens due to the absence of viscoelastic behavior in the used non-Newtonian fluid. In laminar region (*Re* < 10-20), the flow number of all shear thinning solutions increases rapidly with *Re*. While in the transition region (10-20 < *Re* < 10^4), it gradually increases with *Re*. In turbulent region (10^4 < *Re*), N_q for all shear thinning solutions are found almost constant, and it is equal to 0.70 which is found little less compared to 0.78 for Newtonian fluid given in the literature (Dyster et al., 1993).

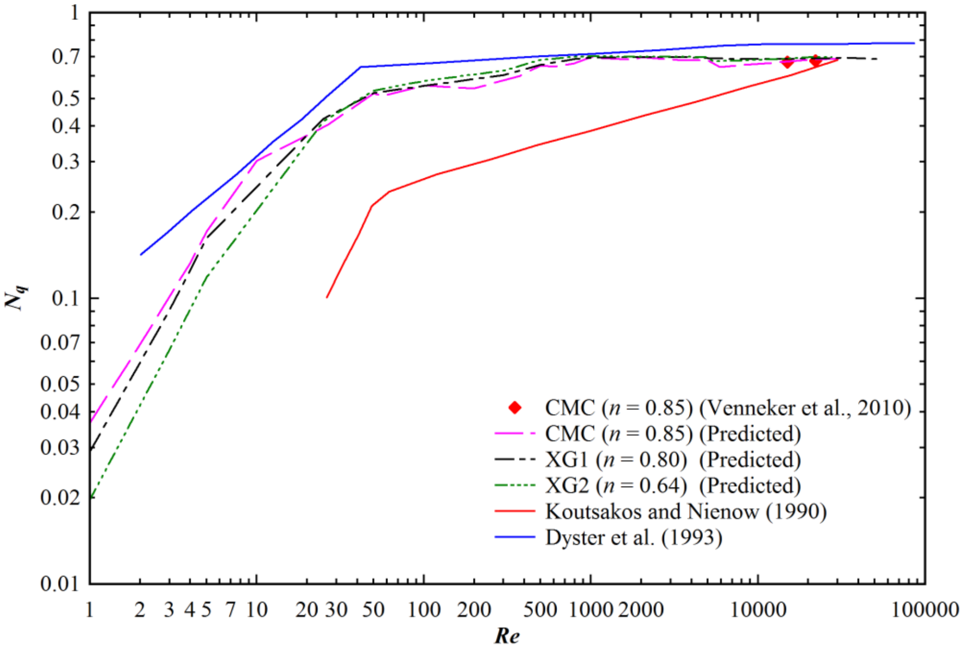

Figure 3.7 Variation of impeller flow number, N_q with impeller Reynolds number, *Re*.

3.5.5 Prediction of Power Number

An accurate CFD model should be able to predict the overall power input to a stirred tank (Deglon and Meyer, 2006). Many researchers have used the impeller power number, N_p, to check the validity of CFD models used for flow simulation in stirred tank (Dyster et al., 1993; Brucato et al., 1998; Bartels et al., 2002). Due to unavailability of the experimental data, the power number is computed and presented for the present physical system in Figure 3.8(a) at different flow index of the working fluid. The power number is also compared with the power number of Newtonian fluid available in the literature (Bates et al. 1963). On the log-log plot, the power number (N_p) of the shear thinning fluid decreases linearly with Reynolds number (*Re*) in the laminar region, i.e., $N_p \cdot Re$ = constant. It slowly approaches a constant value of 5.0 at high Reynolds number, i.e., in the turbulent region. In the laminar zone, it is observed that N_p of non-Newtonian fluid is less than the Newtonian fluid. In the turbulent region, the power curve is found almost independent of *Re*, and the N_p of shear thinning fluid approaches the power number of the Newtonian fluid.

Figure 3.8(b) shows the distribution of power number with the impeller Reynolds number at different clearance for $n = 0.85$. The power number decreases with Reynolds number up to $Re = 50$ and then increases to a constant value in the turbulent zone. For $Re < 10$: the N_P for $C_i = 0.33D$ is the lowest i.e. N_p for $C_i = 0.2$, 0.5, 0.7, 0.75 and 0.8 of *D* is more than $C_i = 0.33D$. The reason behind this is, the more pressure drop across the impeller blade for $C_i = 0.2D$ than 0.33*D*. When the impeller placed at a higher level than $C_i = 0.33D$, the fluid around the impeller are mostly stagnant (these are examined through velocity contour plots) and hence more shear force is required to move the impeller. These leads to more power number for the impeller clearance greater than 0.33*D*.

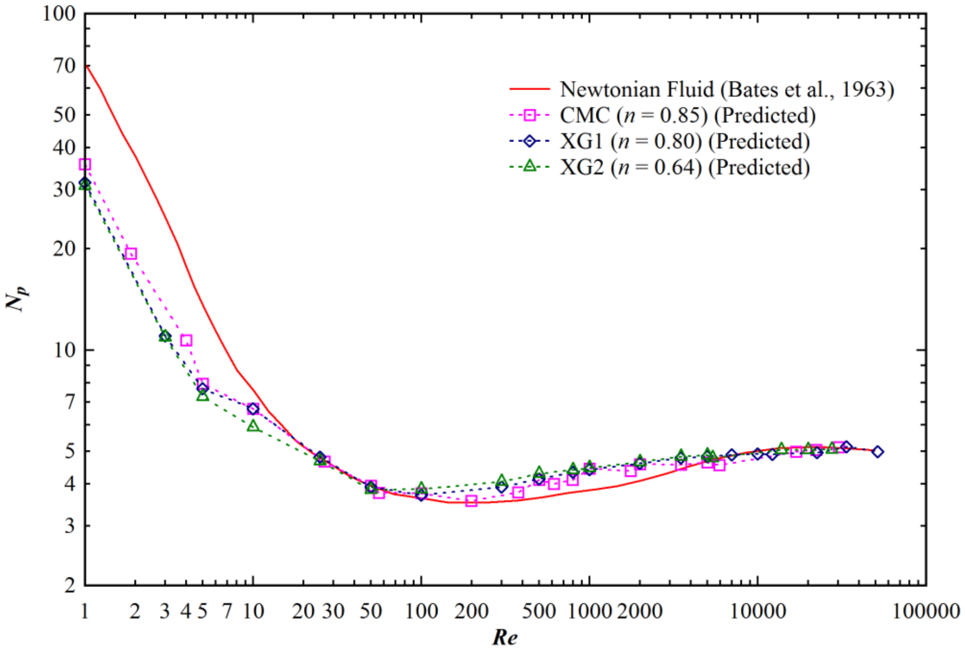

(a)

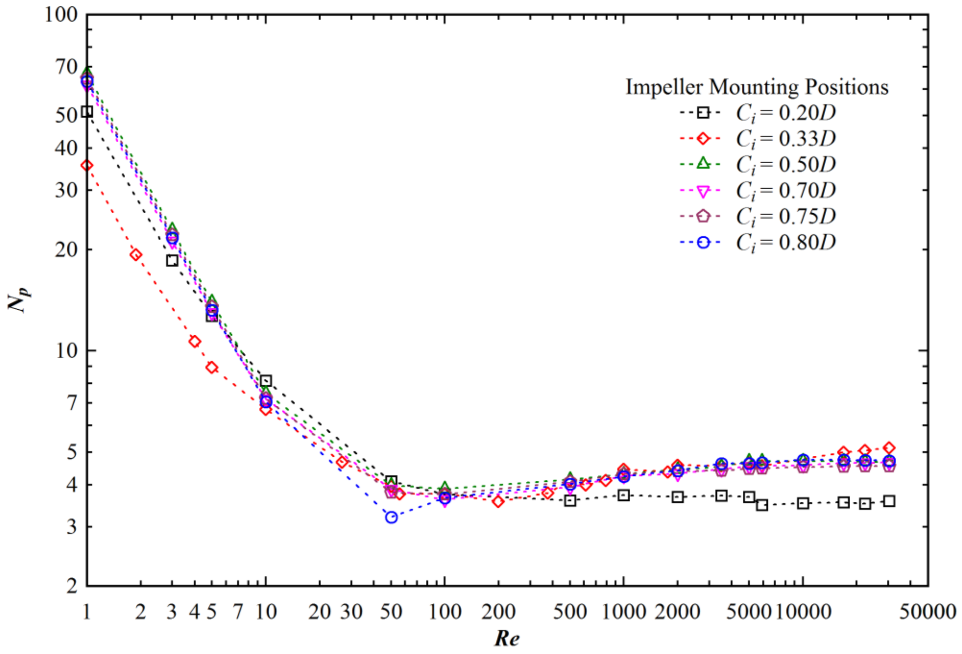

(b)

Figure 3.8 Distributions of (a) Impeller power number (N_p) with impeller Reynolds number (Re) for different shear thinning fluids (b) Impeller power number (N_p) with impeller Reynolds number (Re) for CMC at different impeller mounting positions from bottom wall of tank.

3.5.6 Prediction of Mixing Time and efficiency

In this section, the mixing times at different locations in the tank with Rushton turbine are determined from the CFD predicted tracer concentration versus time curves. Experimentally, the mixing time is estimated by giving an input of tracer at a certain location in the tank and monitoring the concentration, C of the tracer with time at some other location (Zhou et al., 2003). The mixing time, at the particular locations (P_1, P_2, P_3 and P_4 in Figure 3.1(b)), is considered as the time required for reaching the concentration of tracer within 95% or 105% of the final steady state concentration, C_∞ at that location. A tracer with the same physical properties of the working fluid is injected initially at center of bottom surface of the tank, i.e., at point P_5 and the concentrations at remaining cells are initialized to zero. Numerically the concentrations at locations P_1 to P_4 are collected with time and the respective non-dimensional traction concentration distributions are demonstrated in Figure 3.9. The effect of impellers on fluid flow decreases as move from location P_1 to P_4. Therefore, as depicted in the figure, the mixing time, t_m increases from the location P_1 to P_4 at all the impeller speeds irrespective of the flow behavior index. It is also observed that the impeller speed has the huge effect on the mixing time.

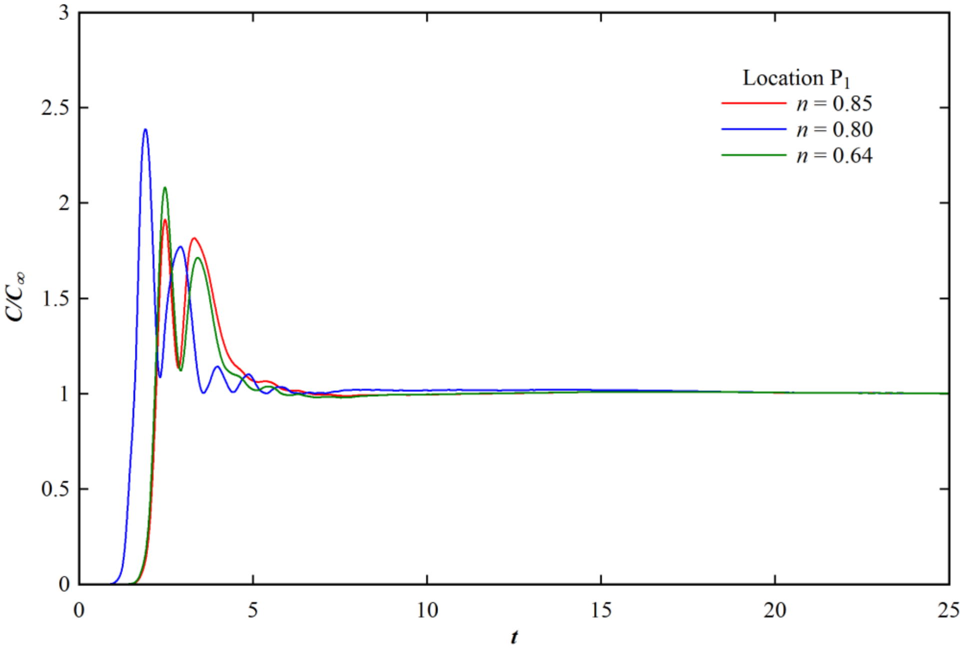

(a)

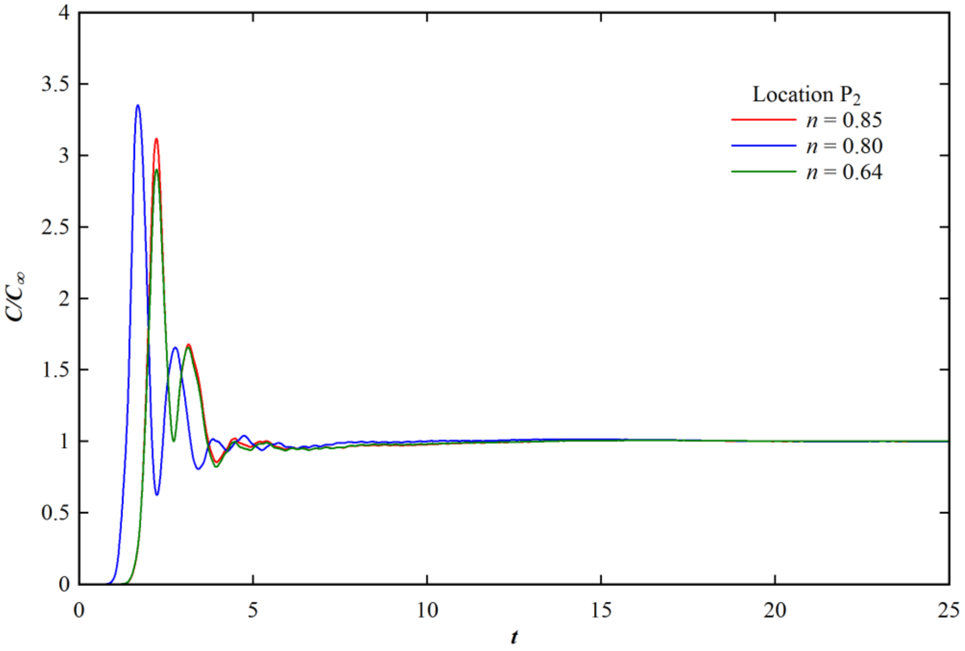

(b)

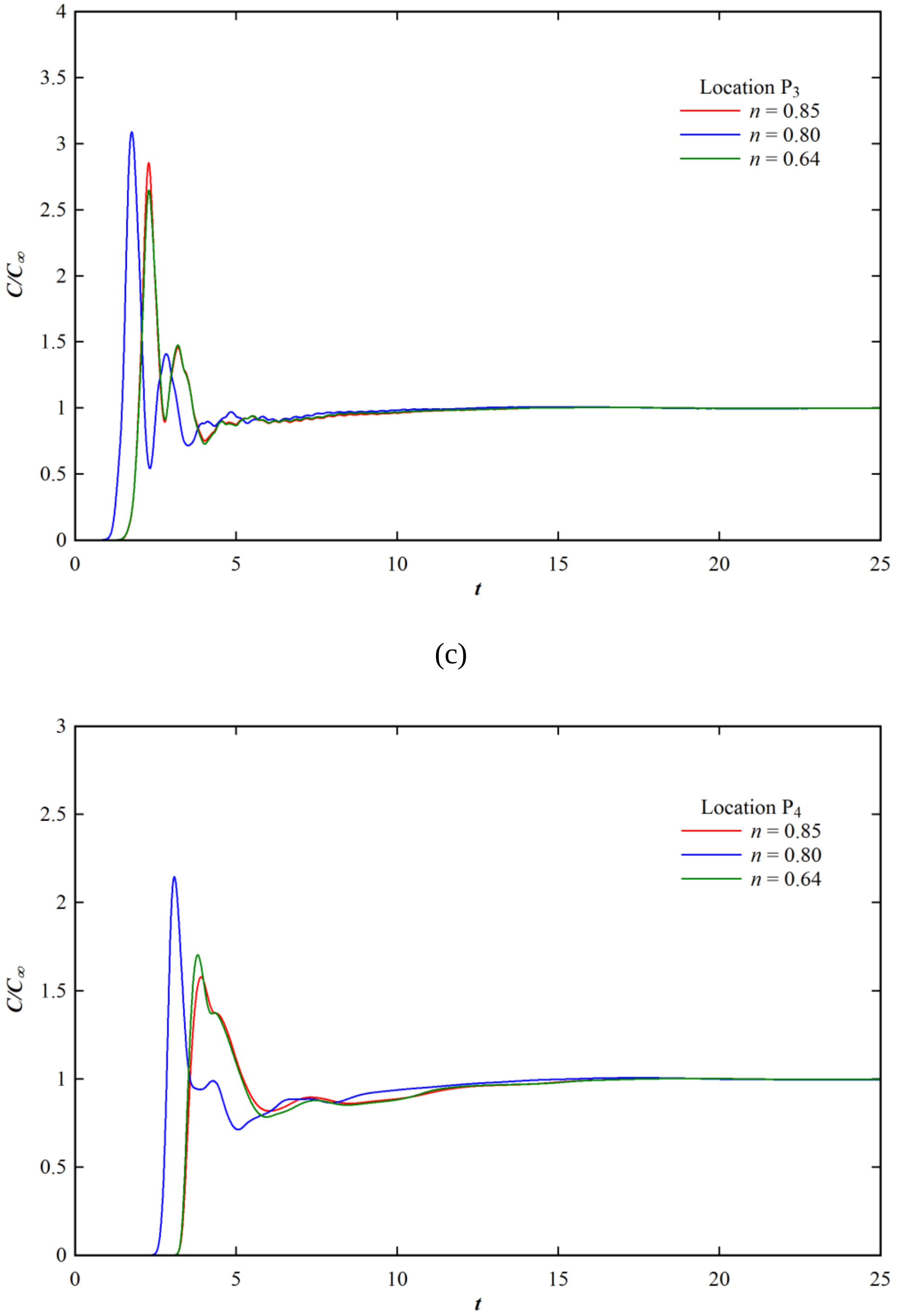

(c)

(d)

Figure 3.9 Response curve for the shear thinning fluid at 180 rpm impeller speed.

The calculated mixing time, t_m is multiplied by the impeller rotations, N to obtain the non-dimensional mixing time, Nt_m. The chosen range of the impeller speed makes sure that the flow is in transition or in the turbulent flow state. The distributions of the non-dimensional mixing time with the impeller speed are illustrated in Figure 3.10. The figure shows that the nature of distribution of the Nt_m is dependent on the mixing study location and the distribution of the non-dimensional mixing time is scattered in nature.

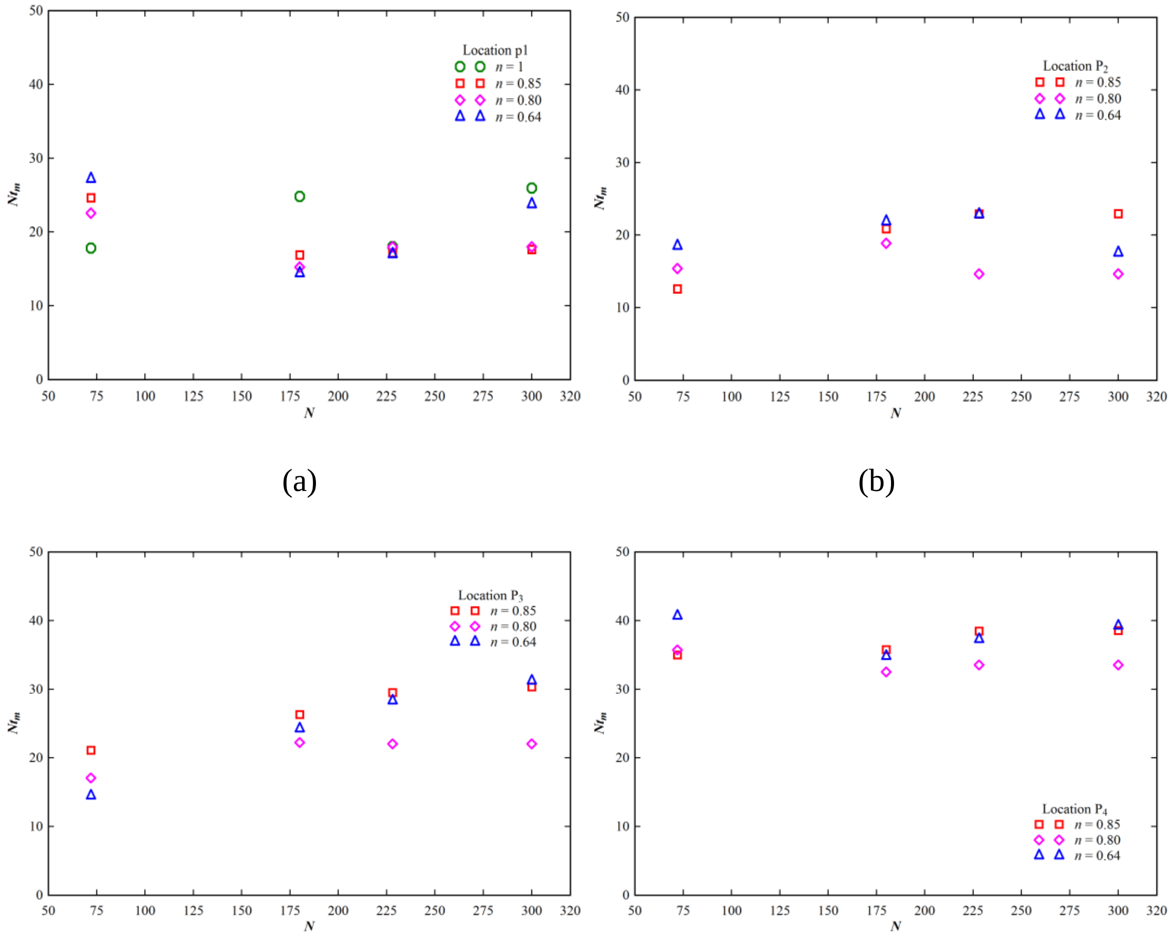

(a) (b)

(c) (d)

Figure 3.10 Distributions of the non-dimensional mixing time with impeller rotations for non-Newtonian fluids.

3.5.7 Prediction of Dispersive mixing efficiency

De la Villeon et al. (1998) and Emin and Schuchmann (2013) have studied mixing efficiency in terms of dispersive mixing efficiency. It is denoted by α_{DME} and defined as

$$\alpha_{DME} = \frac{\|\dot{\gamma}\|}{\|\dot{\gamma}\| + \|\omega\|} \qquad 3.45$$

where, $\dot{\gamma}$ is the rate of strain tensor and $\omega = 1/2\left[\nabla v - (\nabla v)^T\right]$ is the vorticity tensor. For a mixing index of 0, the system is undergoing purely rotational flow and no effective mixing can occur. A mixing index of 0.5 denotes simple shear flow, while a value of 1.0 denotes irrotational flow (i.e. elongational or dispersive flow). Figure 3.11 illustrates the distribution of α_{DME} for the Rushton turbine impeller. The figure shows that the average α_{DME} is little more than 0.5 for all impeller rotations and flow behavior indexes. Hence, overall, the flow inside the stirred tank is a simple shear flow.

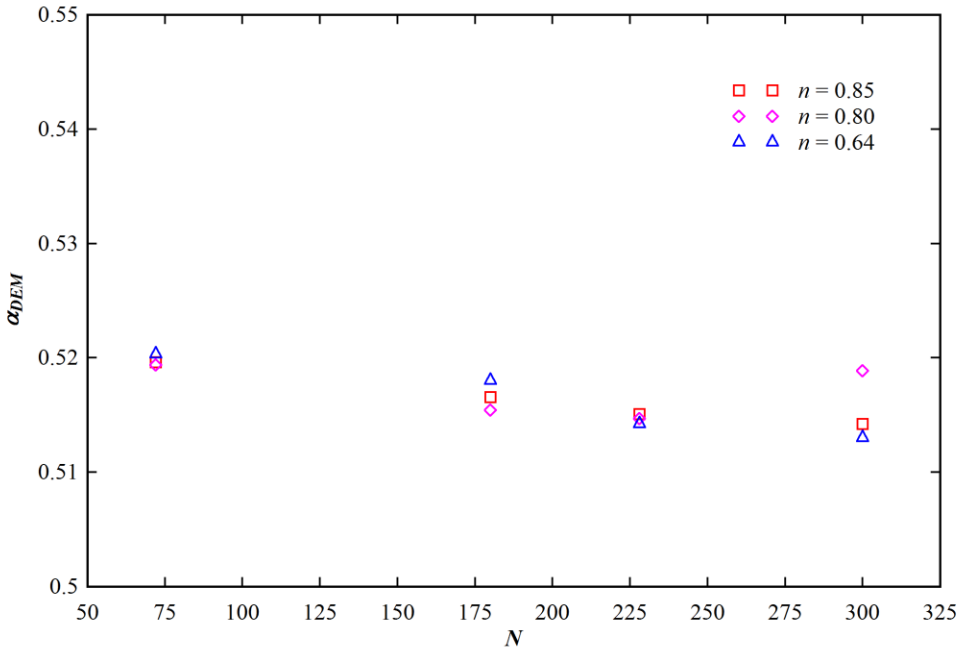

Figure 3.11 Distribution of the average dispersive mixing efficiency with impeller rotations.

3.5.8 Prediction of Entropy Generation of Isothermal Batch Stirred Tank

The entropy generation of the universe should be positive for any feasible process. It may increase either monotonically or non-monotonically with change in the system parameters. Entropy generation reduction results in more efficient designs of energy systems. For non-isothermal system, entropy generation passes through minimal, and it is necessary to keep it minimum for achieving the economically viable process. The present section uses only isothermal working fluid where the entropy generation occurs only due to fluid friction. For turbulent flow, the entropy generation is computed from Equation 3.38. According to it, the entropy generation occurs due to both the time average velocity gradient and velocity fluctuation gradient. At steady state, the rate of loss of energy due to entropy generation is equal to the power delivered by the stirrer (Norris et al., 2011). The computed values of $\rho\varepsilon$ are found to be almost equal to $\mu_{eff}\varphi_v$ and the sum of these two under predicts / over predicts the power input to the impeller. They are shown in Table 3.5. Hence, the contribution to the fluctuating entropy generation needs to be modified according to the following equation.

$$P = T\,\dot{S}_{VD'} = \mu_{eff}\varphi_v + f \cdot \rho\varepsilon \qquad 3.46$$

The factor f determines the contribution of turbulence energy dissipation on the system entropy generation and P is the power exerted by the impeller on fluid. The values of f at different impeller clearances are shown in Table 3.5. It is well understood that the extent of turbulence decreases with increase in C_i which results in the decrease of f with C_i. It is also observed that f varies largely with impeller clearance and less with the impeller rotational speed. Hence, an average f is found at each C_i, and Equation 3.46 is used for further parametric sensitivity study with the average f at the given value of C_i.

Table 3.5 Effect of impeller clearance and speed of impeller on the factor *f*

(a) $C_i = 0.2D$					(b) $C_i = 0.33D$				
rpm	P	$\mu_{eff}\varphi_v$	$\rho\varepsilon$	f	rpm	P	$\mu_{eff}\varphi_v$	$\rho\varepsilon$	f
72	2.396	1.183	1.161	1.045	72	3.139	2.562	2.463	0.234
180	38.069	19.259	17.145	1.097	180	53.758	40.792	40.637	0.319
228	76.729	37.774	34.730	1.122	228	110.495	83.170	83.064	0.329
300	178.158	82.580	79.939	1.196	300	256.256	190.443	190.33	0.346
				Average f = 1.12					Average f = 0.31

(c) C_i =0.5D					(d) C_i = 0.7D				
rpm	P	$\mu_{eff}\varphi_v$	$\rho\varepsilon$	f	rpm	P	$\mu_{eff}\varphi_v$	$\rho\varepsilon$	f
72	3.234	2.654	2.550	0.228	72	3.129	2.770	2.665	0.135
180	50.531	41.414	41.277	0.221	180	49.810	42.981	41.830	0.163
228	102.336	87.114	85.668	0.178	228	101.488	86.741	85.147	0.173
300	232.025	193.591	193.522	0.199	300	231.527	196.387	194.071	0.181
				Average f = 0.21					Average f = 0.163
(e) C_i = 0.75D					(f) C_i = 0.8D				
rpm	P	$\mu_{eff}\varphi_v$	$\rho\varepsilon$	f	rpm	P	$\mu_{eff}\varphi_v$	$\rho\varepsilon$	f
72	3.082	2.742	2.636	0.129	72	2.321	2.056	1.998	0.133
180	48.681	42.181	41.123	0.158	180	36.570	31.839	31.013	0.153
228	99.128	85.045	83.601	0.168	228	74.392	64.285	63.014	0.160
300	226.160	192.788	190.731	0.175	300	169.464	145.425	143.518	0.168
				Average f = 0.158					Average f = 0.154

The contours of local entropy generation due to viscous dissipation of CMC solution with n = 0.85 are shown in Figure 3.12. The rate of entropy generation is large in the vicinity of the impeller especially in the space between two consecutive impeller blades. It occurs due to the entry of the bulk liquid in the displaced liquid volume by the impeller and also due to the transfer of momentum from the impeller to the fluid. The entropy generation becomes negligible at the distance half way between the center and the wall of the tank. It happens due to the movement of the liquid with uniform velocity at those positions. As expected dimensionless entropy generation increases with an increase in impeller rotational speed and thus more mixing in the tank at the cost of power (Figure 3.13).

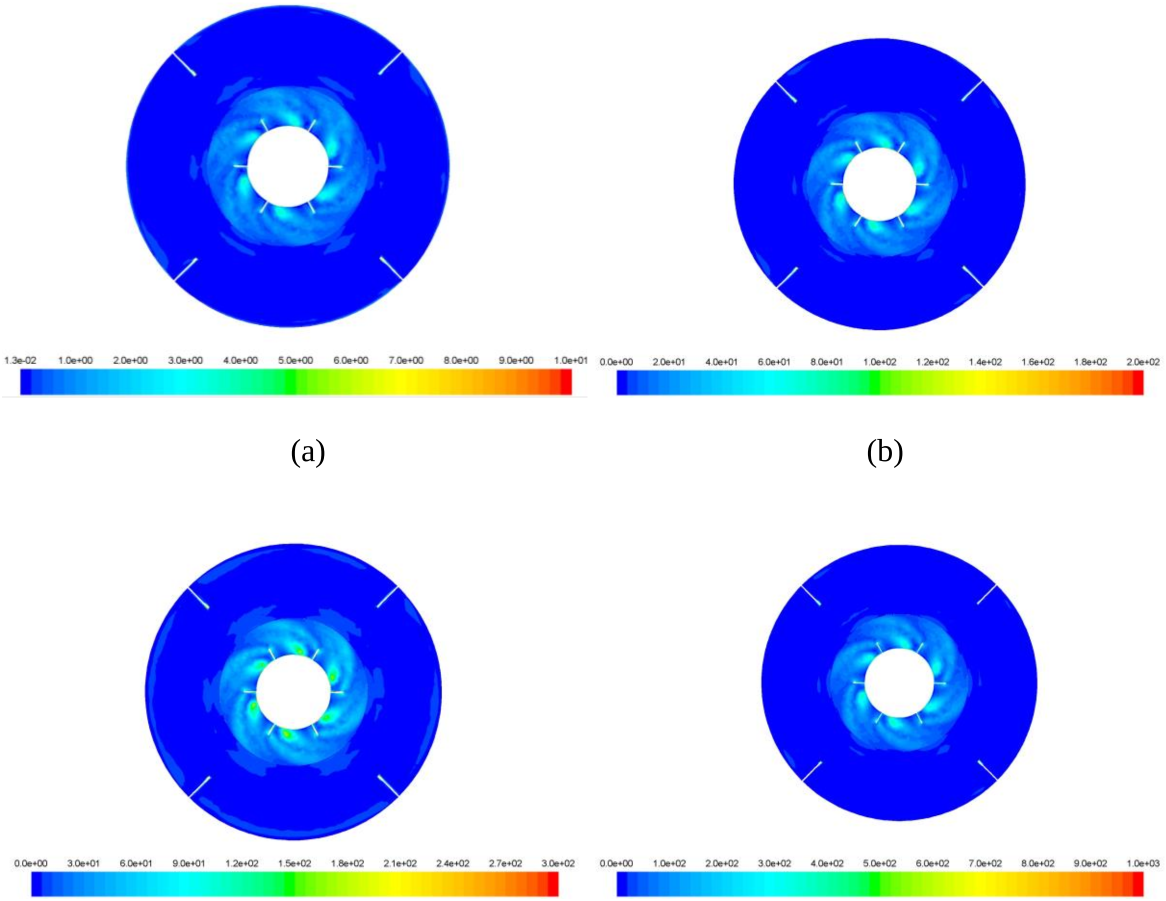

(a) (b)

(c) (d)

Figure 3.12 Contours of entropy generation at different impeller rotations in tank for n = 0.85 and impeller position at 1/3D, (a) N = 72 rpm, (b) N = 180 rpm, (c) N = 228 rpm, (d) N = 300 rpm.

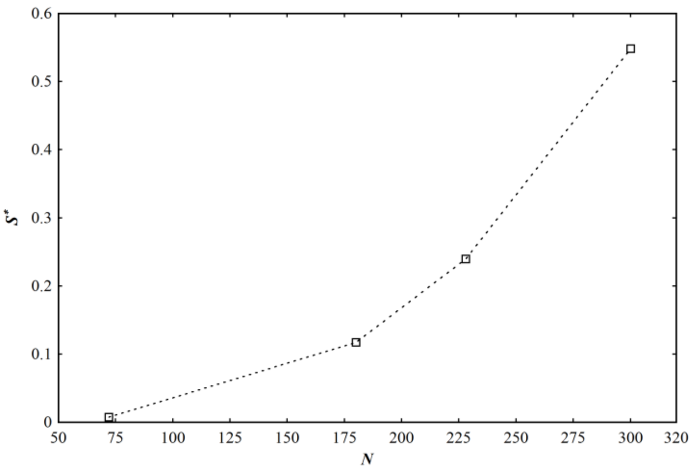

Figure 3.13 Variation of dimensionless entropy generation with impeller speed.

The effect of the impeller off bottom clearance on the entropy generation for CMC solution (n = 0.85) at the different speed of the impeller is depicted in Figure 3.14. At low rotation of the impeller, N = 72 rpm, the entropy generation is almost constant with magnitude nearly equal to zero for all impeller clearances. It happens because of the non-development of significant velocity gradient and hence less dissipation of the viscous energy. But as rotation increases, the viscous dissipation in the fluid increases, and thus the rate of entropy generation increases. At higher rotations, 180, 228 and 300 rpm, the entropy generation initially increases while C_i changes from 0.2 to 0.33, after that it starts to decrease for further raising of the impeller up to C_i = 0.8. Overall, it is found that the extent of mixing is less when the impeller is placed at the extreme top and bottom side of the tank. It is due to the formation of the stagnant zone respectively above and below the impeller.

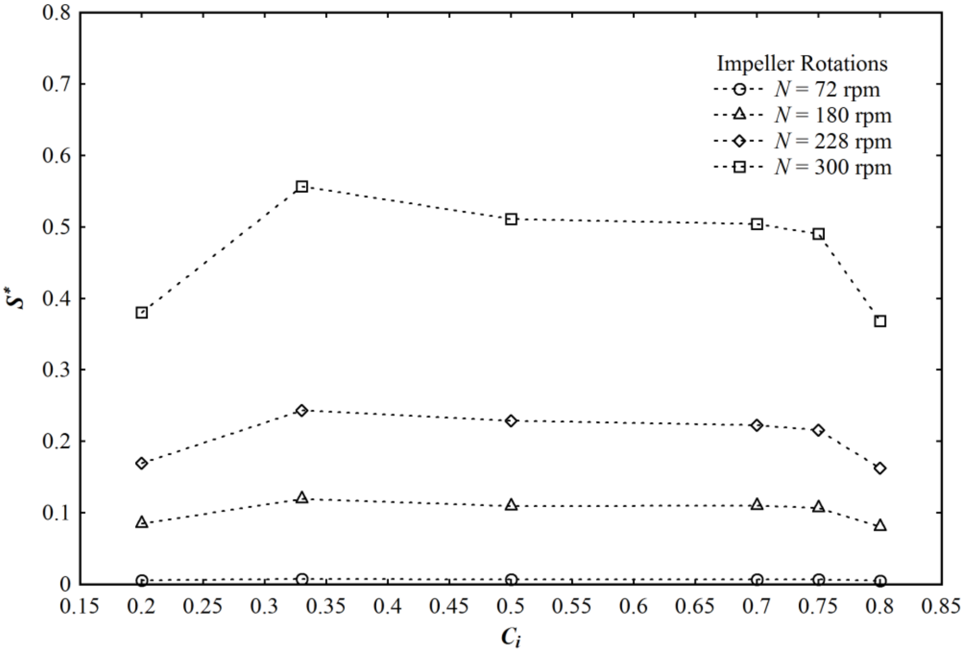

Figure 3.14 Dimensionless entropy generation for the different impeller rotations at different impeller mounting position for n = 0.85.

Figure 3.15 shows the effect of the width and thickness of the impeller blade on the entropy generation at different impeller speed. The entropy generation increases with the impeller blade width. It happens due to the increasing contact area between the impeller blade and the surrounding fluid, and hence more mixing. In Figure 3.15(b), the entropy generation is observed almost independent of the blade thickness. The variation of the entropy generation with the flow index of the shear thinning fluid, as depicted in Figure 3.16, is found more at higher impeller speed. The figure also illustrates that the entropy generation of non-Newtonian fluid is more than Newtonian fluid. It may be due to the more viscous dissipation near the impeller surface as the rheological property of the non-Newtonian fluid changes sharply within the impeller vicinity.

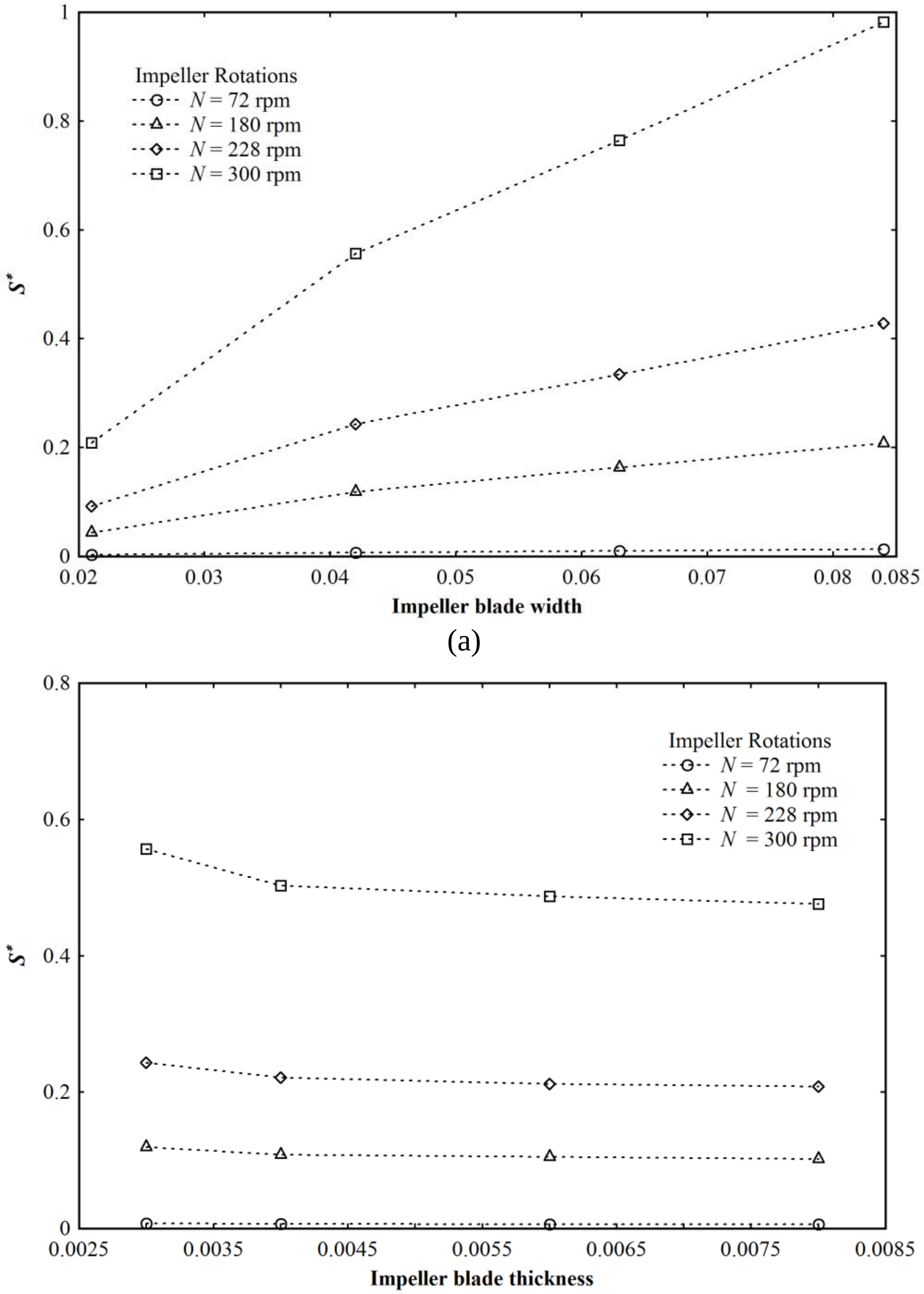

(a)

(b)

Figure 3.15 (a) Dimensionless entropy generation with impeller width at different impeller rotations for *n* = 0.85, (b) Dimensionless Entropy generation with impeller blade thickness at different impeller rotations for *n* = 0.85.

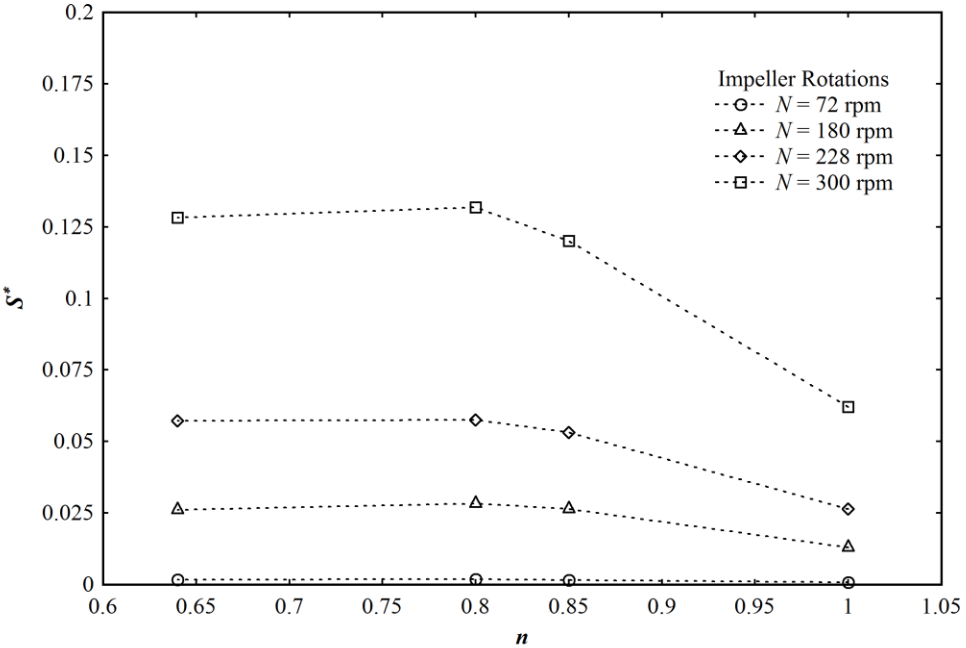

Figure 3.16 Dimensionless entropy generation with flow behavior index at different impeller speed.

3.5.9 Prediction of Entropy Generation in Continuous Stirred Tank

To analyze entropy generation of continuous stirred tank, a pair of inlet and outlet pipe of diameter (*d*) 0.025m is added to the batch stirred tank. They are placed on the side wall of the tank and in between two baffles. Carboxymethyl cellulose (CMC) is taken as the working fluid with consistency index, *K*, 0.0132 and flow index, *n*, 0.85 (Venneker et al., 2010). For non-isothermal reactor, a temperature dependent viscosity is considered. The thermal conductivity $(\lambda)$of the fluid is 0.7 W/(m K) (Denys et al., 2007).

The optimization study consists of minimizing the total entropy generation rate in the stirred tank by varying tank parameters and keeping either constant wall temperature or constant wall heat flux as the heating source for the tank's liquid. For each thermal boundary condition of the wall, the optimization is involved with four systematic steps where the entropy generation is minimized in each step with respect to the inlet Reynolds number (Re_i), impeller rotation, impeller clearance and the blade width.

Step 1: Entropy generation is minimized with respect to inlet fluid flow Reynolds number, Re_i, using 180 rpm speed of the impeller, 0.33D impeller clearance and 0.042m impeller blade width.

Step 2: Entropy generation is minimized with respect to impeller rotation using optimized inlet Re_i obtained in the step 1, 0.33D impeller clearance and 0.042m impeller blade width.

Step 3: Entropy generation is minimized with respect to impeller clearance using optimized inlet Re_i, optimized impeller rotation and 0.042m impeller blade width.

Step 4: Entropy generation is minimized with respect to impeller blade width using optimized inlet Re_i, optimized impeller rotation and optimized bottom clearance obtained in step 3.

3.5.9.1 Constant Wall Temperature Thermal Boundary Condition

3.5.9.1.1 Optimization with respect to inlet Reynolds number

The dimensionless entropy generation in stirred tank at different boundary wall temperature is shown in Figure 3.17. The optimum inlet Reynolds number is determined as a function of wall temperature. Due to the large temperature gradient near the wall, the entropy generation is found high at very low Re_i. The convective energy transport increases with Re_i, and it reduces the temperature gradient in the stirred tank. Therefore, the entropy generation due to heat transfer irreversibility decreases with the increase in Re_i. However, the entropy generation due to frictional loss increases with the increase in Re_i. The total entropy generation, therefore, passes through a minimal. On the left side of the minimal point, the contribution of thermal entropy generation and on the right side of it the contribution of viscous entropy generation to the total entropy generation is more. The entropy generation is found higher at the higher wall temperature. The figure also shows that the magnitude of minimum entropy generation is higher for the higher wall temperature. At high temperature, the viscosity of the liquid is less and hence, the frictional loss is also less. Therefore, the optimized Re_i increases with the wall temperature. The optimized inlet Reynolds numbers are 3600, 3400, 3200 and 3000 for the wall temperatures 353, 343, 333 and 323K, respectively.

Figure 3.18 shows the profile of Bejan number, Be, with inlet Reynolds number. Be is approximately equal to 1.0 till the Re_i equals to 3000, and it becomes 0.5 for Re_i between 8000 and 10000. Thus, over a wide range of Re_i, the thermal entropy generation is more than the entropy generation due to the viscous dissipation. Comparison of Figure 3.17 and Figure 3.18 shows that around the entropy minimization point, the heat transfer irreversibility is much larger than the frictional irreversibility. The linear and sharp variation of *Be* at higher Re_i occurs due to the domination of the convective energy transport over the conductive heat transfer. The higher wall temperature leads to larger temperature gradients, which results in the higher Bejan number.

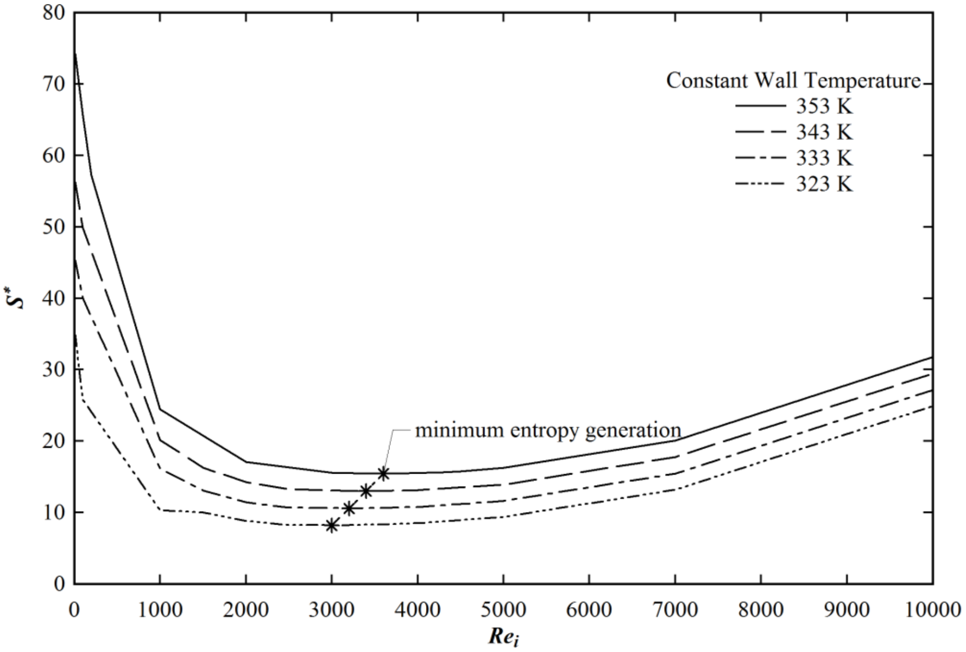

Figure 3.17 Dimensionless entropy generation with inlet Reynolds number at a constant wall temperature with 180 rpm of the impeller rotations, 0.33*D* impeller clearance and 0.042m impeller blade width.

3.5.9.1.2 Optimization with respect to impeller rotations

The comparison of Figure 3.17 and Figure 3.19 reveals that the entropy generation varies more with the Re_i than the impeller rotations. It occurs due to the larger variation of the temperature gradient of fluid inside the reactor with Re_i. The less dependency of the entropy generation on the impeller rotations proves that the entropy generation shown in Figure 3.19 is affected mainly by the heat transfer irreversibility. The same is also observed in Figure 3.20 where *Be* is closer to 1.0 at all the impeller rotations. The optimum impeller rotations are 104, 100, 91 and 85 rpm for the wall temperatures 353, 343, 333 and 323K, respectively. Hence, a little increase in optimum impeller rotations is observed with the temperature of the wall of the continuous stirred tank.

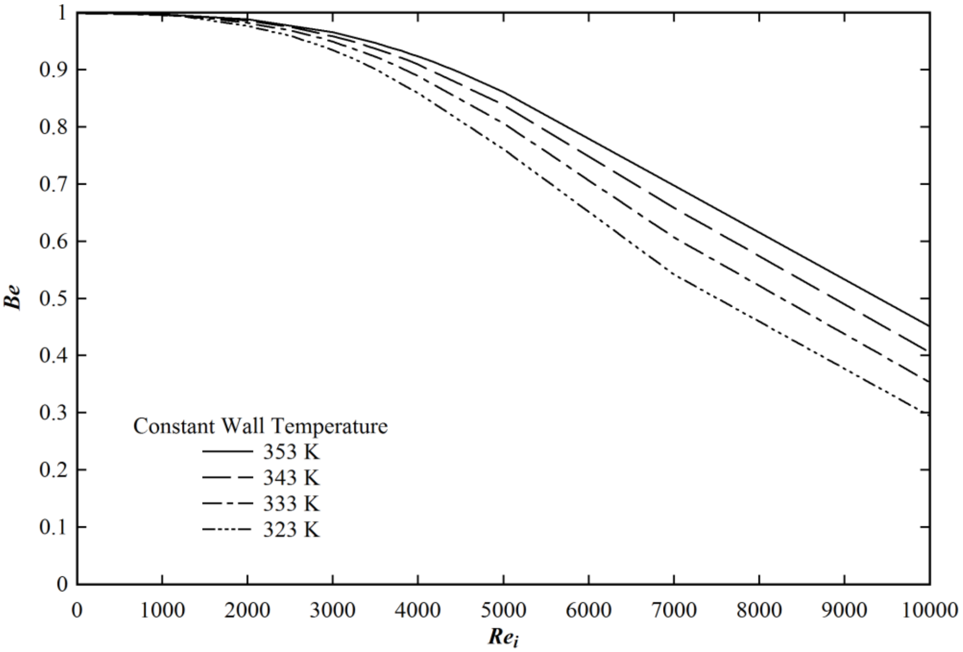

Figure 3.18 Distribution of Bejan number with inlet Reynolds number at a constant wall temperature with 180 rpm of the impeller rotations, 0.33*D* impeller clearance and 0.042m impeller blade width.

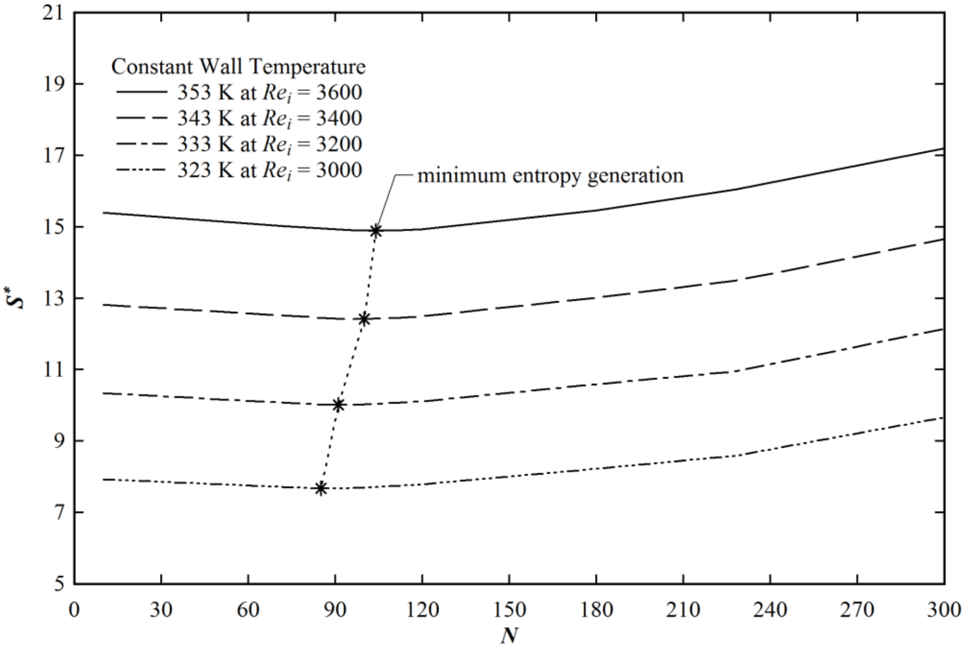

Figure 3.19 Dimensionless entropy generation with impeller rotations at a constant wall temperature with optimized Re_i, 0.33*D* impeller clearance and 0.042m impeller blade width.

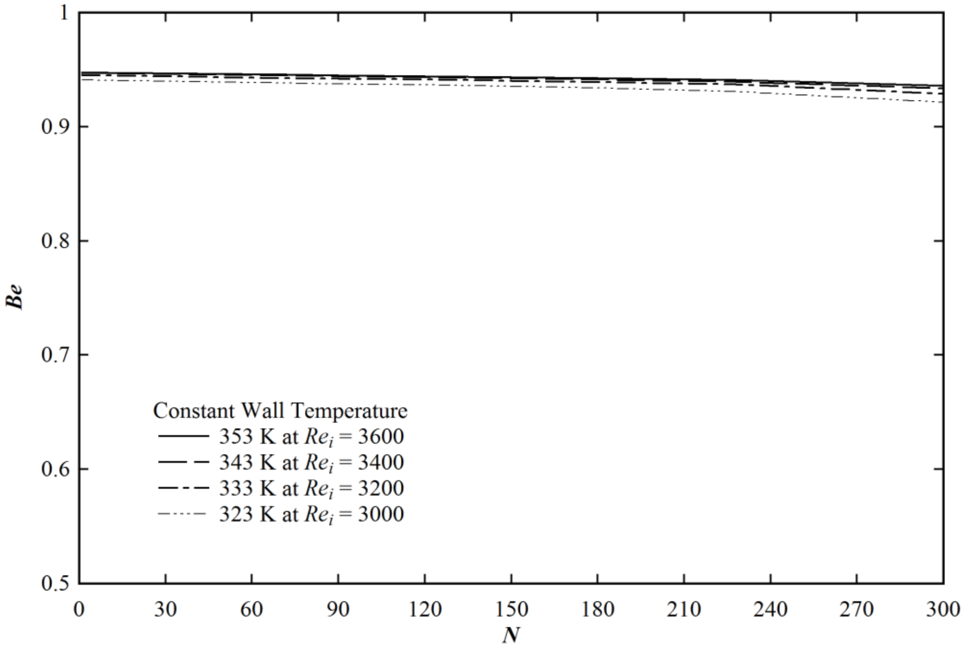

Figure 3.20 Distribution of Bejan number with impeller rotations at a constant wall temperature with optimized Re_i, 0.33*D* impeller clearance and 0.042m impeller blade width.

3.5.9.1.3 Optimization with respect to impeller clearance

The impeller clearance affects the flow and temperature distribution inside the stirred tank. The effect causes the variation of the entropy generation, and it is shown in Figure 3.21. The figure depicts that for wall temperature 353K, the entropy generation is minimum at impeller clearance, C_i = 0.33*D*. Whereas, for other wall temperatures, the minimum entropy generation occurs at impeller clearance, C_i = 0.2*D*. The respective Bejan number distribution is shown in Figure 3.22. It shows that the entropy generation at all the impeller clearance is affected predominantly by the heat transfer irreversibility. At lower clearance than 0.33*D*, the flow around the impeller forms single loop and it results in axially up movement of the fluid. Whereas, the two loops are formed around the impeller, and it gives better mixing for C_i = 0.33*D*. Due to this the temperature gradient for the latter case is higher, and hence, more entropy is generated due to the thermal irreversibility. Therefore, *Be* is found maximum at C_i = 0.33*D*.

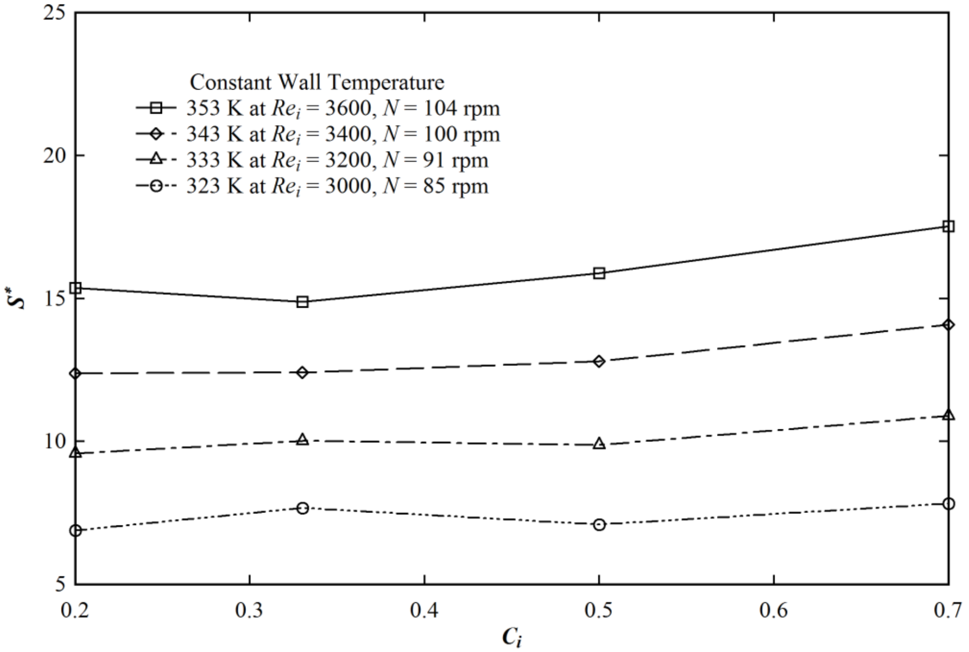

Figure 3.21 Dimensionless entropy generation with impeller clearance at constant wall temperature with optimized *Re*ᵢ, optimized impeller rotations and 0.042m impeller blade width.

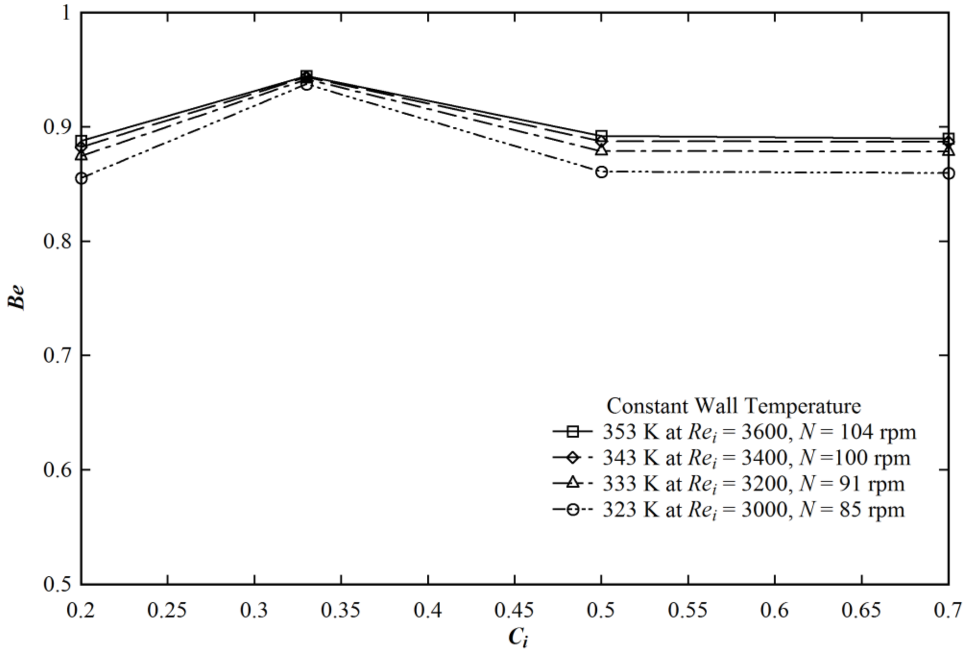

Figure 3.22 Distribution of Bejan number vs. impeller clearance at constant wall temperature with optimized *Re*ᵢ, optimized impeller rotations and 0.042m impeller blade width.

3.5.9.1.4 Optimization with respect to impeller blade width

The variation of entropy generation with the impeller blade width is shown in Figure 3.23. In case of $C_i = 0.2D$, the entropy generation is observed to decrease up to the width of 0.042m, and after that it becomes invariant with the width of the impeller. For the smaller impeller blade width, the mixing of liquid inside the tank is low and hence, there is more thermal irreversibility due to the presence of the larger thickness of the thermal boundary layer. It can also be seen in the Bejan number distribution in Figure 3.24. The convective energy transport reaches at saturated state if the impeller width is more than 0.042 m. Hence, the entropy generation becomes constant at higher impeller blade width. For the wall temperature 353 K, the impeller is mounted at higher position with clearance $C_i = 0.33D$. The higher impeller position finds a little dependency of heat transfer irreversibility on the impeller blade width. Therefore, the entropy generation is found almost invariant with the blade width of the impeller for $C_i = 0.33D$. Figure 3.23 also shows that there is a definite optimum value of impeller blade width that corresponds to the minimum entropy generation and the optimum impeller blade width is 0.042 m.

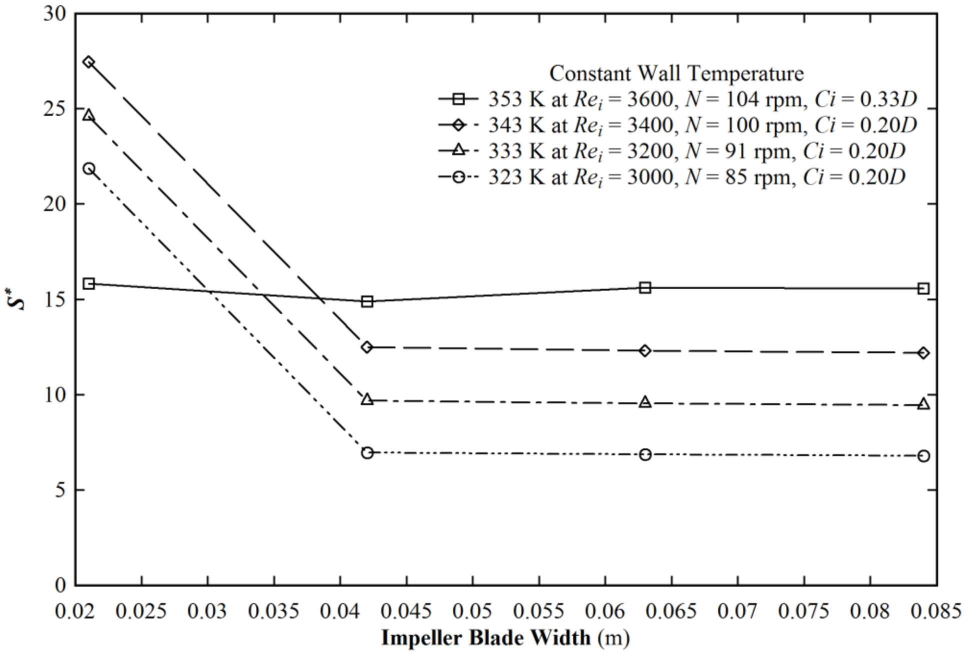

Figure 3.23 Dimensionless entropy generation with impeller blade width at constant wall temperature with optimized Re_i, impeller rotations and impeller clearance.

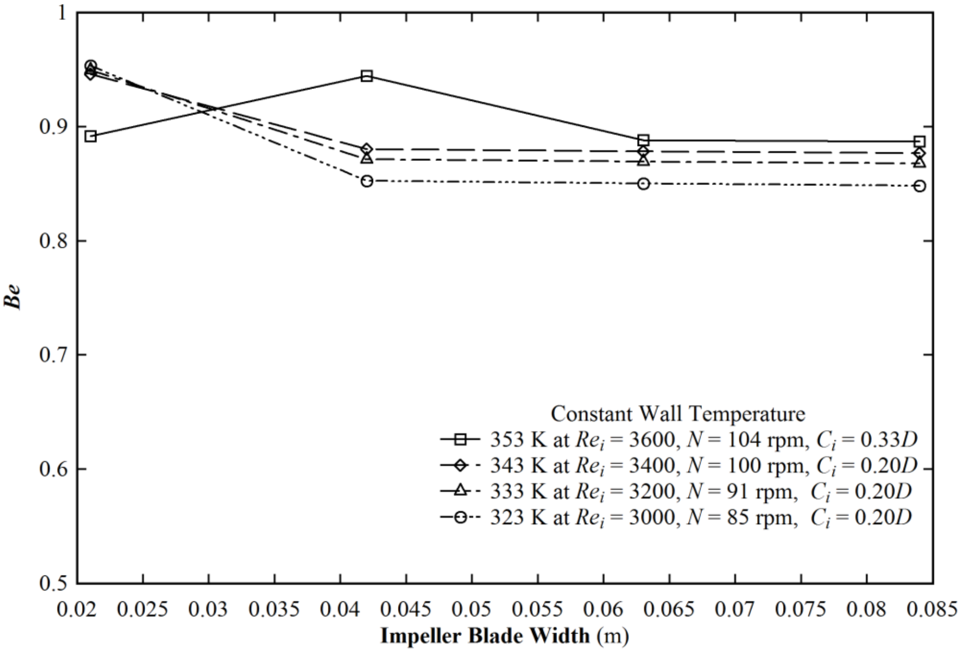

Figure 3.24 Distribution of Bejan number with impeller blade width at constant wall temperature with optimized Re_i, impeller rotations and impeller clearance.

Table 3.6 denotes the optimal tank parameters for the specified wall temperature boundary condition. Tabulated data shows that the optimal impeller widths are independent of the wall temperatures.

Table 3.6 Optimal tank parameters at the specified wall temperature

Wall Temperature (K)	Inlet Reynolds Number(Re_i)	Impeller Rotations (rpm)	Impeller Clearance (m)	Impeller Blade Width (m)
353	3600	104	0.33*D*	0.042
343	3400	100	0.20*D*	0.042
333	3200	91	0.20*D*	0.042
323	3000	85	0.20*D*	0.042

3.5.9.2 Constant Wall Heat Flux thermal Boundary Condition

3.5.9.2.1 Optimization with respect to inlet Reynolds number

The entropy minimization study is also carried out at the specified constant wall heat flux. The effect of Re_i on the total entropy generation at specified wall heat fluxes is shown in Figure 3.25. Due to the high temperature gradient, the entropy generation is found more at higher heat flux. The entropy generation decreases, reaches the minimum and it further increases with Re_i. Thus, the minimum entropy generation point is clearly observed on each curve. If the Re_i is lower than the optimum, the entropy generation is significantly affected by the wall heat flux magnitude. If Re_i is more than the optimum, the effect of the heat flux on the entropy generation is decreased. The entropy production becomes independent of the heat flux at higher Re_i. The explanation can be drawn from the corresponding Bejan number distribution plot given in Figure 3.26. It shows that *Be* approaches zero with Re_i. At higher Re_i, the convective energy transport dominates over the thermal conduction. Hence, the effect of wall heat flux on entropy generation becomes negligible. The calculated optimum Re_i is 2800, 2500, 2100 and 1700 for wall heat flux 3000, 2000, 1000 and 500 W/m^2, respectively. The figure finds that the optimum Re_i increases linearly with the wall heat flux. It also shows that around the minimum entropy generation point, *Be* is greater than 0.5 in all the cases. Hence, the effect of heat transfer irreversibility on the total entropy generation is more than the frictional irreversibility.

3.5.9.2.2 Optimization with respect to impeller rotations

Figure 3.27 shows the effect of the rotational speed of the impeller on the entropy generation. The minimum entropy is obtained at impeller rotations 79, 67, 55 and 45 rpm for the respective wall heat fluxes of 3000, 2000, 1000 and 500 W/m^2. The entropy generation increases with the heat flux, and it leads to increase in the optimum impeller rotations with the wall heat flux. The figure also shows that the total entropy generation is almost independent of the impeller rotations. The distribution of *Be* in Figure 3.28 depicts that the contribution of thermal entropy generation decreases with the impeller speed and the rate of decline increases above 180 rpm speed of the impeller. It happens due to substantial decrease in thermal entropy generation and the increase in frictional entropy generation.

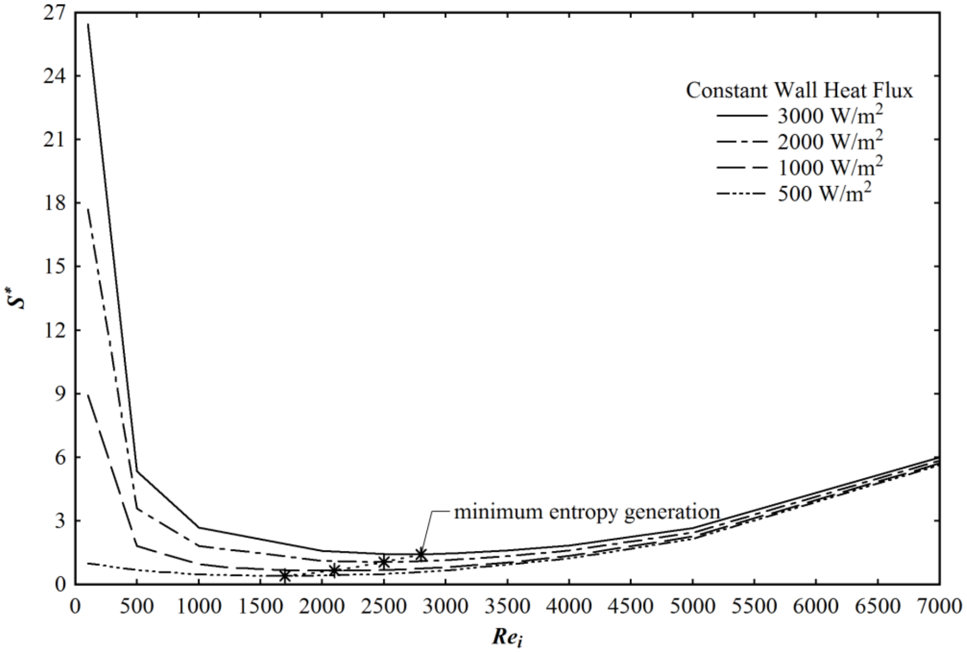

Figure 3.25 Dimensionless entropy generation with inlet Reynolds number at constant wall heat flux with 180 rpm of the impeller rotations, 0.33*D* impeller clearance and 0.042m impeller blade width.

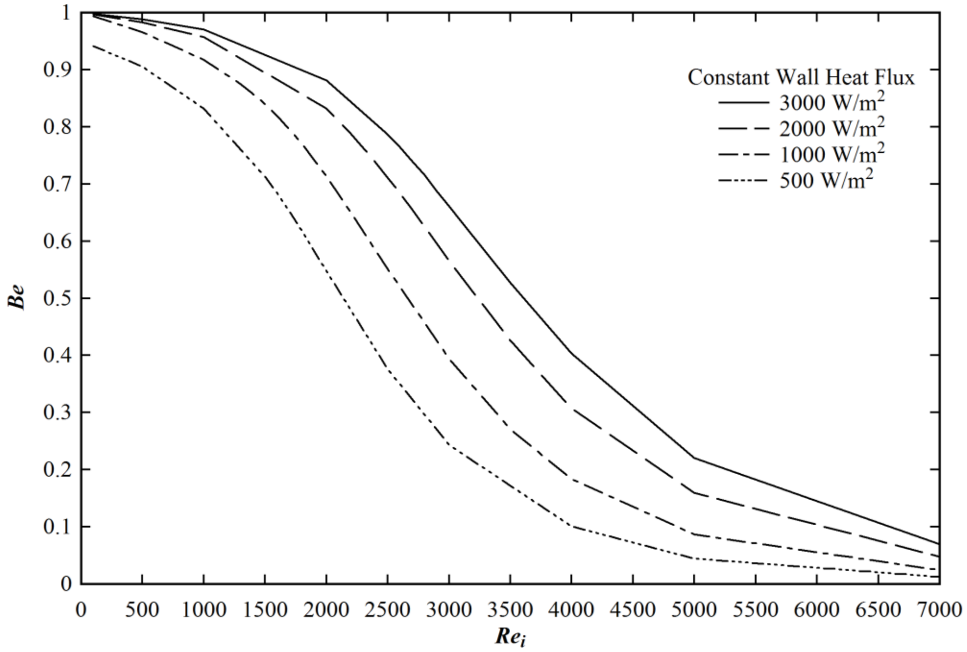

Figure 3.26 Distribution of Bejan number with inlet Reynolds number at constant wall heat flux with 180 rpm of the impeller rotations, 0.33*D* impeller clearance and 0.042m impeller blade width.

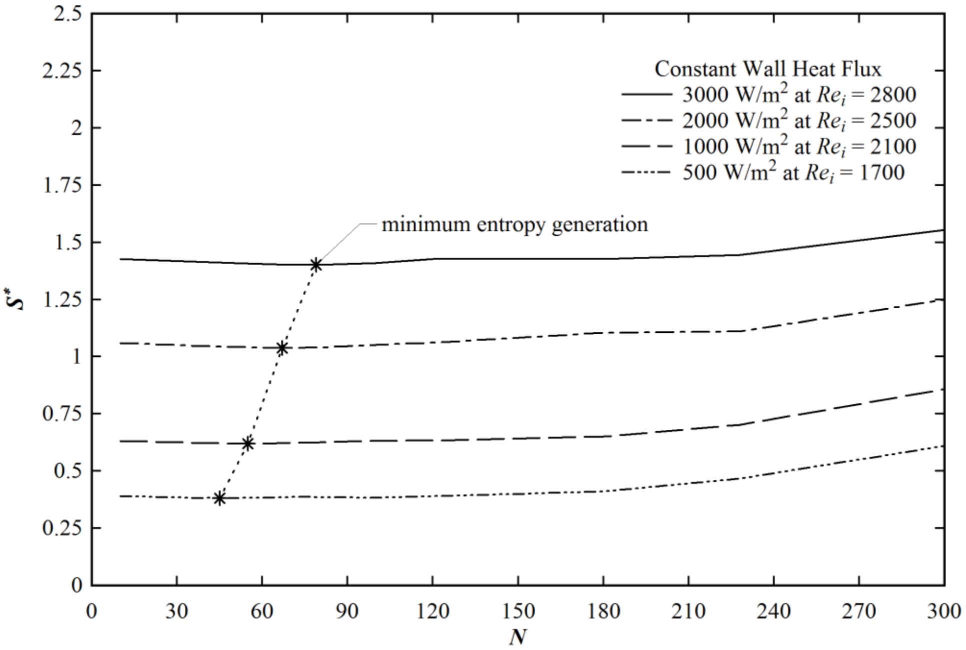

Figure 3.27 Dimensionless entropy generation with impeller rotation at constant wall heat flux with optimized Re_i, 0.33D impeller clearance and 0.042m impeller blade width.

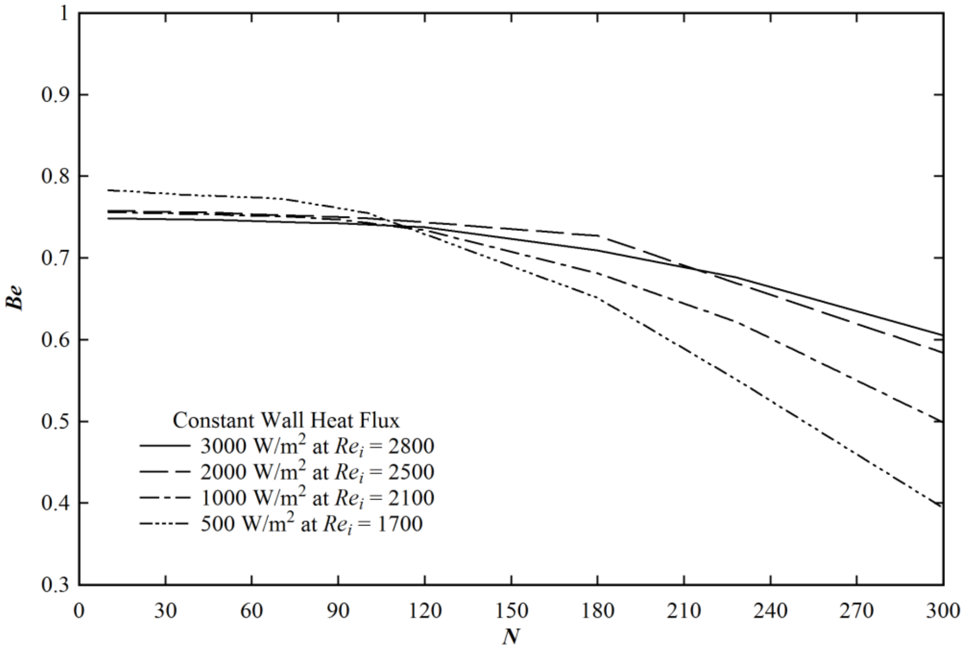

Figure 3.28 Distribution of Bejan number with impeller rotation at constant wall heat flux with optimized Re_i, 0.33D impeller clearance and 0.042m impeller blade width.

3.5.9.2.3 Optimization with respect to impeller clearance

The effect of the impeller clearance on the total entropy generation is shown in Figure 3.29. The minimum entropy generation occurs at impeller clearance, $C_i = 0.33D$, for all the cases except for 500 W/m^2 wall heat transfer flux where entropy generation is found almost constant. The optima become more distinct at higher wall heat flux. The corresponding *Be* distribution as shown in Figure 3.30 finds that the *Be* passes through the maximum at impeller clearance of $0.33D$ for all the wall heat fluxes except the lowest one. The physical explanations follow the same given for the specified wall temperature case in section 3.5.9.2.1.

3.5.9.2.4 Optimization with respect to impeller blade width

The effect of the blade width of the impeller on the entropy generation at the specified heat flux is shown in Figure 3.31. The minimum entropy generation point becomes prominent at higher wall heat flux, and it is obtained at blade width 0.042m. The Bejan number distribution with respect to blade width is shown in Figure 3.32 and the nature of its distribution is found similar to Figure 3.30.

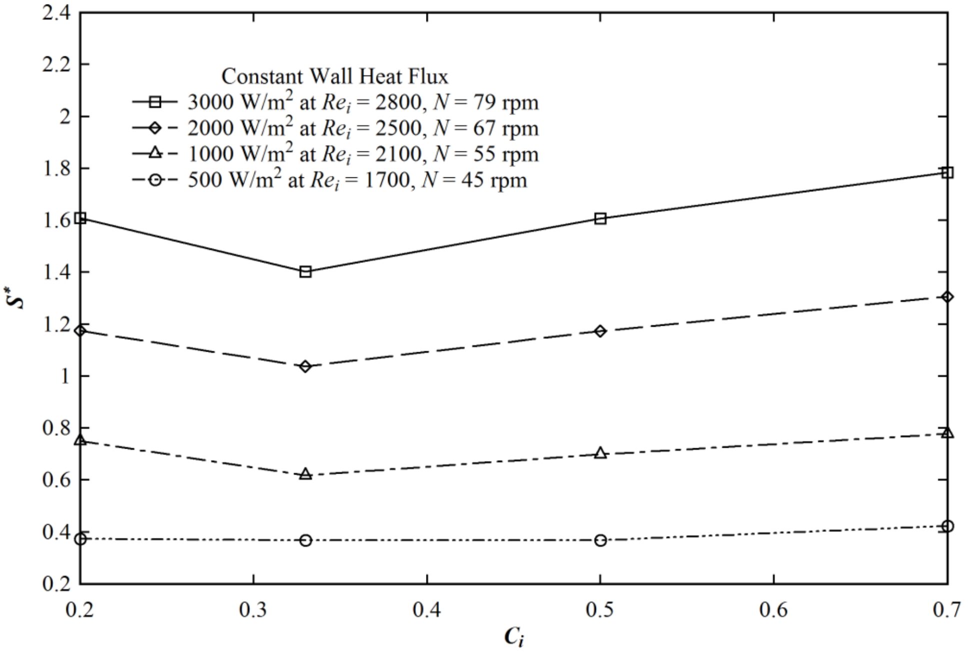

Figure 3.29 Dimensionless entropy generation with impeller clearance at constant wall heat flux with optimized Re_i, optimized impeller rotations and 0.042m impeller blade width.

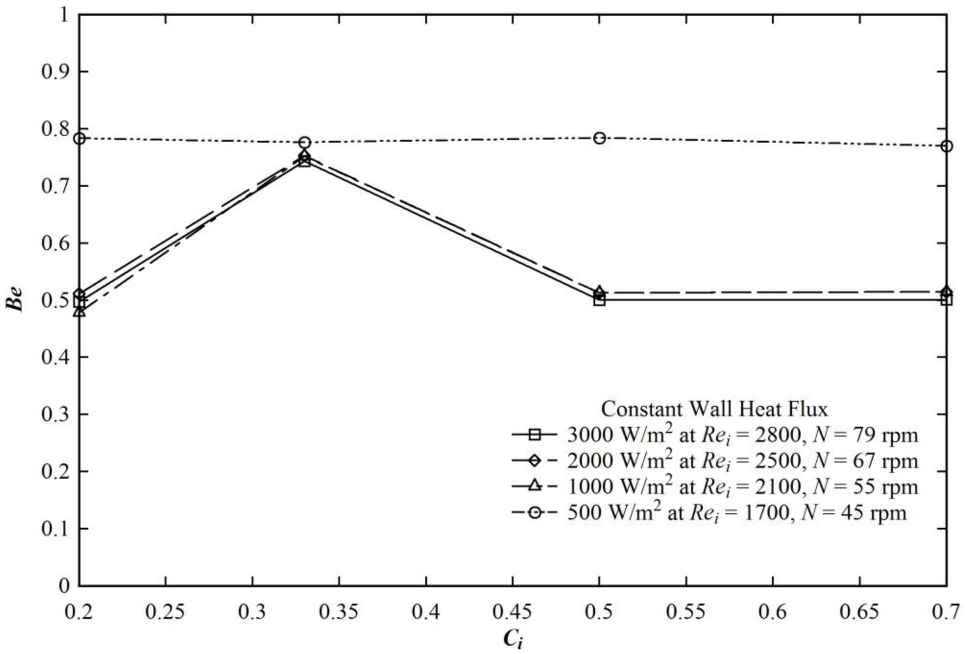

Figure 3.30 Distribution of Bejan number with impeller clearance at constant wall heat flux with optimized Re_i, optimized impeller rotations and 0.042m impeller blade width.

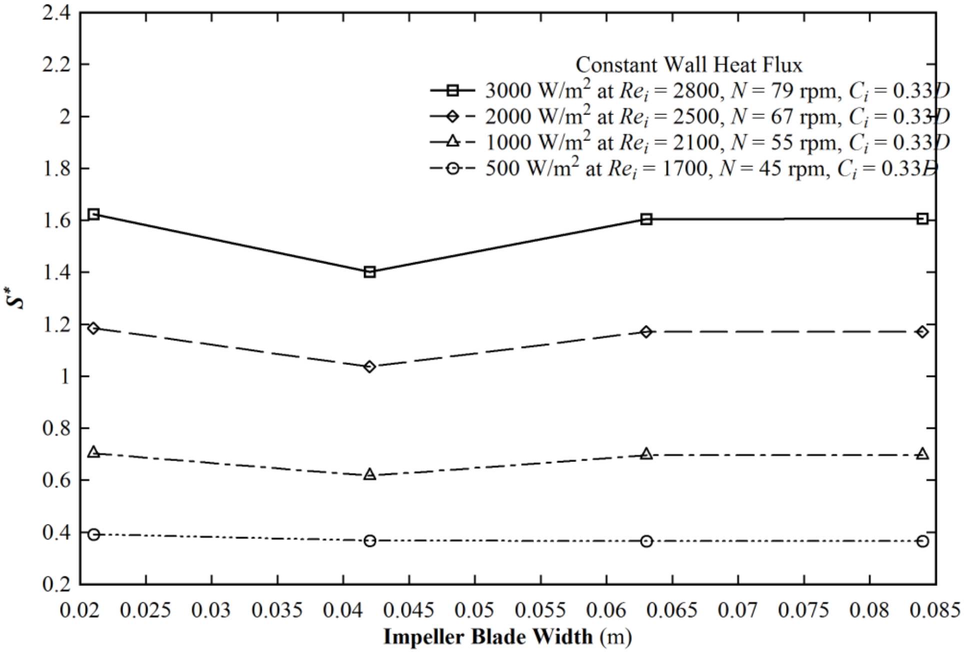

Figure 3.31 Dimensionless entropy generation vs. impeller blade width at constant wall heat flux with optimized Re_i, impeller rotations and impeller clearance

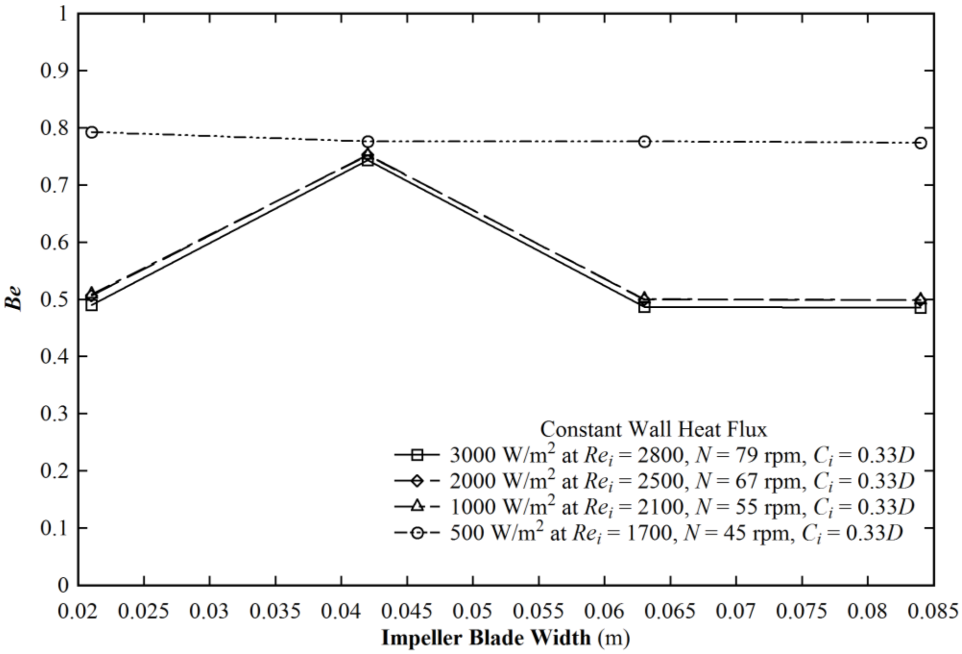

Figure 3.32 Distribution of Bejan number with impeller blade width at constant wall heat flux with optimized Re_i, impeller rotations and impeller clearance.

Table 3.7 denotes the optimal tank parameters for the specified wall heat flux boundary condition. The table shows that the optimal impeller clearance and impeller blade width are independent of the magnitude of the wall heat flux.

Table 3.7 Optimal tank parameters at the specified wall heat flux

Wall Heat Flux (W/m^2)	Inlet Reynolds Number (Re_i)	Impeller Rotations (rpm)	Impeller Clearance (m)	Impeller Blade Width (m)
3000	2800	79	0.33D	0.042
2000	2500	67	0.33D	0.042
1000	2100	55	0.33D	0.042
500	1700	45	0.33D	0.042

The computational fluid dynamics study of a stirred tank reactor has been carried out to know the hydrodynamic and thermodynamics behavior in terms of entropy generation. All the axial, radial and tangential velocities of water and shear thinning fluids given in the literature have been predicted successfully in the present numerical study. The prediction has become better at higher

Reynolds number. The discharge velocities of Venneker et al. (2010) and the width of the radial and tangential velocity profiles have also been predicted successfully. The mixing performance of the batch stirred tank has been studied in the transition and turbulent zone. The distributions of the mixing time have shown scattered distributions with the impeller rotations. The effect of the system parameters on the entropy generations of the batch stirred tank has been found. The entropy generation has been increased with impeller speed and blade width, found invariant to blade thickness, and weak function of impeller clearance and strong function of the flow behavior index as flow index tends to 1.0. The continuous stirred tank has been optimized by using entropy generation minimization concept where the total entropy generation of the system has been minimized with respect to the inlet Reynolds number, impeller speed, impeller clearance and blade width. The optimized design parameters have been tabulated in Tables 3.6 and 3.7.

CHAPTER 4

NUMERICAL STUDY OF NEWTONIAN AND SHEAR THINNING FLUID IN STIRRED TANK WITH HELICAL RIBBON IMPELLER

4.1 INTRODUCTION

Helical ribbon impeller is a close clearance impeller. Among different impellers available in the market, the helical ribbon impeller is considered to be the most efficient for agitating highly viscous Newtonian and non-Newtonian liquids (Wang et al., 2000). The effective viscosity of liquid plays an important role in power consumption of the mixing equipment. For Newtonian fluid, the viscosity is constant throughout the mixing equipment. But the viscosity of non-Newtonian fluid varies with locations in the tank. To overcome this difficulty, Metzner and Otto (1957) proposed the concept of the effective shear rate to calculate the effective viscosity in mixing equipment by the following linear function.

$$\dot{\gamma}_{eff} = K_s N \tag{4.1}$$

in which K_s is a proportionality constant, also known as geometry constant or Metzner-Otto constant, evaluated experimentally separately for each mixing equipment. This correlation is widely accepted in the literature to estimate the power consumption of Newtonian and non-Newtonian fluids in laminar regime. Chhabra et al. (2007) presented experimental and numerically calculated mixing times for highly viscous Newtonian and non-Newtonian viscoelastic fluids agitated with the Paravisc helical ribbon impeller (Ekato). They observed a scattered distribution of the non-dimensional mixing times with Reynolds number. Like power consumption, entropy generation is also an important factor for the mixing process. Many researchers studied the rate of entropy generation of various systems with and without thermal process (Shuja et al., 2001; Yapici et al., 2004, 2005; Kock and Herwig, 2004; Basha et al., 2007; Naterer and Adeyinka, 2009; Norris et al., 2011; Driss et al., 2012). As mentioned in the previous chapter, only a few research works on the study of entropy generation in the stirred tank

(Naterer and Adeyinka, 2009; Driss et al. 2012) are available in the literature. The design of stirred stank with Rushton turbine using EGM technique was carried out by us, and presented in the previous chapter. But none of the previous studies has designed the stirred tank mixing process with helical ribbon impeller using entropy generation minimization (EGM) technique.

Through literature survey finds that no one has predicted numerically the impeller geometry constant, K_s, for the helical ribbon impeller with screw (HRS). Therefore, in the current chapter, K_s values for different geometries of the helical ribbon impeller with screw are numerically predicted and compared with the experimental data available in the open literature (Brito-De La Fuente et al., 1997, Chavan and Ulbrecht, 1973; Yap et al., 1979). The study also determines the dependency of K_s on the flow behavior index, n. The flow number is a very much important characteristic parameter for the rotating impeller. It quantifies the amount of pumped liquid imparted by the impeller on the stagnant liquid in the tank. To the best of our knowledge, no one has yet found either experimentally or theoretically the flow number of HRS impeller. Therefore, the present chapter has calculated the flow number of the helical ribbon impellers for different non-Newtonian fluids. The study on mixing time for HRS impeller is unavailable in the literature and hence, the study on the mixing time of flat bottomed tank with HRS impeller is presented here. In addition, the hydrodynamic behavior of the mixing process with HRS and other helical ribbon impeller is demonstrated in terms of velocity profiles. The chapter also includes the optimum designing of the non-isothermal stirred tank with HRS impeller using EGM technique.

4.2 SYSTEM SPECIFICATION

The stirred tank equipped with a helical ribbon impeller and helical screw ribbon impeller is shown in Figure 4.1 (Brito-De La Fuente et al., 1997). The diameter (D) and height (H) of the tank is 0.210 m and 0.239 m, respectively. The impeller diameter (D_i) is 0.185 m, and the off-bottom clearance (C_i) of the impeller is 0.027 m. Six different type impellers are used to evaluate the effect of the impeller geometry on the power consumption. The geometrical details of the impellers are given in Table 4.1.

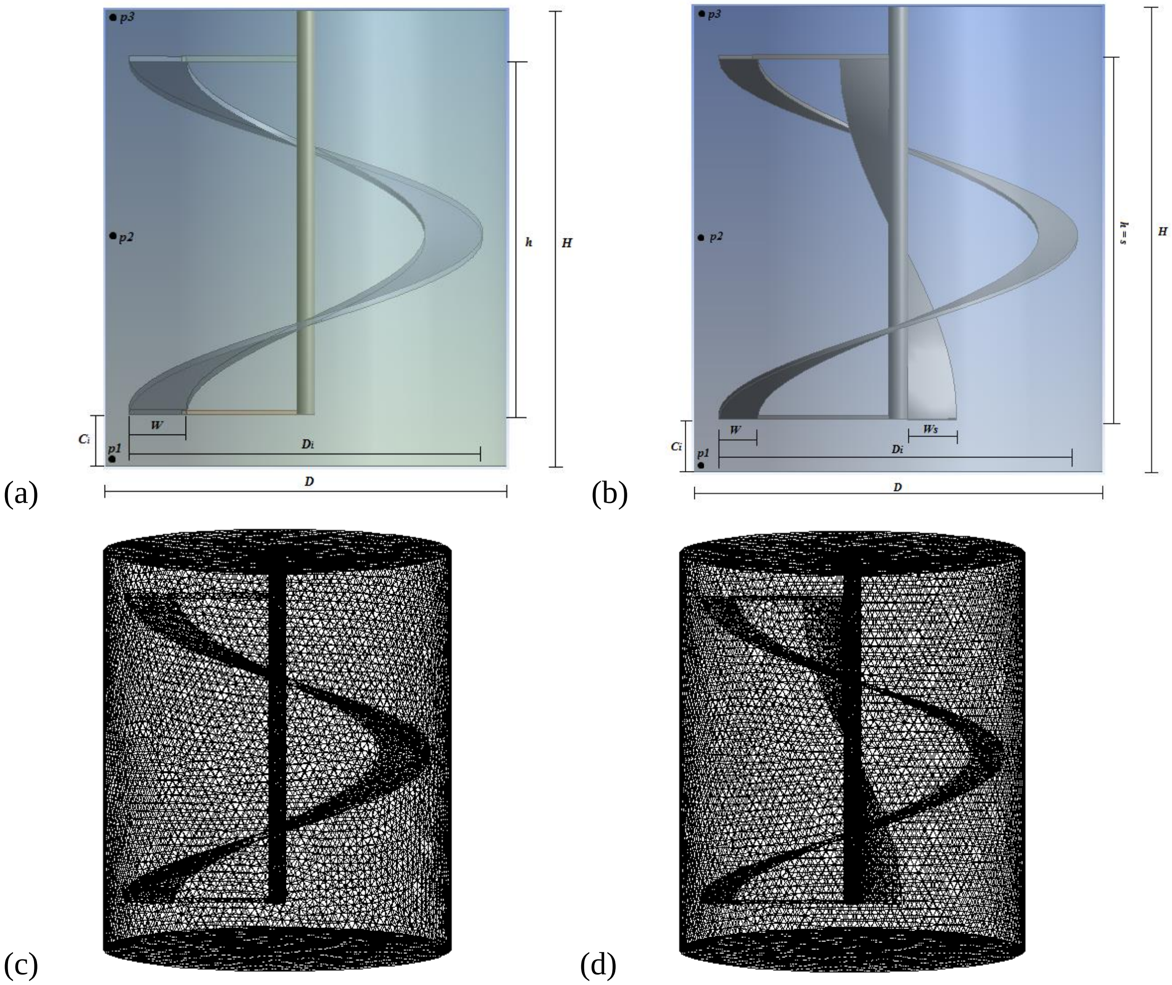

Figure 4.1 Stirred tank configuration, (a) helical ribbon impeller, (b) helical screw ribbon impeller, with P_1 (0.002, 0.1), P_2 (0.1195, 0.1) and P_3 (0.237, 0.1) are tracer measuring points in (r, z) coordinates in m, (c) computational Mesh for helical ribbon impeller, (d) computational Mesh for helical screw ribbon impeller.

Table 4.1 Geometrical configuration of impellers (Brito-De La Fuente et al., 1997)

Impeller Type	D/D_i	h/D_i	W/D_i	s/D_i	W_s/W	S_s
HR-1B	1.135	1	0.162	1	-	-
HRS-1.5	1.135	1	0.135	0.7	1.2	0.247
HRS-1A	1.135	1	0.108	1	1.25	0.37
HRS-2A	1.135	1	0.108	0.5	1.25	0.185
HRS-1B	1.135	1	0.162	1	1.17	0.37
HRS-2B	1.135	1	0.162	0.5	1.17	0.185

A high viscous Newtonian fluid and five shear thinning non-Newtonian fluids are used as the working liquid. The flow behavior index of the shear thinning solutions is varied from 0.1377 to 0.6536. The detail rheological properties of solutions are mentioned in Table 4.2.

Table 4.2 Fluid properties (Brito-De La Fuente et al., 1997)

Fluids	Power law model parameters
Newtonian solution	$n = 1$, $K = 33.67$
CMC 3% solution (VE1)	$n = 0.359$, $K = 62.2$
XG 3% solution (PST2)	$n = 0.1377$, $K = 21.34$
CMC 1.5% solution (PST4)	$n = 0.6536$, $K = 7.406$
CMC 1.5% solution (PST5)	$n = 0.6044$, $K = 14.8765$
Gellan fermentation broth (PST6)	$n = 0.19$, $K = 9.7$

4.3 CFD GOVERNING EQUATION

The velocity components are calculated by solving the momentum Equation 3.2 along the equation of continuity (Equation 3.1). The temperature distributions are calculated from Equation 3.3. In mixing study with tracer injection method, the tracer distributions in the tank are obtained from Equation 3.5. In the transition zone, the turbulent model Equations 3.6 to 3.16 is solved. The impeller Reynolds number for Newtonian fluid is calculated using Equation 3.17.

Equation 3.18 is used to calculate the apparent viscosity of the non-Newtonian fluids. The Reynolds number of the shear thinning fluid is calculated by (Bourne and Butler, 1969)

$$Re = {\rho N^{2-n} D_i^2}\big/{K} \tag{4.2}$$

Thus, the power consumption of impeller in the laminar flow regime is given by

$$N_P \cdot Re = K_P \tag{4.3}$$

and hence,

$$N_P \cdot Re = K_P(n) \tag{4.4}$$

where K_P and $K_P(n)$ is the power constant for Newtonian and non-Newtonian fluid. In the equation, N_P is power number and expressed as,

$$N_P = P \big/ \rho N^3 D_i^5 \tag{4.5}$$

where, P is the power input.

Flow number of impeller is determined by

$$N_q = \frac{Q}{N D_i^3} \tag{4.6}$$

where Q is volumetric discharge from impeller blade.

Rieger and Novak (1973) proposed the analytical expression to determine impeller constant, K_s, which is expressed as

$$K_s = \left(\frac{K_p(n)}{K_p} \right)^{1/(n-1)} \tag{4.7}$$

The above equation can also be written as

$$\ln K_p(n) = \ln K_p - (1-n) \ln K_s \tag{4.8}$$

The K_s value can be obtained from the slope of the linear plot of $K_p(n)$ versus $(1-n)$.

The total entropy generation in laminar flow regime due to both the heat transfer irreversibility and fluid viscous dissipation can be written as

$$S_{gen,Total} = S_{gen,HT} + S_{gen,VD} \tag{4.9}$$

in which $S_{gen,VD}$ and $S_{gen,HT}$ are calculated from Equation 3.32 and 3.31, respectively.

In isothermal process, the entropy production due to heat transfer is zero. Thus, the entropy generation of the isothermal system is obtained from

$$S_{gen,Total} = S_{gen,VD} = \frac{\eta \phi_v}{T} \tag{4.10}$$

where η is the apparent or effective viscosity, T is the temperature and φ_v is the viscous dissipation due to mean velocity components and given as (Kock and Herwig, 2005)

$$\varphi_v = 2\left[\left(\frac{\partial u}{\partial r}\right)^2 + \left(\frac{\partial v}{r\partial\theta} + \frac{u}{r}\right)^2 + \left(\frac{\partial w}{\partial z}\right)^2\right] + \left[\frac{\partial v}{\partial r} - \frac{v}{r} + \frac{\partial u}{r\partial\theta}\right]^2 + \left[\frac{\partial w}{r\partial\theta} + \frac{\partial v}{\partial z}\right]^2 + \left[\frac{\partial u}{\partial z} + \frac{\partial w}{\partial r}\right]^2 \quad 4.11$$

Further, the total entropy generation can be written in dimensionless form and the non-dimensional entropy generation can be calculated from Equation 3.36.

4.4 NUMERICAL METHODOLOGY AND BOUNDARY CONDITION

Before the simulation study, it is necessary to obtain grid independent results. Four different meshes of 433401, 565848, 645264 and 763636 elements are considered. The root mean square (RMS) errors between the predicted and experimental power number, N_p (Brito-De La Fuente et al., 1997) are presented in Table 4.3. The RMS error decreases with the mesh size. Further increase in the number of meshes beyond 645264 becomes not only computationally exorbitant, but produces no change in the value of N_p virtually. Thus, mesh size of 645264 are taken for all the simulation works presented in this chapter.

Table 4.3 Distribution of RMS error with number of mesh elements

Mesh elements	RMS error (in %)
433401	11.27483
565848	4.856103
645264	0.380388
763636	0.340671

Multiple Reference Frame commonly known as MRF is used to model rotating impeller. The details on MRF are given in Chapter 3. The transient behavior of the impeller is captured by the sliding mesh approach. A no-slip boundary condition is applied to the tank walls. The finite volume method is used to discretize the governing equations. All transport equations are discretized using second order upwind difference scheme. A pressure-correction method, SIMPLE (Semi-Implicate Method for Pressure Linked Equations), is used to couple pressure and velocity equations. A user defined function is used for the modelling the empirical viscosity models (Brito-De La Fuente et al., 1997) of the non-Newtonian fluids. The convergence criterion for each transport equation is set to 10^{-5}. The computations are carried out using a 3.2 GHz Intel Core i5 CPU having 4 GB RAM. The computational time was about 9-10 hours.

4.5 RESULTS AND DISCUSSION

4.5.1 Validation of CFD Models

4.5.1.1 Power Number and Power Constant for impellers with Newtonian Fluid

The effect of the Reynolds number on the power number distribution of Newtonian fluid is presented in Figure 4.2. The curves are drawn for different geometries specified in Table 4.1. Among all the geometries, the experimental power number distribution of Newtonian fluid with Re is available only for HRS-1.5 geometry. Thus, the comparison of the simulated data with the experimental data is carried out for HRS-1.5 in Figure 4.2. The results of the present simulation study show an excellent agreement with the experimental data. The comparison between the experimental and present simulated results of power constant, K_p of Newtonian fluid is depicted in Table 4.4 for all the impeller geometries. The results show an excellent agreement between the experimental and numerically predicted K_p. Therefore, the CFD model of Ansys Fluent used in the present work is validated satisfactorily for Newtonian fluid, and the same is used for further simulation study of the stirred tank with helical ribbon impeller. Figure 4.2 also includes the variation of power number of the Newtonian fluid with impeller Reynolds number for other impeller geometries. It shows that N_p–Re relation in the laminar zone is linear for all the geometries. It also shows that power number is dependent on the number of pitches and blade width, W of the helical impeller, but independent of the blade width, W_s of screw. N_p increases with the number of pitches and blade width of impeller. The equality of N_p of HRS-1B and HR-1B impeller confirms independency of N_p on the screw blade width, W_s. Having lower helical impeller blade width, the N_p of HRS-1A is less than HRS-1B/HR-1B. With more number of pitches, the N_p of HRS-2A is greater than HRS-1.5, and HRS-1.5 is greater than HRS-1B. The width, W, of the HRS-2B is more than HRS-2A, and thus HRS-2B shows the maximum N_p among all the geometries of the impeller.

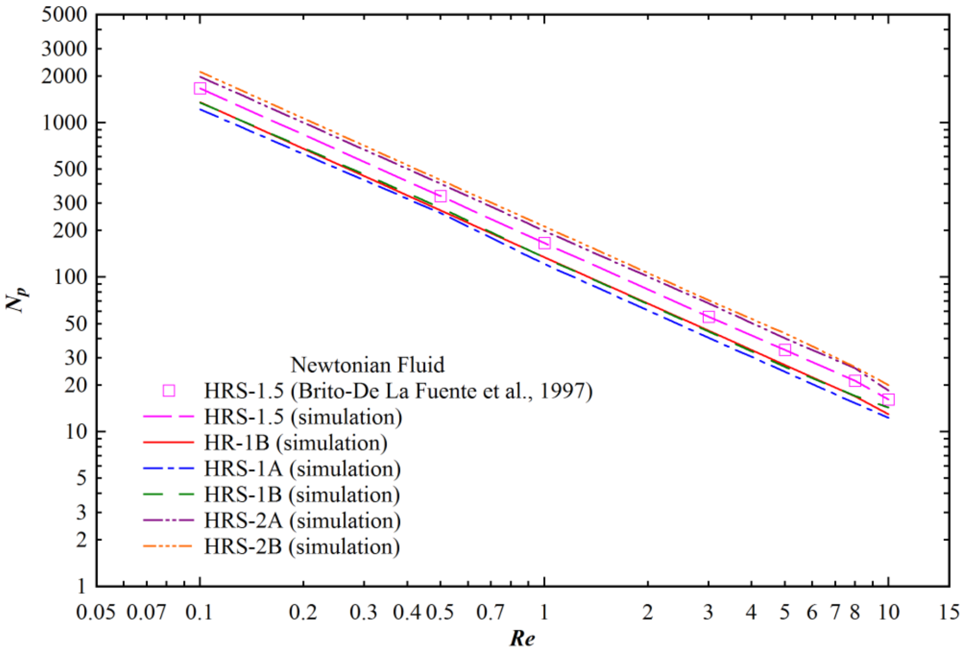

Figure 4.2 Distribution of N_p with *Re* for Newtonian fluid.

Table 4.4 Power constant value for HR and HRS impeller for Newtonian fluid mixing

Impeller Type	$N_p \cdot Re = K_p$	
	Experiment (Brito-De La Fuente et al., 1997)	Present Simulation
HR-1B	135.2	135.12
HRS-1A	127.6	125.89
HRS-1B	132.6	133.96
HRS-1.5	168.6	167.88
HRS-2A	208.1	201.56
HRS-2B	222.7	212.83

4.5.1.2 *Power Number and Power Constant for impellers with non-Newtonian Fluid*

The effects of shear thinning fluids on the power number are numerically predicted and analyzed in the present work. Due to availability of the experimental data, the predicted power number distributions for viscous Newtonian and non-Newtonian fluids are compared with the experimental data only for HR-1B impeller in Figure 4.3. Please note that the experimental power numbers for all the fluids are not available for the whole range of Reynolds number studied here. The figure shows that the CFD model used in the present work predict excellently the experimental power curves except for *n* = 0.1377. At any *Re*, the experimental N_p increases continuously with *n* except for *n* = 0.1377. The simulation data are also finding the same increasing trend of power number with lowest N_p for the lowest *n* (0.1377). It can be concluded here that there might be some error in the experimental data for *n* = 0.1377. Thus the validated CFD models will be used for the further simulation study of the shear thinning fluids. The figure depicts that all shear thinning fluids data show a linear relation between N_p and *Re* in the laminar flow regime. The product of N_p and *Re*, i.e., K_p is therefore constant for all the fluids in the laminar zone. The figure also shows that as the value of *n* tends to 1.0, the computed power consumption data of shear thinning fluids tends to Newtonian power data. The same observations are also made on power curves for other impeller geometries.

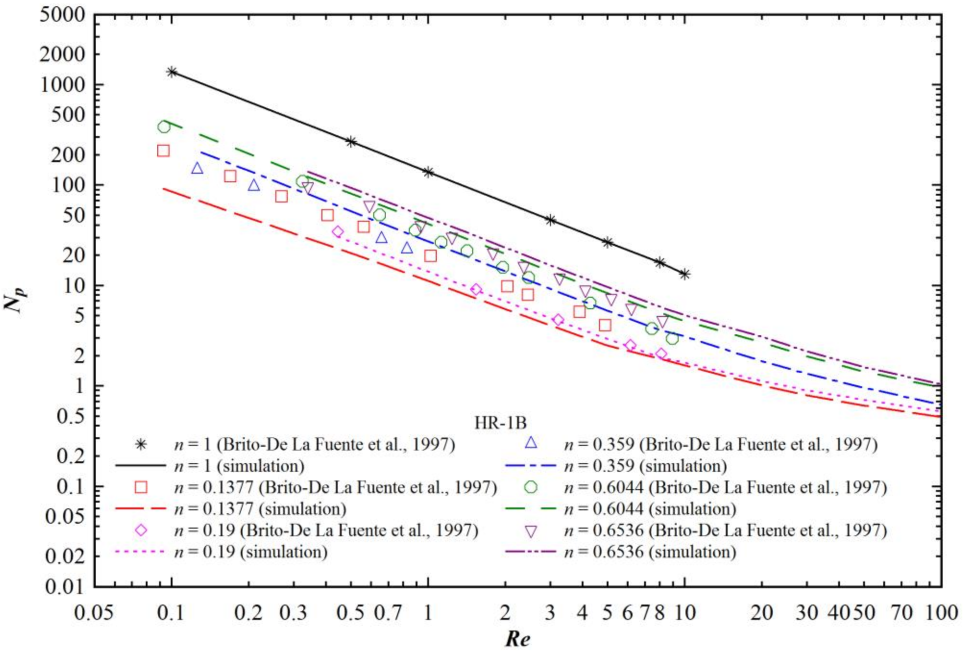

Figure 4.3 Distribution of N_p with *Re* for impeller geometry HR-1B using flow behavior index, *n* as the parameter.

4.5.2 Prediction of Power Number, Power Constant, K_p and Impeller Constant, K_s

The experimental power curves are unavailable for all the impellers except for HR-1B. The present study has calculated power curves for all the impellers and those are shown in Figure 4.4. The flow behavior index, *n*, is used as the parameter in the figures. All the curves are linear and hence, the flow inside the tank is in the laminar regime up to *Re* about 8–9. The extent of the laminar regime thus depends on the geometry of the impeller and the flow behavior index, *n*, of the working fluid. Overall, Figure 4.4(a) shows that at very low $Re \approx 0.1$, all the impellers except HRS-1.5 produces the same N_p and the distance among the curves increases with increasing *Re*. The figure also finds that at low *Re*, the N_p of HRS-2A is less than HR-1B. It becomes equal for both the impeller at higher *Re*. Further increase of *Re* above 2.0 shows that HRS-2A produces less N_p and even it gives lesser N_p than HRS-1A for $Re > 6.0$. For the full range of the power curve, the order of power consumption is HRS-2B > HRS-1B > HRS-1.5.

Figure 4.4(b) shows another set of power curves for $n = 0.19$. Like Figure 4.4(a), it also shows the maximum and minimum power consumptions by HRS-2B and HRS-1A impeller. But there is some dissimilarity in the trend of the results between these two figurers. The power number of HR-1B impeller is found less than HRS-2A and HRS-1.5 impellers at *Re* about 5.5. The HRS-1B, HRS-2A and HRS-1.5 have the same N_p up to *Re* about 2.3.

Figure 4.4(c) displays the power curves for fluids with $n = 0.359$. The figure finds that both HRS-1A and HRS-1B have produced the minimum power number. The order of power consumption by other impellers are HRS-2B > HRS-2A > HRS-1.5 > HR-1B.

Similarly, both Figure 4.4(d) and Figure 4.4(e) show the distribution of power curves for all the impellers and non-Newtonian fluids with *n* equal to 0.6044 and 0.6536. The computed power consumption order of the impellers for both fluids is the same, and the order is HRS-2B > HRS-2A > HRS- 1.5 > HRS-1B >HR-1B > HRS-1A.

The trend of the power curve of the non-Newtonian fluids confirms that they approach Newtonian power curves given in Figure 4.2 as the fluid flow index tends to 1.0. One more important observation can be made from Figure 4.2 and Figure 4.4 that Power number at any *Re* and for any particular geometry increases with the flow behavior index, *n*.

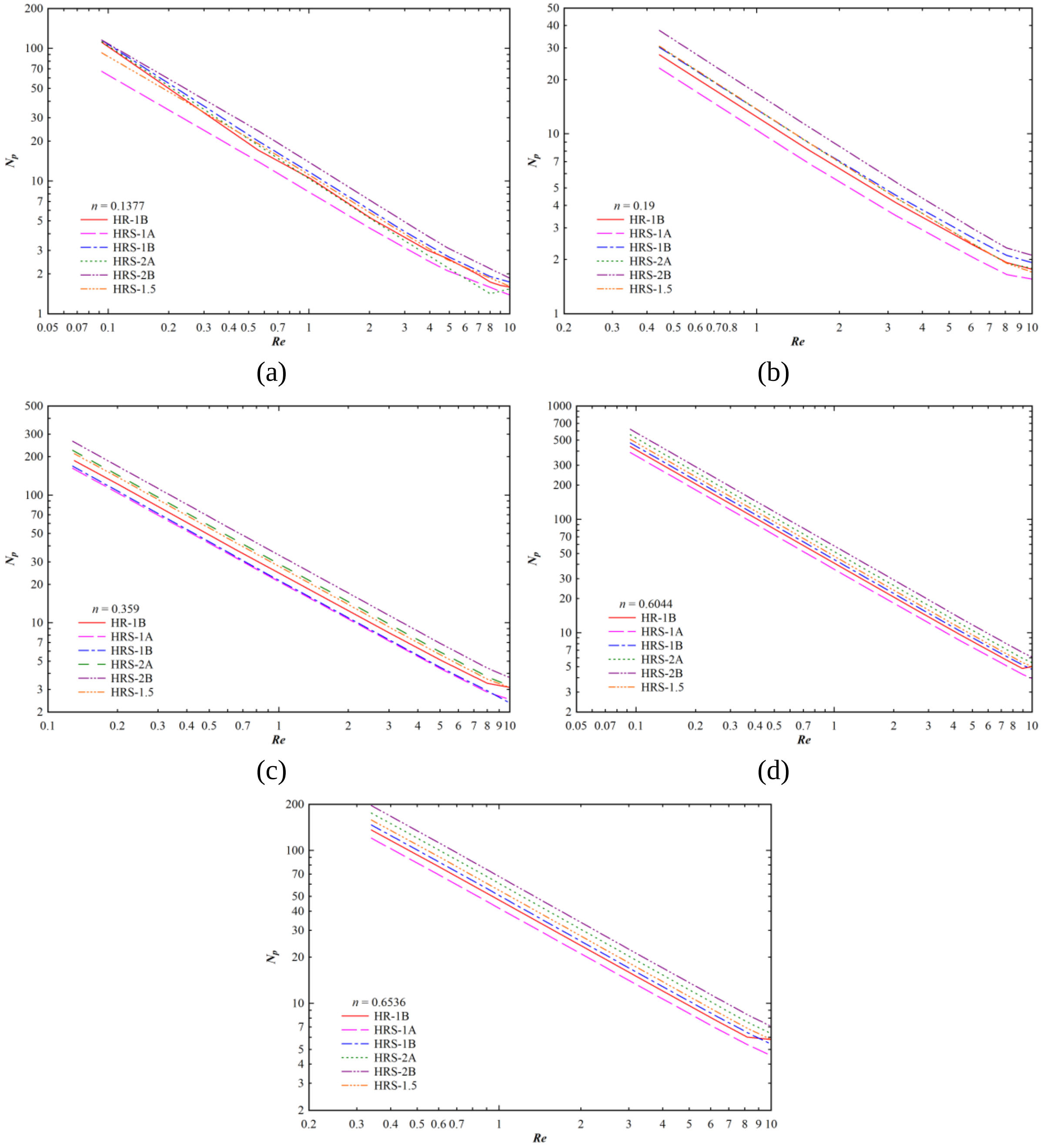

(a) (b) (c) (d) (e)

Figure 4.4 Distribution of N_p with Re for impeller geometry HRS-1.5, HRS-1A, HRS-1B, HRS-2A and HRS-2B.

According to Equations 4.3 and 4.4, N_p vs. Re results shown in Figure 4.4 allow us to estimate the values of K_p as a function of n, and the distributions of K_p are shown in Figure 4.5 for all the impeller geometries. The computed K_p increases with the flow behavior index, n for each impeller geometry. At any n, K_p varies with the geometry of the impeller and the sequence of variation of K_p follows the variation order of N_p with the geometry. Among all the geometries, the predicted K_p of HR-1B impeller is compared with the experimental data of Brito-De La Fuente et al. (1997). The comparison shows that prediction is satisfactory for $n \geq 0.359$. The experimental power numbers are higher than the present computed values for shear thinning fluid with n equal to 0.1377 and 0.19. Therefore, the experimental K_p is also higher than the predicted values for n equal to 0.1377 and 0.19. Also, the experimental K_p values do not follow the monotonic increasing trend with n as observed for the predicted values.

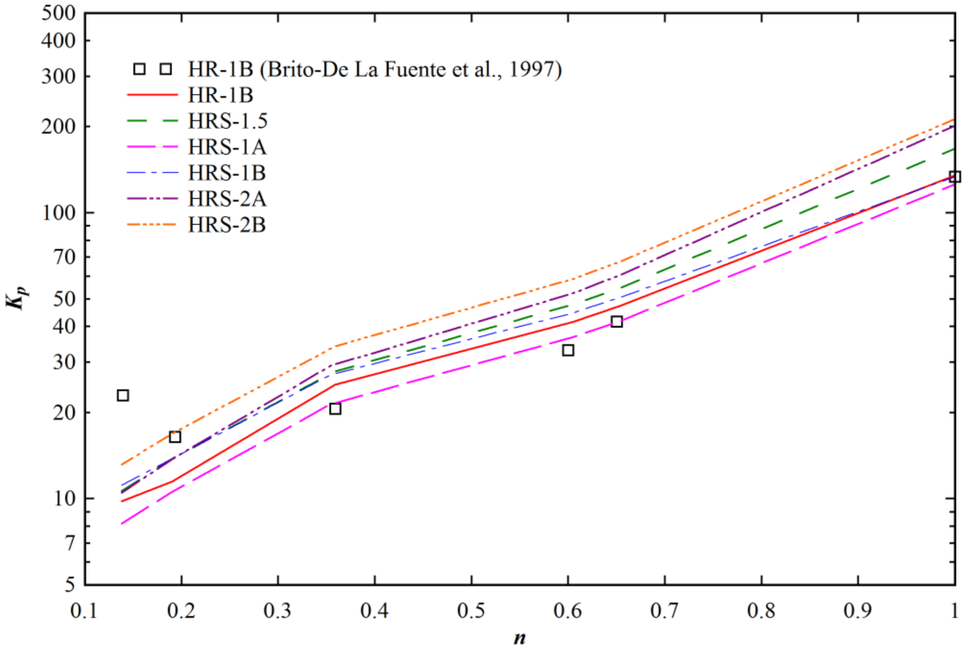

Figure 4.5 The distribution of $K_p(n)$ with the fluid flow index, n for different geometries of the impeller. The numerically predicted $K_p(n)$ are compared with the experimental (Brito-De La Fuente et al., 1997) data.

The values of K_s depend on the determination technique. In this work, four different methods are adopted.

Method I: Following Equation 4.8, K_s independent of n is obtained from the slope of the linear plot of $K_p(n)$ versus (1-n) on the semi-logarithmic scale is shown in Figure 4.6. This method gives an average value of K_s for a particular geometry. In Table 4.5, the calculated K_s for different impeller geometries are compared with the experimental data given in Delaplace et al. (2000). The comparison shows a satisfactory prediction of the experimental data by the present simulation work. The tabulated data of K_s in the table also establishes the influence of geometrical parameters of the impeller on the mixing process.

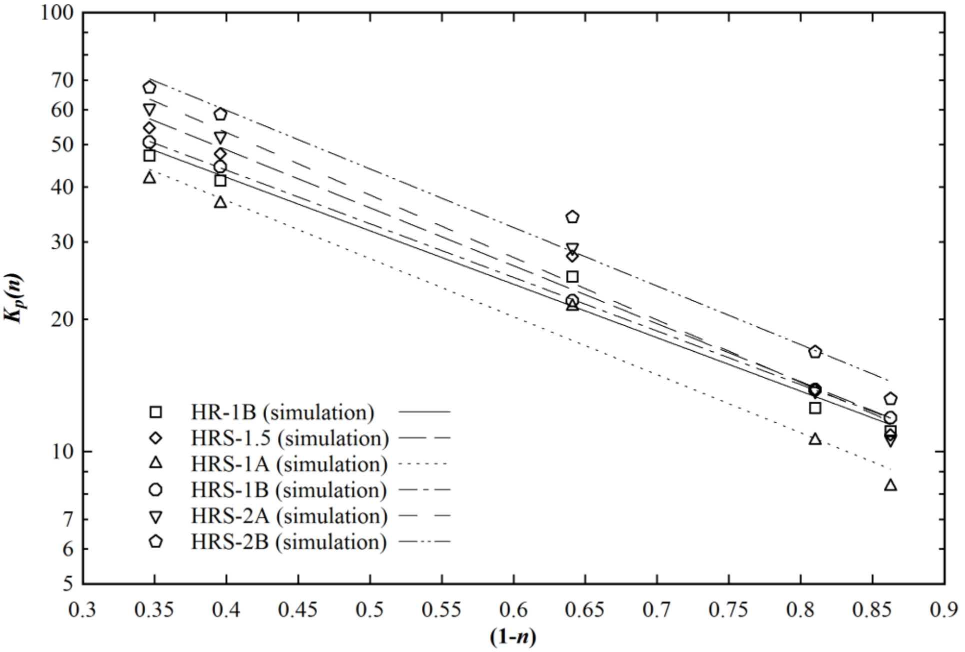

Figure 4.6 Determination of K_s from the slope of K_p(n) vs. (1-n).

Table 4.5 Comparison of Predicted K_s with the experimental K_s (Delaplace et al. 2000)

Impeller type	K_s (predicted)	K_s (Delaplace et al. 2000)
HR-1B	20.79	23.0
HRS-1.5	21.42	-
HRS-1A	21.33	22.0
HRS-1B	21.92	23.0
HRS-2A	26.79	34.6
HRS-2B	27.16	36.7

Method II: The K_s as a function of n can be determined by solving Equation 4.7. The equation needs $K_p(n)$, which was calculated and given in Figure 4.5. The required K_p for Newtonian fluid is given in Table 4.4. The computed values of K_s as a function of fluid flow behavior index are presented in Figure 4.7. In the figure, the predicted K_s are compared with the experimental K_s values of Brito-De La Fuente et al. (1997), Chavan and Ulbrecht (1973) and in Yap et al. (1979).

It was already shown in Figure 4.5 that the experimental K_p, at n equal to 0.1377 and 0.19, of HR-1B impeller are more than the computed values. Hence, the present numerical study over predicts K_s at n equal to 0.1377 and 0.19. On the contrary, at higher n, the computed values of K_p are about 25% more than the experimental values for HR-1B impeller. It leads to under prediction of K_s by the present study. Overall, K_s is found to vary with flow behavior index. But, if the K_s of n = 0.3559 is excluded from the set of K_s values then the variations of other K_s with flow behavior index become less. The K_s profiles for other impellers follow the same trend except for HRS-1B where K_s is observed independent of n. The geometry dependent K_s orders are HRS-2A >HRS-2B > HRS-1.5 > HRS-1A > HR-1B.

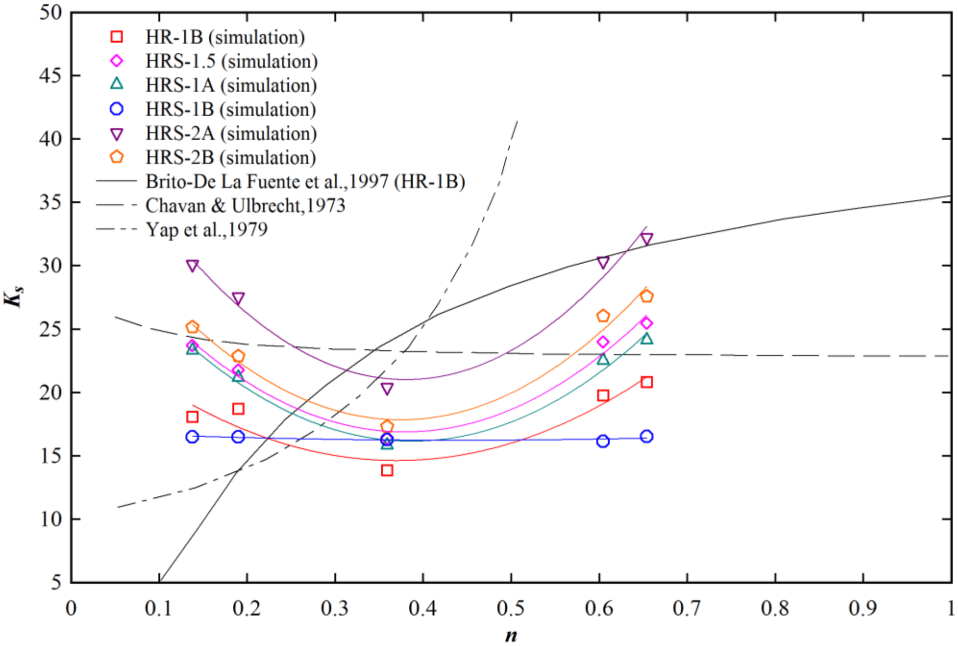

Figure 4.7 Distribution of K_s as a function of the flow behavior index, n.

Method III: According to Equation 4.1, K_s can also be determined from the slope of the shear rate vs. impeller rotational speed plot. Shekhar and Jayanti (2003) have drawn the curve of circumferential averaged local shear rate versus the radius of the tank at the mid-height of the impeller. The maximum shear rate was found from the graph at each rotational speed of the impeller. Then the curve of the maximal shear rate versus rotational speed was plotted and K_s were found by them from the slope of the plot. In this work, the same method is adopted for finding K_s. An illustrative curve of shear rate vs. impeller speed for the flow behavior index

0.6044 is depicted in Figure 4.8(a). In Figure 4.8(b), the calculated K_s following method (III) is plotted against the flow behavior index, n, and also compared with the previous experimental data only for HR-1B impeller. The figure shows that the computed K_s values over predict and under predict the Brito-De La Fuente et al. (1997) values for $n \leq 0.4$ and $n > 0.4$, respectively. In the figure, the decreasing trend of K_s with n follows the trend of Chavan and Ulbrecht (1973) results.

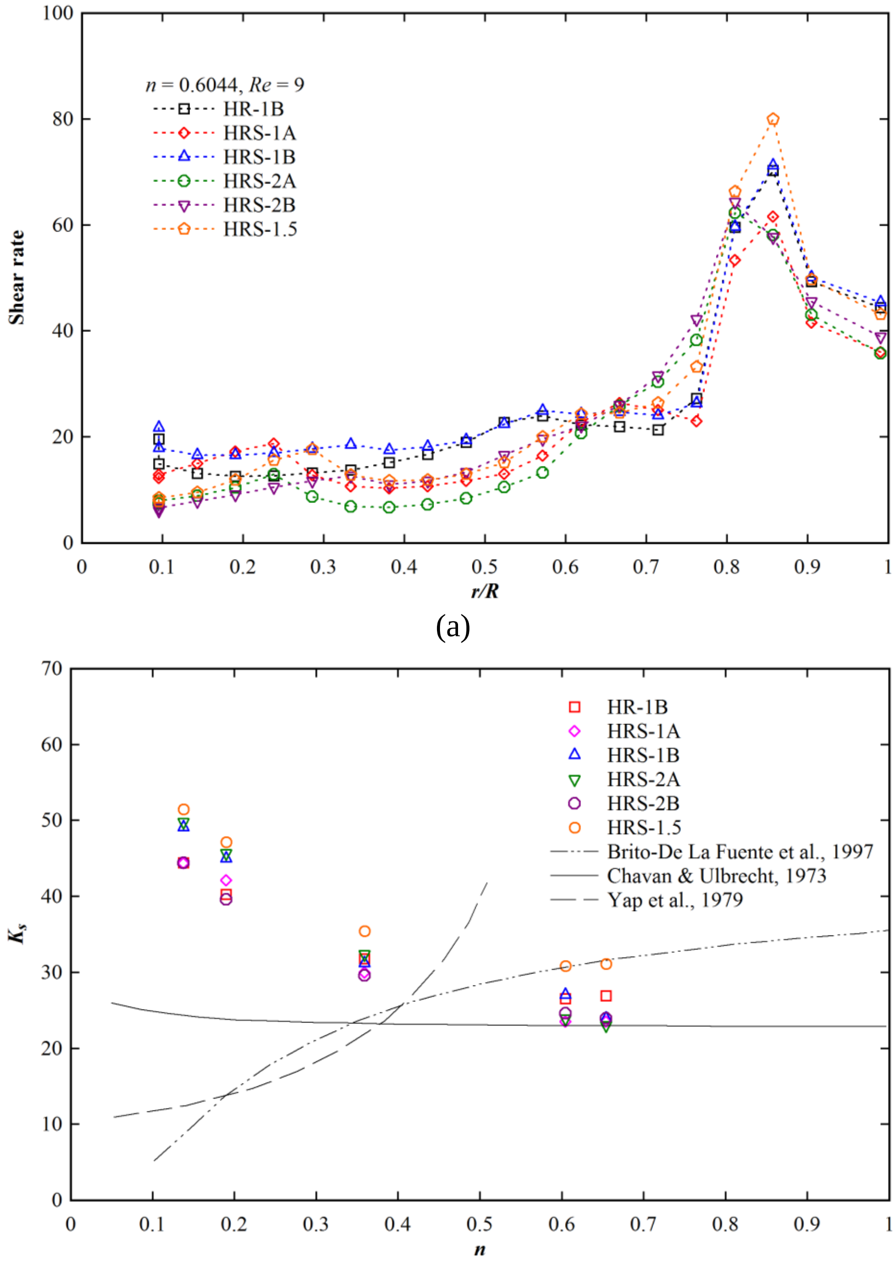

(a)

(b)

Figure 4.8 (a) Variation of shear rate with radial distance, (b) Determination of K_s following method (III).

Method IV: Chhabra and Richardson (2008) have discussed the K_s determination method which was first established by Metzner and Otto (1957). According to this method, the power number of the non-Newtonian fluid is determined for a particular impeller speed. The corresponding value of Reynolds number is determined from the power curve of the Newtonian fluid. The apparent viscosity is determined from the Reynolds number. The shear rate is then calculated from the viscosity-shear strain relation. The value of K_s is finally calculated from Equation 4.1. The process is repeated for all the flow behavior indexes and impeller geometries. In the present study, the same procedure of finding K_s is adopted. The distribution of the calculated values with flow behavior index for different geometries is shown in Figure 4.9. In the same figure, the present K_s values are also compared with the literature values. Qualitatively, the nature of K_s distributions using the method (IV) is found similar to Method (II). The computed K_s values over predict and under predict the experimental K_s data of Brito-De La Fuente et al. (1997) at lower and higher flow behavior indexes.

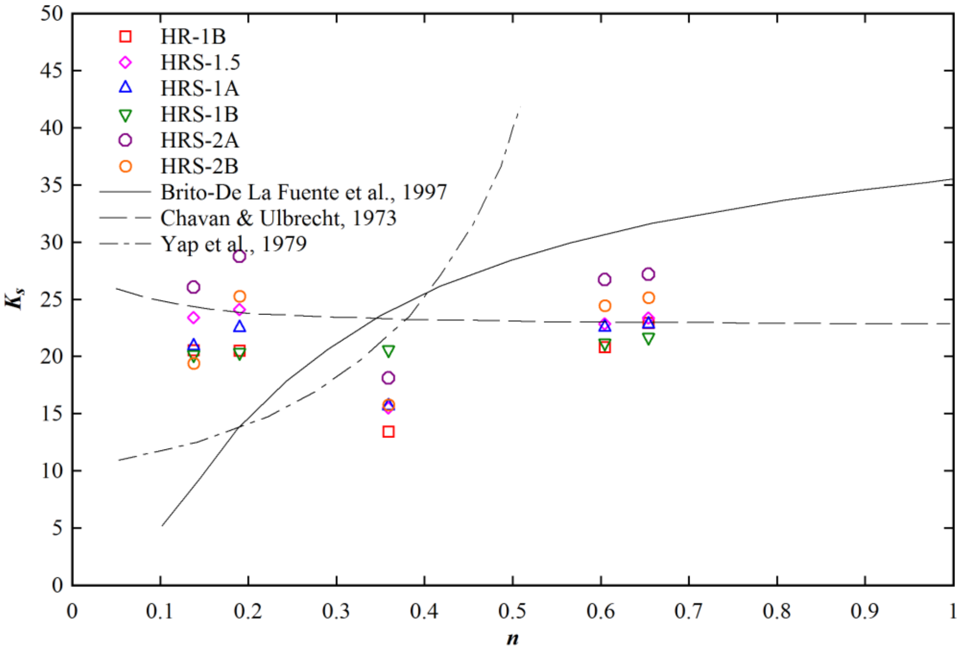

Figure 4.9 Determination of K_s following the method of Metzner and Otto (1957).

4.5.3 Generalized Power Consumption Curve

The unique representation of power number, N_p distributions of both the Newtonian and non-Newtonian fluids can be obtained with the help of apparent Reynolds number, Re^*. It is defined by equalizing the power number of both the Newtonian and non-Newtonian fluids. The mathematical expression of the apparent Reynolds number is

$$Re^* = \frac{\rho N^{2-n} d}{K \cdot K_s^{n-1}} \qquad 4.12$$

The apparent Reynolds number is calculated using the computed values of K_s in Method (II). Figure 4.10 shows the generalized dimensionless power consumption curve for all impeller geometries. It can be observed in the figures that all the power curves, including the curve for Newtonian fluid, are brought together into a single power curve. The similar observation was made by Brito-De La Fuente et al. Moreover, it can be concluded from these observations that the present computed K_s values can predict correctly the superimposition of generalized power curves for both the Newtonian and shear thinning fluids. The linear generalized power distribution curves show that the laminar flow for the impeller geometry persists up to $Re \approx 100$. The generalized power curve was also developed by the computed K_s using Method I, III and IV. But these methods do not create a single power curve like Method II. The analysis shows that K_s value obtained by Method III is the worst and by Method II is the best.

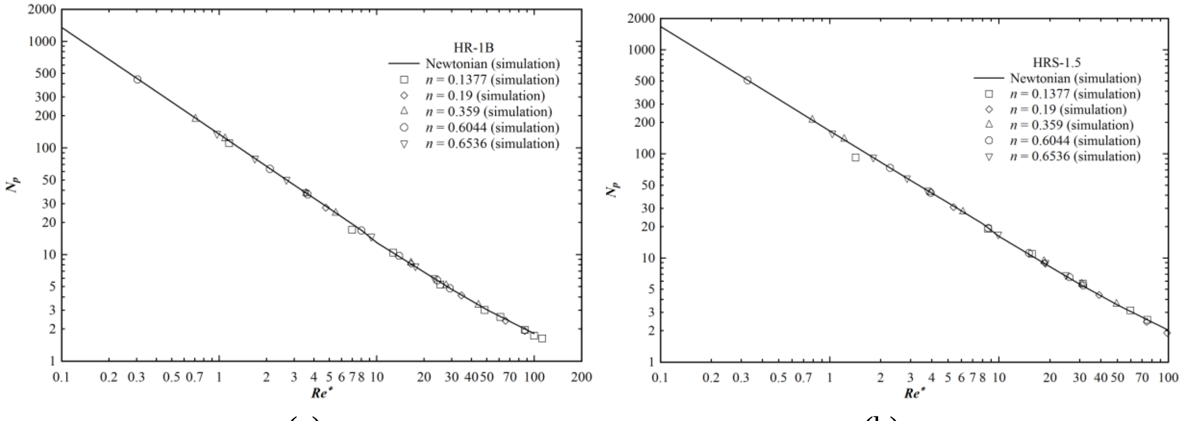

(a) (b)

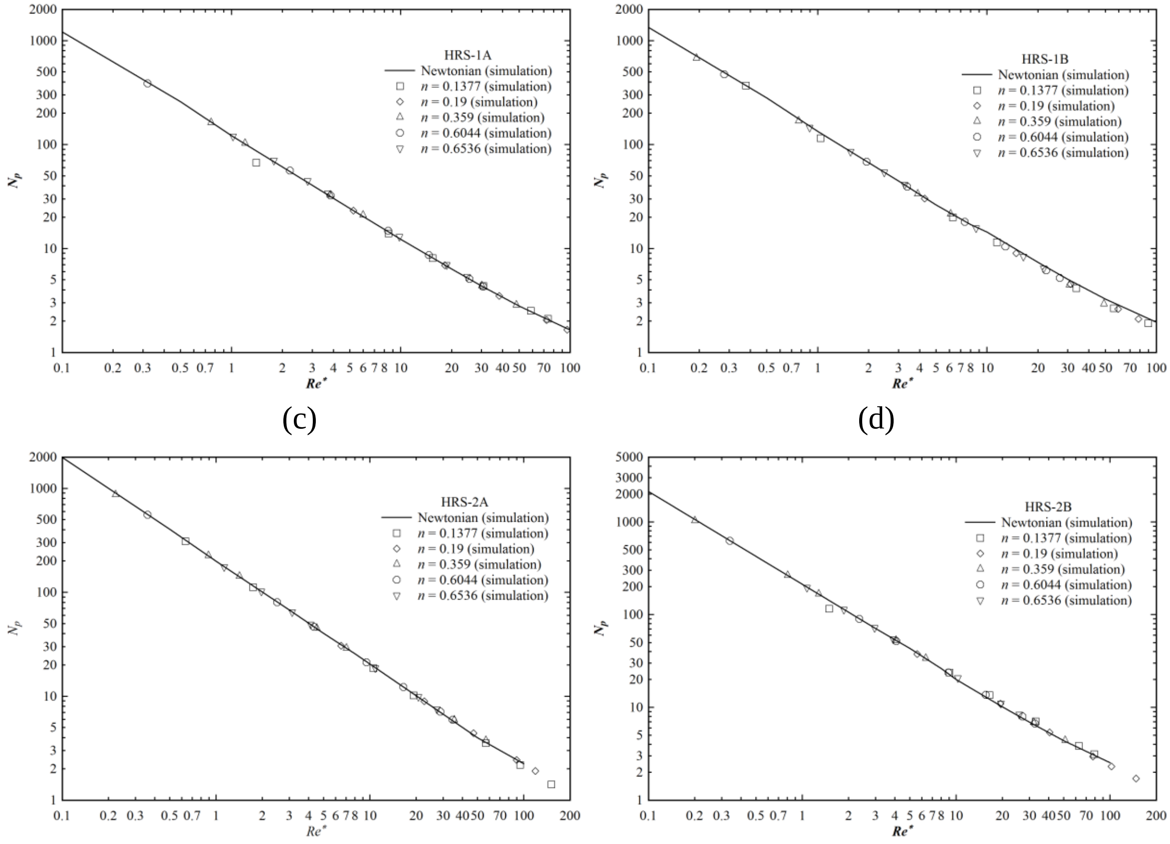

(c) (d)

(e) (f)

Figure 4.10 Generalized power consumption curve.

4.5.4 Prediction of Power Consumption for Shear Thinning Fluids

The unavailability of power distribution curves for stirred tank with the HRS impeller in transition zone has encouraged to find the power distribution curves up to Reynolds number of 10000 which includes both the laminar and transition regimes. The study comprises of the estimation and comparative study of power curves of the helical ribbon impeller and helical ribbon with screw impeller. The power curves in Figure 4.11 show the extension of the laminar zone to higher *Re* as *n* tends to 1.0. The figure shows that the power curves vary with impeller geometry and flow behavior index. Both in the laminar and transition zones, a decreasing trend of the power curve are observed in all the figures. But the rate of decrease of N_p becomes less in the transition zone than the laminar zone. Among all the curves, the rate of decrease of N_p in the transition zone is the highest for HRS-2A impeller. The same power curve as shown in Figure 4.11 can be presented for any impeller geometry using *n* as the parameter. As an instance, it is depicted in Figure 4.12 for HRS-2B impeller. The Reynolds number up to which flow regime is laminar vary with the flow behavior index, and those are 10 for n = 0.1377, 18 for n = 0.19, 40 for n = 0.359, 50 for n = 0.6044, 80 for n = 0.6536 and 100 for n = 1.0 (for HRS-2B impeller).The figure shows that the curves are approaching the power curve of Newtonian fluid as n tends to 1.0.

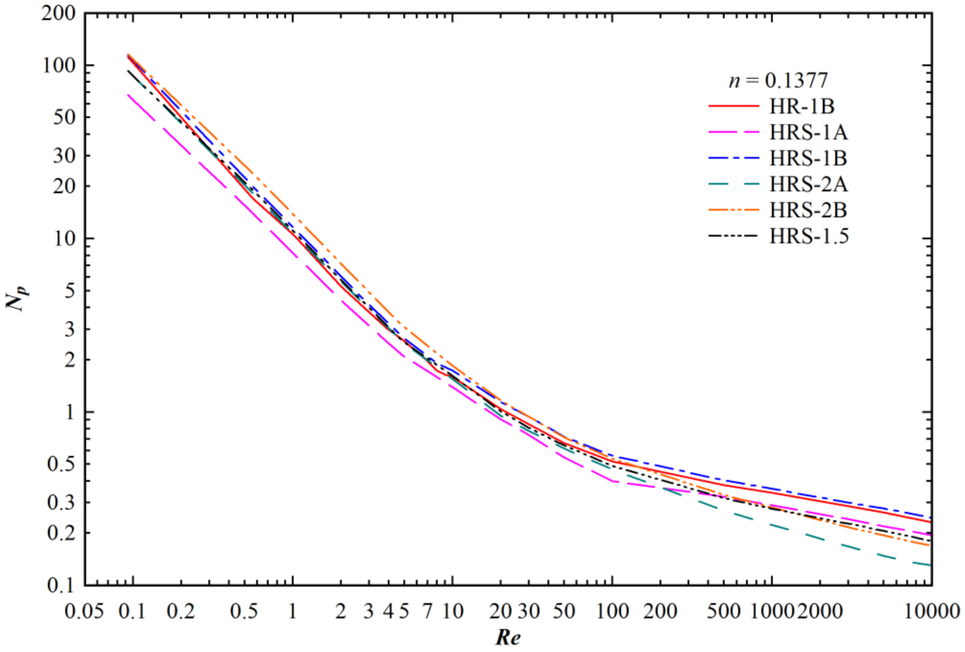

(a)

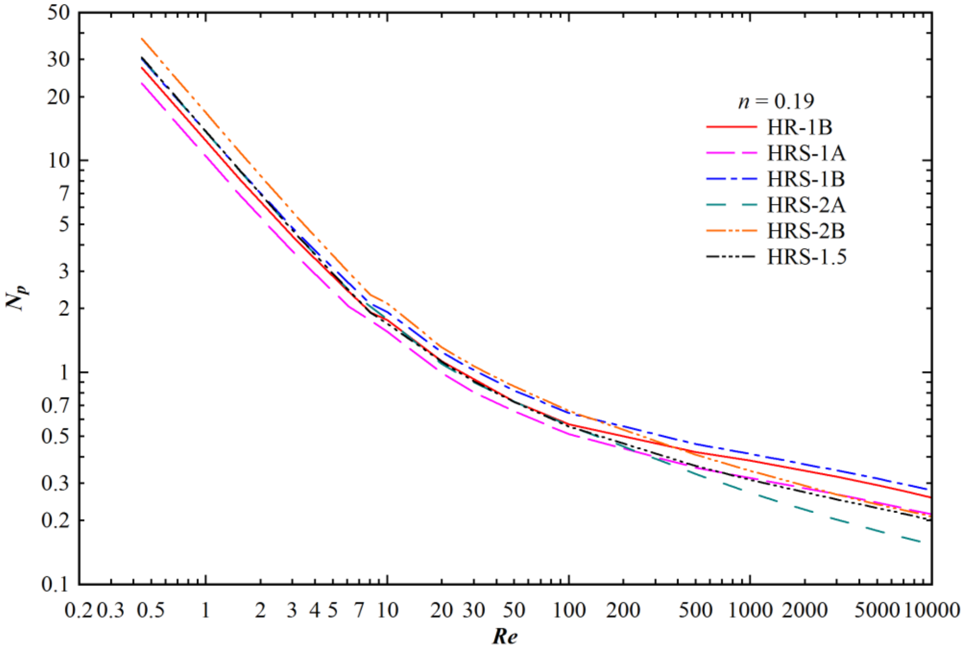

(b)

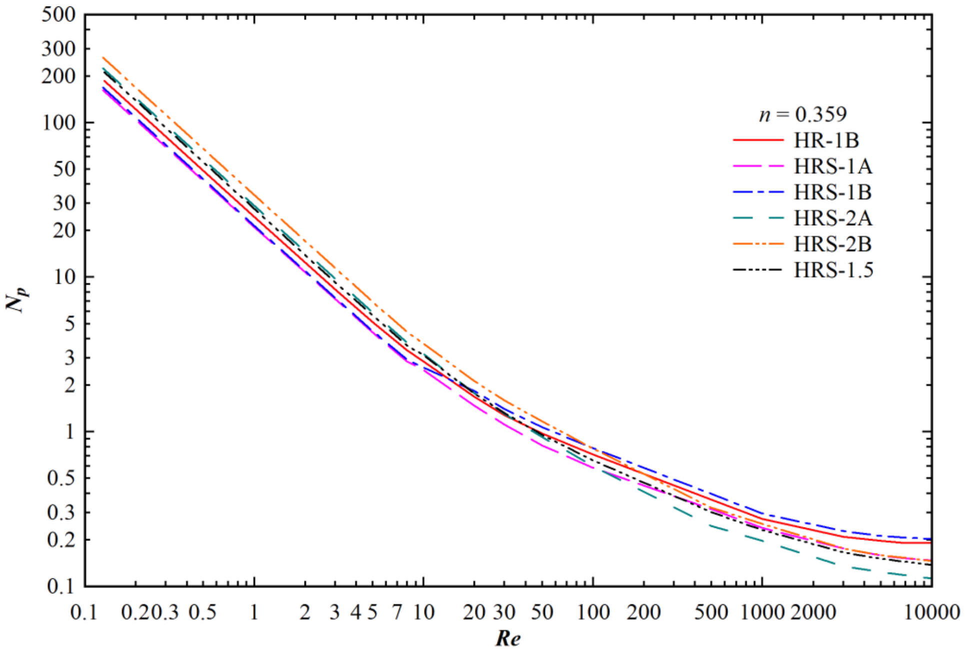

N_p
500
300
200
100
50
30
20
10
5
3
2
1
0.5
0.3
0.2
0.1
0.1
0.2
0.3
0.5
1
2
3
4
5
7
10
20
30
50
100
200
500
1000
2000
10000
Re
n = 0.359
HR-1B
HRS-1A
HRS-1B
HRS-2A
HRS-2B
HRS-1.5

(c)

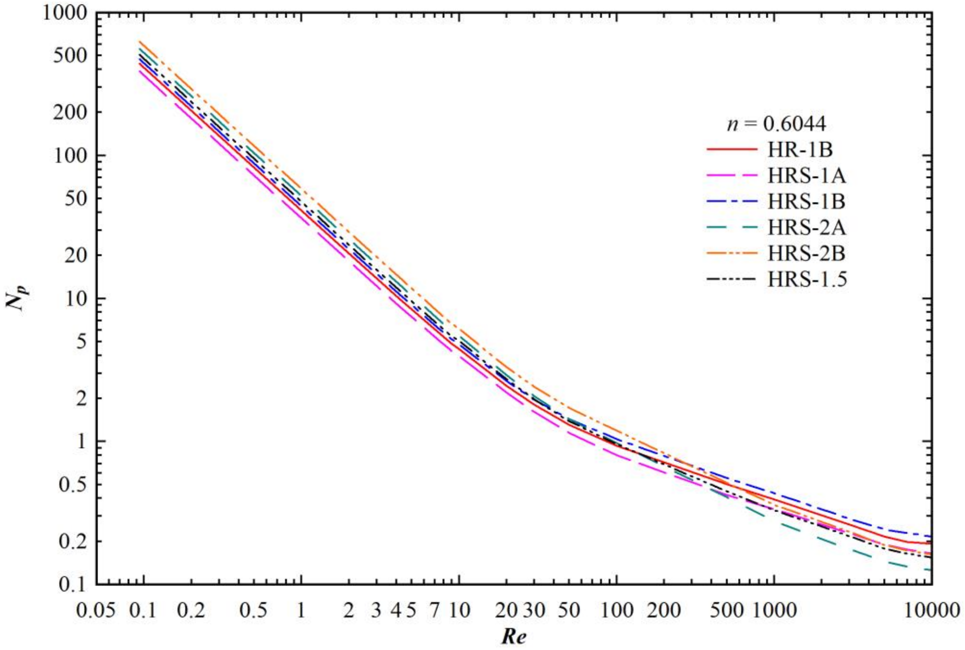

N_p
1000
500
200
100
50
20
10
5
2
1
0.5
0.2
0.1
0.05
0.1
0.2
0.5
1
2
3
4
5
7
10
20
30
50
100
200
500
1000
10000
Re
n = 0.6044
HR-1B
HRS-1A
HRS-1B
HRS-2A
HRS-2B
HRS-1.5

(d)

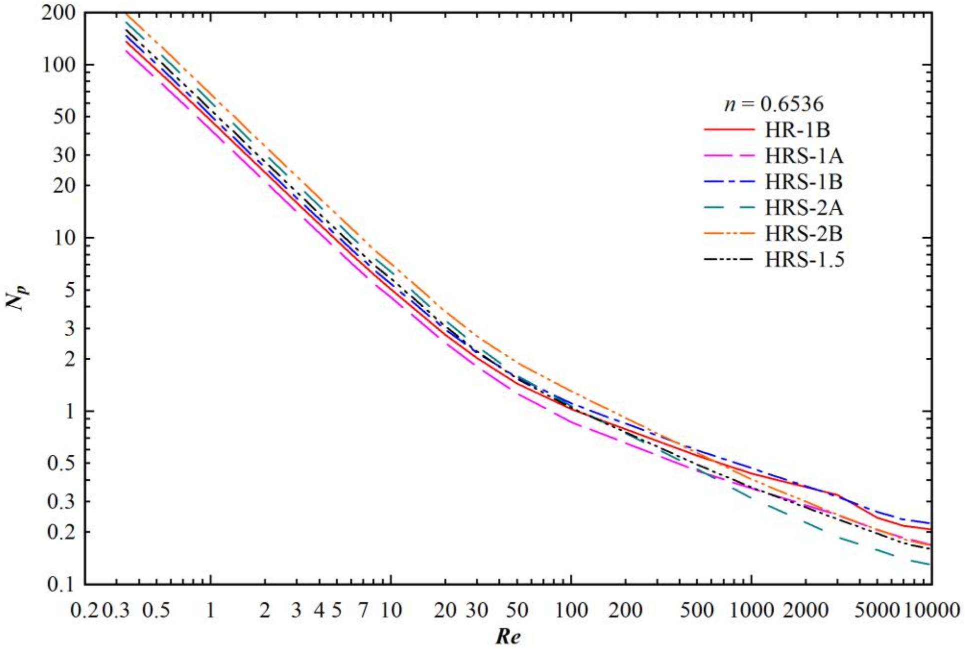

(e)

Figure 4.11 The power curves up to the transition flow regime for the HR and HRS impellers

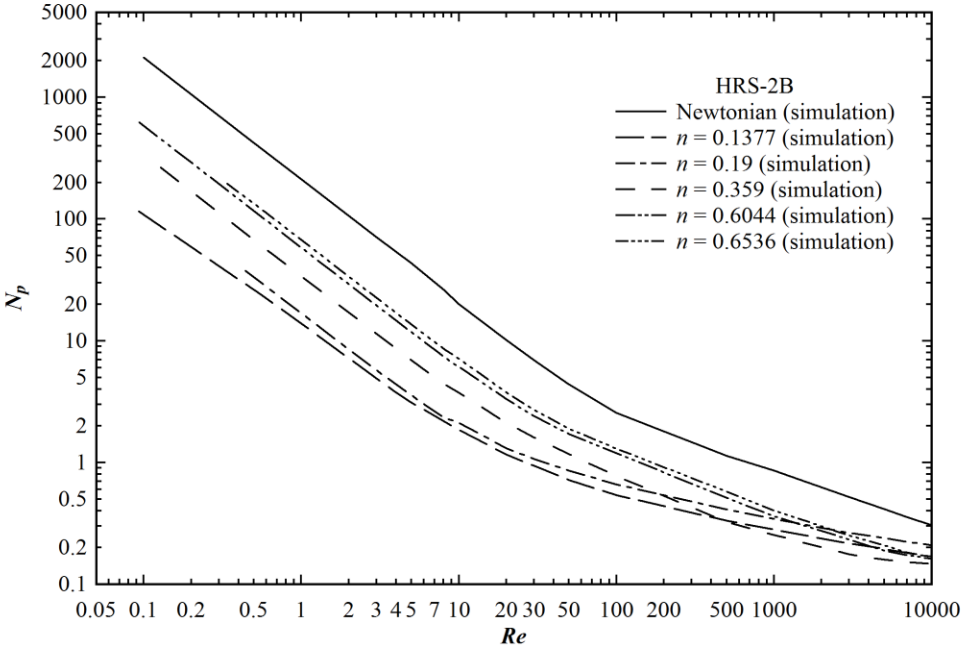

Figure 4.12 The power curves of HRS-2B impeller with different non-Newtonian and Newtonian fluids.

4.5.5 Prediction of Flow Number

Flow number, a direct function of impeller pumping capacity, is an important mixing performance characteristic of any impeller. The discharge flow capacity of the impeller can be easily calculated if flow number distribution curve is available. The flow number also helps to calculate the circulation time. Such an important parameter is not yet experimentally and/or theoretically evaluated for HRS impeller by any researcher. Therefore, in the present study, flow numbers are calculated for different geometries of the HRS impeller and the flow number of HRS impeller are compared with the flow number of HR impeller. The flow number distribution curves are depicted in Figure 4.13. In the laminar zone with $Re \leq 4-7$, the flow number increases gradually with increasing the Reynolds number. In between Reynolds number 7 and 50-100, the flow number increases linearly to reach the maximum flow number. In the transition zone ($100 \leq Re \leq 10000$), the flow number, depending on the impeller geometry and flow behavior index, either decreases gradually or becomes constant. The examination of all the curves shows that irrespective of the geometry of the impeller the maximum flow number is achieved as 0.1. Tending the flow process condition to turbulent regime does not increase the flow number. It is a significant disadvantage of HRS impeller. In the figure, for some impeller (HRS-1B, HR-1B), N_q shows a decreasing trend in the transition zone. But for other impellers (HRS-1A, HRS-2A, HRS-2B, HRS-1.5), N_q reaches asymptotically a constant value in the transition zone. The figure also shows that the rate of decrease of flow number in the transition zone is more for HR-1B impeller than HRS-1B impeller. The effect of the flow behavior index on the flow number is large in the laminar zone, while in the transition zone the effect is negligible especially for HRS impellers.

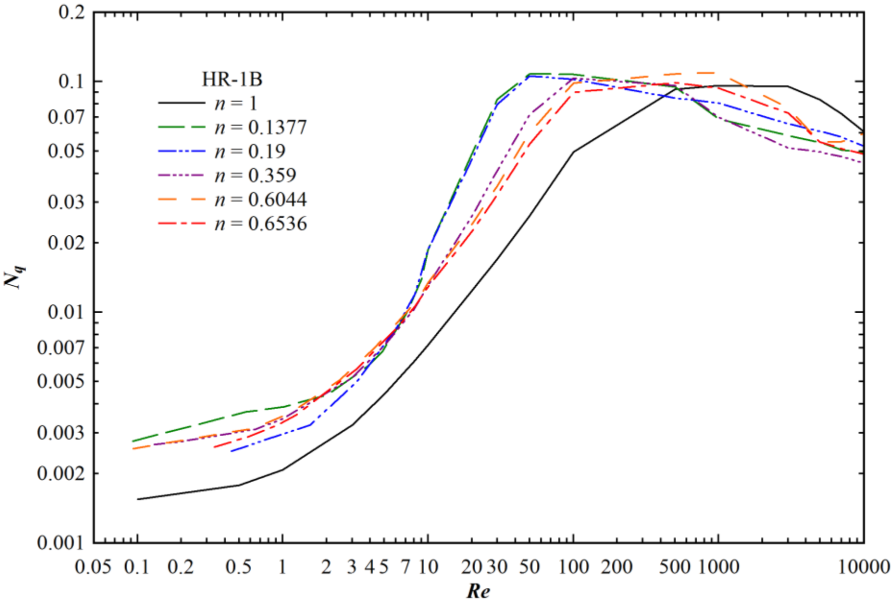
HR-1B
n = 1
n = 0.1377
n = 0.19
n = 0.359
n = 0.6044
n = 0.6536
N_q
Re
0.2
0.1
0.07
0.05
0.03
0.02
0.01
0.007
0.005
0.003
0.002
0.001
0.05 0.1 0.2 0.5 1 2 3 4 5 7 10 20 30 50 100 200 500 1000 10000

(a)

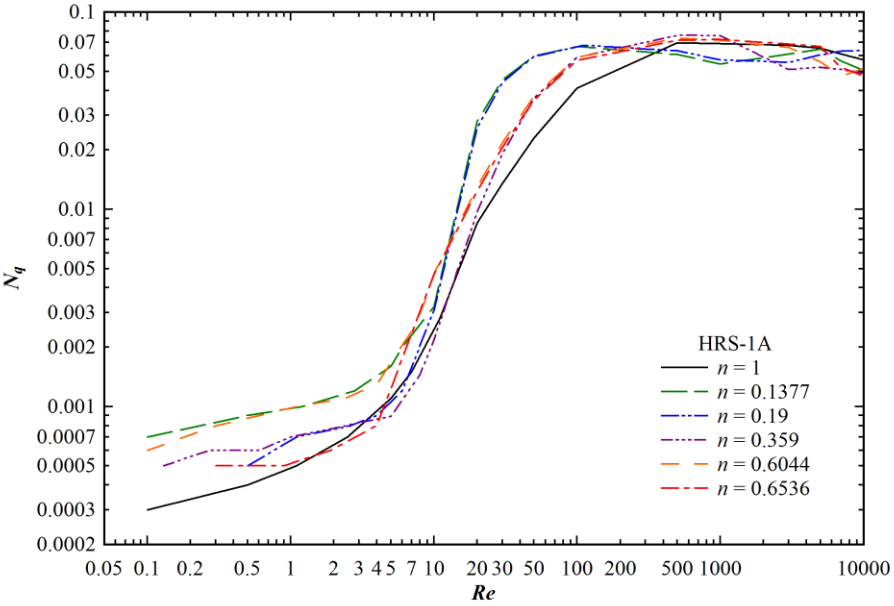
HRS-1A
n = 1
n = 0.1377
n = 0.19
n = 0.359
n = 0.6044
n = 0.6536
N_q
Re
0.1
0.07
0.05
0.03
0.02
0.01
0.007
0.005
0.003
0.002
0.001
0.0007
0.0005
0.0003
0.0002
0.05 0.1 0.2 0.5 1 2 3 4 5 7 10 20 30 50 100 200 500 1000 10000

(b)

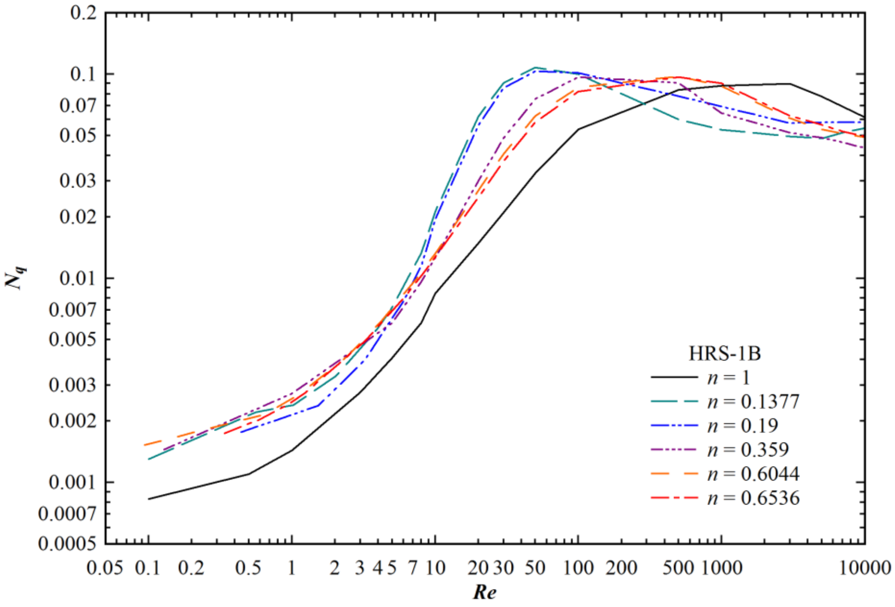
HRS-1B
n = 1
n = 0.1377
n = 0.19
n = 0.359
n = 0.6044
n = 0.6536
Nq
Re
0.2
0.1
0.07
0.05
0.03
0.02
0.01
0.007
0.005
0.003
0.002
0.001
0.0007
0.0005
0.05 0.1 0.2 0.5 1 2 3 4 5 7 10 20 30 50 100 200 500 1000 10000

(c)

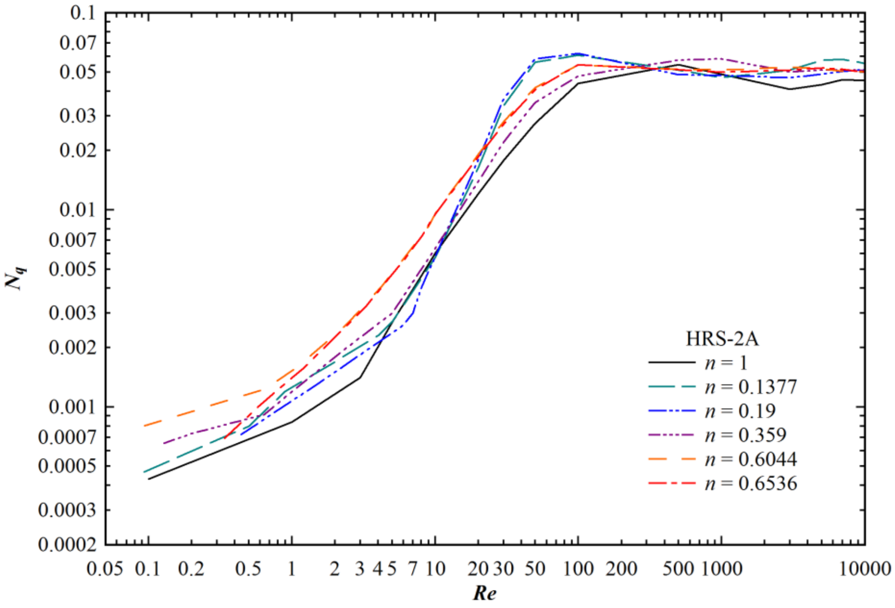
HRS-2A
n = 1
n = 0.1377
n = 0.19
n = 0.359
n = 0.6044
n = 0.6536
Nq
Re
0.1
0.07
0.05
0.03
0.02
0.01
0.007
0.005
0.003
0.002
0.001
0.0007
0.0005
0.0003
0.0002
0.05 0.1 0.2 0.5 1 2 3 4 5 7 10 20 30 50 100 200 500 1000 10000

(d)

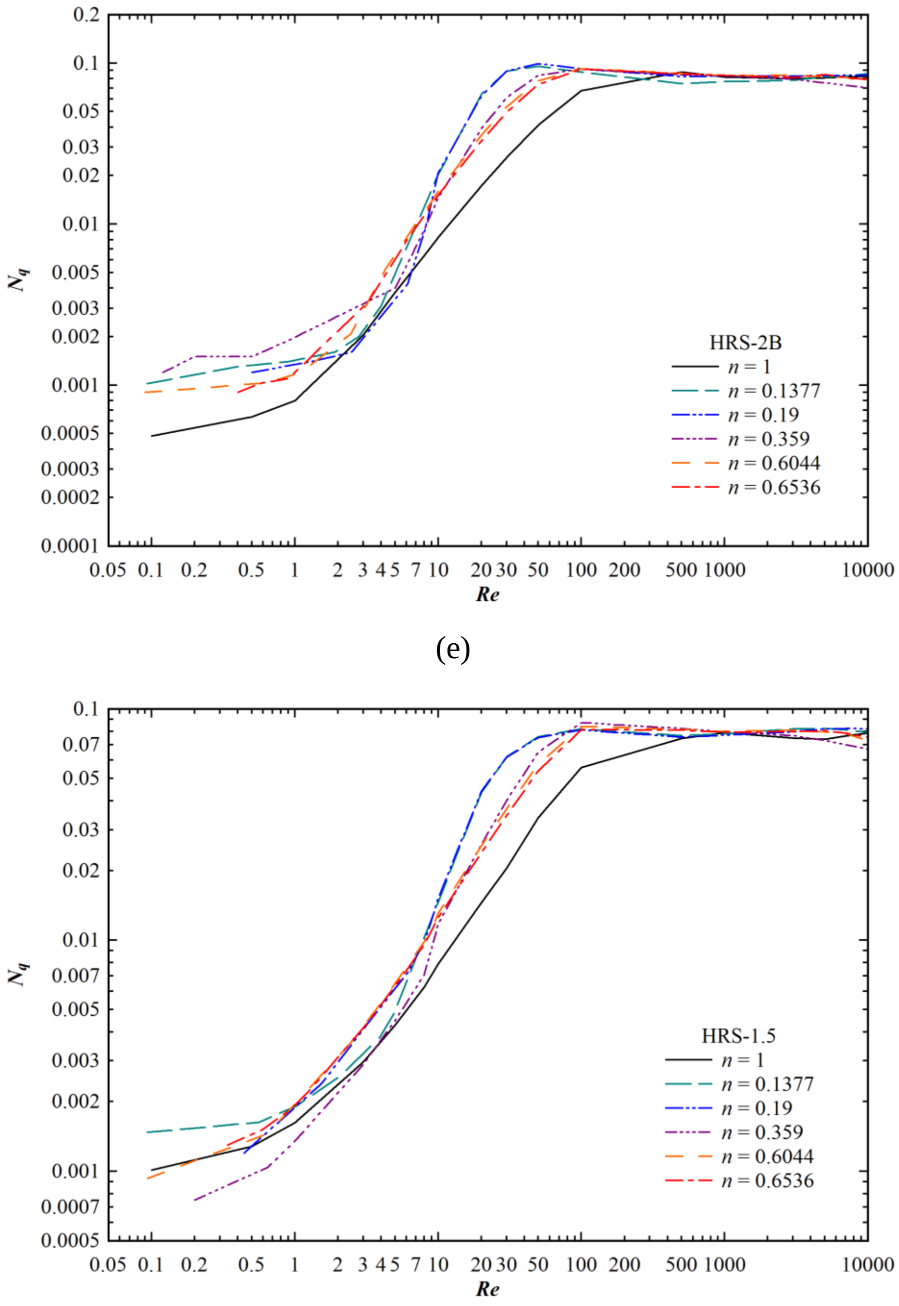

Figure 4.13 Distribution of flow number with Reynolds number.

4.5.6 Prediction of Velocity Profile

The effect of flow parameters on the axial (U), radial (V) and tangential (W) velocity profiles is necessary to find and understand the hydrodynamics behavior of the stirred tank system in presence of rotating impellers.

Looking at the above need velocity profiles at the mid-height of the tank are calculated using Reynolds number as the parameter. Illustrative velocity distribution for HR-1B and HRS-2B impellers are shown in Figure 4.14. Similar trend of velocity distributions for other impellers are observed. The figure shows that the axial velocity of HR impeller is more than HRS impeller except very close to the shaft of the impeller. The distribution of the radial and tangential velocity components finds that the magnitudes of both the velocities of HRS impeller are more than the HR impeller. Figure also shows that the Reynolds number substantially affects the axial velocity components. The effect of Reynolds number on the radial velocity component is negligible for HRS impeller. But a large effect of Reynolds number on the radial velocity distribution of the HR impeller is observed. The tangential velocity component does not show any variation with Reynolds number in the laminar zone.

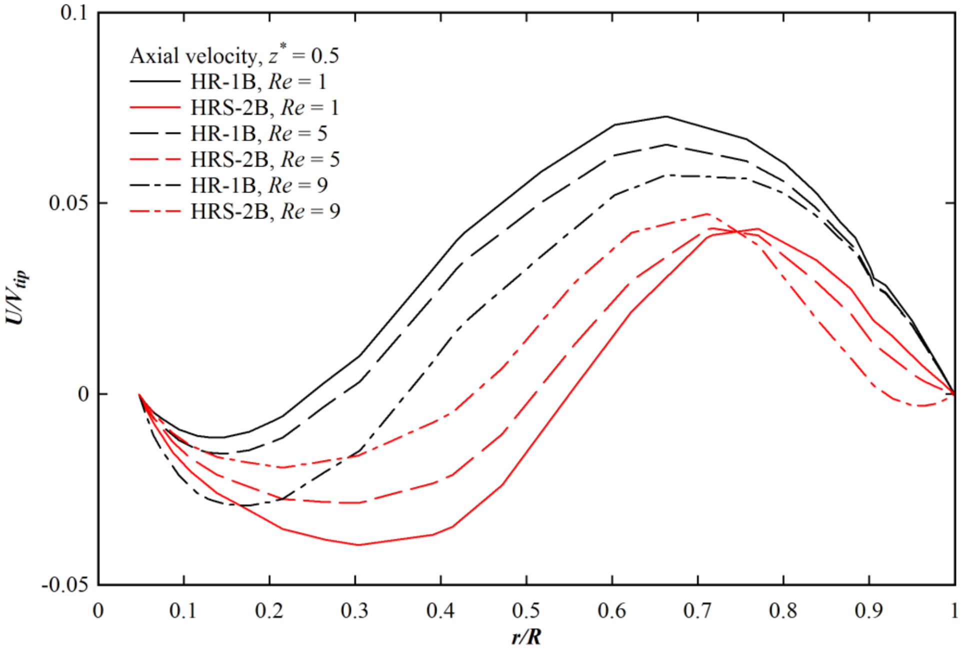

(a)

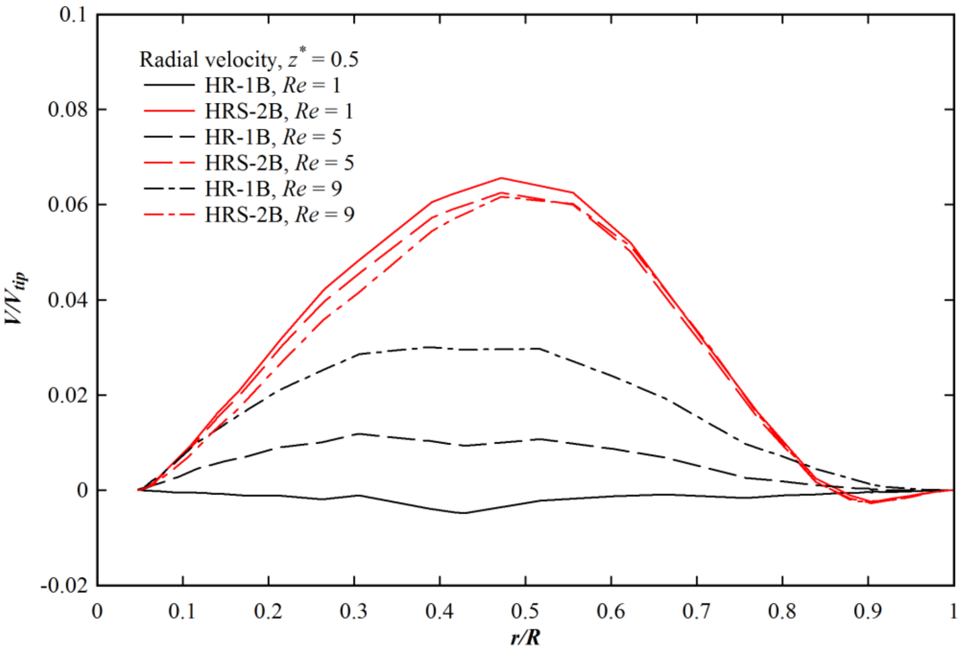

(b)

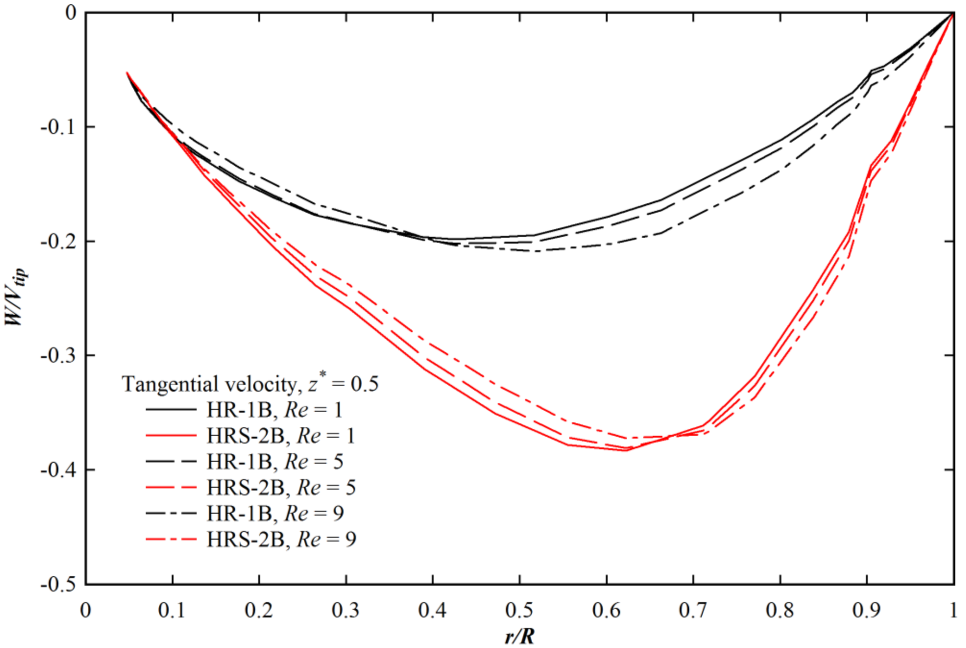

(c)

Figure 4.14 Effects of Reynolds number on the non-dimensional axial, radial and tangential velocity components for $n = 0.6044$. The tip velocity of the impeller, $V_{tip} = \pi N D_i$.

Velocity profiles at Reynolds number 9 and at different height of the tank are shown in Figure 4.15. The purpose here is to examine the nature of the velocity distribution in the radial direction at different height of the tank. Near the bottom of the tank, i.e., at $z^* = 0.2$, the axial velocity of the HRS impeller is found more than the HR impeller for $r/R \leq 0.65$ and axial velocities of both the impellers become equal for $r/R > 0.65$. The figure also shows that the axial velocities of both impellers are approximately same in magnitude at $z^* = 0.5$ and 0.8. Moreover, at $z^* = 0.5$ and 0.8, the axial flow is in the downward direction up to half way in the radial direction, but beyond it, the axial flow occurs in upward direction which is the most desirable characteristic of the HR and HRS impellers. At $z^* = 0.2$, a higher radial flow towards the shaft is found for HR than HRS impeller. For $z^* = 0.5$ and 0.8, a comparable outward radial velocity distribution is found. For all the z^*, a greater rotational flow with higher tangential velocity is observed for HRS impeller than HR impeller. The figure also depicts the presence of rotational flow up to the impeller blade surface.

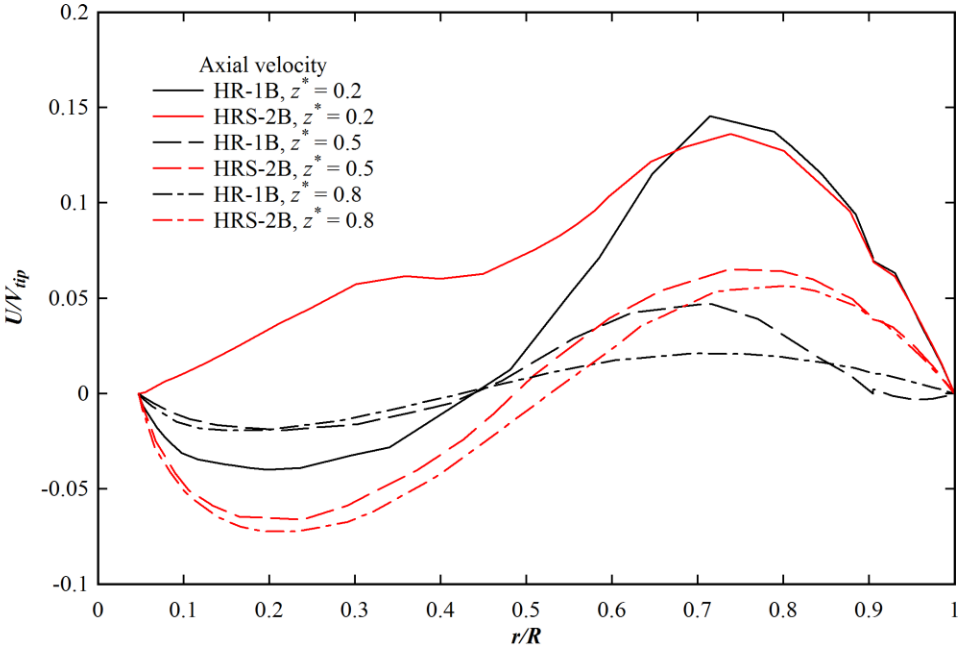

(a)

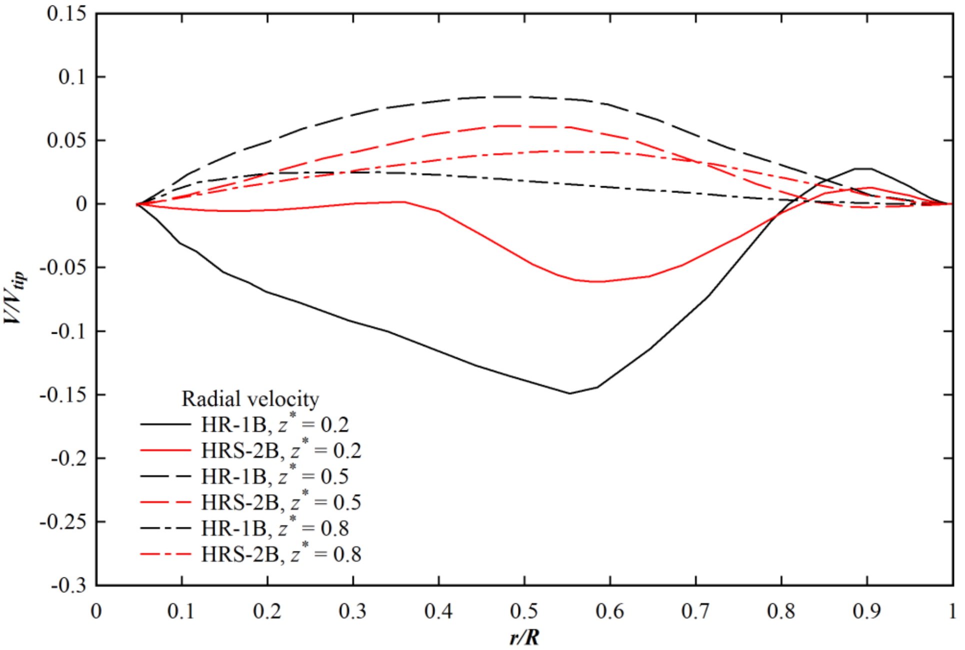

(b)

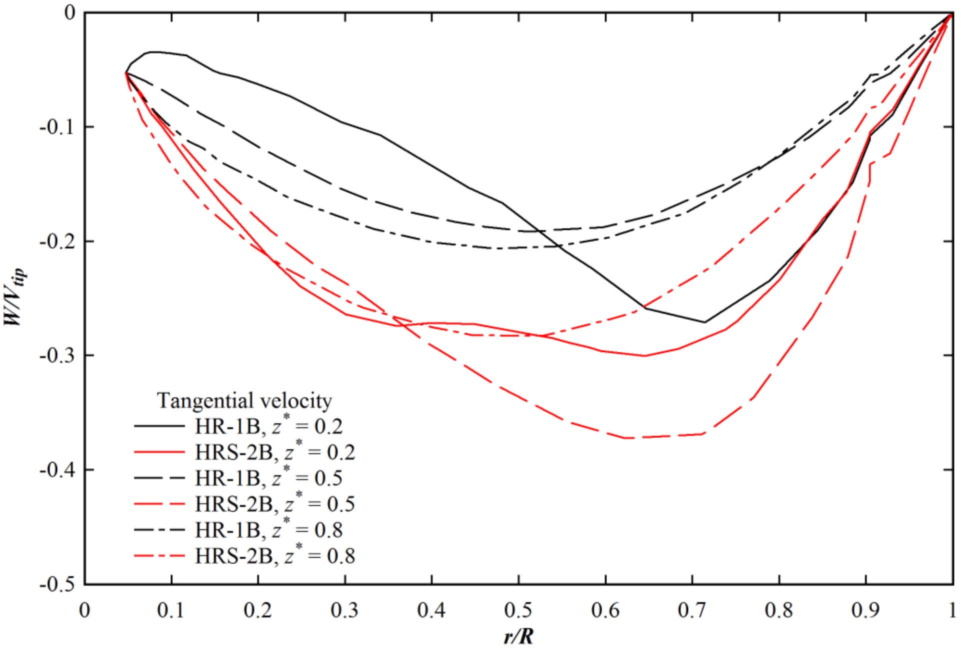

(c)

Figure 4.15 The radial distributions of axial, radial and tangential velocity components at three different heights, $z^* = z/H$ of the tank at *Re* = 9 and for *n* = 0.6536.

The effect of the flow behavior index, *n* on the velocity profile is shown in Figure 4.16. It depicts a considerable effect of the flow behavior index on the velocity profiles. The dependency of the axial velocity on the flow behavior index depends on the radial position. For $r/R < 0.77$, an erratic distribution of axial velocity is observed. Whereas, for $r/R > 0.77$, the axial velocity increases with increasing *n*. It occurs due to the inconsistent distributions of flow consistency index, *m* with the flow behavior index, *n* given in Table 4.2. The radial velocity decreases and approaches Newtonian fluid's velocity profile with increasing *n* for $r/R < 0.77$. For higher radial positions, radial velocity increases and approaches the Newtonian fluid's velocity profile with increasing *n*. The tangential velocity increases with increasing *n* for $r/R < 0.7$, and becomes independent of the flow behavior index for higher r/R. In general, with increasing *n*, the tangential velocity profiles approach the tangential velocity profile of the viscous Newtonian fluid. The figure also depicts much greater tangential velocity in the core area of tank with HRS impeller than other two velocity components. It confirms the rotational movement of the liquid in the core zone for HRS impeller. For other impellers, not shown here, the velocity profiles are found to be dependent on the flow behavior index.

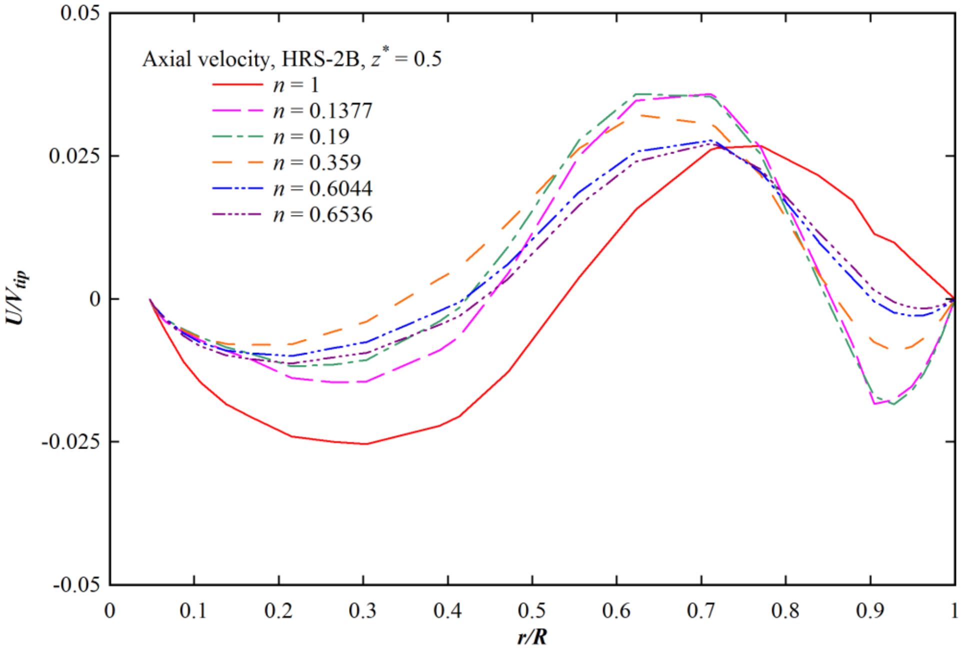

(a)

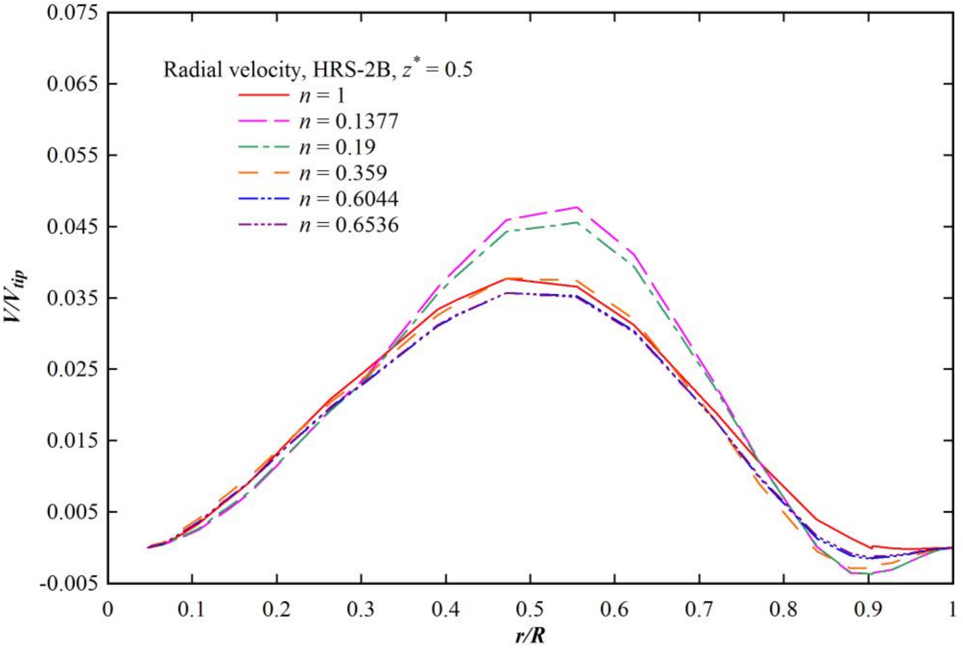

(b)

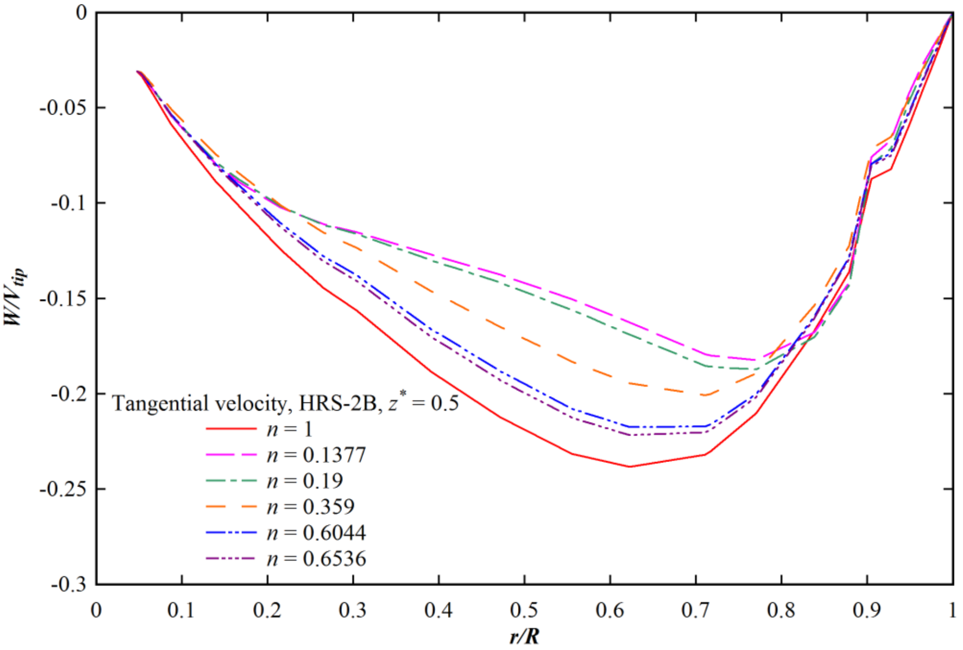

(c)

Figure 4.16 The effect of flow behavior index, *n* on the radial distributions of axial, radial and tangential velocity components at height, $z^* = 0.5$ of the tank at *Re* = 10.

Figure 4.17 shows the velocity vector contours for stirred tank with HR and HRS impeller at Reynolds number 8. It shows a more active flow field near the impeller blade due to high shear stresses which create the low viscous fluid zone. The blade tip pumped the surrounding fluid in the upper direction and recirculated the same in the tank. The size of circulation loop depends on the width of the blade. More number of circulation loops is observed for HRS impeller than HR impeller. The contour plot confirms the downward flow nearer the shaft and upward flow near the tank wall, especially in the upper part of the tank. Higher radial flow is observed below the impeller body. For other impeller geometries and non-Newtonian fluids, similar kinds of velocity contours are also found.

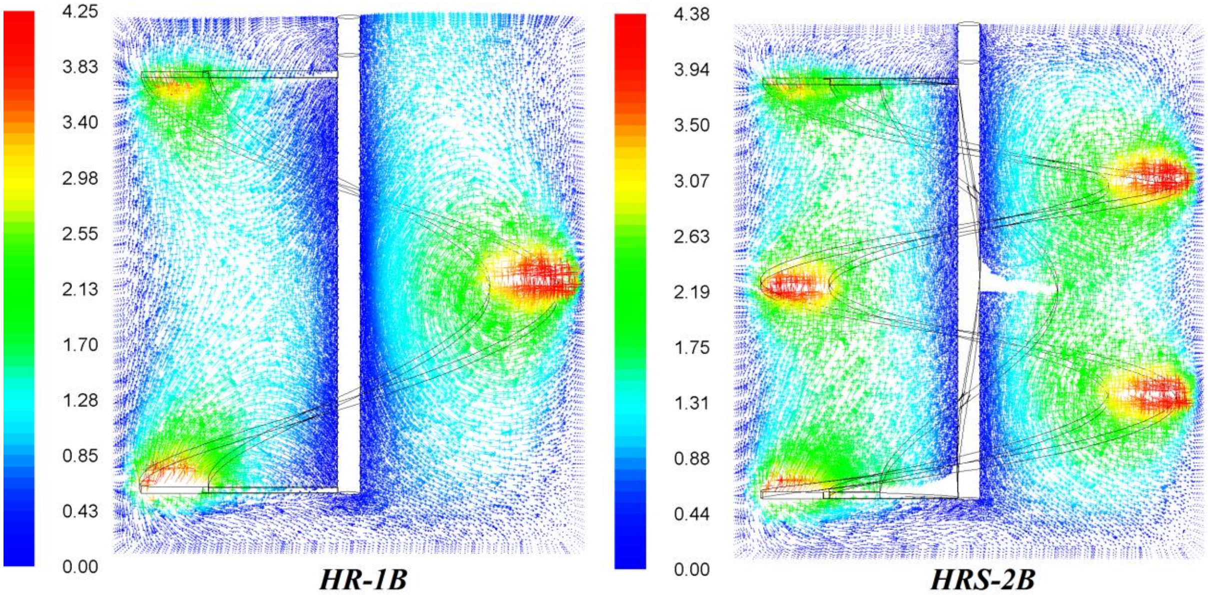

Figure 4.17 Velocity vector contour of viscous Newtonian fluid at $Re = 8$.

4.5.7 Mixing Time and Efficiency

Recently, Chhabra et al. (2007) found experimentally and theoretically the distribution of non-dimensional mixing times with Reynolds number. For low viscous fluids, they showed that the non-dimensional mixing time was constant with Reynolds number. But, the distributions of non-dimensional mixing times with Reynolds number were found as quite scattered for high viscous fluids. They also successfully predicted their experimental data using CFD tools. The Ekato Paravisc (helical ribbon) impeller was used by them to homogenize the viscous fluids. In the present work, high viscous Newtonian and non-Newtonian fluids are mixed by HR and HRS impellers. The study of Chhabra et al. (2007) has encouraged to find the distribution of non-dimensional mixing times with Reynolds number for the high viscous fluids given in Table 4.2. To reach this objective, the stirred tank with HR or HRS impeller is simulated by Ansys Fluent to find the mixing time at the specified locations inside the tank. Tracer is injected, and the tracer concentration is collected with time at those particular locations (P_1, P_2 and P_3). Chhabra et al. (2007) have considered the 80% homogenization time as the mixing time, whereas, in the present study, the time required to reach the 95% or 105% of the final concentration of tracer at that particular location is taken as the mixing time. The choice may affect the distribution pattern of the mixing time with Reynolds number. The response curve for the present work is shown in Figure 4.18. The HR and HRS impeller show the sluggish first order and second order responses, respectively. The response curves determine the dimensional mixing time. The numerically computed distributions of non-dimensional mixing time of HR-1B and HRS-2B impellers are shown Figure 4.19. The figure depicts a scatter distribution of the non-dimensional mixing time. The distributions of non-dimensional mixing times of other impellers are also found equally scattered. Thus, the work of Chhabra et al. (2007) has verified the observations of the present computational results. Further observation of the figures shows that the non-dimensional mixing time is very much dependent on the fluid flow index, *n*. Also at the middle point, P_2, the mixing time is the lowest among all the points especially at low Reynolds number. At very high Reynolds number, the mixing time at all the points becomes almost equal.

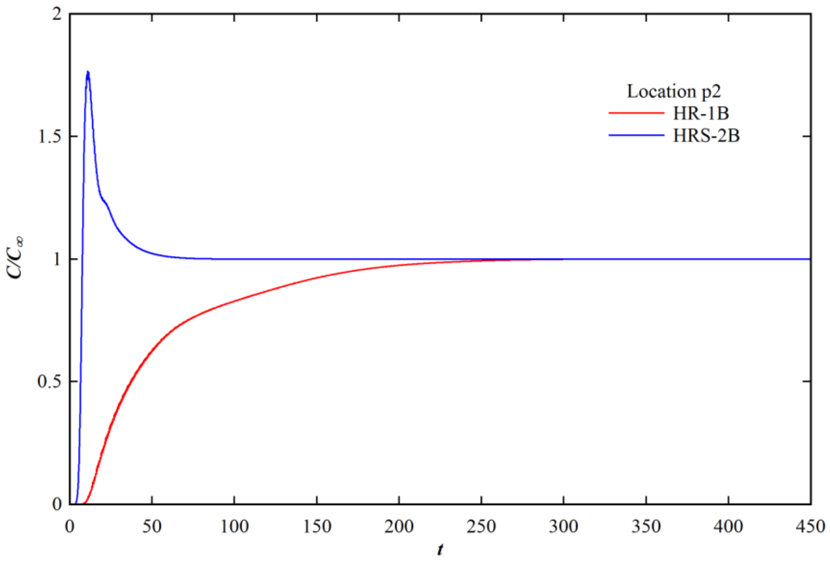

Figure 4.18 Response curve at P_2 of HR and HRS impeller at *Re* = 10 and *n* = 0.6536.

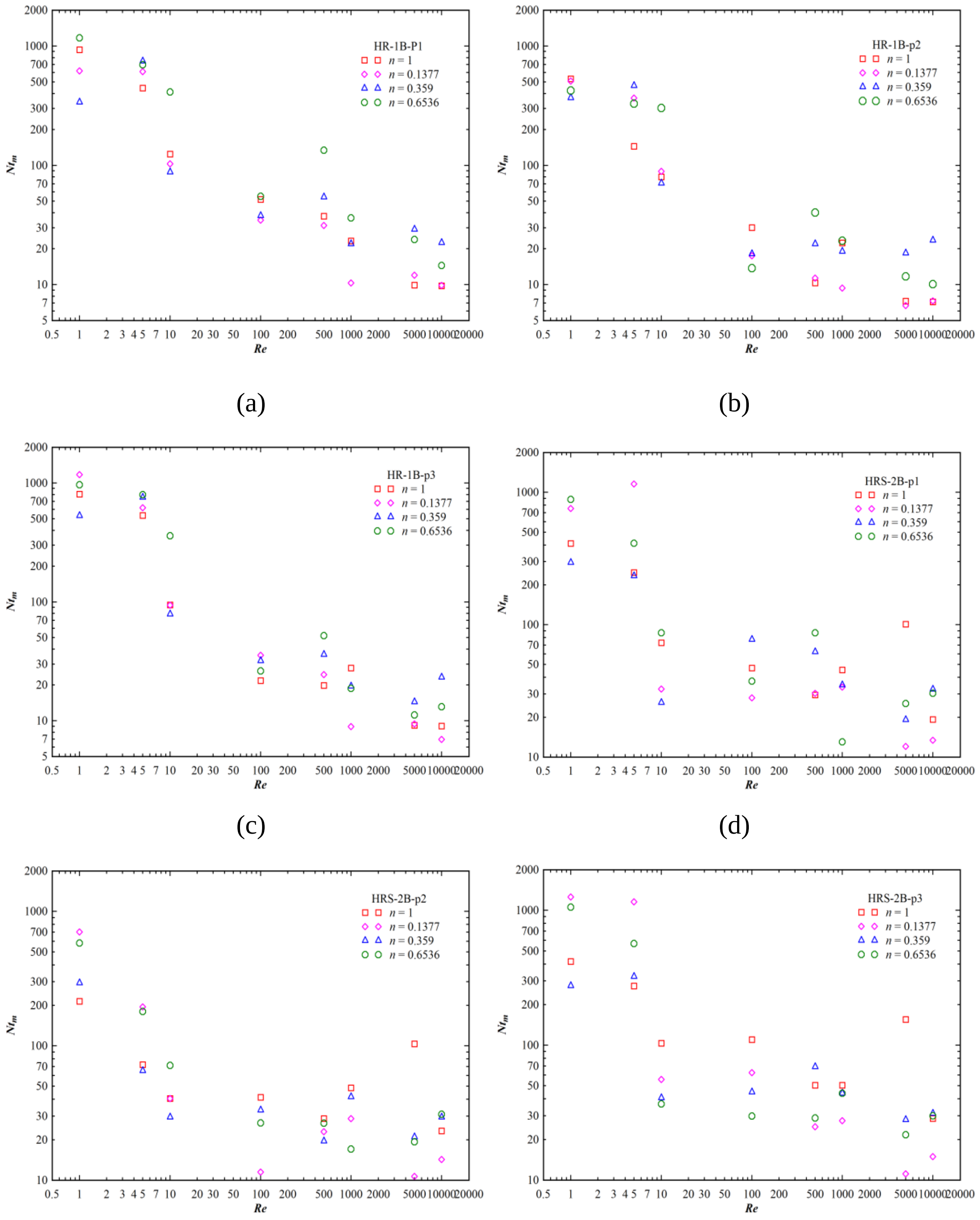

(a)

(b)

(c)

(d)

(e)

(f)

Figure 4.19 Non-dimensional mixing time versus Reynolds number for Newtonian and non-Newtonian fluids.

4.5.7.1 Dispersive Mixing Efficiency

De la Villeon et al. (1998) and Emin and Schuchmann (2013) have studied mixing performance in terms of dispersive mixing efficiency. It is denoted by α_{DME} and its mathematical expression is given in Equation 3.45. For a mixing index of 0, the system is undergoing purely rotational flow and no effective mixing can occur. A mixing index of 0.5 denotes simple shear flow while a value of 1.0 denotes irrotational flow (i.e. elongational or dispersive flow). The work of De la Villeon et al. (1998) and Emin and Schuchmann (2013) did not discuss the effect of Reynolds number and flow behavior index, *n* on the dispersive mixing efficiency. The present work shows the effects in Figure 4.20. The figure illustrates the distribution of α_{DME} for HR and HRS impellers. For other impellers, similar kinds of distributions are observed. Both the figures show that the average α_{DME} is greater than 0.5 at all the Reynolds numbers and flow behavior indexes. Hence, overall, the flow is predominantly dispersive in nature.

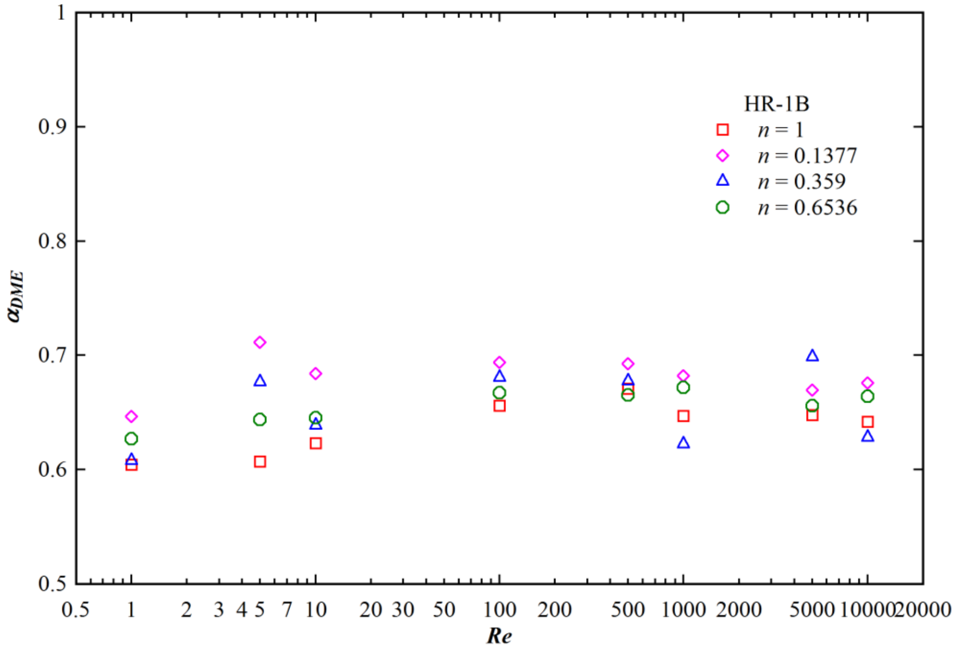

(a)

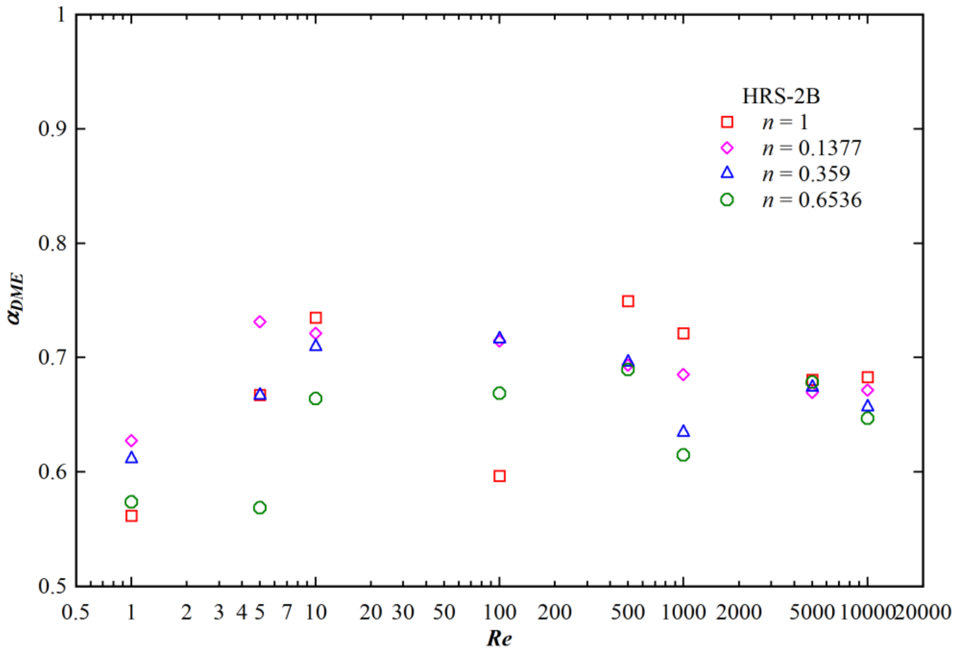

(b)

Figure 4.20 Distribution of the average dispersive Mixing Efficiency with Reynolds number.

Figure 4.21 illustrates the distribution of dispersive mixing efficiency, α_{DME} for non-Newtonian fluids (n = 0.6536) at Reynolds number 5 and 100. For other impeller geometries, Reynolds numbers, and working fluids similar kind of spatial distributions of α_{DME} are observed. Both the figures depicts that around the shaft flow is rotational in nature. Closer to impeller surface the flow is of simple shear type with $\alpha_{DME}=0.5$. In other zones, the flow is more dispersive having $\alpha_{DME}>0.5$. It is also observed that more amount of liquid rotates around the impeller shaft for HRS impeller than HR impeller. It occurs because of the presence of the screw on the shaft of the HRS impeller. The quantity of rotating liquid around the shaft for both impellers get shrink with increasing the Reynolds number. The population of fluid elements with $\alpha_{DME}>0.5$ increases with Reynolds number. The efficiency of mixing therefore increases with increasing impeller Reynolds number. The figure also depicts that HR impeller provides more dispersive flow than the HRS impeller.

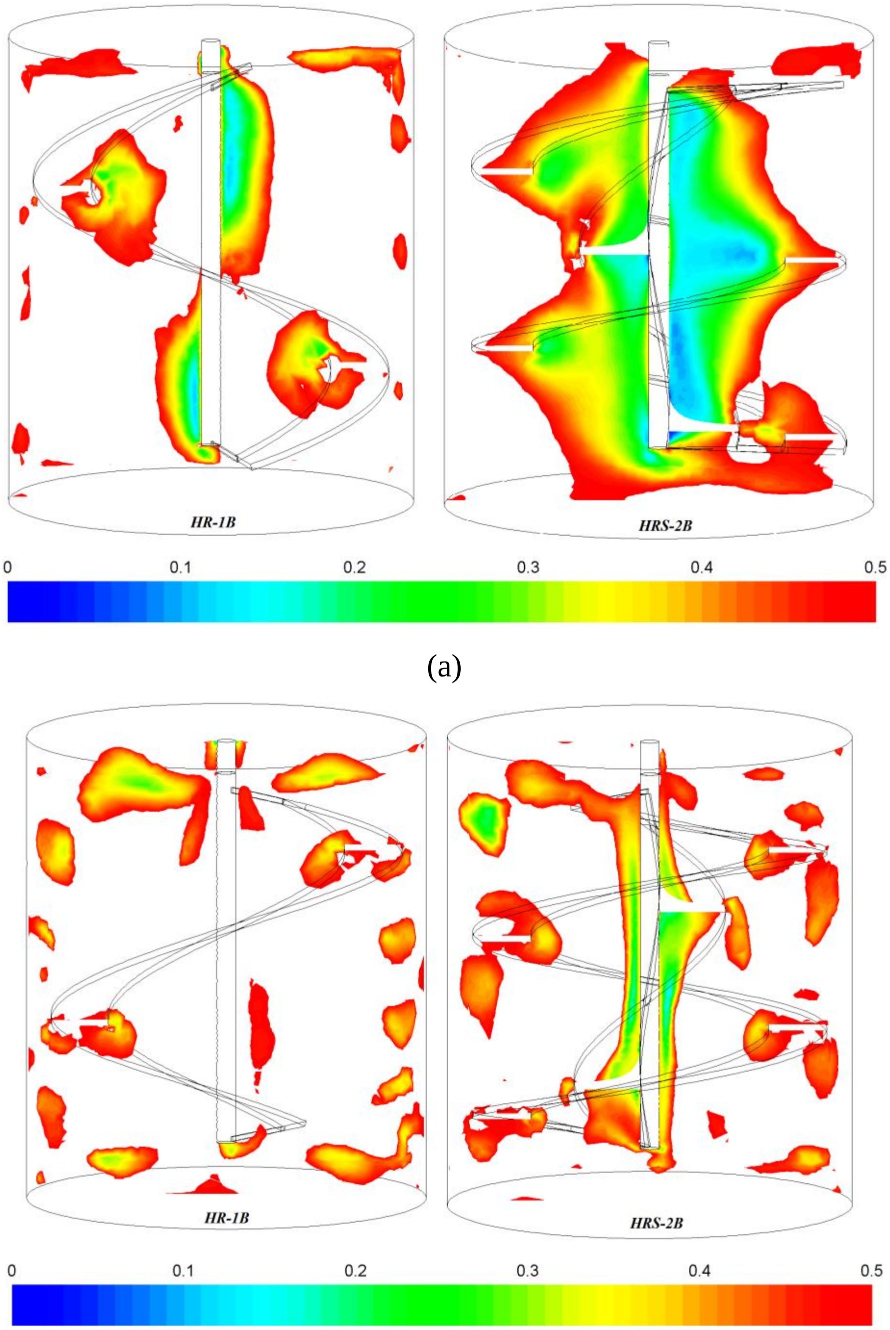

(a)

(b)

Figure 4.21 Contours of dispersive mixing efficiency for $\alpha_{DME} \le 0.5$ for liquids with flow behavior index *n* = 0.6536 at (a) *Re* = 5 and (b) *Re* = 100.

The Figure 4.22 shows the contour plot of dispersive mixing efficiency, α_{DME} for *n* = 0.1377 at impeller Reynolds number of 5. The contours of this figure are compared with Figure 4.21(a), which is drawn for *n* = 0.6536. The purpose here is to find the effect of the flow behavior index on α_{DME}. It is clearly visible that with decreasing the *n*, there is a decrease of the amount of liquid with the rotational flow around the shaft. It occurs due to the decrease in the tangential velocity around the shaft with decreasing the flow behavior index.

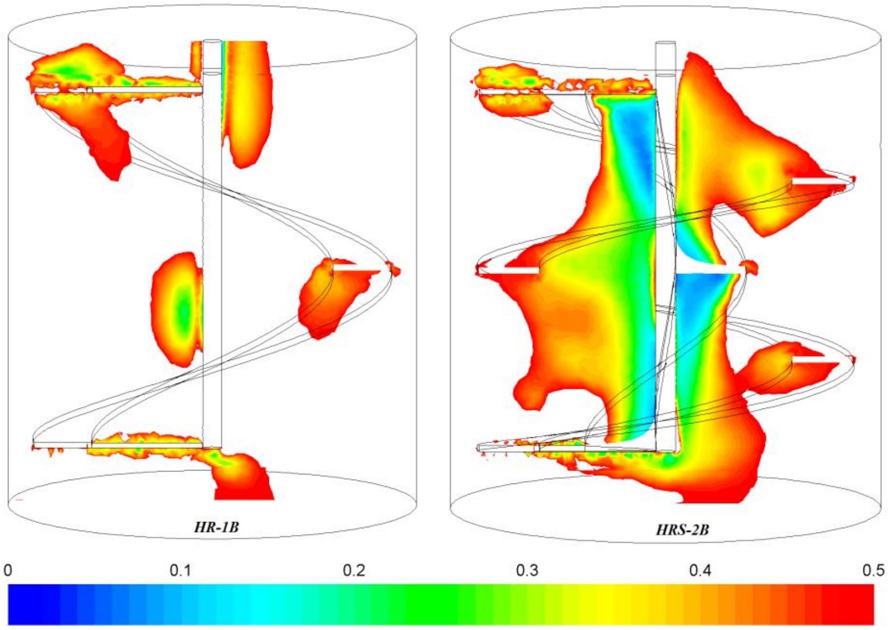

Figure 4.22 Contours of dispersive mixing efficiency for $\alpha_{DME} \leq 0.5$ for liquids with flow behavior index *n* = 0.1377 at *Re* = 5.

4.5.8 Prediction of Entropy Generation of Isothermal Batch Stirred Tank

Entropy generation due to viscous dissipation of the batch stirred tank with HR and HRS impellers is predicted by substituting the computed velocity gradients in Equations 4.10 and 4.11. Figure 4.23 illustrates average non-dimensional volumetric entropy generation of Newtonian fluid in the stirred tank with HR and HRS impellers. The production rate of entropy is higher in the vicinity of impeller blade. It happens due to imparting of more shear stress by the impeller on the nearby fluids which causes larger velocity gradients near the impeller blade. The entropy generation decreases drastically just by moving little away from impeller blade. Although the magnitude of the maximum entropy generation for HR-1B impeller is more than HRS-2B impeller, the spread of high entropy generation zone is more for HRS impellers. For other impellers and working liquids, qualitatively almost similar kinds of entropy generation contours are found.

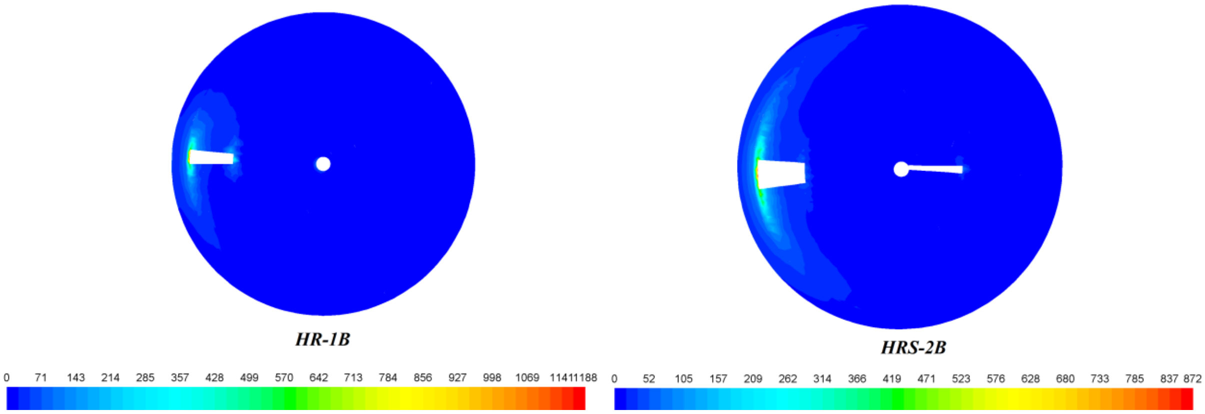

Figure 4.23 Contours of local entropy generation at *Re* = 9 of HR-1B and HRS-2B impellers for non-Newtonian fluid with flow behavior index, *n* = 0.6044.

In general, the viscous dissipation entropy generation is directly proportional to the effective viscosity. For shear thinning fluids the effective viscosity increases with *K* and decreases with decreasing *n*. As given in Table 4.2, *n* and *m* are dependent on each other. Thus, the combined effect of *m* and *n* on the entropy generation is shown in Figure 4.24. Irrespective of the geometry of the impeller and impeller Reynolds number, the decreasing order of the viscous dissipation entropy generation is *n*:1 > *n*:0.6044 > *n*:0.359 > *n*:0.6536 > *n*:0.1377 > *n*:0.19. The figure also shows the entropy generation increases as the pitch ratio (s/D_i) of the impeller geometry decreases. Therefore, HRS-2 group impeller shows higher entropy generation than other impellers at the same Reynolds number. Within the same group of impellers, the entropy generation is found more for the impellers having higher blade width. Thus, HRS-1B and HRS-2B have higher entropy generation than HRS-1A and HRS-2A impellers, respectively.

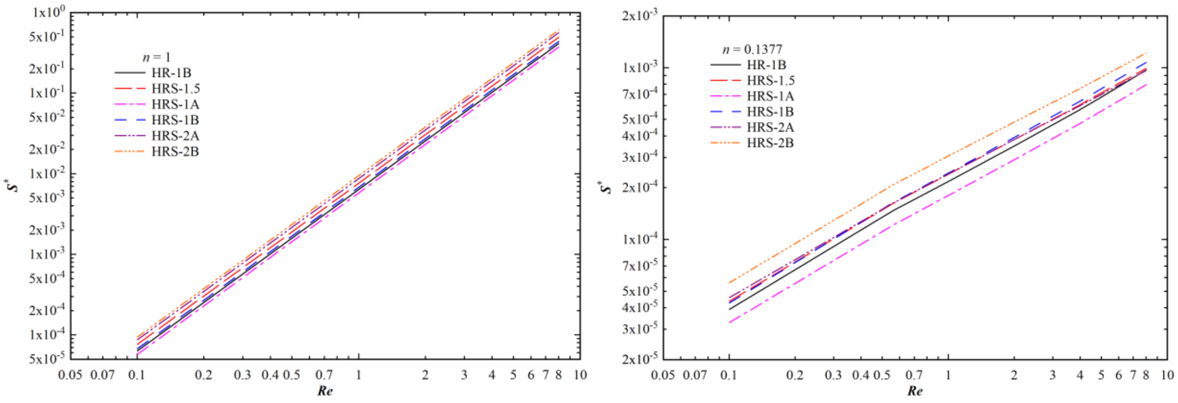

(a) (b)

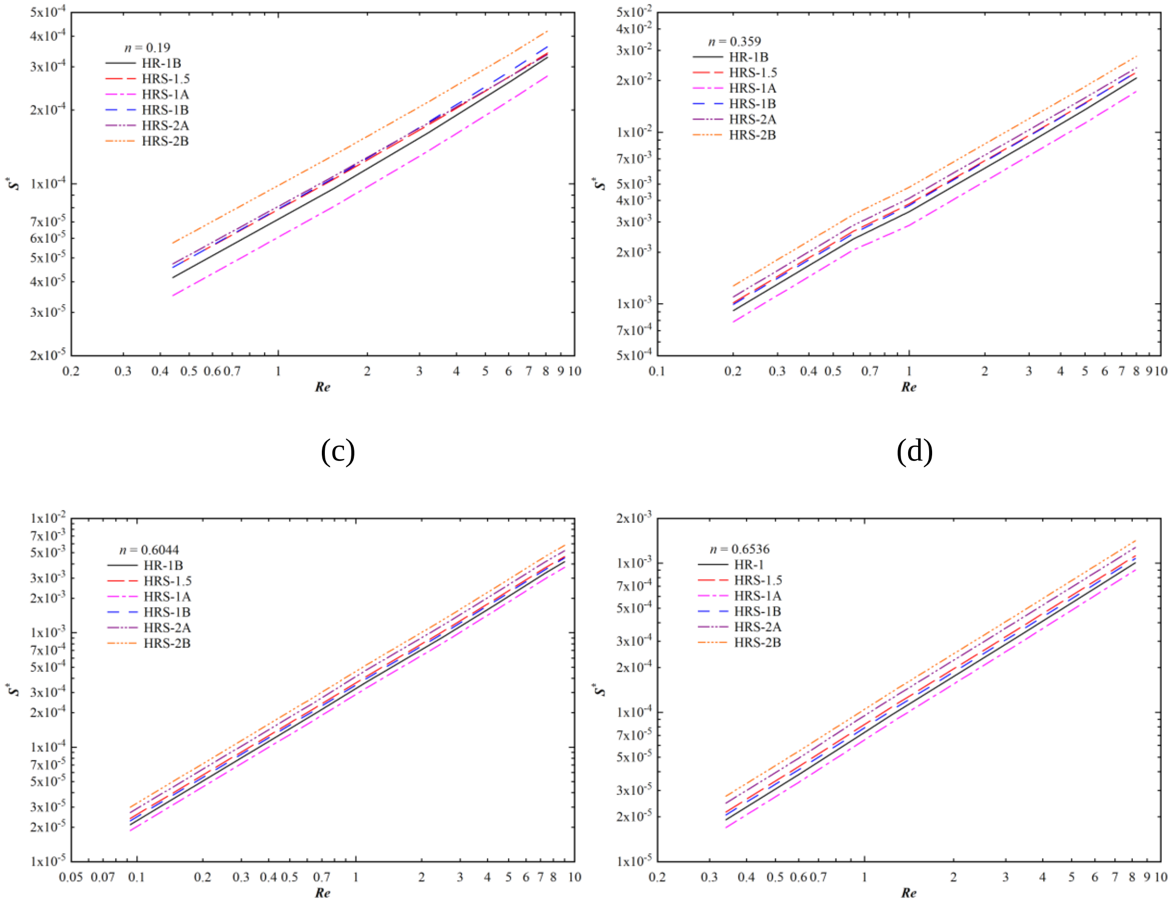

(c) (d)

(e) (f)

Figure 4.24 Distribution of entropy generation with Reynolds number for Newtonian and non-Newtonian liquids.

A careful observation of Figure 4.24 reveals that the variation of entropy generation with the impeller geometry is quite less. Neglecting the dependency on the impeller geometry, it is possible to estimate S^* as a function of *Re* and *n*. S^* and *Re* plot is linear on log-log plot. Thus, the S^*–*Re* relation can be expressed as,

$$S^* = a \cdot Re^b \qquad 4.13$$

where *a* and *b* is function of flow behavior index, *n*, and after regression analysis

$$a = -29.173n^5 + 78.078n^4 - 75.432n^3 + 31.995n^2 - 5.7012n + 0.3523 \qquad 4.14$$

$$b = -0.9426n^3 + 3.061n^2 - 0.9197n + 0.8025 \qquad 4.15$$

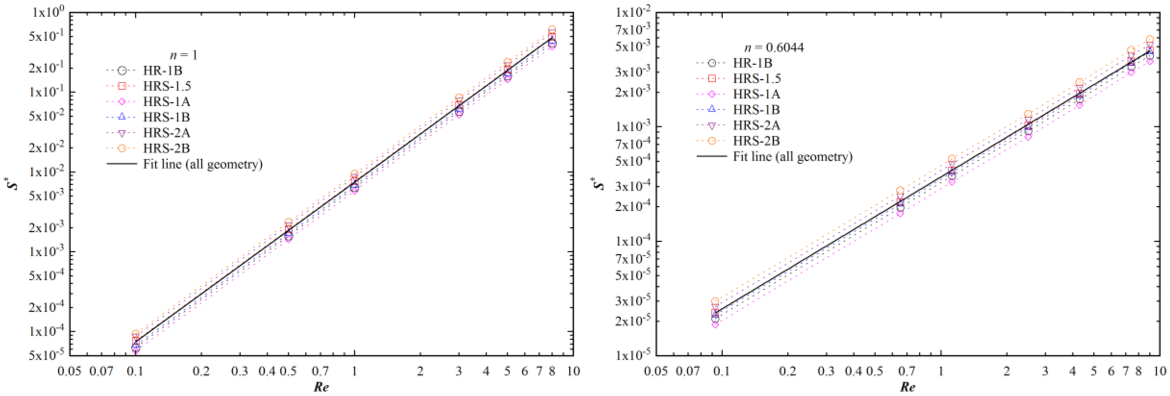

Figure 4.25 Comparison of entropy generation of Newtonian and non-Newtonian fluids with the entropy generation obtained from Equation 4.13 shown as fit line.

The numerically computed S^* are compared in Figure 4.25 with the fit line generated from Equation 4.13. It shows an excellent prediction capability of Equation 4.13. Although Figure 4.25 includes the comparison of the fit line only with Newtonian and non-Newtonian fluid with $n = 0.6044$, the other fluids entropy generation data also can be predicted well by Equation 4.13.

4.5.9 Prediction of Entropy Generation in Continuous Stirred Tank

To design a stirred tank using the entropy generation minimization (EGM) method in presence of HR and HRS impellers given in Table 4.1, the previous batch stirred tank is converted to the continuous stirred tank by adding an inlet and outlet flow pipes to the tank. The diameter and length of the inlet and outlet pipes are taken as 0.025m and 0.03m. Two different solutions with 3% CMC (VE1) and 0.5% xanthan gum (PST1) are taken as the working fluids and the properties of the fluids are given in Table 4.6.

The purpose here is to select the best impeller geometry from the impellers listed in Table 4.1 and also to find optimum inlet Reynolds number and speed of the impeller.

The numerical study consists of minimizing the total entropy generation rate in the stirred tank by varying tank parameters and keeping either constant wall temperature or constant wall heat flux as the heating source for tank's liquid. For each thermal boundary condition of the wall, the optimization of the mixing process is involved with minimizing entropy generation with respect to inlet Reynolds number (Re_i) and impeller rotations. The non-dimensional entropy generation is computed by Equation 3.36.

Table 4.6 Power law model parameters of CMC and XG

Fluids	Power law model parameters	Thermal conductivity
CMC 3% solution (VE1)	$n = 0.359$ $K = 113.8 – 1.72(T\text{-}273)$	0.7 W/m^2
XG 0.5% solution (PST1)	$n = 0.0916 + 0.003(T\text{-}273)$ $K = 5.0817 – 0.0542(T\text{-}273)$	0.7 W/m^2

4.5.9.1 Constant Wall Temperature Thermal Boundary Condition (VE1)

4.5.9.1.1 Optimization with respect to inlet Reynolds number for HR-1B

The dimensionless volumetric entropy generation in continuous stirred tank at different boundary wall temperature for 3% CMC solution (VE1) is shown in Figure 4.26. At very low Re_i, the entropy generation is found high due to large temperature gradient near the wall. The convective energy transport increases with Re_i, and it reduces the temperature gradient in the tank. Therefore, the entropy generation due to heat transfer irreversibility decreases with the increase in Re_i. But, the entropy generation due to frictional loss increases with the increase in Re_i. Hence, the total entropy generation passes through a minimum. The figure also shows that the magnitude of minimum entropy generation is higher for higher wall temperature. At high temperature, the viscosity of the liquid is less and hence, the frictional loss is also less. Therefore, the optimized Re_i increases with the wall temperature. The optimized inlet Reynolds numbers are 18, 12, and 8 for the wall temperatures 333, 323, and 313K, respectively. Due to the same temperature effect on the viscosity, the frictional entropy generation gets reduced at the higher temperature. Therefore, the rate of increase of entropy generation is higher at lower wall temperature.

Figure 4.27 shows the Bejan number, *Be*, profile with Re_i. The Bejan number is computed from Equation 3.37. *Be* is approximately equal to 1.0 for $Re_i = 1$, and it rapidly decreases as Re_i increases. Comparison of Figures 4.26 and 4.27 shows that around the entropy minimization point, the contribution of the heat transfer irreversibility is larger than the frictional irreversibility. The linear and sharp variation of *Be* at lower wall temperature occurs due to the domination of the conductive heat transfer over the convective heat transport. Having larger temperature gradients, the higher wall temperature leads to higher Bejan number.

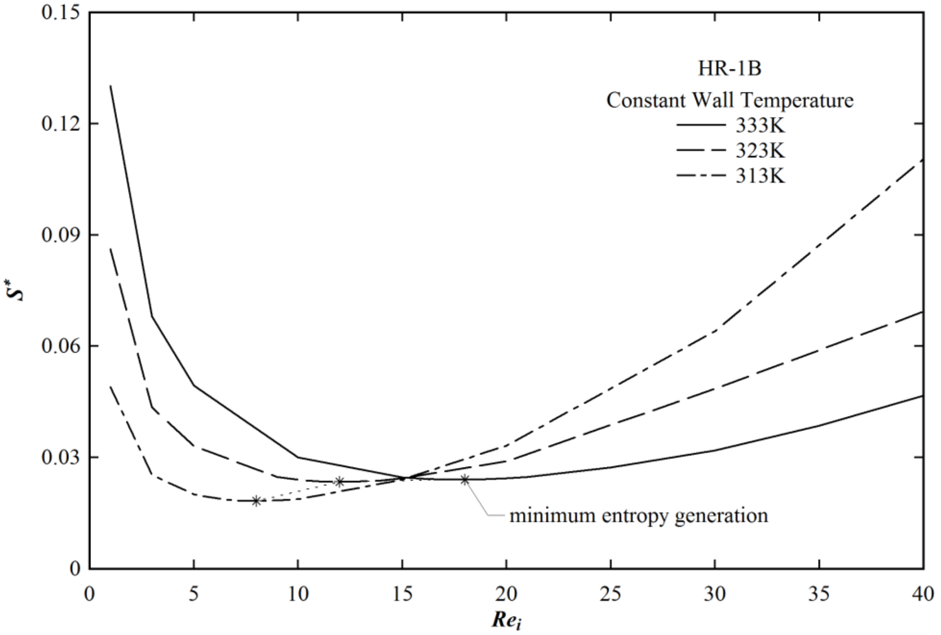

Figure 4.26 Variation of dimensionless entropy generation with inlet Reynolds number at constant wall temperature with 60 rpm of the impeller rotations. The used impeller is HR-1B and working fluid is VE1.

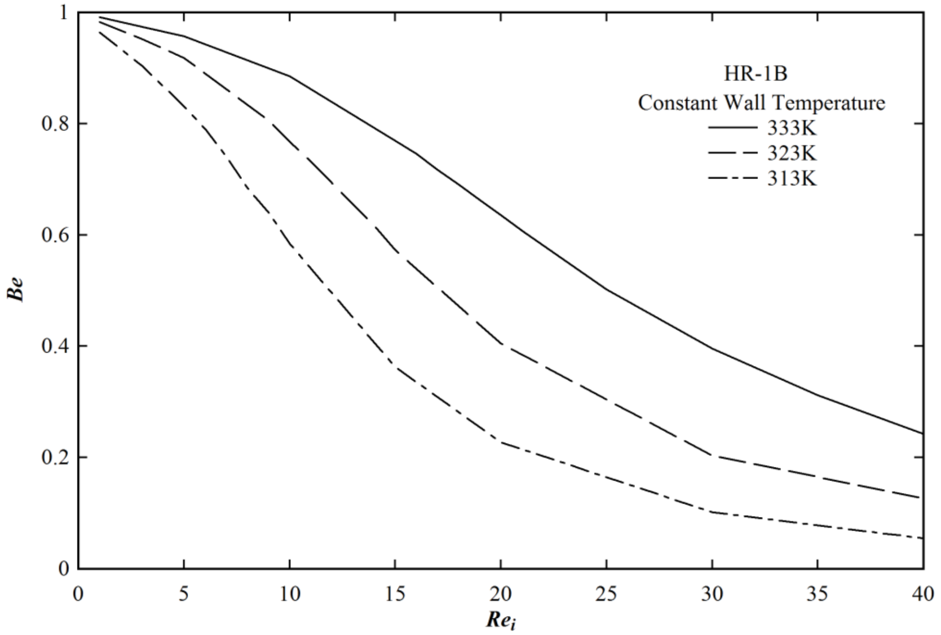

Figure 4.27 Variation of Bejan number with inlet Reynolds number at constant wall temperature with 60 rpm of the impeller rotations. The used impeller is HR-1B and working fluid is VE1.

4.5.9.1.2 Optimization with respect to impeller rotations for HR-1B

The comparison of Figures 4.26 and 4.28 reveals that the entropy generation varies more with the Re_i than the impeller rotations. It occurs due to the larger variation of the temperature gradient of fluid inside the tank with Re_i. The less dependency of entropy generation on the impeller rotations proves that the entropy generation shown in Figure 4.28 is affected mainly by the heat transfer irreversibility. The same is also observed in Figure 4.29 where *Be* is above 0.5 at all the impeller rotations. The optimum impeller rotations are 30, 21, and 15 rpm for the wall temperatures 333, 323, and 313K, respectively.

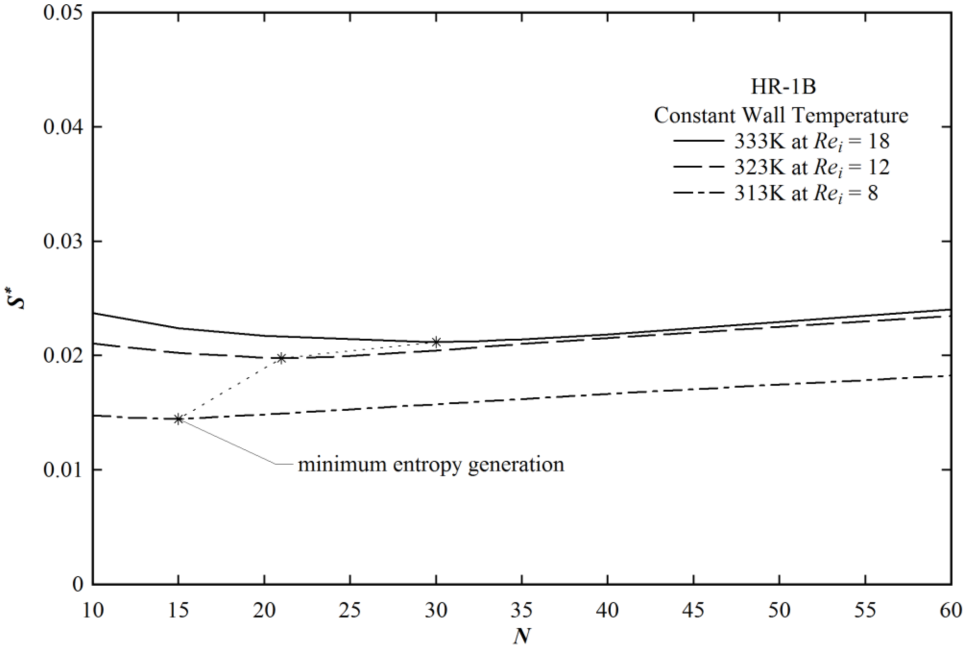

Figure 4.28 Variation of dimensionless entropy generation with impeller rotations at constant wall temperature with optimized inlet Reynolds number. The used impeller is HR-1B and working fluid is VE1.

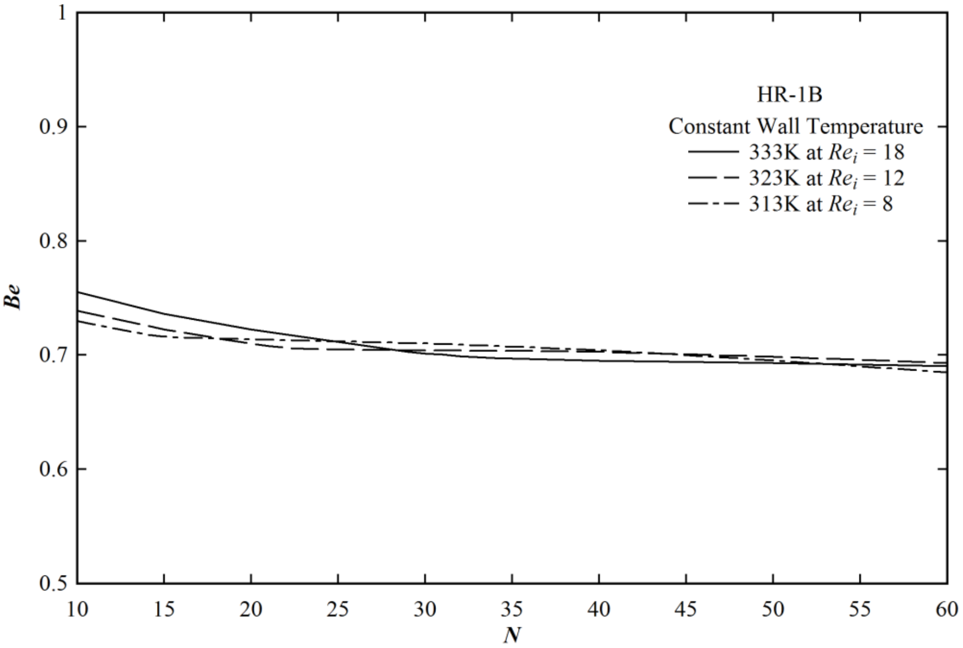

Figure 4.29 Variation of Bejan number with impeller rotations at constant wall temperature with optimized inlet Reynolds number. The used impeller is HR-1B and working fluid is VE1.

4.5.9.1.3 Optimization with respect to inlet Reynolds number for HRS-2B

Figure 4.30 shows the entropy minimization curve for the HRS-2B impeller and Figure 4.31 shows the respective Bejan number profile. The trend of the curves and physical explanations are similar to HR-1B impeller. The optimum Re_i values are 18, 13 and 8 for wall temperatures 333, 323 and 313 K, respectively. Here, also an increasing trend of Re_i with the wall temperature is observed.

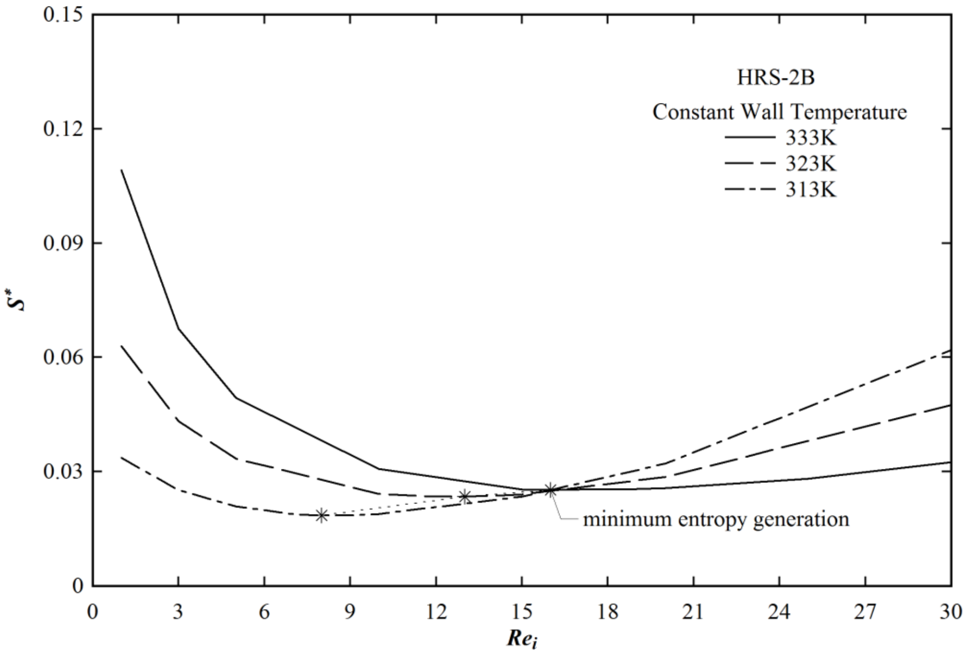

Figure 4.30 Variation of dimensionless entropy generation with inlet Reynolds number at constant wall temperature with 60 rpm of the impeller rotations. The used impeller is HRS-2B and working fluid is VE1.

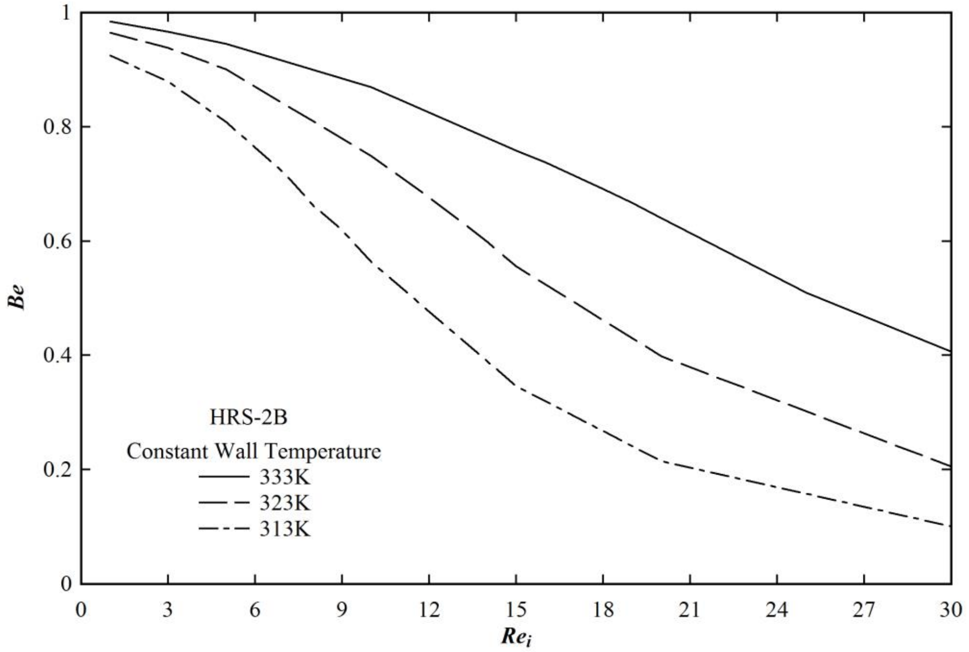

Figure 4.31 Variation of Bejan number with inlet Reynolds number at constant wall temperature with 60 rpm of the impeller rotations. The used impeller is HRS-2B and working fluid is VE1.

4.5.9.1.4 Optimization with respect to impeller rotations for HRS-2B

The entropy generation minimization of the non-isothermal stirred tank with HRS-2B impeller is carried out here. The optimized Re_i in the previous step is used. The minimization is carried out with respect to impeller speed. The wall temperature is kept constant. The optimized impeller rotations are 25, 26 and 17 for wall temperature 333, 323 and 313 K, respectively. The predicted profiles of entropy generation minimization and Bejan number shown in Figure 4.32 and 4.33 for HRS-2B are almost similar to HR-1B. The Bejan number distribution shows a little generation of entropy due to viscous dissipation over the whole range of impeller speeds.

Table 4.7 denotes the optimal tank parameters for the specified wall temperature boundary condition for VE1 fluid. The tabulated data shows a small effect of impeller geometry on the total entropy generation at the optimal point.

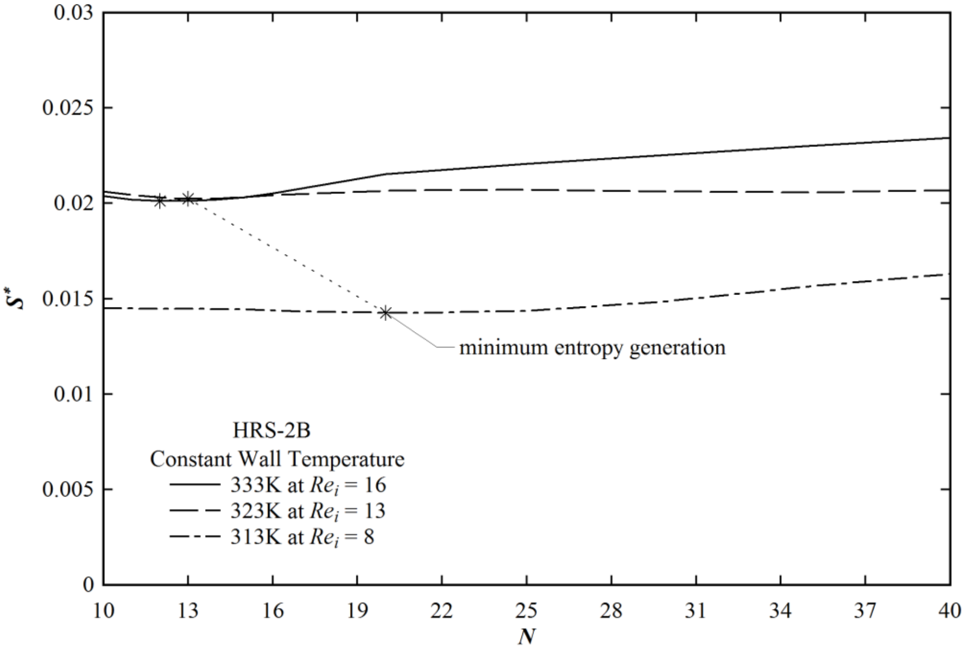

Figure 4.32 Variation of dimensionless entropy generation with impeller rotations at constant wall temperature with optimized inlet Reynolds number. The used impeller is HRS-2B and working fluid is VE1.

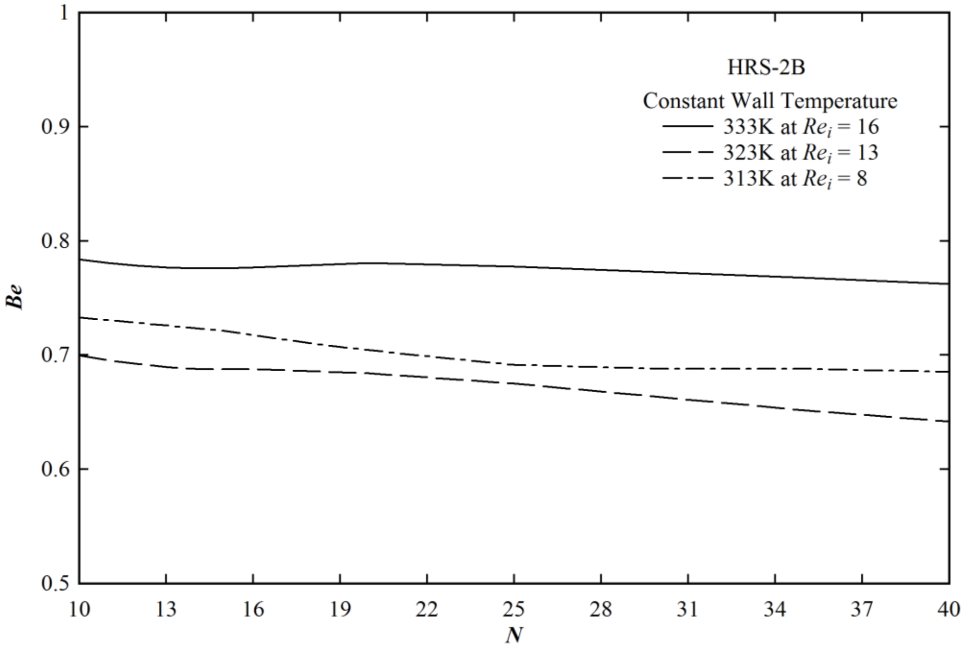

Figure 4.33 Variation of Bejan number with impeller rotations at constant wall temperature with optimized inlet Reynolds number. The used impeller is HRS-2B and working fluid is VE1.

Table 4.7 Optimal tank parameters for different impeller types at the specified wall temperature for VE1 fluid

Impeller Type	333K			323K			313K		
	Re_i	rpm	S^*	Re_i	rpm	S^*	Re_i	rpm	S^*
HR-1B	18	30	0.0212	12	21	0.0198	8	15	0.0145
HRS-1.5	18	25	0.0232	13	26	0.0209	8	17	0.0146
HRS-1A	18	52	0.0215	12	40	0.0198	8	27	0.0144
HRS-1B	19	35	0.0219	12	32	0.0194	8	21	0.0142
HRS-2A	19	34	0.0225	13	37	0.0204	9	26	0.0148
HRS-2B	16	12	0.0201	13	13	0.0202	8	20	0.0143

4.5.9.2 Constant Wall Heat Flux Boundary Condition (VE1)

4.5.9.2.1 Optimization with respect to inlet Reynolds number for HR-1B

The entropy minimization study is also carried out at the specified constant wall heat flux. The effect of inlet Reynolds number (Re_i) on the total volumetric entropy generation at specified wall heat flux is shown in Figure 4.34. Due to the higher temperature gradient, the entropy generation is found more at higher heat flux. The entropy generation decreases, reaches the minimum and further increases with the Re_i. Thus, the minimum entropy generation point is clearly observed on the curve. If Re_i is lower than the optimum, the entropy generation is significantly affected by the wall heat flux magnitude. However, if Re_i is higher than the optimum then the effect of heat flux on entropy generation is decreased, and the entropy generation becomes dependent on the fluid friction. This explanation can be drawn from the corresponding Bejan number profile given in Figure 4.35. It shows that *Be* continuously decreases with Re_i. At higher Re_i, the convective energy transport dominates over thermal conduction. Hence, the effect of wall heat flux on entropy generation becomes insignificant. The figure shows that the optimum Re_i is almost independent of wall heat flux. The calculated optimum inlet Reynolds number is 11, 11, and 9 for wall heat flux 2000, 1500 and 1000 W/m^2, respectively. It also shows that around the minimum entropy generation point, *Be* is greater than 0.5 in all the cases. Hence, the effect of heat transfer irreversibility on the total entropy generation is more than the frictional irreversibility.

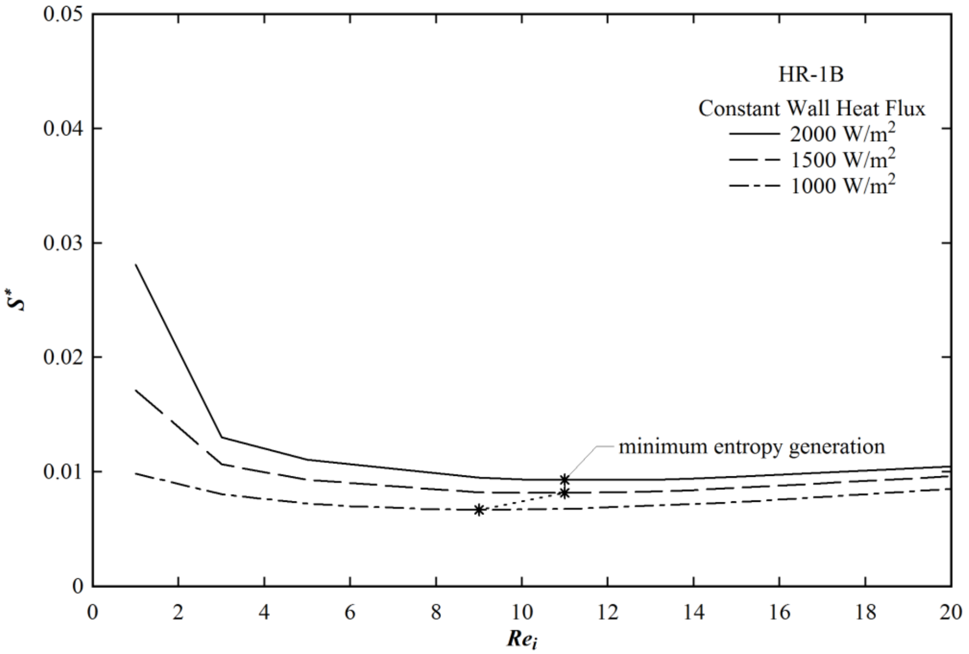

Figure 4.34 Variation of dimensionless entropy generation with inlet Reynolds number at constant wall heat flux with 60 rpm of the impeller rotations. The used impeller is HR-1B and working fluid is VE1.

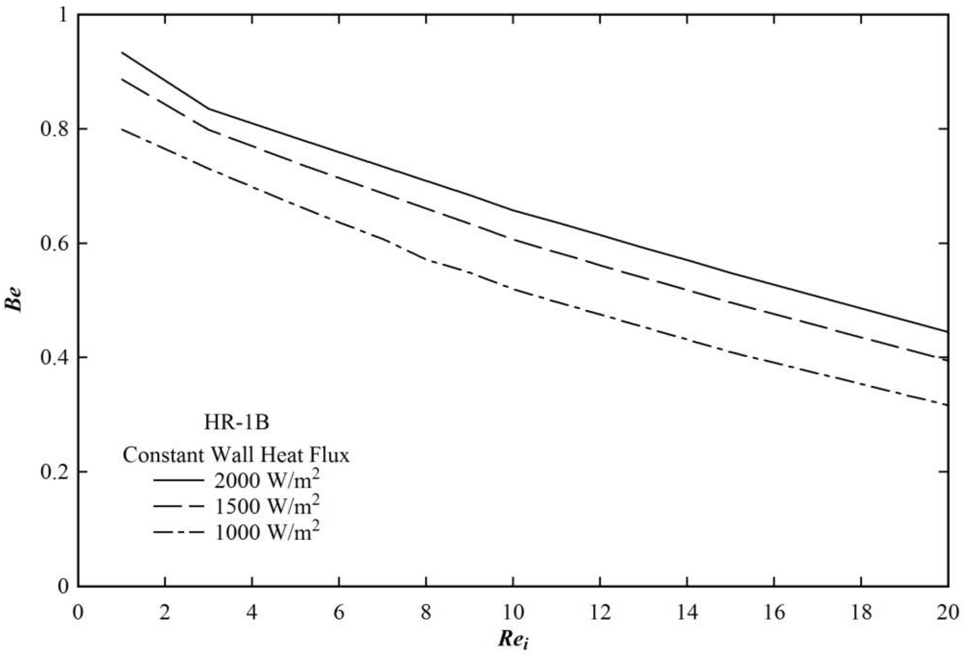

Figure 4.35 Variation of Bejan number with inlet Reynolds number at constant wall heat flux with 60 rpm of the impeller rotations. The used impeller is HR-1B and working fluid is VE1.

4.5.9.2.2 Optimization with respect to impeller rotations for HR-1B

Figure 4.36 shows the effect of the impeller rotations on the volumetric entropy generation. The minimum entropy generation is obtained at impeller rotations 34, 31, and 25 rpm for the respective wall heat fluxes of 2000, 1500 and 1000 W/m^2. The entropy generation increases with heat flux, and it leads to increase of the optimum impeller rotations with the wall heat flux. The distribution of *Be* in Figure 4.37 depicts that the contribution of thermal entropy generation gradually decreases with the impeller rotations.

4.5.9.2.3 Optimization with respect to inlet Reynolds number for HRS-2B

The same type of entropy minimization study is also carried out for HRS-2B impeller geometry with constant wall heat flux. Almost similar nature of the distribution of entropy generation and Bejan number with inlet Reynolds number are found. These are shown in Figures 4.38 and 4.39. The optimized inlet Reynolds numbers are 12, 11 and 8 for wall heat flux of 2000, 1500 and 1000, respectively. The respective Bejan number distribution shows a decreasing trend with inlet Reynolds number. It happens due to increasing domination of frictional entropy generation over the thermal entropy generation with Re_i.

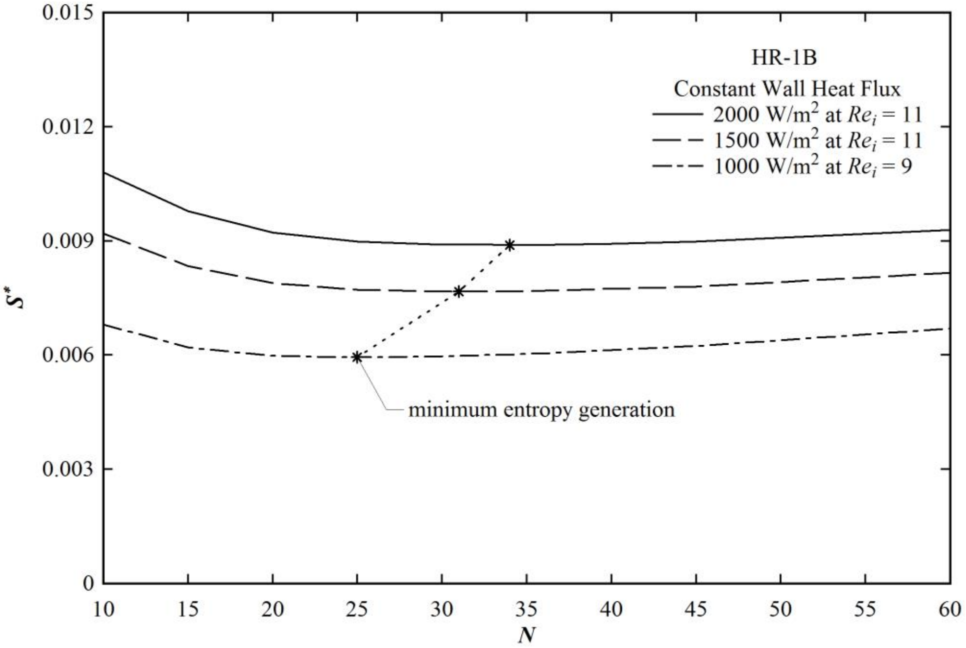

Figure 4.36 Variation of dimensionless entropy generation with impeller rotations at constant wall heat flux with optimized inlet Reynolds number. The used impeller is HR-1B and working fluid is VE1.

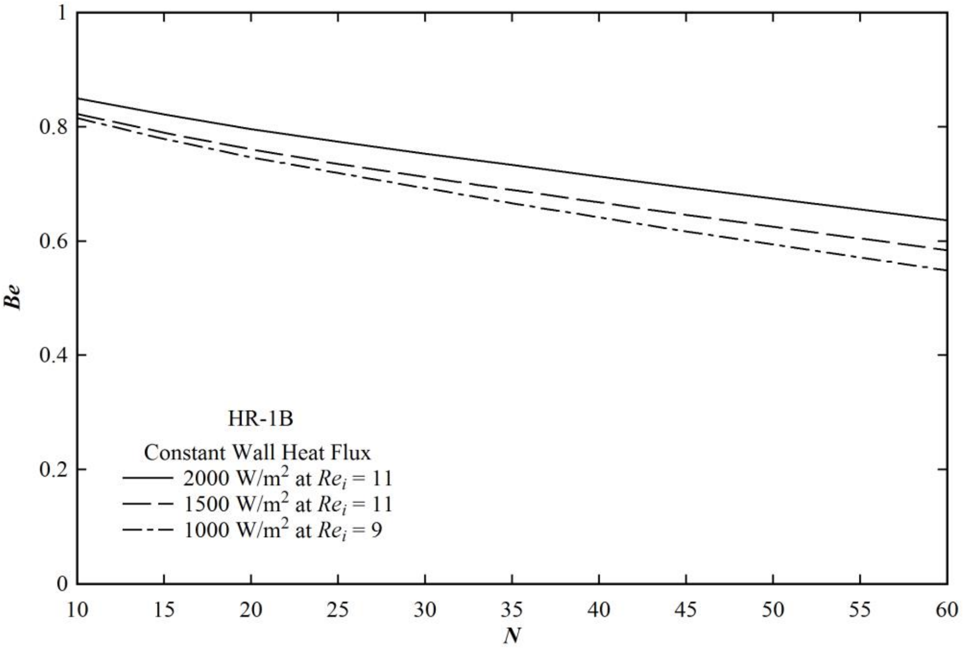

Figure 4.37 Variation of Bejan number with impeller rotations at constant wall heat flux with optimized inlet Reynolds number. The used impeller is HR-1B and working fluid is VE1.

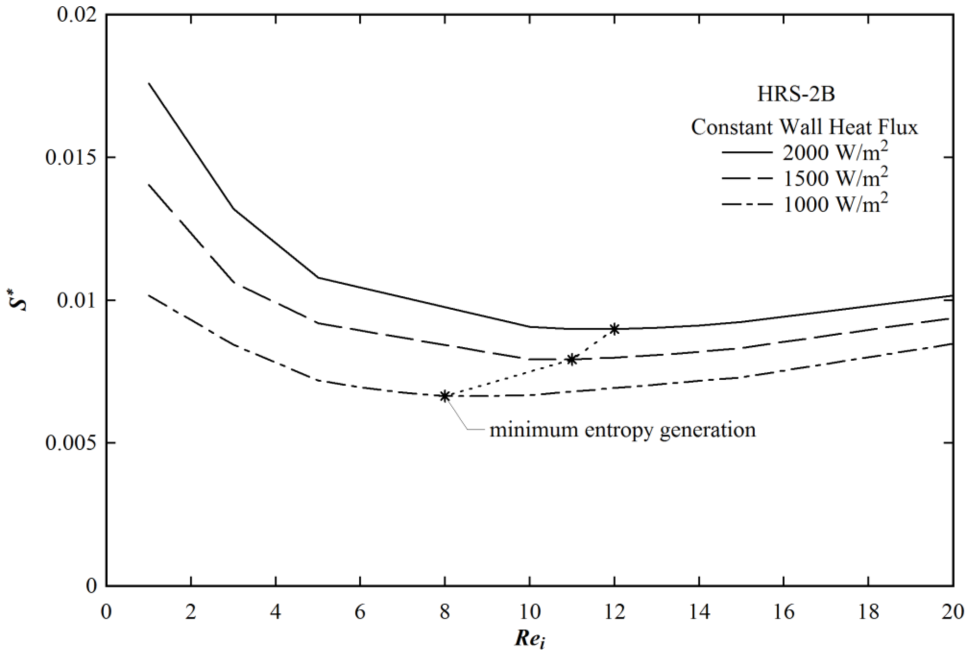

Figure 4.38 Variation of dimensionless entropy generation with inlet Reynolds number at constant wall heat flux with 60 rpm of the impeller rotations. The used impeller is HRS-2B and working fluid is VE1.

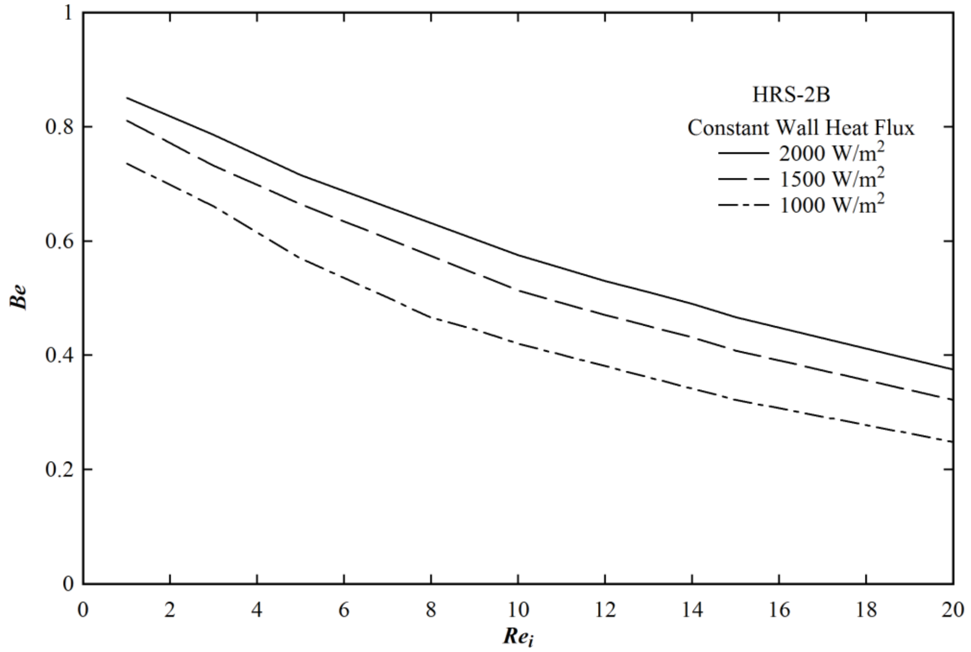

Figure 4.39 Variation of Bejan number with inlet Reynolds number at constant wall heat flux with 60 rpm of the impeller rotations. The used impeller is HRS-2B and working fluid is VE1.

4.5.9.2.4 Optimization with respect to impeller rotations for HRS-2B

The effect of impeller speed on the entropy generation and the respective Bejan number distribution plot of HRS-2B impeller with constant heat flux boundary condition is shown in Figures 4.40 and 4.41. The trends of both the curves follow the expected nature. The optimized impeller speeds are 37, 33 and 26 for 2000, 1500 and 1000 W/m^2 heat fluxes, respectively. Therefore, the optimized impeller speed increases with increasing the wall heat flux.

Table 4.8 shows the optimal inlet Reynolds number and impeller rotations for all the used impeller geometries. It depicts that the minimum entropy generations are almost independent of the impeller geometry. It also can be concluded here that the optimal values of Re_i are almost independent of the impeller geometries. While the optimal values of the impeller rotations are weak function of the impeller geometries. The impeller HRS-1A requires the maximum rotational speed of the impeller to achieve minimum entropy generation point at all specified wall heat fluxes.

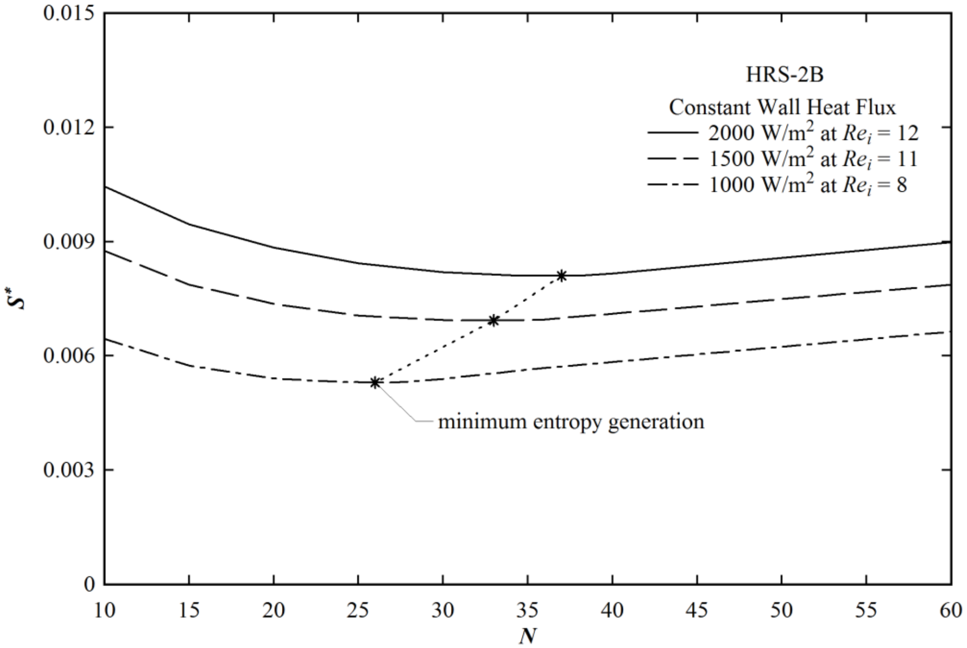

Figure 4.40 Variation of dimensionless entropy generation with impeller rotations at constant wall heat flux with optimized inlet Reynolds number. The used impeller is HRS-2B and working fluid is VE1.

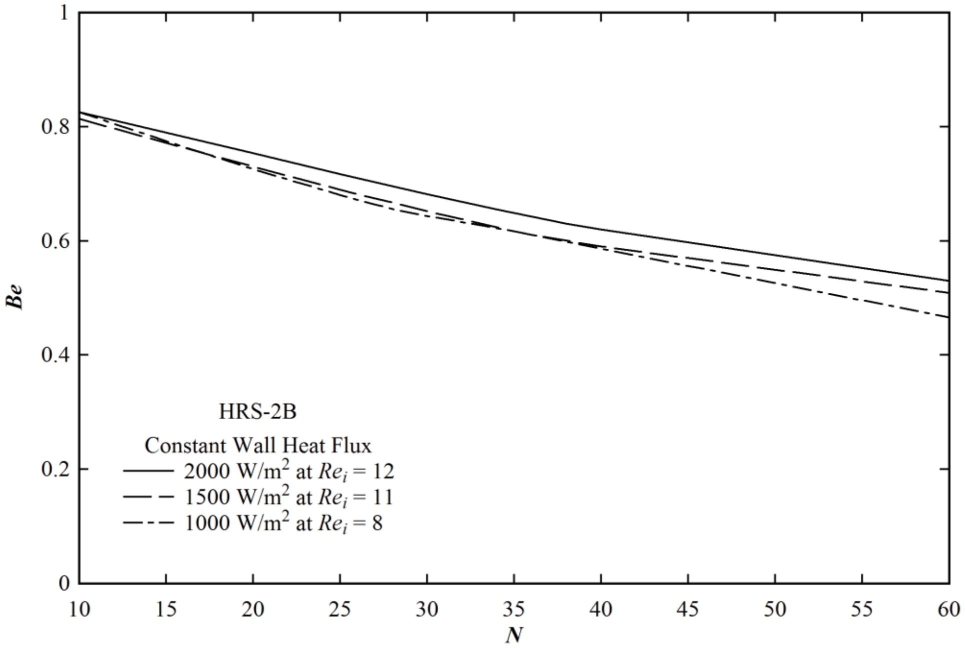

Figure 4.41 Variation of Bejan number with impeller rotations at constant wall heat flux with optimized inlet Reynolds number. The used impeller is HRS-2B and working fluid is VE1.

Table 4.8 Optimal tank parameters for different impeller types at the specified wall heat flux for VE1 fluid

Impeller Type	2000 W/m^2			1500 W/m^2			1000 W/m^2		
	Re_i	rpm	S^*	Re_i	rpm	S^*	Re_i	rpm	S^*
HR-1B	11	34	0.0089	11	31	0.0077	9	25	0.0059
HRS-1.5	13	35	0.0088	11	29	0.0074	9	24	0.0057
HRS-1A	12	45	0.0091	10	40	0.0078	9	36	0.0060
HRS-1B	12	37	0.0086	11	35	0.0075	9	30	0.0058
HRS-2A	11	39	0.0085	10	31	0.0073	8	27	0.0056
HRS-2B	12	37	0.0081	11	33	0.0069	8	26	0.0053

4.5.9.3 Constant Wall Temperature Thermal Boundary Condition (PST1)

4.5.9.3.1 Optimization with respect to inlet Reynolds number for HR-1B

The dimensionless volumetric entropy generation in continuous stirred tank at the different wall temperature boundary condition for 0.5% xanthan gum solution (PST1) is shown in Figure 4.42.

The PST1 solution has the variable viscosity which is incorporated in the simulation using User Defined Function. The rotation of the impeller is considered as 300 rpm. The temperature gradient is higher at higher wall temperature. It results in the higher entropy generation. In the figure, the entropy generation minimal points are clearly observed. At high temperature, the viscosity of the liquid becomes less and hence, the frictional loss also becomes less. Therefore, the optimized Re_i increases with the wall temperature. The optimized inlet Reynolds numbers are 30, 26, and 24 for the wall temperatures 333, 323, and 313K, respectively. The respective Bejan number distribution plot in Figure 4.43 supports the increasing effect of viscous entropy generation on the total entropy generation at lower boundary wall temperatures.

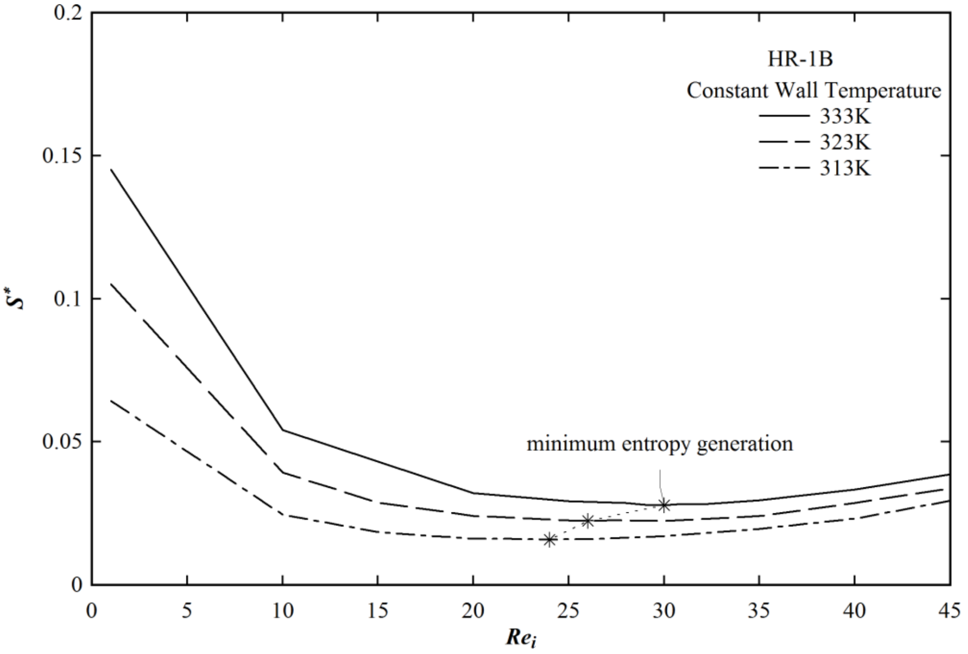

Figure 4.42 Variation of dimensionless entropy generation with inlet Reynolds number at constant wall temperature with 300 rpm of the impeller rotations. The used impeller is HR-1B and working fluid is PST1.

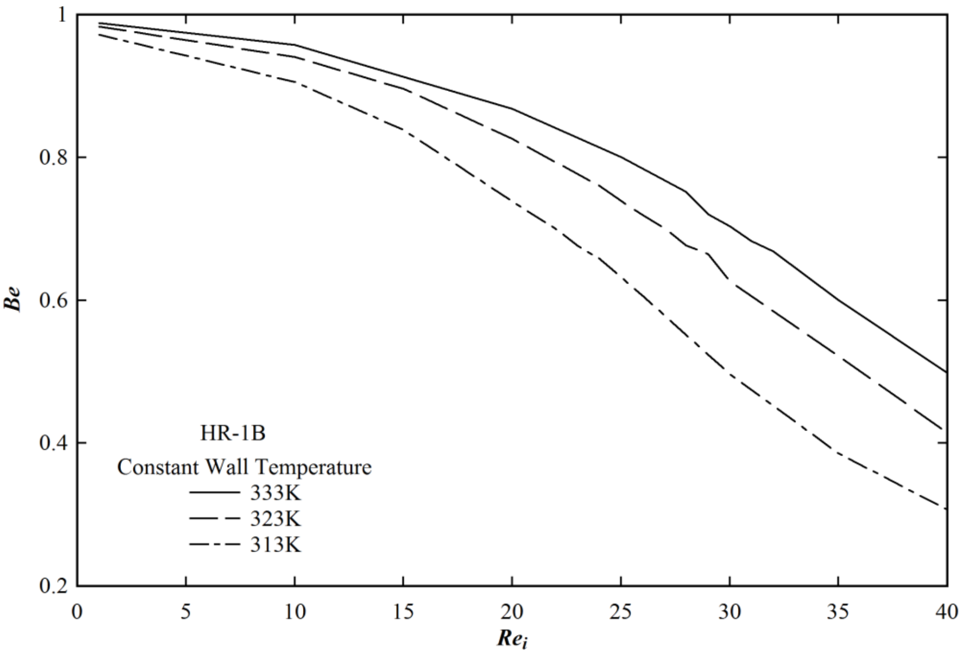

Figure 4.43 Variation of Bejan number with inlet Reynolds number at constant wall temperature with 300 rpm of the impeller rotations. The used impeller is HR-1B and working fluid is PST1.

4.5.9.3.2 Optimization with respect to impeller rotations for HR-1B

The minimization of entropy generation with impeller speed for the specified wall temperature is studied, and the performance is depicted in Figure 4.44. It shows a little effect of impeller speed on the entropy generation. The entropy generation is mostly occurring due to the thermal gradient as can be seen in Bejan number distribution plot in Figure 4.45. The optimized impeller speeds are 250, 225, and 200 rpm for the wall temperatures 333, 323, and 313K, respectively.

4.5.9.3.3 Optimization with respect to inlet Reynolds number for HRS-2B

Similar to HR-1B impeller for PST1 solution, the optimization of stirred tank mixing process with HRS-2B impeller is carried by employing the entropy generation minimization approach. The wall temperature is kept constant. The effect of inlet Reynolds number on entropy generation is shown in Figure 4.46. Like previous cases, it also show increasing trend of the optimum inlet Reynolds number with wall temperature. It is also observed in the figure that entropy generation decreases with Re_i and the total entropy generation around the optimal points are controlled by thermal entropy generation which can be confirmed by the Bejan number distributions shown in Figure 4.47.

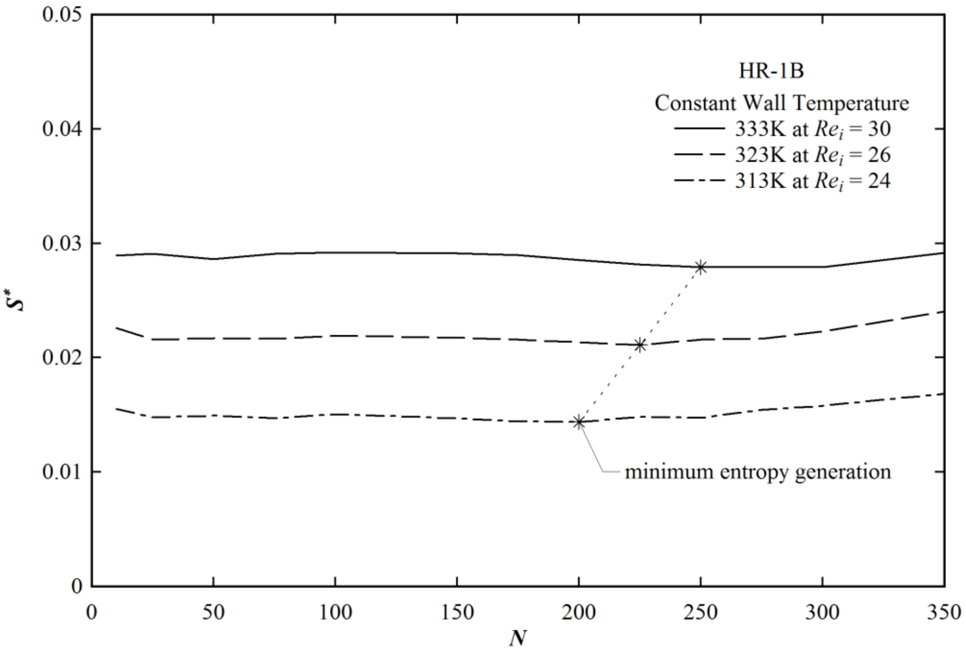

Figure 4.44 Variation of dimensionless entropy generation with impeller rotations at constant wall temperature with optimized inlet Reynolds number. The used impeller is HR-1B and working fluid is PST1.

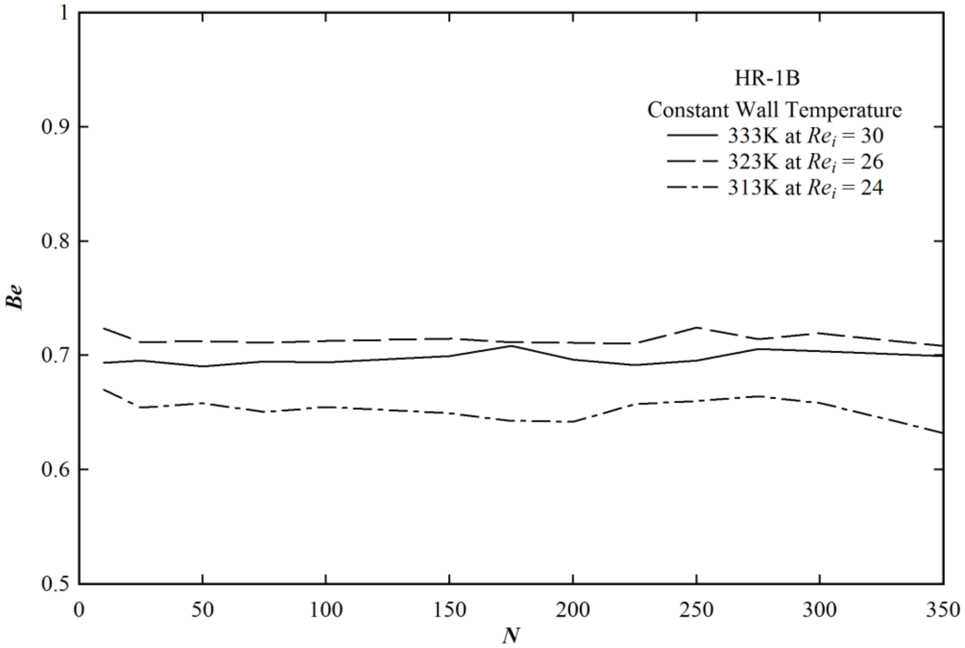

Figure 4.45 Variation of Bejan number with impeller rotations at constant wall temperature with optimized inlet Reynolds number. The used impeller is HR-1B and working fluid is PST1.

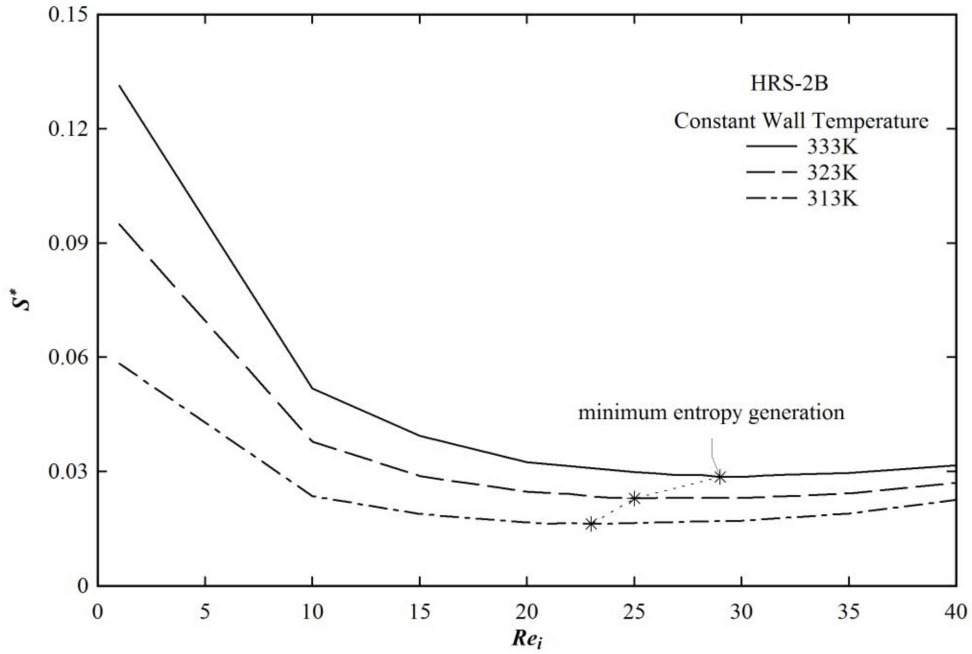

Figure 4.46 Variation of dimensionless entropy generation with inlet Reynolds number at constant wall temperature with 300 rpm of the impeller rotations. The used impeller is HRS-2B and working fluid is PST1.

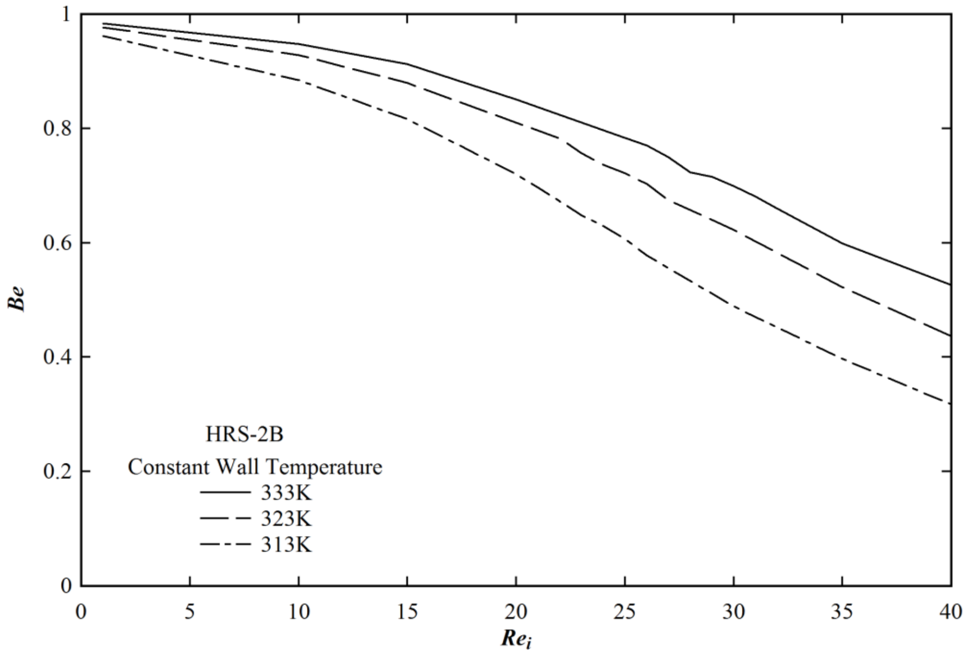

Figure 4.47 Variation of Bejan number with inlet Reynolds number at constant wall temperature with 300 rpm of the impeller rotations. The used impeller is HRS-2B and working fluid is PST1.

4.5.9.3.4 Optimization with respect to impeller rotations for HRS-2B

The stirred tank with HRS-2B impeller and PST1 as working fluid is further optimized with respect to the impeller rotational speed. The minimization of entropy generation with impeller speed is presented in Figure 4.48. It shows a little effect of impeller speed on the entropy generation. The associated Bejan number distribution shown in Figure 4.49 finds that entropy generation is mostly controlled by temperature gradients than velocity gradients.

Table 4.9 shows the optimal inlet Reynolds number and impeller rotations for all the used impeller geometries with PST1 as working fluid. It shows that the minimum entropy generations are almost independent of impeller geometry except for HRS-1A impeller. The optimal impeller speed of the HRS-1A is found very low compared to other impeller. The low value of optimal impeller speed of the HRS-1A is responsible for the very less amount of entropy production compared to other impellers. The optimal values of Re_i are found almost independent of the impeller geometries. While the optimal values of the impeller rotations are weak function of the impeller geometries. The impeller HRS-2A also requires comparatively lower optimal impeller speed. Thus, it can be concluded that the entropy production increases with increasing the impeller width.

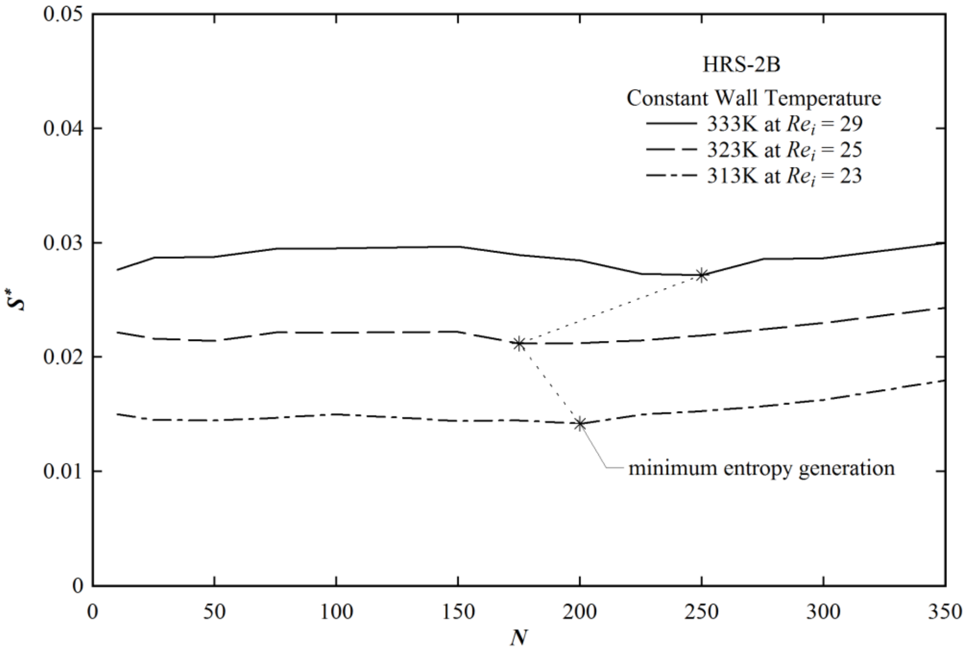

Figure 4.48 Variation of Dimensionless entropy generation with impeller rotations at constant wall temperature with optimized inlet Reynolds number. The used impeller is HRS-2B and

working fluid is PST1.

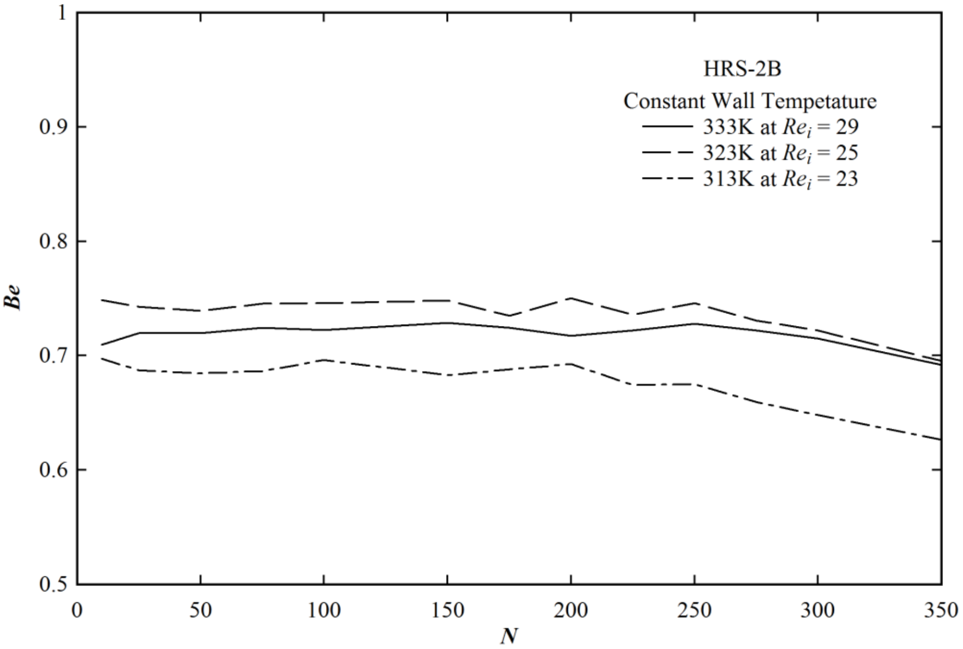

Figure 4.49 Variation of Bejan number with impeller rotations at constant wall temperature with optimized inlet Reynolds number. The used impeller is HRS-2B and working fluid is PST1.

Table 4.9 Optimal tank parameters for different impeller types at the specified wall temperature for PST1 fluid

Impeller Type	333K			323K			313K		
	Re_i	rpm	S^*	Re_i	rpm	S^*	Re_i	rpm	S^*
HR-1B	30	250	0.0279	26	225	0.0211	24	200	0.0144
HRS-1.5	29	250	0.0146	26	250	0.0210	24	225	0.0269
HRS-1A	28	50	0.0276	23	75	0.0205	24	75	0.0145
HRS-1B	29	225	0.0267	27	225	0.0208	24	200	0.0142
HRS-2A	29	250	0.0282	25	200	0.0215	23	175	0.0148
HRS-2B	29	250	0.0272	25	175	0.0212	23	200	0.0142

4.5.9.4 Constant Wall Heat Flux Boundary Condition (PST1)

4.5.9.4.1 Optimization with respect to inlet Reynolds number for HR-1B

The stirred tank mixing process with HR-1B impeller and PST1 as the working fluids is also optimized for constant wall heat flux boundary condition. Figure 4.50 shows the optimum inlet Reynolds number which increases with increasing the magnitude of the wall heat flux. The respective Bejan number distribution shown in Figure 4.51 shows a decreasing trend of thermal entropy generation with inlet Reynolds number and an increasing trend of it with increasing the wall heat flux. The figure also reveals the domination of thermal entropy generation over entropy generation due to viscous dissipation around the optimal points.

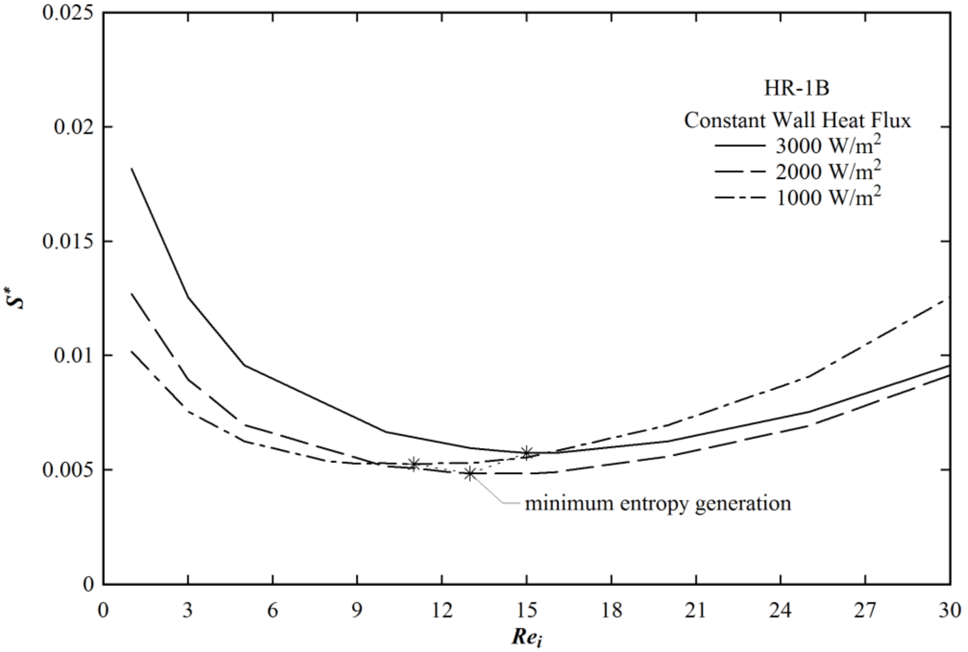

Figure 4.50 Variation of dimensionless entropy generation with inlet Reynolds number at constant wall heat flux with 300 rpm of the impeller rotations. The used impeller is HR-1B and working fluid is PST1.

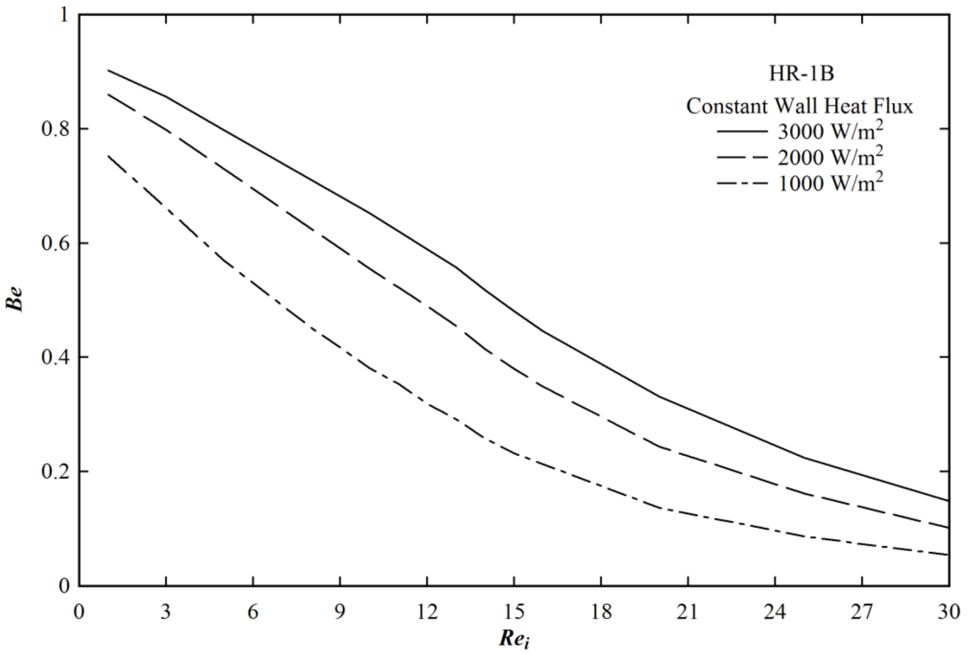

Figure 4.51 Variation of Bejan number with inlet Reynolds number at constant wall heat flux with 300 rpm of the impeller rotations. The used impeller is HR-1B and working fluid is PST1.

4.5.9.4.2 Optimization with respect to impeller rotations for HR-1B

The mixing system is further simulated to minimize the entropy generation with respect to the rotational speed of the impeller. Figure 4.52 shows the effect of impeller speed on the entropy generation at constant wall heat flux. The optimal points are clearly visible in the figure. The related Bejan number distribution with impeller rotational speed is shown in Figure 4.53. It depicts a gradual decrease of entropy generation with the impeller speed. The figure also confirms that the contribution of the thermal entropy generation is more than the entropy generation due to the viscous dissipation at the optimal points.

4.5.9.4.3 Optimization with respect to inlet Reynolds number for HRS-2B

The entropy generation minimization study of the HRS-2B impeller with PST1 liquid at constant wall heat flux is also carried out. Figure 4.54 shows the effect of inlet Reynolds number on the entropy generation. At higher wall heat flux, a sharp decrease of the entropy generation is observed. It happens due to the lager effect of Re_i on the temperature gradient at higher wall heat flux. The Bejan number distribution in Figure 4.55 shows a sharp linear decrease of Bejan number with Reynolds number. The figure also shows higher value of Bejan number at higher wall heat flux and domination of the viscous dissipation entropy generation over the thermal entropy generation around the optimal points.

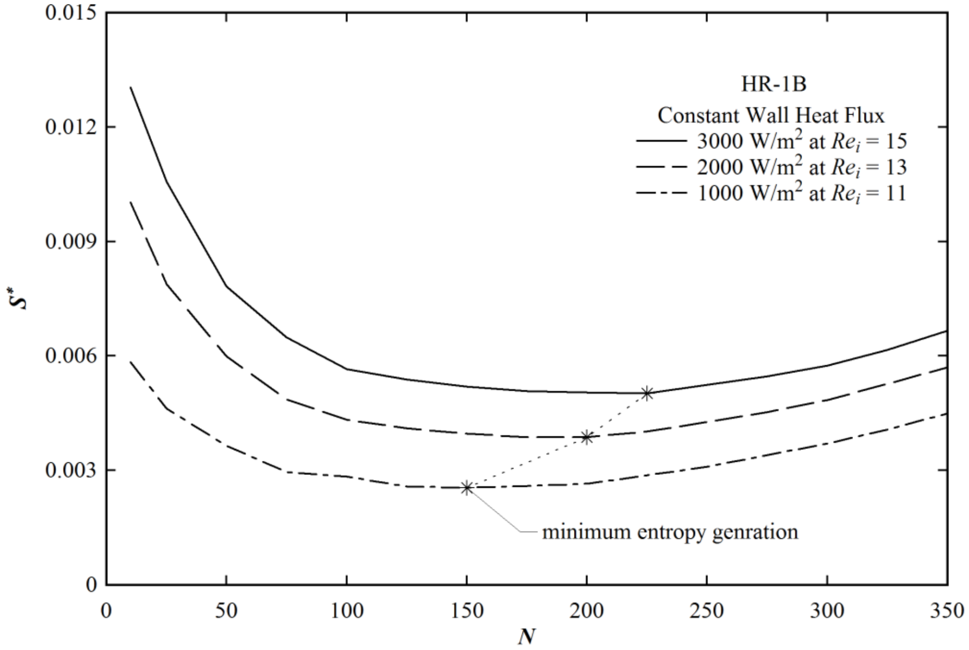

Figure 4.52 Variation of dimensionless entropy generation with impeller rotations at constant wall heat flux with optimized inlet Reynolds number. The used impeller is HR-1B and working fluid is PST1.

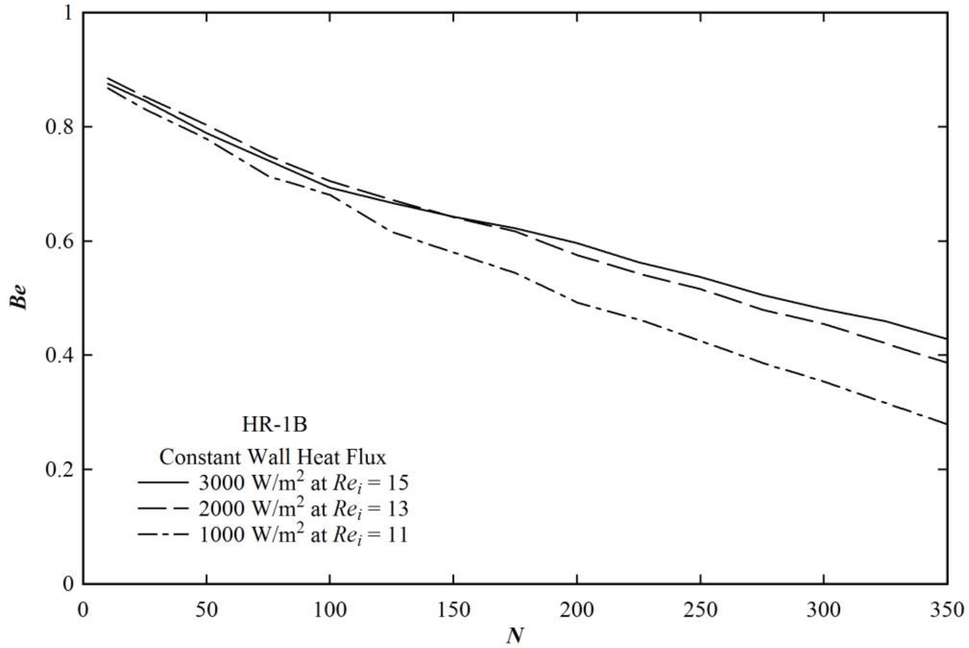

Figure 4.53 Variation of Bejan number with impeller rotations at constant wall heat flux with

optimized inlet Reynolds number. The used impeller is HR-1B and working fluid is PST1.

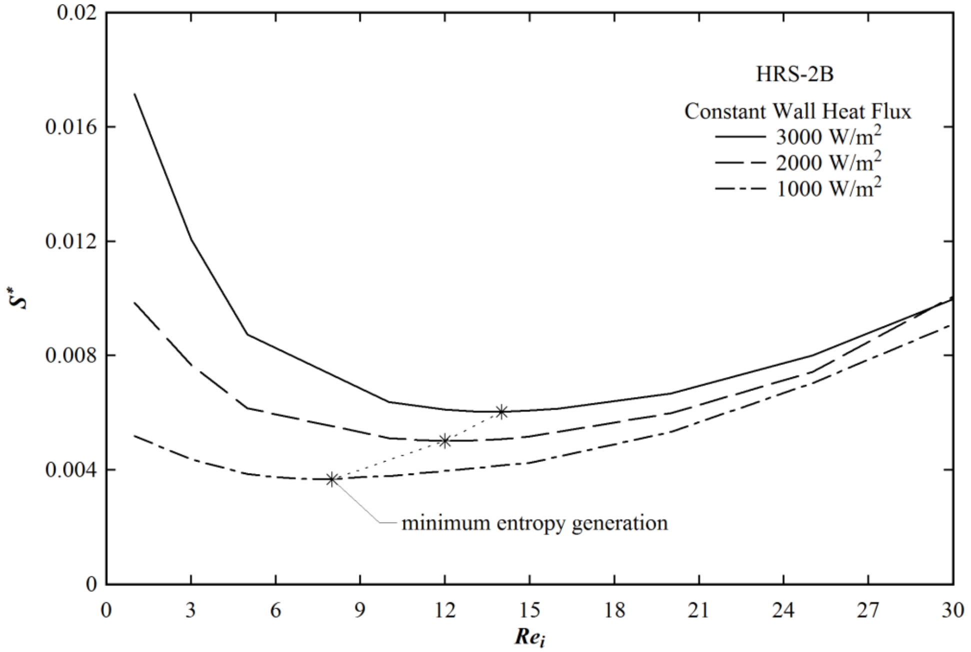

Figure 4.54 Variation of dimensionless entropy generation with inlet Reynolds number at constant wall heat flux with 300 rpm of the impeller rotations. The used impeller is HRS-2B and working fluid is PST1.

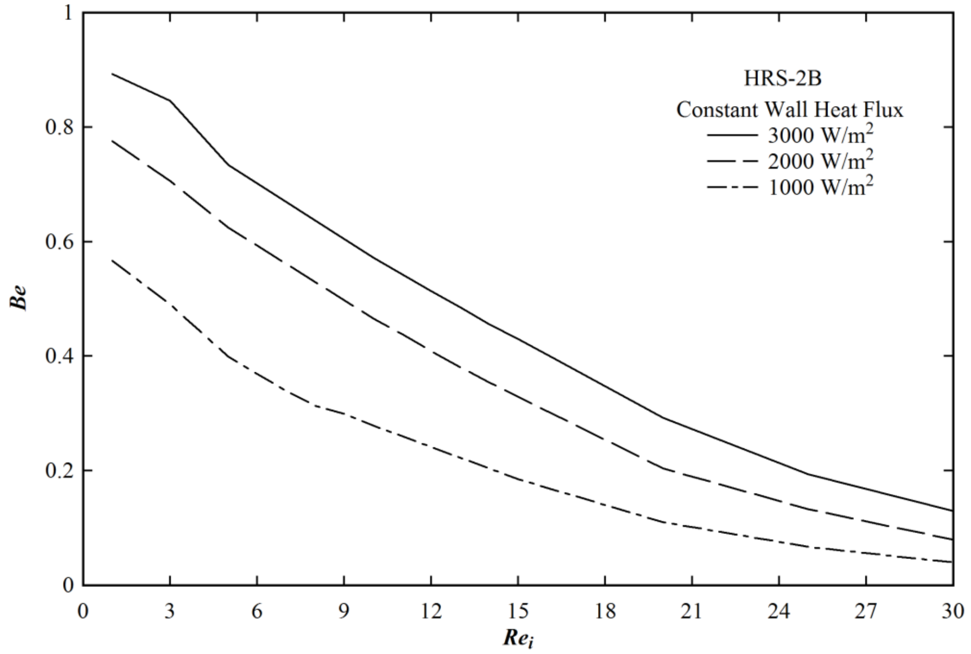

Figure 4.55 Variation of Bejan number with inlet Reynolds number at constant wall heat flux with 300 rpm of the impeller rotations. The used impeller is HRS-2B and working fluid is PST1.

4.5.9.4.4 Optimization with respect to impeller rotations for HRS-2B

After getting the optimized inlet Reynolds number, the mixing stirred tank with HRS-2B impeller and PST1 liquid is optimized with respect to impeller speed. It is illustrated in Figure 4.56. The corresponding Bejan number distribution is shown in Figure 4.57. Figure 4.56 reveals a substantial effect of impeller speed on the entropy generation and it shows clearly all the optimal points. Around the optimal point a distinct decreasing and increasing trend of entropy generation with impeller speed is observed. Figure 4.57 shows a sharp linear variation of Bejan number with the impeller speed, and it also confirms the domination thermal entropy generation at the optimal points.

The optimal tank parameters of the stirred tank for all the impeller geometries with PST1 as working fluid are given in Table 4.10. The table shows that the optimal inlet Reynolds numbers are almost independent of impeller geometry. The optimal impeller speeds are weakly dependent on the impeller geometries. Total entropy generations at the optimal points are found to be independent of the impeller geometry.

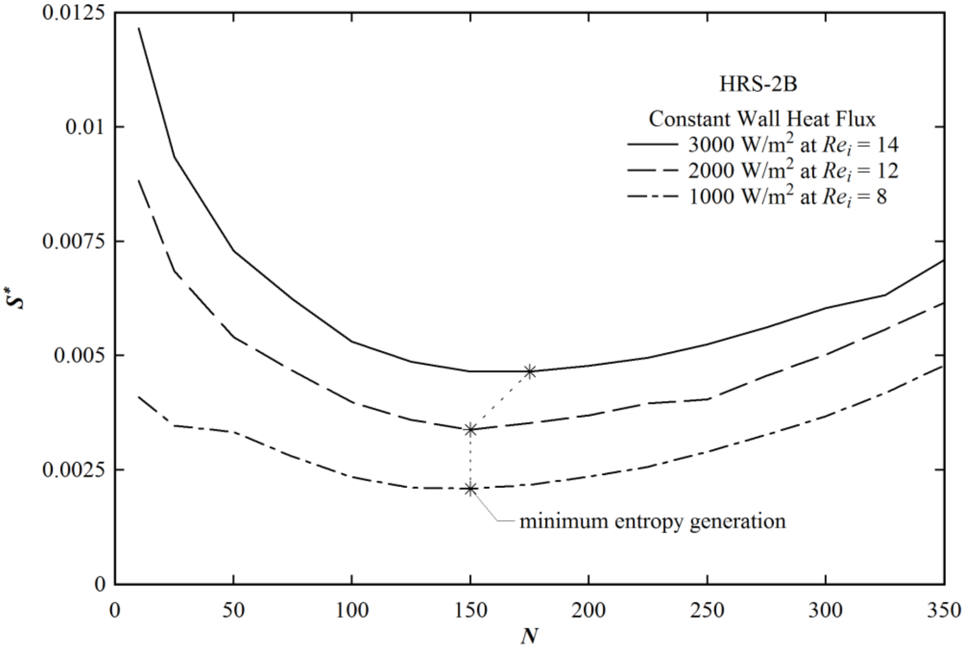

Figure 4.56 Variation of dimensionless entropy generation with impeller rotations at constant wall heat flux with optimized inlet Reynolds number. The used impeller is HRS-2B and working fluid is PST1.

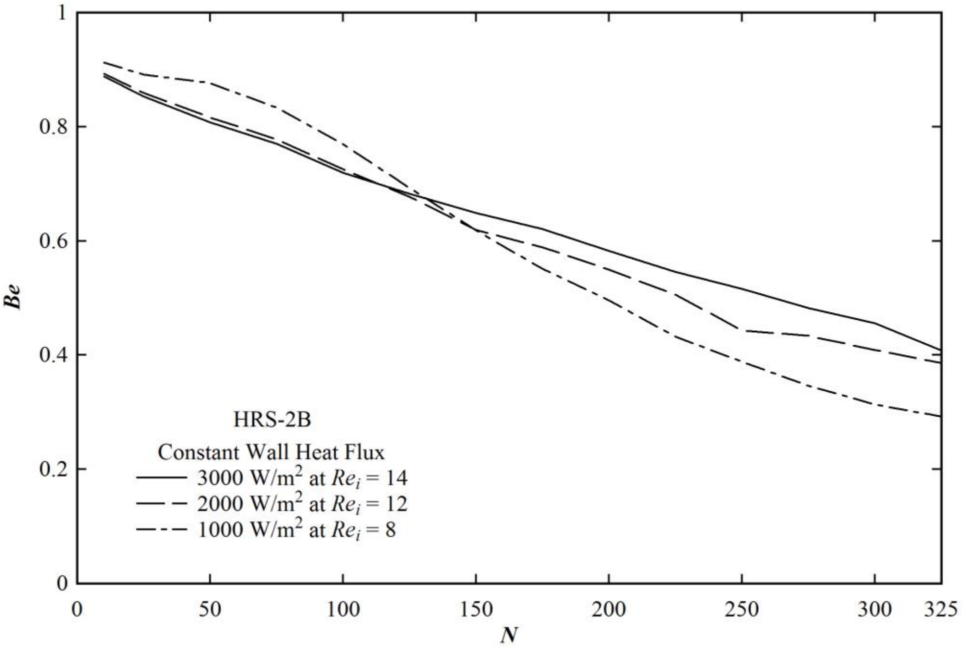

Figure 4.57 Variation of Bejan number with impeller rotations at constant wall heat flux with optimized inlet Reynolds number. The used impeller is HRS-2B and working fluid is PST1.

Table 4.10 Optimal tank parameters for different impeller types at the specified wall heat flux for PST-1 fluid

Impeller Type	3000 W/m^2			2000 W/m^2			1000 W/m^2		
	Re_i	rpm	S^*	Re_i	rpm	S^*	Re_i	rpm	S^*
HR-1B	15	225	0.0050	13	200	0.0039	11	150	0.0026
HRS-1.5	14	175	0.0049	14	175	0.0039	11	150	0.0025
HRS-1A	14	200	0.0050	13	150	0.0039	9	150	0.0024
HRS-1B	15	175	0.0048	11	175	0.0039	9	150	0.0027
HRS-2A	15	150	0.0050	12	150	0.0039	7	225	0.0027
HRS-2B	14	175	0.0047	12	150	0.0034	8	150	0.0021

The numerical study of the stirred tank with helical ribbon (HR) and helical ribbon with screw (HRS) impellers has been carried out successfully. The CFD models have been successfully validated with the experimental power number given in literature (Brito-De La Fuente et al., 1997). The power constant for Newtonian fluid (K_p) and non-Newtonian fluid ($K_p(n)$) have been calculated and compared successfully with the literature data. The Metzner-Otto or geometry constant, K_s has been computed following four different methods and best one has been found by predicting successfully the generalized power curve. The numerical study has been extended to evaluate the power number of HRS impeller in the transition zone. The flow numbers of HRS impeller also have been predicted for wide range of impeller Reynolds number. The comparative hydrodynamic behavior study of HR and HRS impellers have been studied with the help of velocity distribution curves. The mixing performance of the stirred tank with HR and HRS impeller has been studied with the help of non-dimension mixing time which varies in scattered manner with impeller Reynolds number. The mixing study also has been performed in terms of dispersive mixing efficiency, which predicts the dispersive flow away from the impeller shaft. The effects of the system parameters on the entropy generations of the batch and continuous stirred tank with HR and HRS impellers have been studied. The entropy generation has been increased with the impeller Reynolds number. An empirical model of entropy generation has been proposed as a function of impeller Reynolds number. The non-isothermal stirred tank with HR and HRS impellers have been optimized employing the entropy generation minimization (EGM) technique. The optimized design parameters have been tabulated in Tables 4.7 to 4.10.

CHAPTER 5

NUMERICAL STUDY OF RESIDENCE TIME DISTRIBUTION (RTD) OF LIQUID IN TANK WITH AND WITHOUT IMPELLER AND BAFFLES

5.1 INTRODUCTION

Mixing is an important feature for continuous reactors. The mixing performance of a stirred tank can be characterized by the residence time distribution (RTD) analysis. It gives the information on how long the various fluid elements have been in the reactor. It can also find the distribution of stagnant and mixed zones inside the tank. The knowledge of the RTD is essential for designing a non-ideal reactor (Fogler, 1999). RTD tools can also be used in successful process scale-up of chemical reactors. Many researchers carried out the experimental and theoretical works on RTD. Levenspiel and Turner (1970) studied the effect of the methods of injection and measurement of the tracer on the RTD. Choi et al. (2004) compared the experimental RTD results of the baffled stirred tank with the computational fluid dynamics predictions. Xiao-chang et al. (2009) performed the experimental and simulation analysis of RTD of a continuous stirred tubular shaped reactor using number of tee type impeller supported on a coaxial shaft. Liu (2012) used RTD tools to investigate the effect of inlet/outlet locations and flow rates, and the ratio of mean residence time to the batch mixing time on the mixing performance of the continuous stirred tank reactor.

Burghardt and Lipowska (1972) studied the effect of the inlet flow kinetic energy on the mixing behavior of the stirred tank. They also determined the condition of the ideal mixing state in presence of the impeller. Further, they used tracer injection method doing a change in the concentration of the tracer, potassium chloride (KCl), in the feed by a step input to study the RTD of the tank. Water and water-glycerine solutions were used as a working fluid. The relative density difference of the solutions caused by the content of KCl was considered to follow the following relation.

$$\frac{\Delta\rho}{\rho} = 1.7 \times 10^{-3} \qquad 5.1$$

Lipowska (1974) used an unique method based on the swept volume of the impeller and also the tracer injection method for finding experimentally the RTD of the stirred tank with water-glycerine solution. The work covered the effect of viscosity, dimensions of the tank, stirrer and the feed tube diameter on the RTD of the stirred tank.

The thorough search of the literature finds that no one has yet predicted RTD numerically by calculating the swept volume of the impeller (Lipowska, 1974). Also the excellent work of Burghardt and Lipowska (1972) are not used yet to validate the computational fluid dynamics (CFD) models. Therefore, in the present work, the tracer age distribution function is predicted by CFD tools following two methods: (i) tracer injection method and (ii) swept volume method. The predicted data is validated with the experimental RTD data of Burghardt and Lipowska (1972) and Lipowska (1974). The validated models are used to predict the effect of the tank Reynolds number, impeller rotation and viscosity of the working fluid on the fluid flow states (ideal/dispersion. The predicted CFD results are further used to compute the holdback, segregation and the number of ideal continuous stirred tank in series equivalent to single actual stirred tank.

5.2 GEOMETRY SPECIFICATION OF BURGHARDT AND LIPOWSKA (1972) AND LIPOWSKA (1974)

Figure 5.1 shows a schematic representation of a stirred tank with four baffles and a six-blade disk turbine along with a single inlet and outlet streams. The dimensions of tanks are given in Tables 5.1 and 5.2.

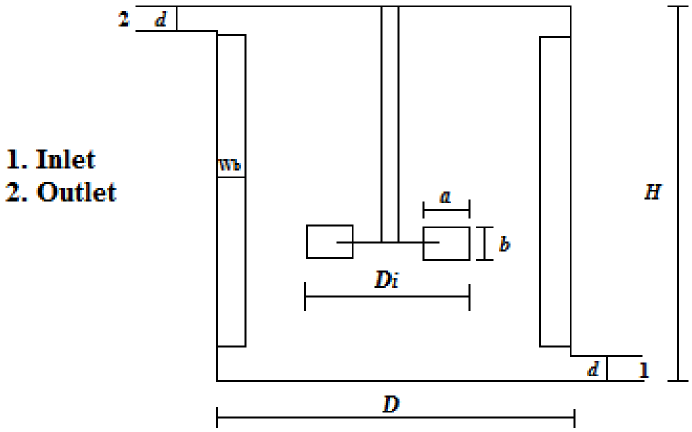

Figure 5.1 Schematic representation of stirred tank (Burghardt and Lipowska, 1972 and Lipowska, 1974).

Table 5.1 Dimensions of the stirred tank (Burghardt and Lipowska, 1972)

Parameters	*Values*
Tank diameter, *D*	0.17 m
Inlet diameter, *d*	0.0066 m
No of baffles	4
Baffles width (W_b)	$D/12$
Type of impeller	Turbine disc impeller
Ratio of impeller to the tank diameter	$(D_i/D) = 1/3$
Length of the impeller blade, *a*	$(D_i/4)$
Height of the impeller blade, *b*	$D_i/5$
Impeller clearance, C_i	D_i
Height of liquid level, *H*	*D*

Table 5.2 Dimensions of the stirred tank (Lipowska, 1974)

Parameters	*Values*
Tank diameter, *D*	0.099, 0.172, 0.250 m
Inlet diameter, *d*	0.002, 0.0072, 0.0088 m
No of baffles	4
Baffles width (W_b)	$D/12$
Type of impeller	Turbine disc impeller
Ratio of impeller to the tank diameter	$(D_i/D) = 1/3$
Length of the impeller blade, *a*	$(D_i/4)$
Height of the impeller blade, *b*	$D_i/5$
Impeller clearance, C_i	D_i
Height of liquid level, *H*	*D*

5.3 MATERIAL AND FLOW PROPERTIES

The required material and flow properties used in the present simulation study are given below.

5.3.1 Material and Flow Properties of Burghardt and Lipowska (1972)

The working fluids are water and water-glycerine solution. The flow conditions of the stirred tank and properties of the solutions are given in Tables 5.3 and 5.4. The diffusivity of KCl is taken as 1.95×10^{-9} m^2/s (Harned and Nuttall, 1949).

Table 5.3 Flow conditions of the tank without impeller and baffles (Burghardt and Lipowska, 1972)

Sr. No.	μ (cP)	ρ (kg/m^3)	V^* (l/hr)	τ (min)	Re_t	*Type of Flow*
1	1	1000	105	1.85	218.4	Ideal
2	1	1000	75	2.66	156.0	Ideal
3	1	1000	55	3.74	114.4	Ideal
4	1	1000	14.3	13.75	29.3	Ideal
5	1	1000	10	19.32	20.8	Ideal
6	1.0	1141	8	87.40	4.7	Dispersion
7	4.2	1110	20.25	10.64	11.1	Dispersion
8	6.2	1130	24.75	8.62	9.5	Dispersion
9	8	1144	41.40	5.14	12.2	Dispersion

Table 5.4 Flow conditions of the stirred tank with impeller and baffles (Burghardt and Lipowska, 1972)

Sr. No.	μ (cP)	ρ (kg/m^3)	V^* (l/hr)	τ (min)	Re_t	N(rpm)	*Type of flow*
1	11	1152	3.50	60.43	0.753	10	Dispersion
2	11	1152	3.45	63.30	0.753	20	Dispersion
3	11	1152	3.45	60.70	0.753	30	Dispersion
4	11	1152	3.45	63.91	0.753	40	Ideal
5	21	1180	4.42	53.76	0.516	12	Dispersion
6	21	1180	4.34	54.74	0.508	25	Dispersion
7	21	1180	4.46	53.27	0.520	50	Dispersion
8	21	1180	4.35	54.64	0.508	70	Ideal
9	43	1200	13.95	16.12	0.788	25	Dispersion
10	43	1200	12.75	16.52	0.741	50	Dispersion
11	43	1200	13.50	15.60	0.784	80	Dispersion
12	43	1200	16.80	12.54	0.974	100	Dispersion
13	43	1200	13.95	15.10	0.811	150	Ideal
14	43	1200	13.65	15.40	0.792	200	Ideal

5.3.2 Material and Flow Properties of Lipowska (1974)

The same working fluids, water and water-glycerine solution are used here. The properties of the working fluid and operating conditions of the tank both in absence and in the presence of the impellers and baffles are given in Tables 5.5 and 5.6.

Table 5.5 Flow conditions of the tank without impellers and baffles (Lipowska, 1974)

Sr. No.	*D* (m)	*d* (m)	μ (cP)	ρ (kg/m^3)	V^* (l/hr)	τ (min)	*Type of Flow*
1	0.099	0.002	1	1000	0.621	72.6	Dispersion
2	0.099	0.002	1	1000	1.028	44.86	Dispersion
3	0.099	0.002	1	1000	1.563	29.33	Dispersion
4	0.099	0.002	1	1000	1.922	24.84	Ideal
5	0.250	0.002	7.75	1141	12.82	57.44	Dispersion
6	0.250	0.002	7.75	1141	12.30	61.07	Dispersion
7	0.250	0.002	7.75	1141	17.42	42.27	Ideal

Table 5.6 Flow conditions of the stirred tank with impellers and baffles (Lipowska, 1974)

Sr. No.	*D* (m)	*d* (m)	μ (cP)	ρ (kg/m^3)	V^* (l/hr)	τ (min)	*N* (rpm)	*Type of Flow*
1	0.099	0.0072	9.2	1150	2.653	20.46	50	Dispersion
2	0.099	0.0072	9.2	1150	2.653	20.46	70	Dispersion
3	0.099	0.0072	9.2	1150	2.524	18.11	80	Ideal
4	0.099	0.0072	9.2	1150	2.524	18.11	90	Ideal
5	0.172	0.002	9.8	1183	12.24	19.58	20	Dispersion
6	0.172	0.002	9.8	1183	12.56	19.04	30	Dispersion
7	0.172	0.002	9.8	1183	12.56	19.04	35	Ideal
8	0.250	0.0088	19.7	1179	16.42	44.83	12	Dispersion
9	0.250	0.0088	19.7	1179	16.50	44.60	20	Dispersion
10	0.250	0.0088	19.7	1179	16.50	44.60	25	Ideal
11	0.250	0.0088	19.7	1179	16.50	44.60	40	Ideal

5.4 GOVERNING AND MATHEMATICAL EQUATIONS

For the ideal mixing of liquid only by the inlet flow energy, Equation 5.2 must be fulfilled (Burghardt and Lipowska, 1972)

$$Re_t = \frac{4V^*\rho}{\pi D\mu} \geq 13.5 \qquad 5.2$$

where Re_t is the tank Reynolds number based on the tank diameter, μ and ρ are the liquid viscosity and density respectively, $V^* = A_i u_i$ is the inlet volumetric flow rate, A_i is the inlet cross-sectional area and u_i is the inlet velocity. It can be noted that Equation 5.2 was developed for a fixed inlet (0.0066 m) and tank diameter (0.170 m). Burghardt and Lipowska (1972) have correlated the inlet Reynolds number, Re_{in} with the tank Reynolds number in Equation 5.3.

$$Re_{in} = \frac{Re_t}{d/D} = \frac{4V^*\rho}{\pi d\mu} \geq 347 \qquad 5.3$$

Lipowska (1974) extended the work of Burghardt and Lipowska (1972) to determine the dependence of Re_t and Re_{in} on the d/D ratio. The equations are given below.

$$Re_t \geq 569.1\left(\frac{d}{D}\right)^{1.09} \qquad 5.4$$

$$Re_{in} \geq 569.1\left(\frac{d}{D}\right)^{0.09} \qquad 5.5$$

Equations 5.4 and 5.5 can be used to determine the minimum inlet volumetric flow rate to obtain the ideal mixing of liquid in the tank without impeller.

The minimum rotational speed of the impeller to achieve the ideal mixing state in stirred tank can be evaluated from Equation 5.6 (Lipowska, 1974).

$$N = 2428.2\ Re_t^{-1.215}\left(\frac{d}{D}\right)^{0.088} \qquad 5.6$$

The correlations between impeller Reynolds number, Re, and tank Reynolds number, Re_t, for ideal mixing of liquid in the stirred tank is given in Equation 5.7.

$$Re = \frac{N D_i^2 \rho}{\mu} = 269.8\, Re_t^{-0.215}\left(\frac{d}{D}\right)^{0.088} \qquad 5.7$$

Lipowska (1974) developed the RTD function, $I(\theta)$ (internal age distribution function) which varies with the impeller swept volume. The mathematical expression of it is

$$I(\theta) = \exp\left[-\left(\frac{V^*}{Q}+1\right)\theta\right] \qquad 5.8$$

in which $\theta = t/\tau$, τ is the holdup time of the liquid in the tank, V^* is the inlet volumetric flow rate and Q is the impeller pumping capacity given by

$$Q = 2.3 N D_i^2 b \ \text{cm}^3/\text{sec} \qquad 5.9$$

where N is the rpm of the impeller. According to Equation 5.8, the mixing is ideal when $V^*/Q \to 0$.

In general, the expression of Q (Mishra et al., 1998) for the impeller is given as

$$Q = 2\pi \int_0^{D_i/2} \left(r v_z\right)\Big|_{z_1} dr + \pi D_i \int_{z_1}^{z_2} v_r\Big|_{D_i/2} dz \qquad 5.10$$

in which v_r and v_z are the radial and axial velocity components; z_1 and z_2 are the boundaries of the impeller swept volume in the axial direction.

In a stirred tank without impeller and baffles, the definition of Q is not valid. Hence, the tracer, KCl injection method is used for finding *I(θ)* using the following expression.

$$I(\theta) = \frac{C_0^+ - C(t)}{C_0^+ - C_0^-} \qquad 5.11$$

where the concentration of KCl in the inlet changes from C_0^- to C_0^+ at $t = 0$, and $C(t)$ is the concentration of KCl in the outlet at any time, *t*.

The present numerical computations are carried out using a laminar flow model with multiple reference frame and sliding mesh approximation. The steady state multiple reference frame (MRF) approach is used to model the interaction between the rotating impeller and baffles. The detail of the MRF approach is given in Chapter 3. The transient behavior of the stirred tank is captured by the sliding mesh approach. The general conservation of mass (Equation 3.1), momentum (Equation 3.2) and species transport (Equation 3.5) are solved to obtain the velocity and tracer distributions inside the tank.

In the mixing process for a step change of inlet tracer concentration the RTD function, $F(t)$ or $F(\theta)$ can be calculated by

$$F(t) = \frac{C(t) - C_0^-}{C_0^+ - C_0^-} \qquad 5.12$$

For the step change of tracer concentration, the relation among $I(\theta)$, $I(t)$ and $F(t)$ (Burghardt and Lipowska, 1972) is

$$I(\theta) = \tau\, I(t) = 1 - F(t) = \frac{C_0^+ - C(t)}{C_0^+ - C_0^-} \qquad 5.13$$

where the dimensionless time is, $\theta = t/\tau$ and the residence time or holdup time, τ is defined as

$$\tau = \frac{V}{V^*} \qquad 5.14$$

where V^* is the inlet volumetric flow rate and V is the reactor liquid volume.

The mean residence time, τ_m is the first moment of the residence time distribution function, $E(t)$ and computed by (Fogler, 1999)

$$\tau_m = \int_0^\infty t \cdot E(t) dt \qquad 5.15$$

The $E(t)$ is calculated from

$$E(t) = \frac{1}{C_0^+ - C_0^-} \frac{dC(t)}{dt} \qquad 5.16$$

and the variance, σ from

$$\sigma^2 = \int_0^\infty (t - \tau_m) E(t) dt \qquad 5.17$$

For understanding the relative efficiency of the real reactor over an ideal reactor, the number of the ideal stirred tank in series giving equivalent performance of the actual stirred tank can be calculated by

$$N_{CSTR} = \frac{\tau_m^2}{\sigma^2} \qquad 5.18$$

The holdback is defined as the average spending time of the fluid inside the reactor compared to the hydraulic residence time, τ . It can be defined as (Danckwerts, 1953)

$$\text{Holdback} = \frac{1}{\tau}\int_0^{\tau} F(t)dt \qquad 5.19$$

Holdback varies between 0 and 1 for piston or plug flow. For completely mixed flow state Holdback becomes *1/e.*

The efficiency of mixing in a vessel can be given by another quantity, S called “segregation”. Mathematically, it is defined as (Danckwerts, 1953)

$$S = \int_0^{\tau}\left(F_{Ideal}(t) - F(t)\right)dt \qquad 5.20$$

with

$$F_{Ideal}(t) = 1 - e^{-V^{*}t/V} = 1 - e^{-\theta} \qquad 5.21$$

where *S* varies from $+1/e$ for piston flow to -1 when most of the space in the system is a dead zone.

5.5 CFD METHODOLOGY

5.5.1 Computational Domain of Burghardt and Lipowska (1972)

The geometry of stirred tank prepared in Ansys Workbench with four baffles and an impeller with six blades is shown in Figure 5.2(a). The meshed geometry is depicted in Figure 5.2(b). The computational domain is discretized into 623089 unstructured tetrahedral mesh cells with denser mesh near the impeller to capture the high velocity gradient. The quality of the mesh depends on the skewness factor, which should be less than 0.95. In this study, the skewness of the mesh is kept as 0.889.

5.5.2 Computational Domain of Lipowska (1974)

Unstructured tetrahedral meshes with 735231, 814782 and 874273 cells are used to discretize the tanks for diameter 0.099 m, 0.172 m and 0.250 m respectively.

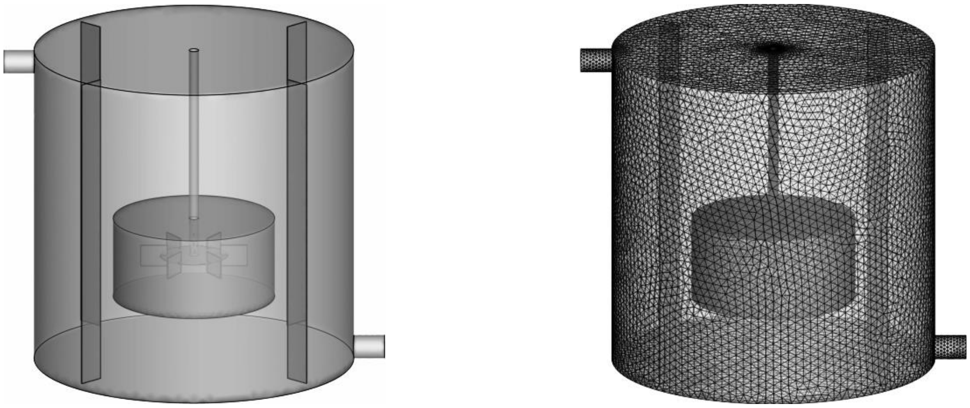
(a) (b)

Figure 5.2 (a) Computational domain of the stirred tank, (b) Meshed stirred tank.

5.5.3 Simulation Details

The equation of continuity and momentum is discretized using the finite volume method in Ansys Fluent. The convective and transient terms of the governing equations are discretized using first order upwind differencing scheme and the first order implicit scheme. No-slip boundary condition is applied on all the walls. The velocity boundary condition at the inlet and a pressure boundary condition at the outlet are used. Rotating boundary condition is specified on the impeller shaft. The working temperature and pressure of the system are 293K and 101325 Pa, respectively. The discretized Navier-Stokes equations coupled with a pressure correction equation are solved followed by solving the discretized species component balance equation using SIMPLE (Semi-Implicit Method for Pressure-Linked Equation) algorithm and Gauss-Seidel iterative method (Ansys Fluent 13: Theory Guide, 2011).

The hydrodynamics equations of the continuous stirred tank without tracer injection are solved with steady state MRF solver to attain an initial hydrodynamic condition for the transient solver. The tracer, KCl, is then introduced into the tank by a step change. The transient transport equations of the tracer along with the hydrodynamic equations are solved to find the distributions of the tracer in the tank with time. The time increment is taken as 0.001 second. All dependent variables are modified by an under relaxation method and used in the next iteration until the solutions are converged. The convergence criteria, i.e., the residual of all the discretized transport equations are satisfactorily taken equal to 10^{-3}. No further improvements in the results are found with the reduction of the residual value. Thirty iterations per time increment are found enough to achieve the converged solution at each time step. The computations are carried out using a 3.2 GHz Intel Core i5 CPU having 4 GB RAM. The computational time was about 12-13 hours.

5.6 RESULTS AND DISCUSSIONS

5.6.1 Validation of CFD Models

5.6.1.1 Prediction of the Mixing Behavior of the Tank in Absence of Impeller and Baffles Studied by Burghardt and Lipowska (1972)

The stirred tank is simulated using the parameters given in Table 5.3. Here, the residence time distribution is studied in terms of $I(\theta)$, which is calculated from Equation 5.13. The comparative presentations of the simulation and experimental results (Burghardt and Lipowska, 1972) are shown in Figures 5.3 and 5.4. Both the figures contain the ideal mixing line computed from $I(\theta) = \exp(-\theta)$ relation. Figure 5.3 shows the distribution of $I(\theta)$ for the first five sets of input data given in Table 5.3. The tank Reynolds numbers vary from 20.8 to 218.4. The working fluid has the same physical properties like viscosity and density. The figure shows that with increasing the tank Reynolds number, the RTD curves approach towards the ideal mixing line and the simulated data predicts the experimental results better. The figure also shows that the prediction is better at the early stage of the simulation. Overall the simulated data satisfactorily predict the experimental values of $I(\theta)$ given in Burghardt and Lipowska (1972). The effect of the tank Reynolds number on $I(\theta)$ is also predicted well. Figure 5.4 depicts the distributions of $I(\theta)$ for the last four input sets given in Table 5.3. In all the cases, the tank Reynolds numbers are less than 20, and each set of data consists of different viscosity and density of the working fluids. The figure depicts that the computed values are following experimental data satisfactorily. The detailed study of Figures 5.3 and 5.4 reveals that the $I(\theta)$ curve moves away from the ideal mixing line with decreasing the tank Reynolds number and increasing the viscosity of the working fluid. Therefore, the computed fluid flow tends to the dispersed flow state at lower tank Reynolds number, and it follows the experimental observation made by Burghardt and Lipowska (1972).

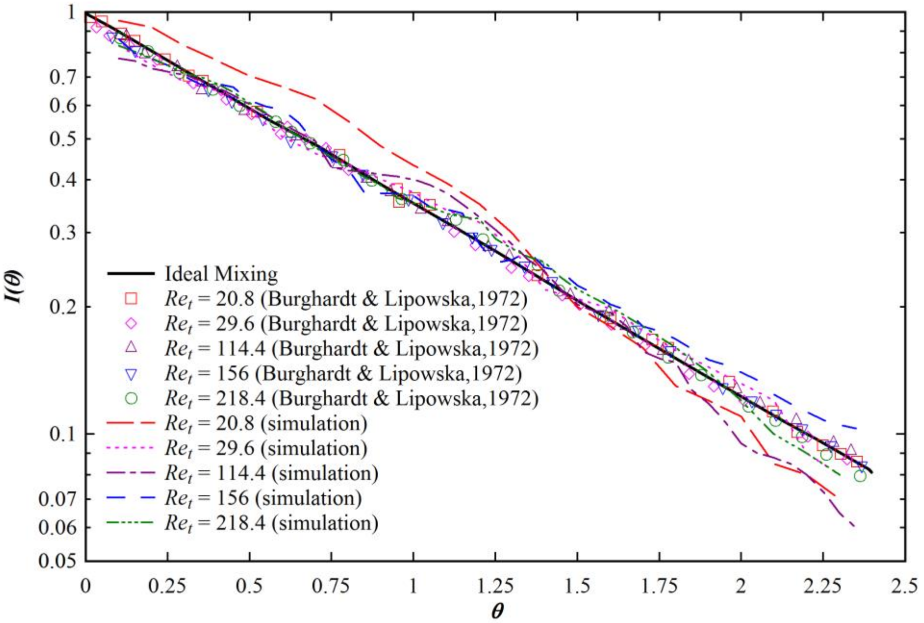

Figure 5.3 Distribution of *I(θ)* with θ of the tank without impeller and baffles. μ = 1 cP and ρ = 1000 kg/m^3. Inlet KCl concentration is 0.00177 mass fraction.

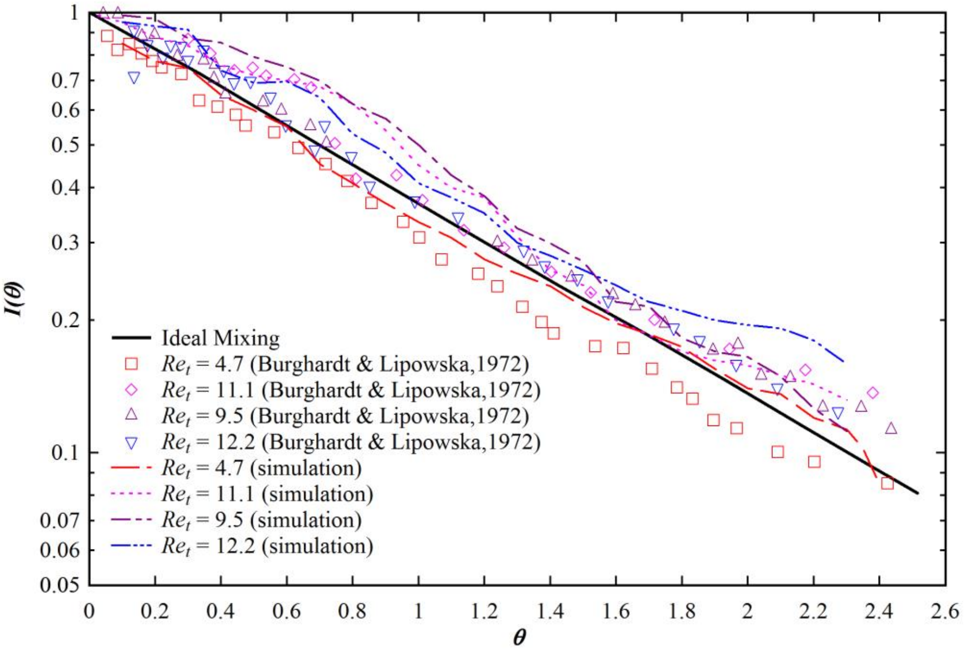

Figure 5.4 Distribution of *I(θ)* with θ of the tank without impeller and baffles, For Re_t = 4.7: μ = 1 cP and ρ = 1000 kg/m^3; For Re_t = 11.1: μ = 4.2 cP and ρ = 1110 kg/m^3; For Re_t = 9.5: μ = 6.2 cP and ρ = 1130 kg/m^3, For Re_t = *12.2*: μ = 8 cP and ρ = 1144 kg/m^3. The inlet tracer concentration is 0.00177 mass fractions.

5.6.1.2 Prediction of the Mixing Behavior of the Stirred tank in Presence of Impeller and Baffles Studied by Burghardt and Lipowska (1972)

The present work has simulated the stirred tank to predict the experimental *I(θ)* given in Burghardt and Lipowska (1972) in presence of the impeller and baffles. For given values of ρ and μ, the simulations are carried out for different inlet liquid flow rates and impeller speeds given in Table 5.4. The numerically predicted *I(θ*) are compared with the experimental data of Burghardt and Lipowska (1972) in Figure 5.5 to 5.7. All the figures depict that the computed values are in good agreement with the experimental data. Each figure finds that the computed *I(θ*) approaches the ideal mixing line with increasing the impeller rotations, *N*. It occurs due to increase of the rate of mixing with the impeller rotations. The flow behavior of the fluid inside the stirred tank changes from the dispersed state to the ideal mixing state with increasing the speed of the impeller. The visible fluid mixing state is reasonably matching with the experimental mixing state as mentioned in Table 5.4. The nature of mixing depends on the magnitude of viscosity. The tank Reynolds number decreases with increasing the viscosity. For a particular tank Reynolds number, the impeller speed should be more at higher viscosity of the stirred liquid. Therefore, the required Reynolds number, to reach the ideal mixing state, increases with increasing the viscosity of the working fluid. The results in the figures show that the required impeller speed to reach the ideal mixing state increases with the viscosity of the working fluid. The numerical analysis predicts the experimental observation about the effect of impeller speed on the fluid flow state given in Table 5.4.

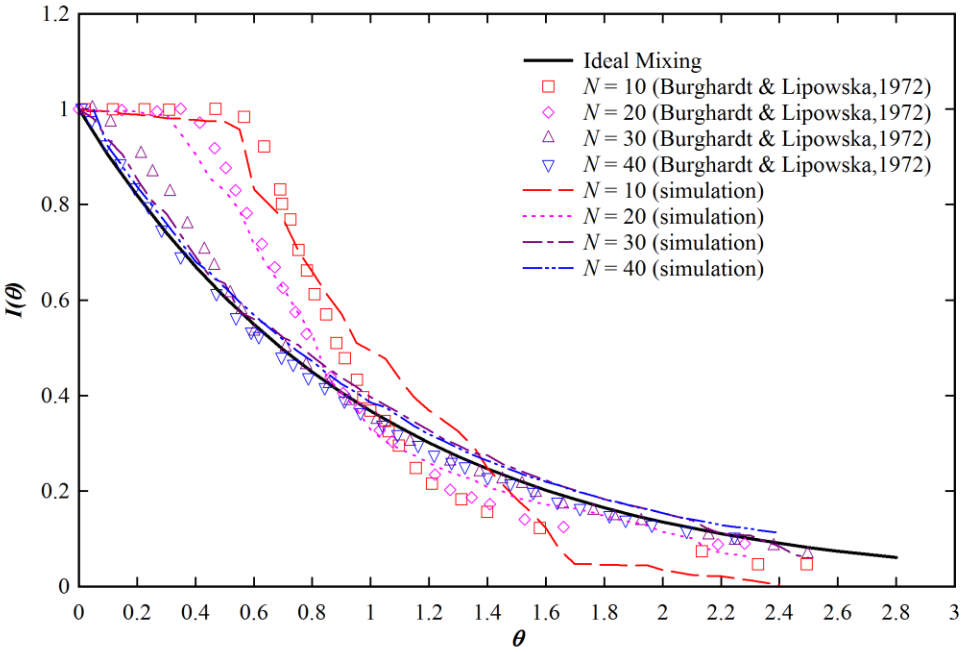

Figure 5.5 Distribution of *I(θ)* with *θ* in the stirred tank with impeller and baffles and with μ = 11 cP and ρ = 1152 kg/m^3. The inlet KCl mass fractions are, for *N* = 10 rpm, 0.00169; for *N* = 20 rpm, 0.0019173; for *N* = 30 rpm, 0.00171 and for *N* = 40 rpm, 0.00171.

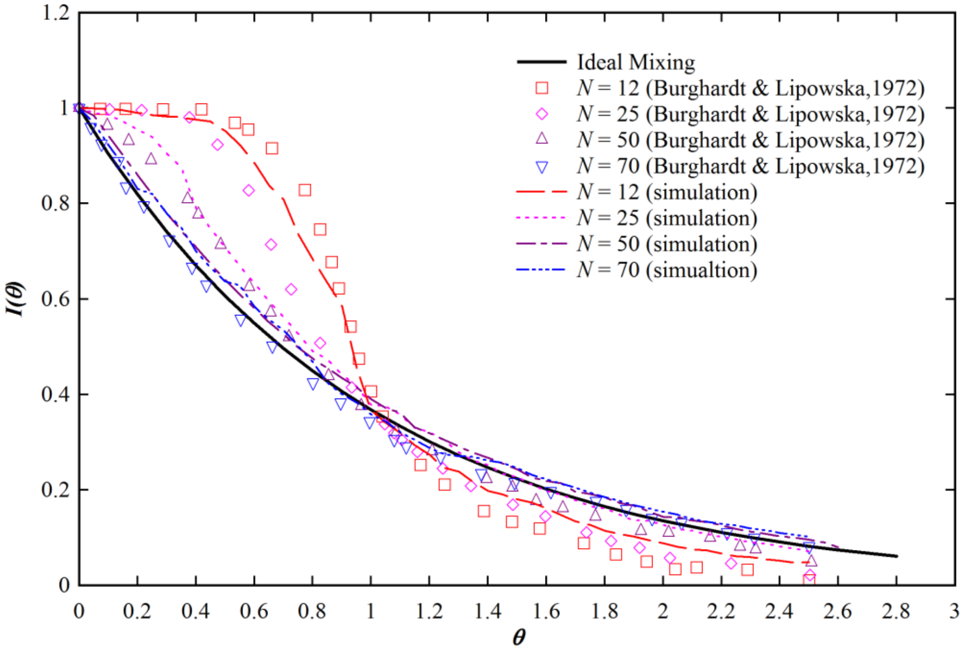

Figure 5.6 Distribution of *I(θ)* with *θ* in the stirred tank with impeller and baffles and with Re_t = 0.75, μ = 21 cP and ρ = 1180 kg/m^3. The inlet KCl mass fractions are, for *N* = 12 rpm, 0.001513; for *N* = 25 rpm, 0.00168; for *N* = 50 rpm, 0.001705 and for *N* = 70 rpm, 0.00171.

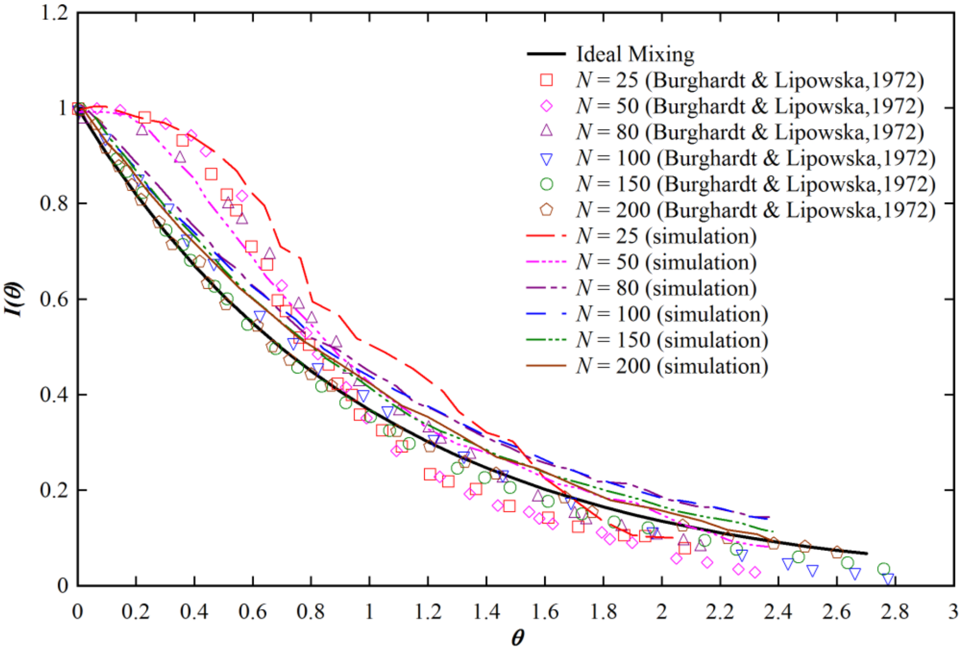

Figure 5.7 Distribution of *I(θ)* with *θ* in the stirred tank with impeller and baffles and with Re_t = 0.2, μ = 43 cP and ρ = 1200 kg/m^3. The inlet KCl mass fractions are, for *N* = 25 rpm, 0.00169; for *N* = 50, 100 and 200 rpm, 0.001664; for *N* = 80 rpm, 0.001668 and for *N* = 150 rpm, 0.001603.

5.6.1.3 Prediction of the Mixing Behavior of the Tank in Absence of Impeller and Baffles Studied by Lipowska (1974)

To predict the experimental data of Lipowska (1974) for the tank without impeller and baffles, tracer injection method is employed. The feed concentration of KCl is unavailable in Lipowska (1974) and hence, in the present study, the inlet concentration of KCl is taken in the range of 10^{-4} to 10^{-6} mass fraction. The computed values of *I(θ)* are compared with experimental data of Lipowska (1974) in Figures 5.8 and 5.9. The figures depict a satisfactory prediction of the experimental *I(θ)* by the present CFD simulations. The prediction accuracy becomes better with the tank Reynolds number. The figures also show that the flow state inside the tank is dispersion type at the lower tank Reynolds number and the computed *I(θ)* approaches the ideal mixing line at higher tank Reynolds number. The predicted fluid flow states are found in good agreement with the experimentally observed flow state given in Table 5.5.

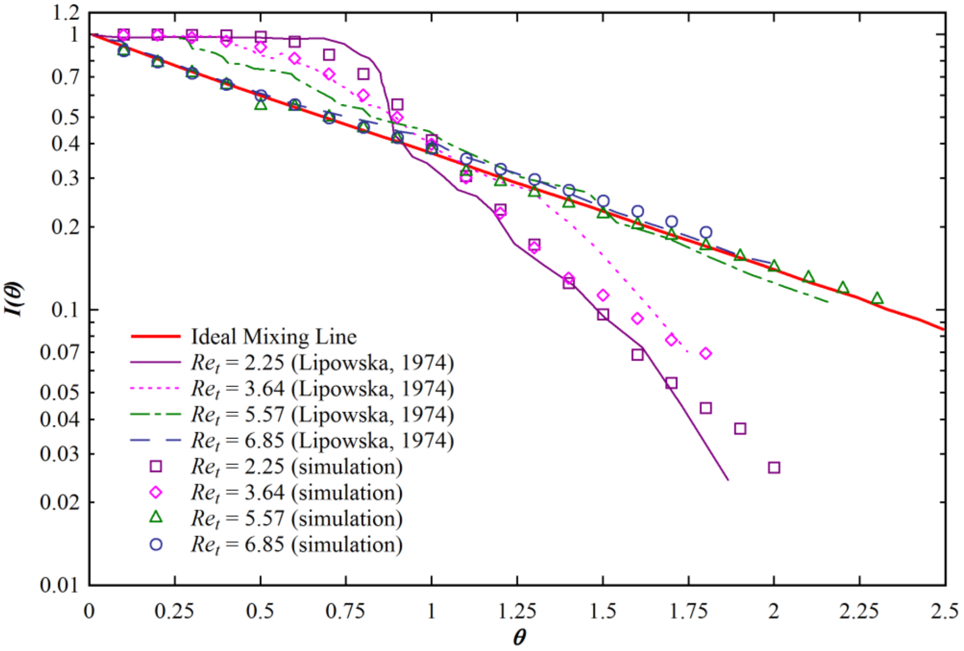

Figure 5.8 Distribution of *I(θ)* of the tank without impeller and baffles. D = 0.099 m, d = 0.002 m, μ = 1 cP and ρ = 1000 kg/m^3.

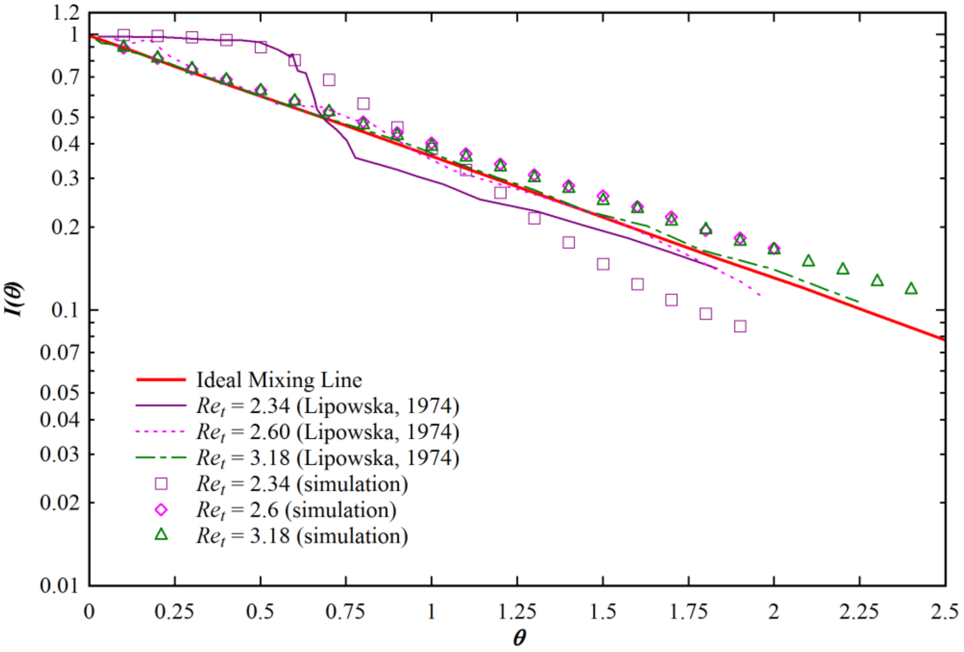

Figure 5.9 Distribution of *I(θ)* of the tank without impeller and baffles. D = 0.250 m, d = 0.0088 m, μ = 7.75 cP and ρ = 1000 kg/m^3.

5.6.1.4 Prediction of the Mixing Behavior of the Stirred tank in Presence of Impeller and Baffles Studied by Lipowska (1974)

The internal age distribution, $I(\theta)$ using Equation 5.8 is determined for finding the liquid mixing state in moving impeller case. The swept volume or impeller pumping capacity, Q, in each case, is estimated using Equation 5.10 by considering the iso-surface around the impeller. The comparative study of experimental results (Lipowska, 1974) and the present computed values for the moving impeller case are shown in Figures 5.10 to 5.12. The conditions are mentioned along each figure. Equation 5.8 shows that the value Q is constant for an impeller with fixed angular motion. Thus, V^*/Q is constant for a particular run. Therefore, theoretically, the variation of $I(\theta)$ with θ is linear. The linear variation is also observed in the present computed values as shown in the figures. The discrepancy between the experimental values and the present values is evident. But a careful observation finds that the computed values can predict the fluid mixing state perfectly as mentioned in Table 5.6. The computed $I(\theta)$ approaches the ideal mixing line with increasing the impeller rotations, N, and the plots depict that at higher values of N, the predicted results are in better agreement with the experimental data. The figures also show that at the initial moment there is a transient Q up to certain θ, and hence a relatively better agreement of computed $I(\theta)$ with the experimental data is observed at lower θ. It is also observed in the figures that the required rotation of the impeller decreases to reach the ideal mixing state with increasing the diameter of the tank.

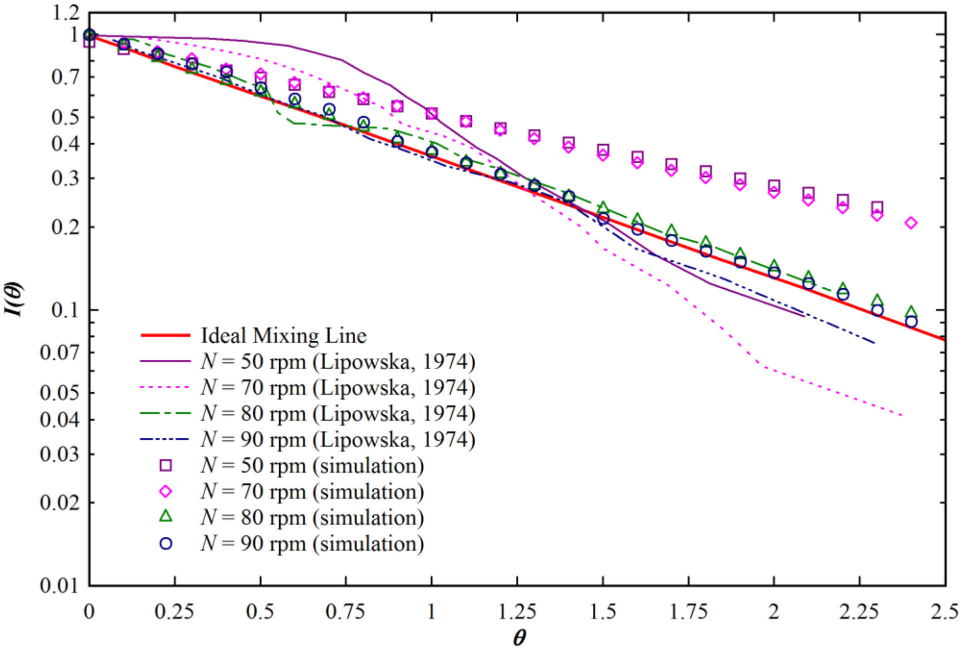

Figure 5.10 Distribution of $I(\theta)$ with θ for the stirred tank with impeller and baffles and with D = 0.099 m, d = 0.0072 m, μ = 92 cP and ρ = 1145 kg/m^3.

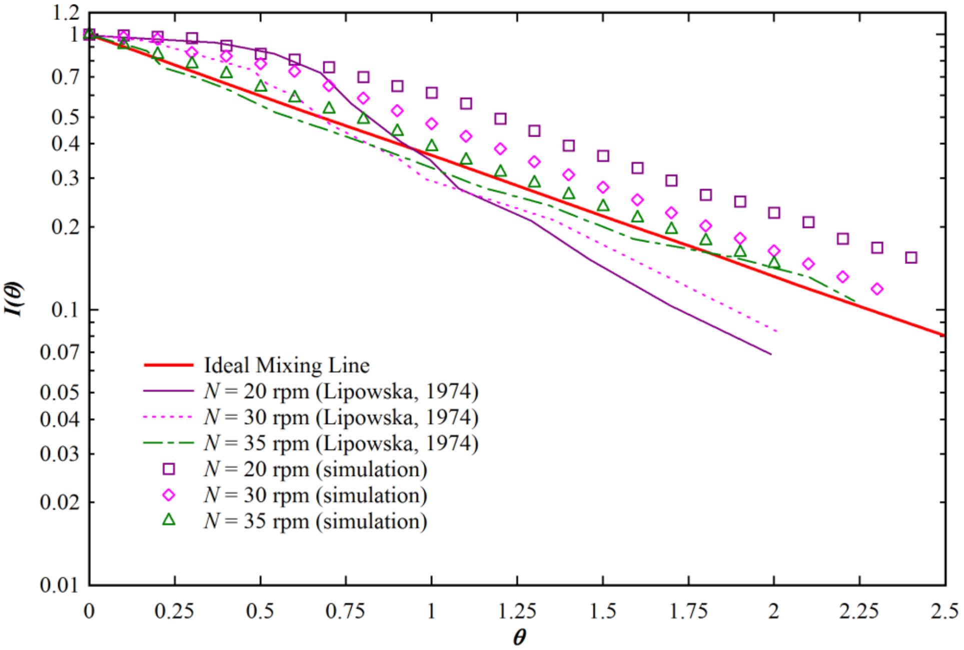

Figure 5.11 Distribution of $I(\theta)$ with θ for the stirred tank with impeller and baffles and with D = 0.172 m, d = 0.002 m, μ = 9.8 cP and ρ = 1163 kg/m^3.

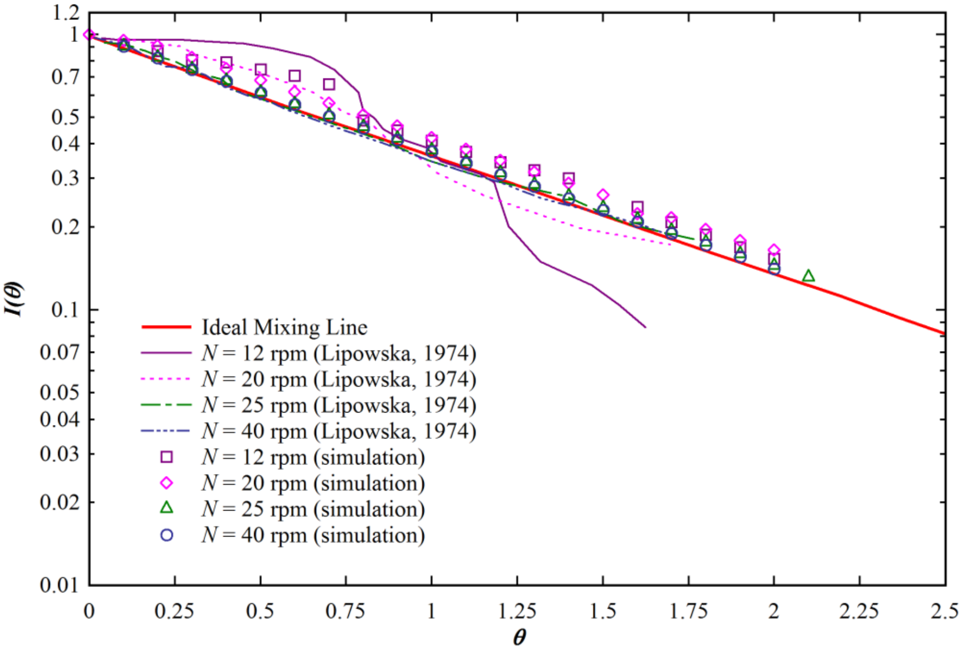

Figure 5.12 Distribution of *I(θ)* with *θ* for the stirred tank with impeller and baffles and with D = 0.250 m, d = 0.0088 m, μ = 19.7 cP and ρ = 1179 kg/m^3.

5.6.2 Analysis of the Velocity Vectors

The study of the hydrodynamics of the stirred tank in terms of the velocity profile is a very important issue to identify the fluid flow state inside the stirred tank. Figure 5.13 includes the velocity vectors for the tank without impeller and baffles (Burghardt and Lipowska, 1972). The movement of fluids inside the tank is developed due to the inlet kinetic energy of fluid. The inlet volumetric flow rates as given in Table 5.3 increase with increasing the tank Reynolds number. It is comparatively very high for Re_t = 218.4. Hence, the inlet fluid flows like a jet towards the opposite wall along which it flows up to exit finally from the tank. However, at lower Re_t, the inlet fluid moves axially up and then mix with the bulk liquid of the tank until it leaves through the outlet. This happens due to having low energy of the inlet fluid. Further reduction of Re_t results in the flow of the fluid along the wall surface connected to the inlet pipe. All the velocity vector plots in the figure represent the plug flow, i.e., ideal flow state of the fluid which validates the observation given in Table 5.3.

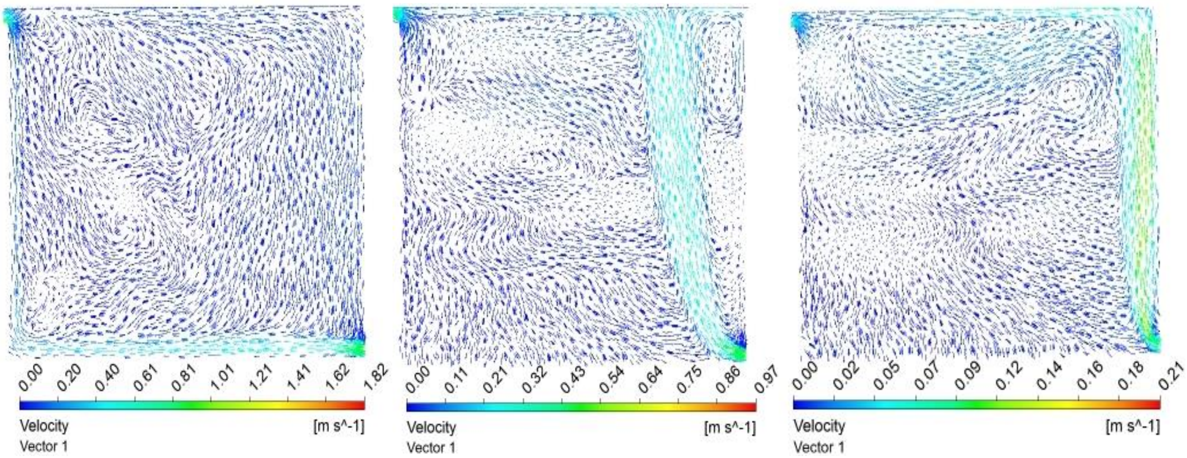

(a) Re_t = 218.4 (b) Re_t = 114.4 (c) Re_t = 20.8

Figure 5.13 Velocity vectors of the tank without impeller and baffles and with μ = 1cp and ρ = 1000 kg/m^3.

Figure 5.14 and 5.15 show the velocity distribution in the stirred tank in presence of the impeller and baffles. The tank Reynolds number in all the figures is very low. The movement of liquid inside the tank is predominantly developed by the rotational movement of the impeller. An exception is found in Figures 5.14(a) and 5.15(a) where both the inlet flow and impeller rotations equally affect the velocity distribution. At low impeller speed, the velocity near the inlet is found more than the velocity around the impeller. Thus, the velocity distribution at lower impeller speed is almost similar to the velocity distribution of the tank without impeller shown in Figure 5.13. All the figures depict a radial discharge flow by the impeller. After impacting the wall, a part of the flow goes to the bottom side and rest part moves to the top surface of the tank. These develop two circulation loops around the impeller especially at higher impeller speed. With increasing the impeller rotational speed, the size of the loops increases and the loops move towards the tank wall. It helps to reach the ideal fluid flow state at a higher impeller speed shown in Figures 5.14(c) and 5.15(c). As expected, the velocity of the liquid near the impeller increases with the speed of the impeller.

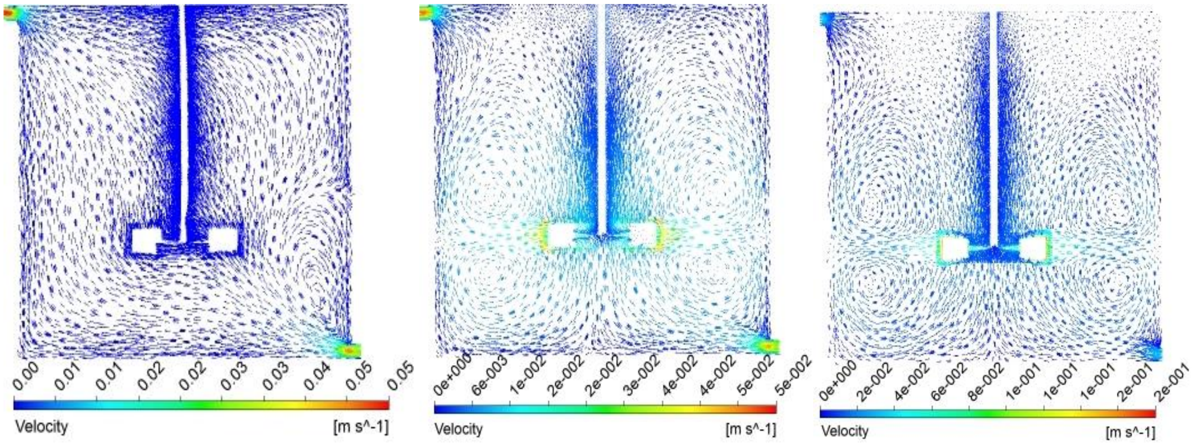

(a) N = 10 rpm (b) N = 20 rpm (c) N = 40 rpm

Figure 5.14 Velocity vectors of the stirred tank with moving impeller and with μ = 11 cP and ρ = 1152 kg/m^3, Re_t = 0.753.

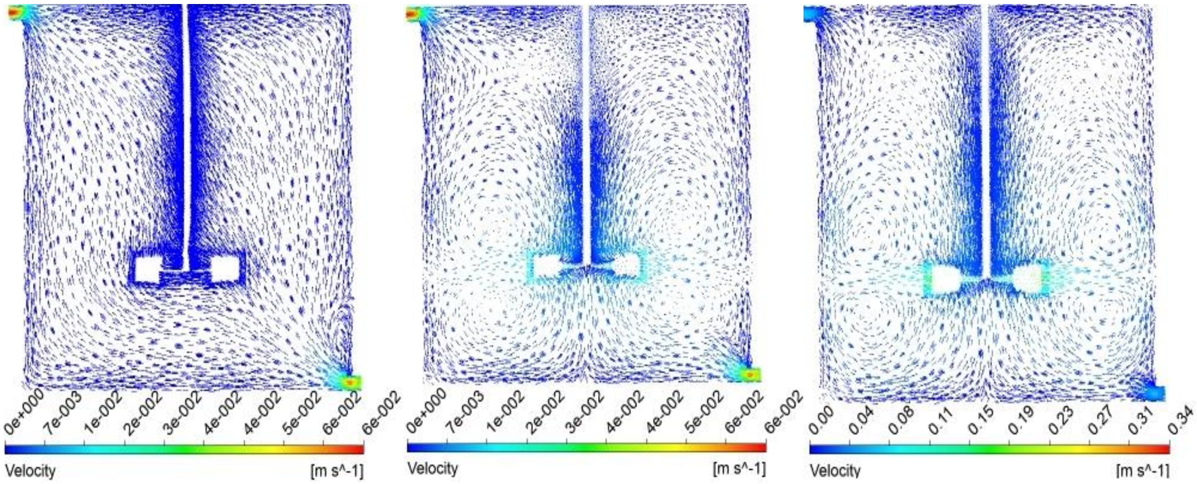

(a) N = 12 rpm (b) N = 25 rpm (c) N = 70 rpm

Figure 5.15 Velocity vectors of the stirred tank with moving impeller and with μ = 21 cP and ρ = 1180 kg/m^3, (a) Re_t = 0.516, (b) Re_t = 0.508 and (c) Re_t = 0.508.

5.6.3 Analysis of the Contours of Mass Fraction of KCl in the Tank in Absence of Impeller and Baffles

The distribution of tracer, KCl in the tank helps to understand the fluid flow behavior of liquid inside the tank. The contours of mass fraction of KCl in the tank without impeller and baffles (Burghardt and Lipowska, 1972) are shown in Figures 5.16 to 5.17. The transient contours are shown in decreasing order of tank Reynolds number. In absence of the impeller and baffles, the tracer moves along the inlet flow stream. The accumulation of tracer in the tank increases with time until it reaches at the exit point. At higher tank Reynolds number shown in Figure 5.16, the tracer moves like a jet towards the opposite wall and moves up along the wall. Whereas at lower Re_t shown in Figure 5.17, the tracer moves axially up and then mix with the bulk liquid of the tank. Therefore, the tracer needs more time to reach at the outlet at lower Re_t. Both the figures show that the homogeneity of the tank liquid increases with the inlet Reynolds number and also with time. Therefore, the flow inside the tank tends to ideal flow state with increasing the tank Reynolds number. The figure also reveals that at the lower tank Reynolds number, KCl disperses more in the solution at early time.

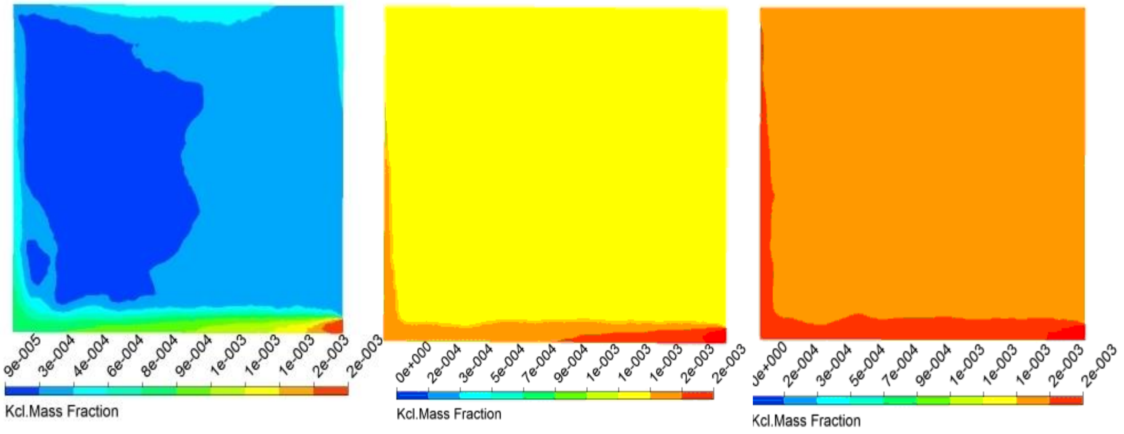

(a) $\theta = 0.4$ (b) $\theta = 1.0$ (c) $\theta = 2.0$

Figure 5.16 Contours of tracer mass fraction in the tank without impeller and baffles at Re_t = 218.4, μ = 1 cP and ρ = 1000 kg/m^3.

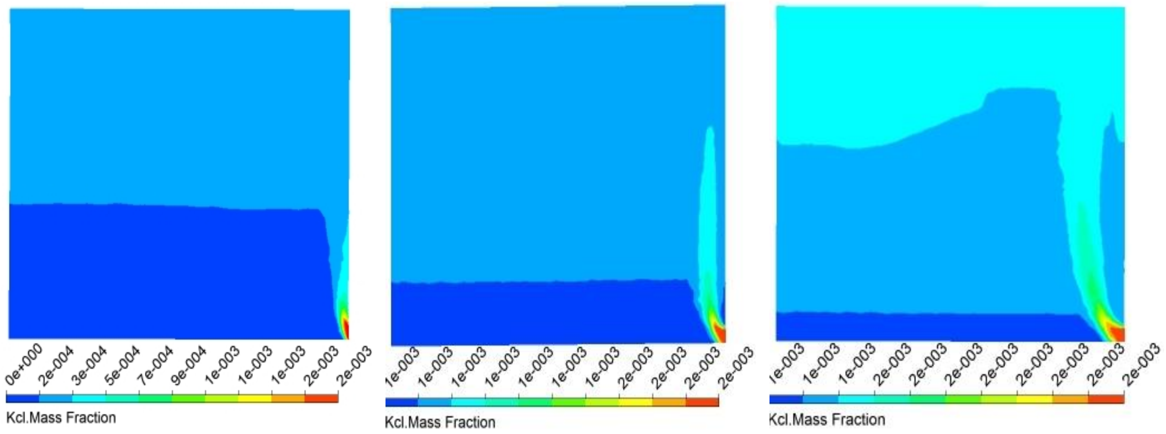

(a) $\theta = 0.4$ (b) $\theta = 1.0$ (c) $\theta = 2.0$

Figure 5.17 Contours of tracer mass fraction in the tank without impeller and baffles at Re_t = 29.6, μ = 1 cP and ρ = 1000 kg/m^3.

5.6.4 Analysis of the Contours of Mass fraction of KCl in the Stirred Tank in Presence of Impeller and Baffles

The effect of the viscosity of the working fluid and the impeller speed on the transient distribution of the mass fraction of the tracer in the stirred tank with impeller and baffles (Burghardt and Lipowska, 1972) is shown in Figures 5.18 to 5.21. The figures show that the concentration of KCl is higher near the inlet and beneath the impeller at initial moments. As time passes, the impeller disperses KCl throughout the tank. The contours of KCl therefore show the advantage of using the impeller while mixing KCl in the tank even at very low tank Reynolds number. The comparison of Figure 5.18 with 5.19 and Figure 5.20 with 5.21 shows that the dead zone and channelling decrease with increasing the impeller speed and hence, homogeneity in the stirred tank in terms of the tracer distribution increases with the impeller speed. The comparison also finds that the mixing time decreases with increasing the impeller speed. With increasing the viscosity of the working liquid, the tank Reynolds number decreases. It reduces the transport of inlet kinetic energy at higher viscosity. Therefore, the speed of the impeller to achieve the same degree of mixing (say ideal mixing state) increases with increasing the viscosity of working fluid.

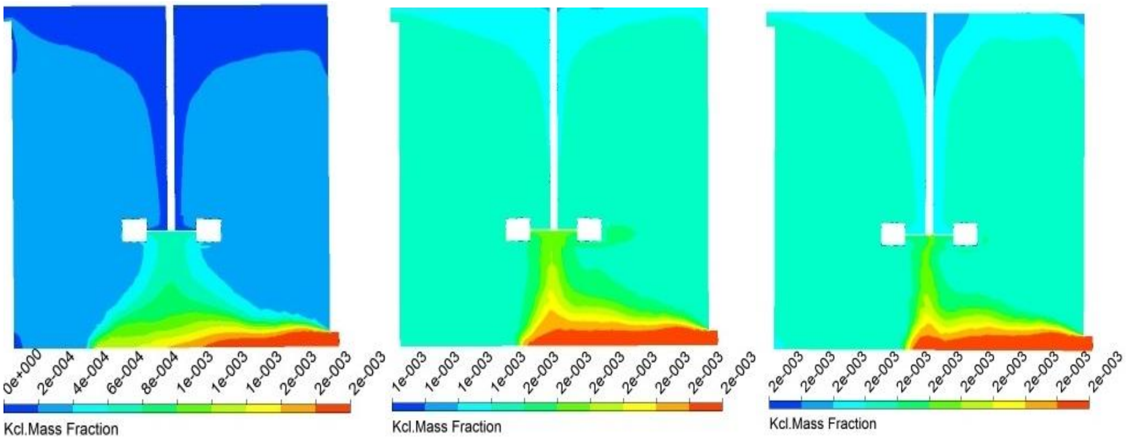

(a) $\theta = 0.4$ (b) $\theta = 1.0$ (c) $\theta = 2.0$

Figure 5.18 Distribution of tracer in the stirred tank in presence of impeller and baffles with μ = 11 cP, N = 20 rpm, $Re_t = 0.753$ and $\rho = 1152$ kg/m^3.

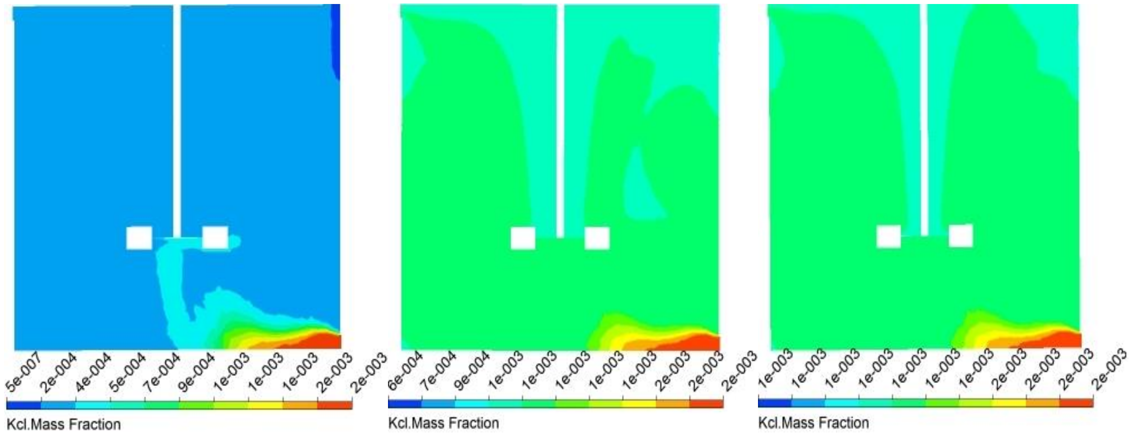

(a) $\theta = 0.4$ (b) $\theta = 1.0$ (c) $\theta = 2.0$

Figure 5.19 Distribution of tracer in the stirred tank in presence of impeller and baffles with μ = 11 cP, N = 40 rpm, $Re_t = 0.753$ and ρ = 1152 kg/m^3.

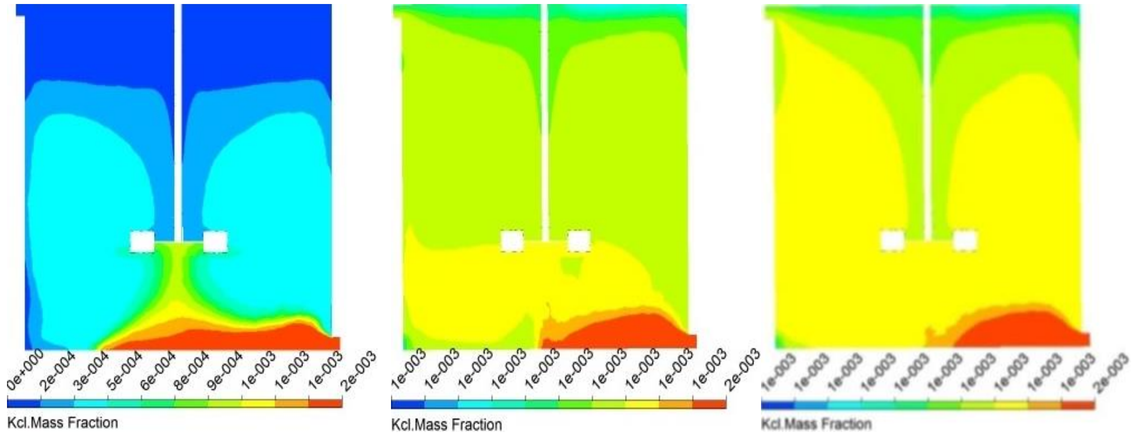

(a) $\theta = 0.4$ (b) $\theta = 1.0$ (c) $\theta = 2.0$

Figure 5.20 Distribution of tracer in the stirred tank in presence of impeller and baffles with μ = 21 cP, N = 25 rpm, $Re_t = 0.508$ and ρ = 1180 kg/m^3.

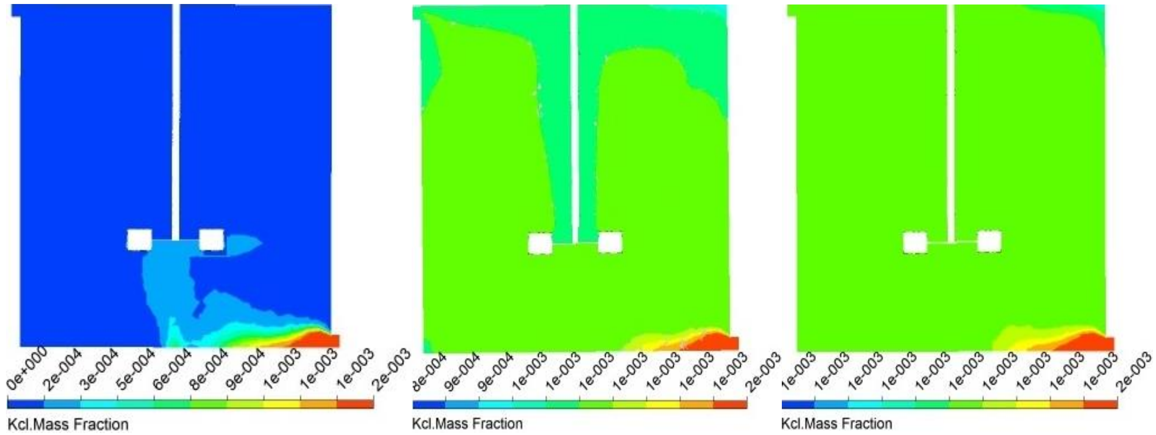

(a) $\theta = 0.4$ (b) $\theta = 1.0$ (c) $\theta = 2.0$

Figure 5.21 Distribution of tracer in the stirred tank in presence of impeller and baffles with μ =

21 cP, N = 70 rpm, Re_t = 0.508 and ρ = 1180 kg/m^3.

5.6.5 Effect of the Tank Reynolds Number, Rotations of Impeller, and Viscosity of Liquid on the RTD of the Stirred Tank with Impeller and Baffles studied by Burghardt and Lipowska (1972)

At the given impeller speed and physical properties of the liquid, the effect of tank Reynolds number on the RTD of stirred tank is studied and displayed in Figure 5.22. The magnitude of the inlet kinetic energy increases and hence, the mixing efficiency of liquid in the tank simultaneously increases with increasing the tank Reynolds number. Therefore, the $I(\theta)$ curve approaches the ideal mixing line at higher tank Reynolds number as depicted in the figure.

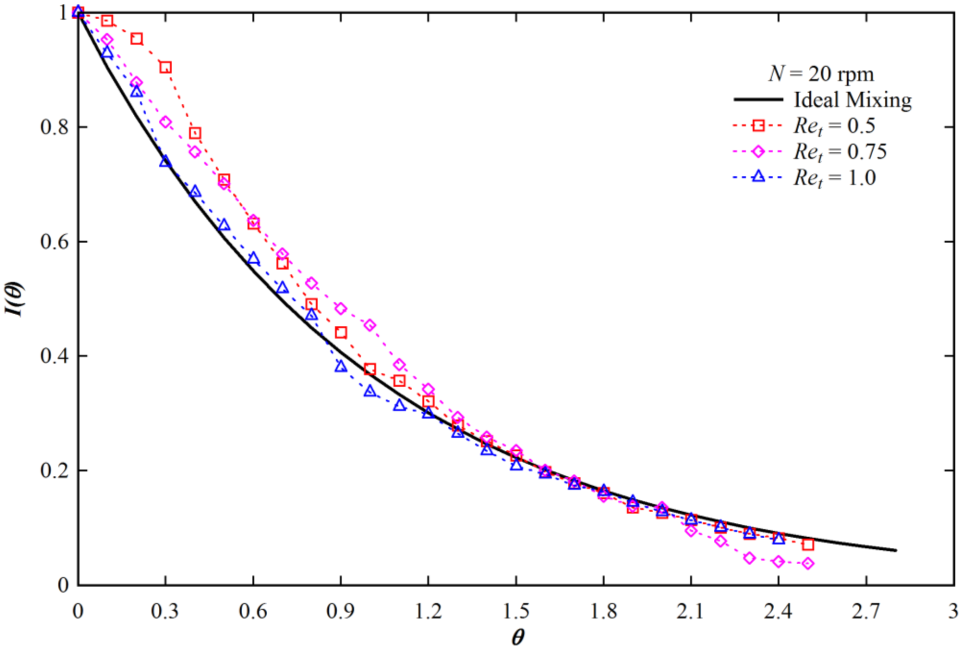

Figure 5.22 Effect of tank Reynolds number on $I(\theta)$ for the stirred tank with impeller and baffles having μ = 11 cP, ρ = 1152 kg/m^3 and N = 20 rpm.

The effect of impeller speed on the mixing efficiency is demonstrated in Figure 5.23. The figure shows that the nature of flow changes from dispersion to ideal mixing state with increasing the rotational speed of impeller. The amount of mechanical energy imparted on the fluid increases with the increasing N. Therefore, a distinct dispersion flow occurs at the impeller speed 20, whereas, for 40 to 60, the mixing is very near to ideal mixing state.

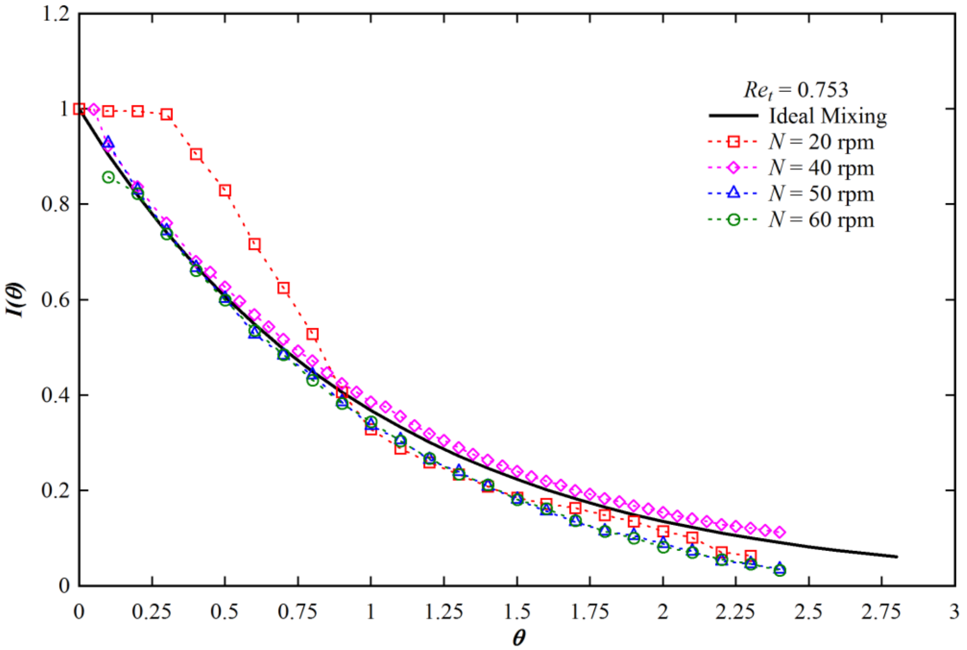

Figure 5.23 Effect of impeller speed on $I(\theta)$ of the stirred tank with impeller and baffles having μ = 11 cP, ρ = 1152 kg/m^3 and Re_t = 0.753.

Viscosity of liquid plays an important role in the RTD study. The effect of the viscosity of liquid on $I(\theta)$ at two selected impeller rotations is shown in Figure 5.24. The figure shows that the mixing line moves towards ideal mixing state with decreasing the viscosity. According to the data given in Table 5.4, the inlet Re_t of 11 cP fluid is greater than that of the 21 cP fluid, and hence, the amount of kinetic energy that enters the system is more with the lower viscosity fluid. It leads the $I(\theta)$ distribution curve to approach the ideal mixing line. In another sense, at 20 and 40 rpm impeller speeds, the kinetic energy transported with the inlet fluid becomes negligible compared to the mechanical energy imparted by the impeller on the stirred liquid. At high impeller speed, the mixing efficiency of low viscous fluid is greater than that of the high viscous fluids. Therefore, at lower viscosity, the approach of $I(\theta)$ curve towards the ideal mixing line is justified.

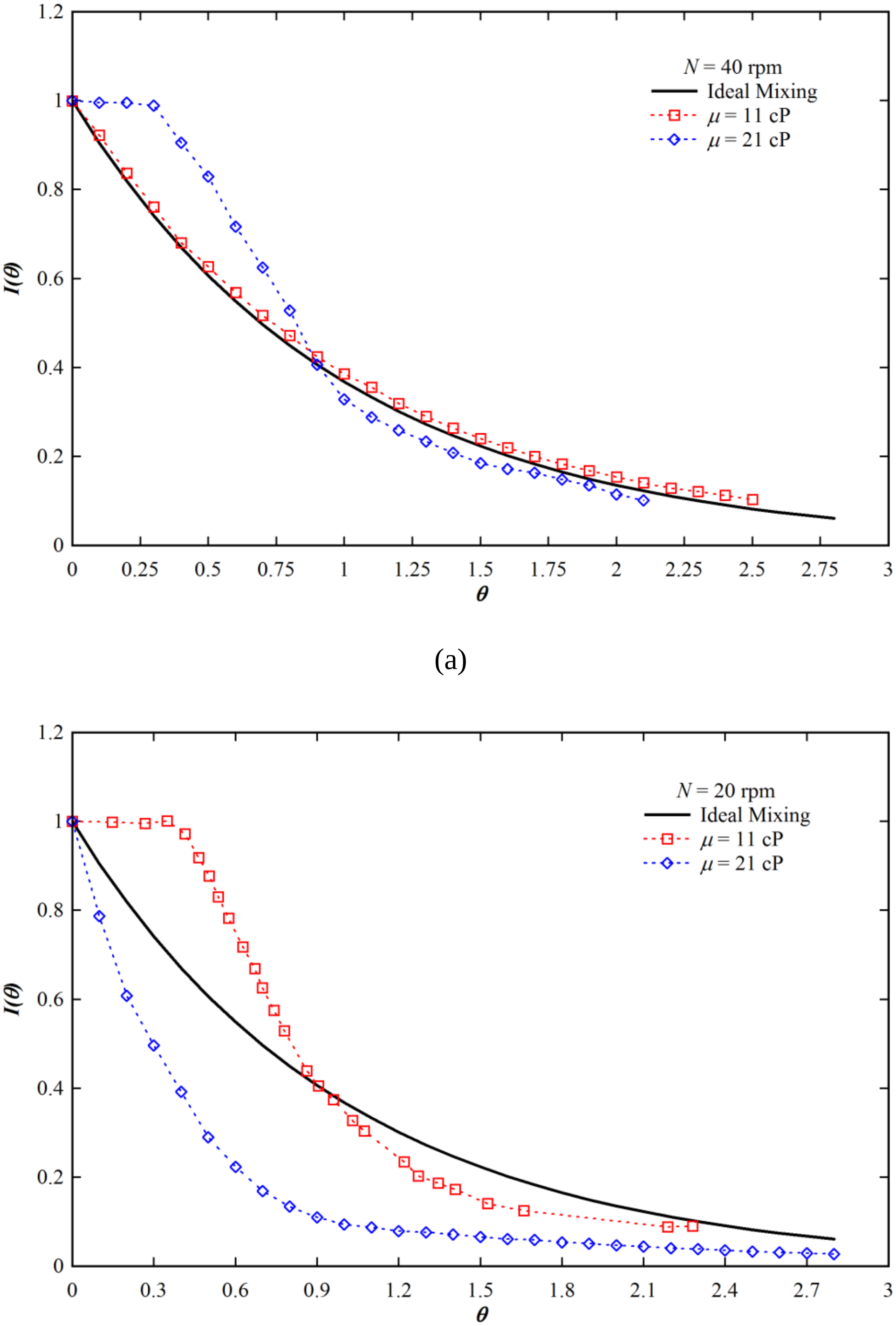

(a)

(b)

Figure 5.24 Effect of the viscosity of the working fluid on *I(θ)* of the stirred tank with impeller and baffles for (a) *N* = 40 rpm, (b) *N* = 20 rpm.

5.6.6 Effect of the Tank Reynolds Number, Rotation of the Impeller and Viscosity of Liquid on the RTD of liquid in the Stirred Tank Studied by Lipowska (1974)

The effect of tank Reynolds number, impeller speed and fluid viscosity on the mixing behavior of liquid in the stirred tank is studied. Figure 5.25 represents the effect of tank Reynolds number on *I(θ)*. At $Re_t = 0.98$, the dispersion flow occurs, at $Re_t = 1.03$, the mixing line goes relatively closer to the ideal mixing line and further increase of Re_t to 1.5 and then to 2.03 results in the mixing line to follow the ideal mixing line. The energy with inlet flow increases with the tank Reynolds number. This inlet energy helps to mix-up the liquid mixture. Therefore, *I(θ)* approaches an ideal mixing line with increasing Re_t as observed in Figure 5.25.

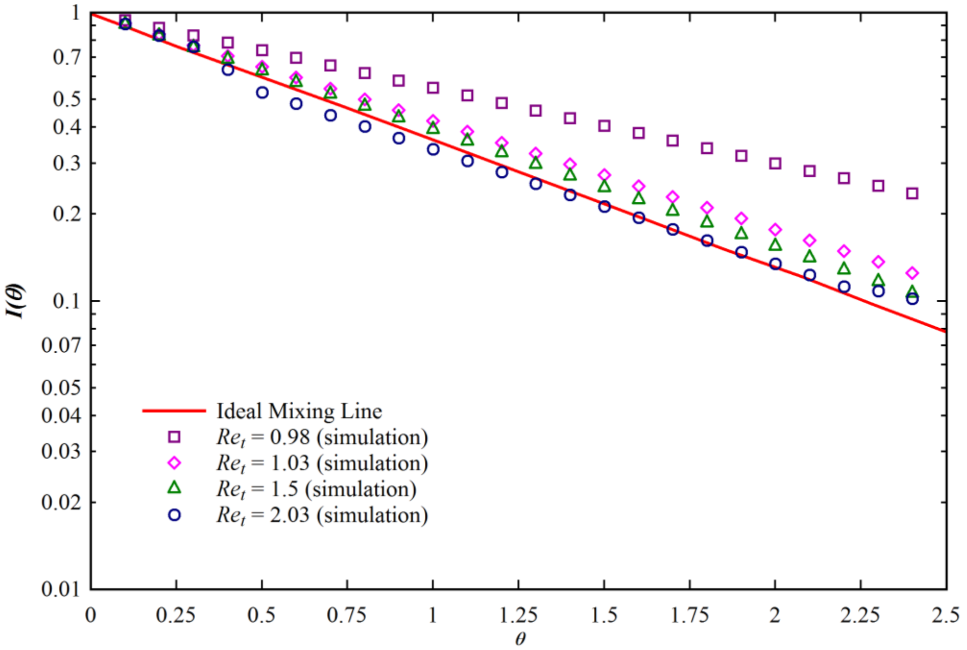

Figure 5.25 Effect of the tank Reynolds number, Re_t on *I(θ)* for a CSTR with impeller and baffles and with $D = 0.099$ m, $d = 0.0072$ m, $N = 50$ rpm, $\mu = 9.2$ cP.

The effect of impeller rotation on the mixing efficiency is demonstrated in Figure 5.26. It can be observed in the figure that the nature of flow changes from dispersion to ideal mixing state with increasing the impeller speed. A distinct dispersion flow occurs at *N* equal to 30, 40 and 50; whereas at *N* equal to 80, the mixing is very near to the ideal mixing condition. This happens due to increase in the amount of imparted mechanical energy on the fluid with increasing the impeller speed, and hence, better mixing occurs at higher impeller rotations.

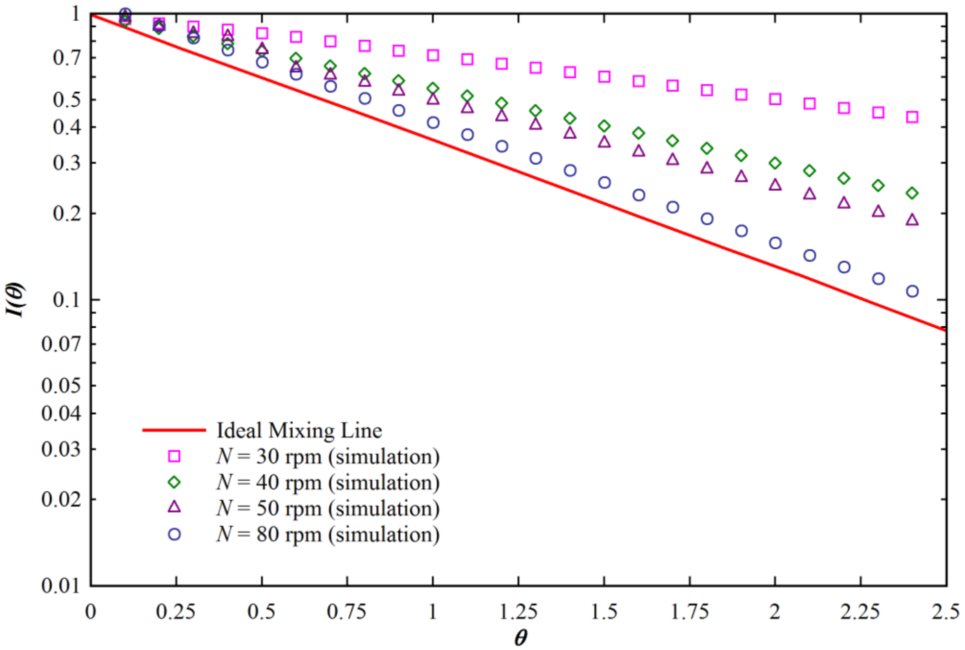

Figure 5.26 Effect of the impeller speed on *I(θ)* for the stirred tank with impeller and baffles and with $D = 0.250$ m, $d = 0.0072$ m, $\mu = 9.2$ cP and $\rho = 1145$ kg/m^3, $Re_t = 1.03$.

The viscosity of fluid has a certain effect on the hydrodynamic behavior of it and in turn on the mixing behavior. The effect of viscosity of liquid on *I(θ)* at different impeller speeds is shown in Figure 5.27. The effect of viscosity on *I(θ)* at high impeller rotation is just reverse of lower values of it. The figure depicts that the mixing of liquid moves towards the ideal mixing state with increasing the viscosity at *N* equal to 50 and 70, whereas it moves away from the ideal mixing line for *N* equal to 25 and 10. At higher values of impeller speed, the impeller does more mechanical work and the viscous force becomes negligible. Therefore, the mixing state of liquid moves towards ideal mixing condition at higher impeller rotations. But at lower values of impeller speed, the amount of energy given by the impeller to the liquid is relatively smaller, and it becomes insufficient for overcoming the effect of viscous resistant on flow. Thus, at low impeller rotations, the curve shows a dispersed flow with partial circulation of liquid. Due to the domination of viscous force at lower *N*, the mixing line moves away from the ideal mixing line.

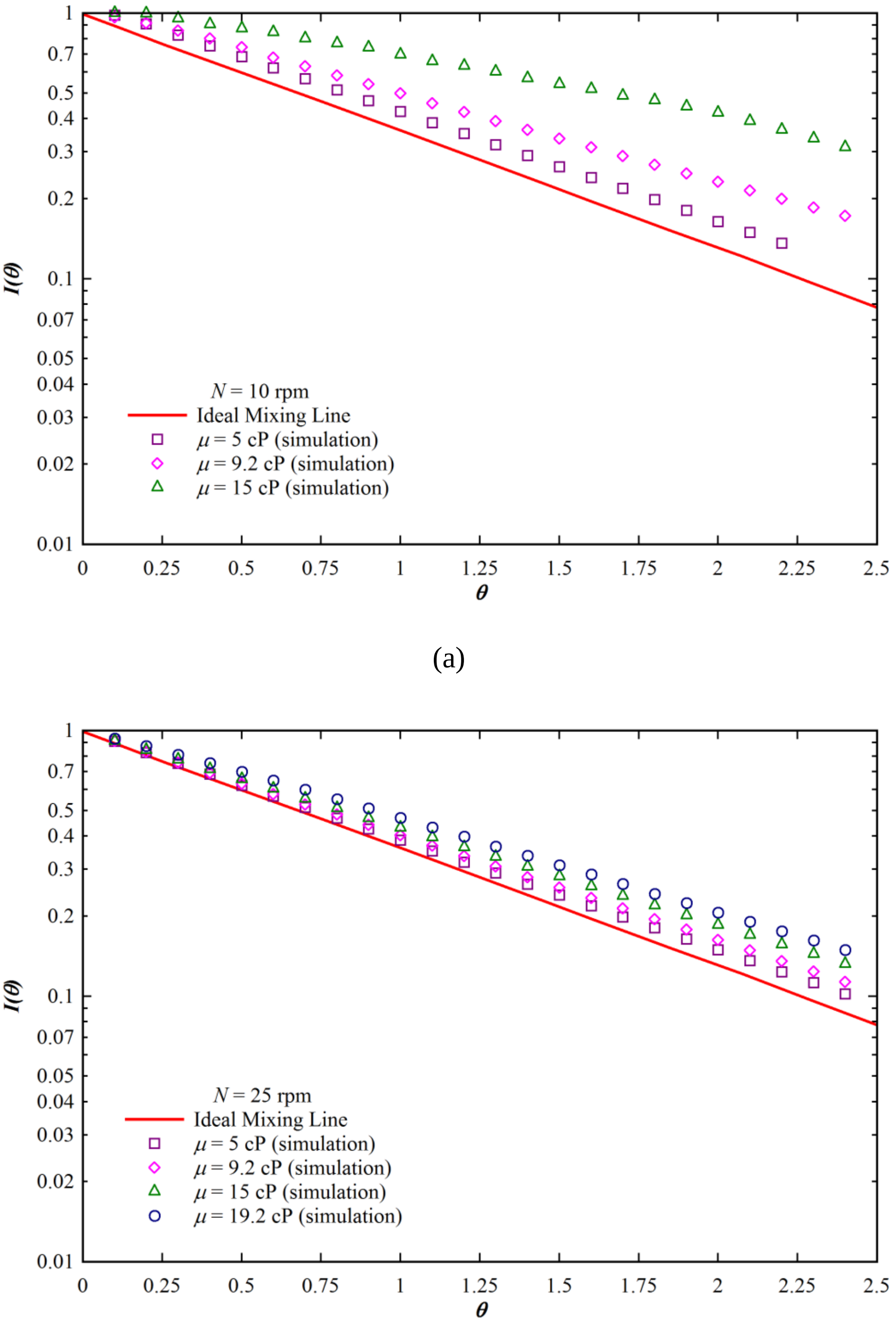
I(θ)
θ
1
0.7
0.5
0.4
0.3
0.2
0.1
0.07
0.05
0.04
0.03
0.02
0.01
0
0.25
0.5
0.75
1
1.25
1.5
1.75
2
2.25
2.5
N = 10 rpm
Ideal Mixing Line
μ = 5 cP (simulation)
μ = 9.2 cP (simulation)
μ = 15 cP (simulation)
N = 25 rpm
Ideal Mixing Line
μ = 5 cP (simulation)
μ = 9.2 cP (simulation)
μ = 15 cP (simulation)
μ = 19.2 cP (simulation)

(a)

(b)

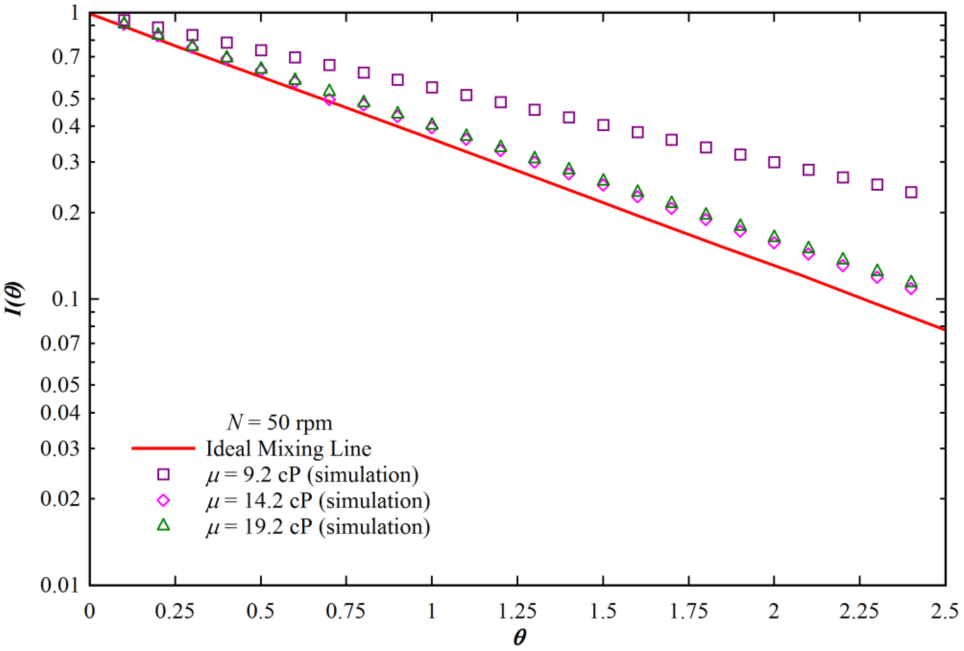

(c)

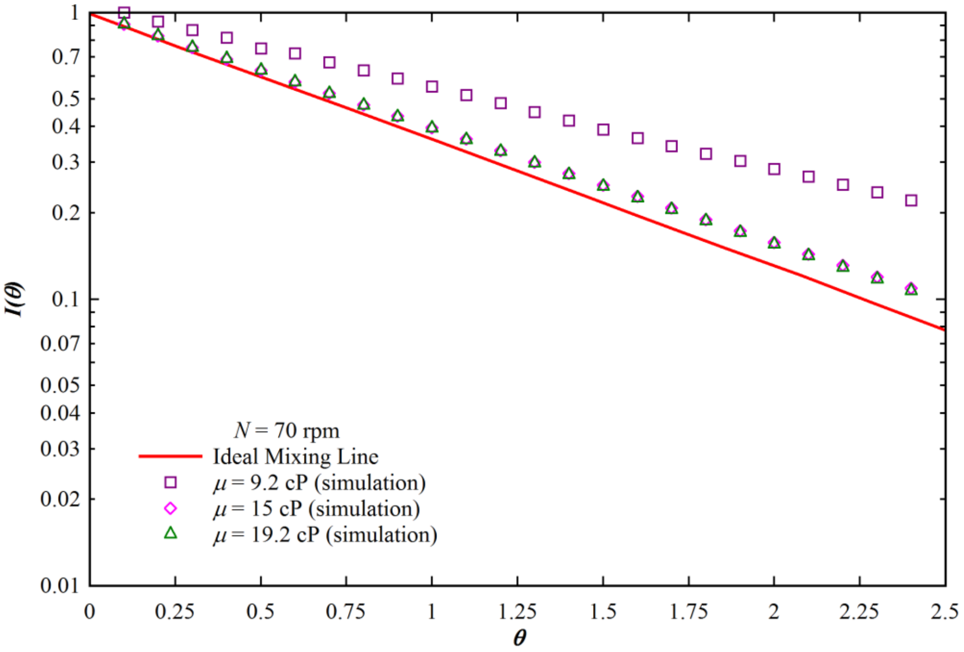

(d)

Figure 5.27 Effect of the viscosity of liquid on *I(θ)* of the stirred tank with impeller and baffles and with D = 0.099 m, d = 0.0072 m, Re_t = 1.03: (a) N = 10 rpm; (b) N = 25 rpm; (c) N = 50 rpm and (d) N = 70 rpm.

5.6.7 Analysis of the Mean Residence Time, Variance, Holdback and Segregation of the Stirred Tank Studied by Burghardt and Lipowska (1972)

Theoretically, the mean residence time, τ_m, is equal to the variance, σ, for the ideal reactor. The variation of τ_m and σ with tank Reynolds number is depicted in Figure 5.28 for the tank without impeller and baffles. The figure shows that there is a significant difference between the σ and τ_m at Re_t = 20. Hence, the fluid flow state is non-ideal at Re_t = 20 and it becomes ideal with increasing the tank Reynolds number beyond 20. The similar conclusion was also made in the Figure 5.3.

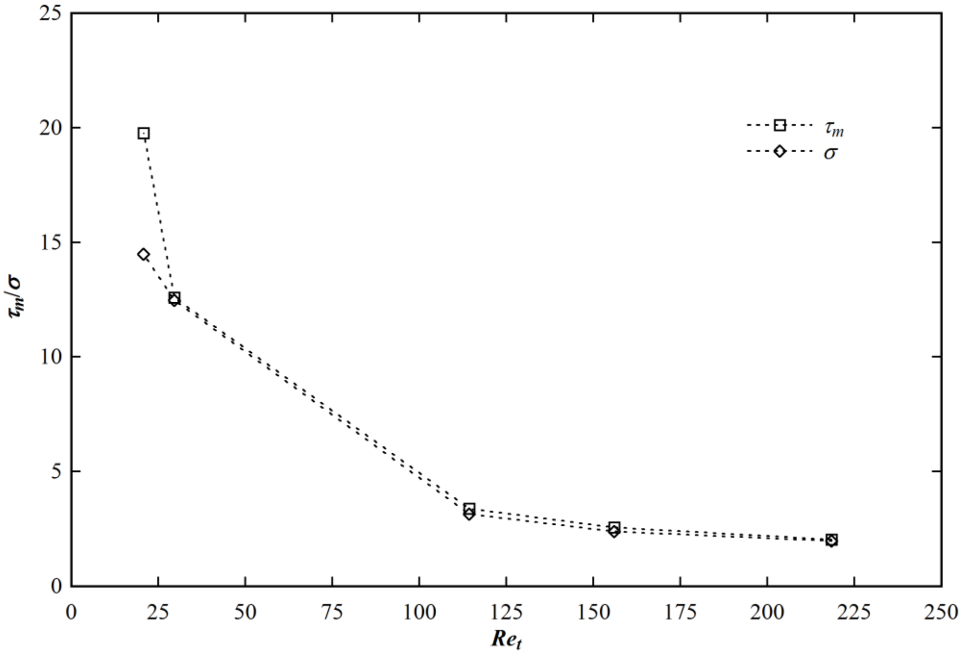

Figure 5.28 Distribution of τ_m and σ with tank Reynolds number for the tank without impeller and baffles with μ = 1 cP and ρ = 1000 kg/m^3.

The difference between the mean residence time and variance decreases with the speed of impeller as depicted in Figure 5.29. Hence, the mixing of stirred tank approaches the ideal-mixing state with increasing the speed of impeller. The required mechanical energy imparted by the impeller on fluid increases with increasing the viscosity of fluid to achieve the same extent of mixing. Therefore, the ideal mixing state with equality of τ_m and σ is achieved at higher impeller speeds for the working fluid with higher viscosity and it is revealed in the figure.

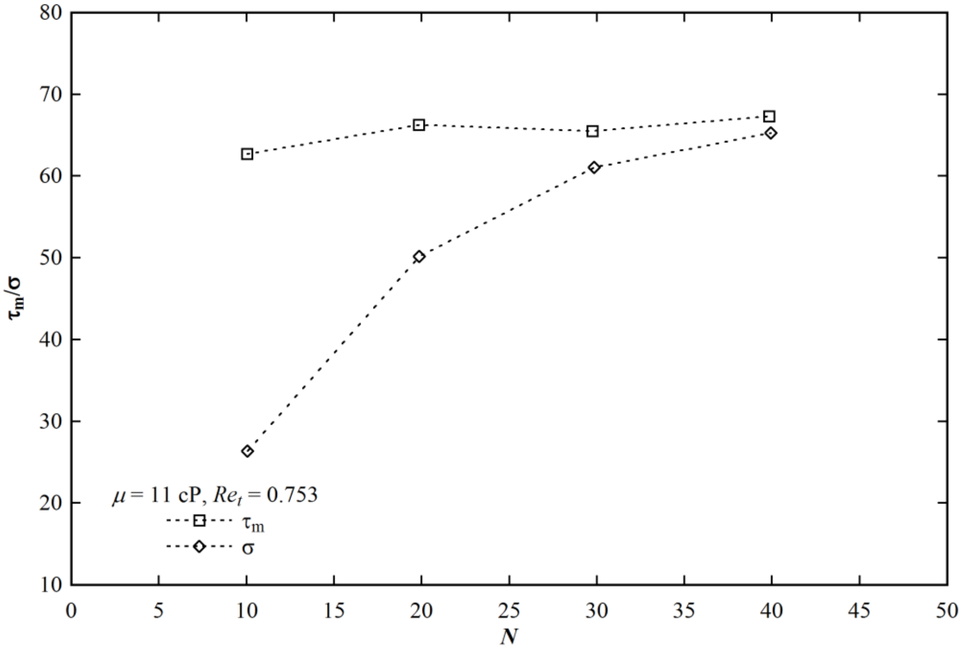

τ_m/σ
N
μ = 11 cP, Re_t = 0.753
τ_m
σ
80
70
60
50
40
30
20
10
0
5
10
15
20
25
30
35
40
45
50

(a)

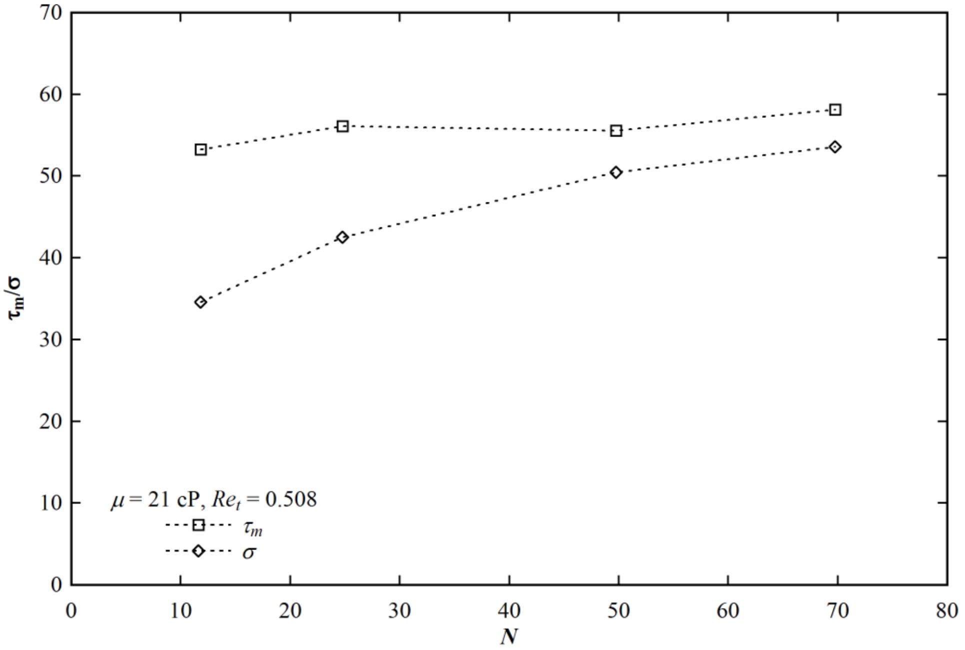

τ_m/σ
N
μ = 21 cP, Re_t = 0.508
τ_m
σ
70
60
50
40
30
20
10
0
0
10
20
30
40
50
60
70
80

(b)

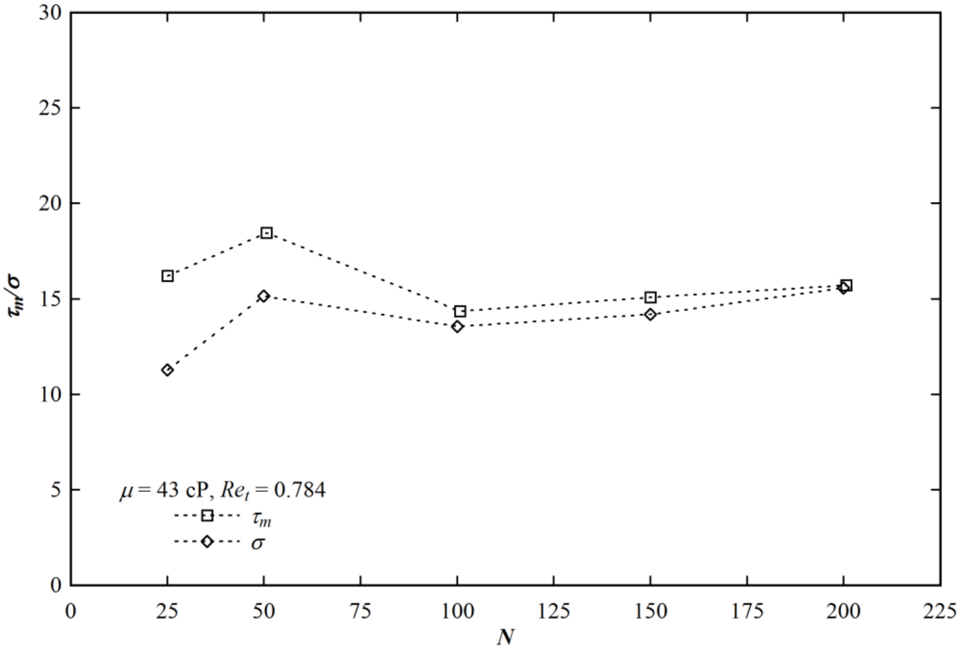

(c)

Figure 5.29 Distribution of τ_m and σ with the impeller speed for the stirred tank with impeller and baffles.

The distribution of holdback, segregation and N_{cstr} with the tank Reynolds number of the tank without impeller and baffles is shown in Figure 5.30. Theoretically, the liquid is completely mixed when holdback is equal to 0.36 (i.e. 1/e). The figure shows that the value of holdback is little less than 0.36 for Re_t = 20, and for other tank Reynolds number, it is around 0.36. Hence, exclusively based on the holdback distribution, it can be concluded that the mixing is ideal for Re_t greater than 20. The figure also shows that the segregation is negative at low Re_t. It increases and tends to 0.36 with increasing the tank Reynolds number. It can be concluded from the segregation curve that the mixing process becomes ideal only at high Re_t and the liquid in stirred tank is mostly dead fluid at lower Re_t. The observation from hold back distribution curve therefore partially contradicts the observation from the segregation distribution curve. The N_{cstr} is equal to 1.0 for an ideal reactor. The figure depicts that N_{cstr} decreases and tends to 1.0, i.e., towards the ideal flow state with increasing the tank Reynolds number.

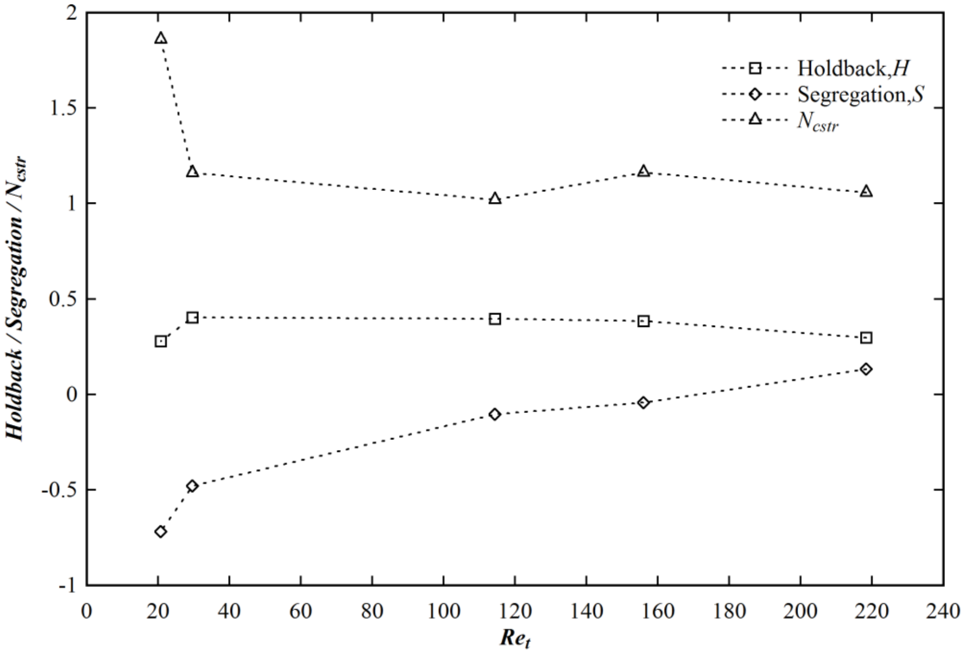

Figure 5.30 Distribution of Holdback, Segregation and N_{cstr} with the tank Reynolds number for the stirred tank with impeller and baffles with μ = 1 cP and ρ = 1000 kg/m^3.

The effect of impeller speed and viscosity on the holdback distributions are shown in Figure 5.31(a). It shows that the holdback increases and then reaches near about 0.36 with increasing the impeller speed especially for fluid with the lowest viscosity, 11 cP. The segregation, *S*, as shown in Figure 5.31(b), decreases with increasing the impeller speed. The variation of N_{cstr} with the impeller speed of liquids with different viscosity is presented in Figure 5.31(c). It shows that N_{cstr} tends to 1.0 with increasing speed of the impeller. The viscosity dependent mixing of liquid in stirred tank, therefore, tends to the ideal mixing state at higher impeller speed.

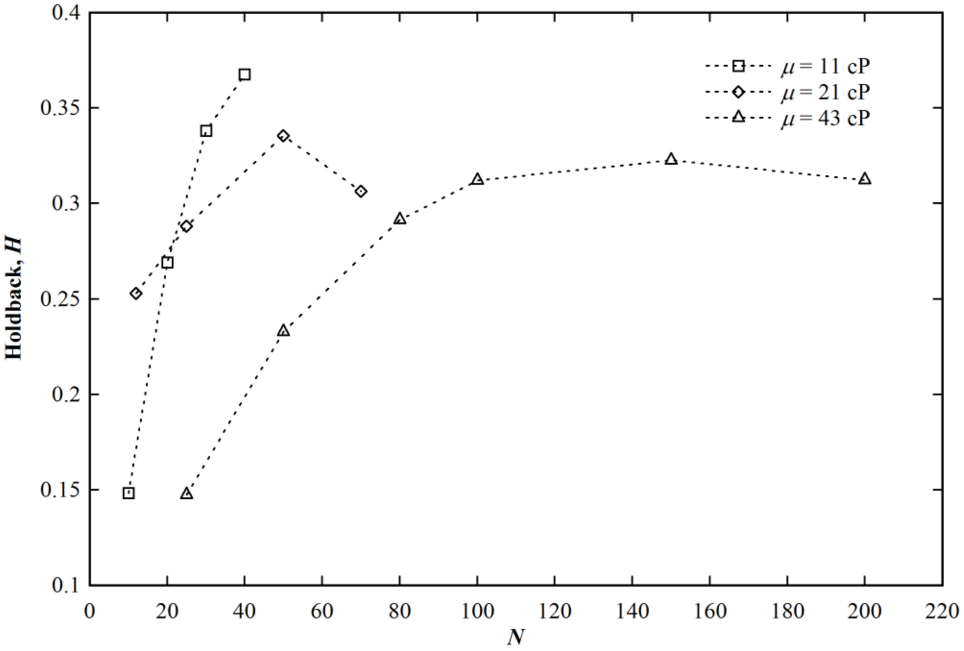
Holdback, H
N
μ = 11 cP
μ = 21 cP
μ = 43 cP
0.4
0.35
0.3
0.25
0.2
0.15
0.1
0
20
40
60
80
100
120
140
160
180
200
220

(a)

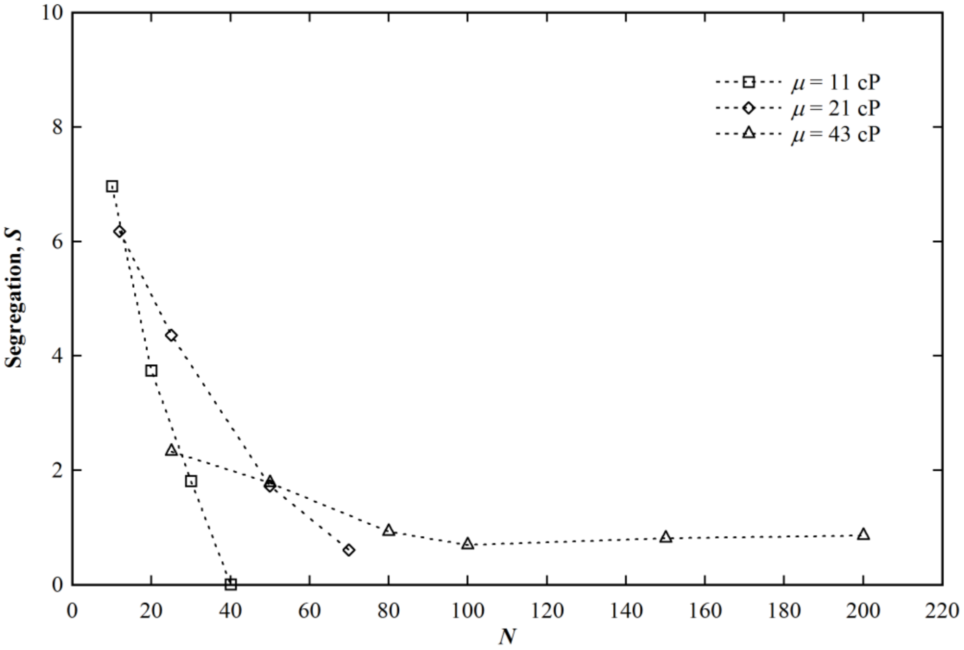
Segregation, S
N
μ = 11 cP
μ = 21 cP
μ = 43 cP
10
8
6
4
2
0
0
20
40
60
80
100
120
140
160
180
200
220

(b)

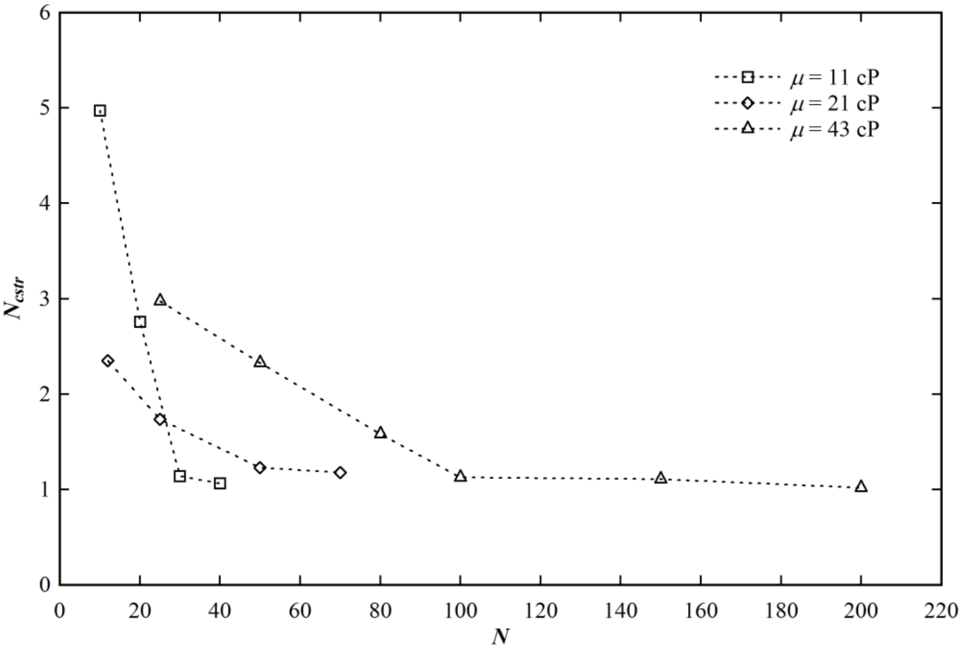

(c)

Figure 5.31 Distribution of Holdback, Segregation and N_{cstr} with the impeller speed of the stirred tank with impeller and baffles, and with (a) μ = 11 cP, Re_t = 0.753 and ρ = 1152 kg/m^3, (b) μ = 21 cP, Re_t = 0.508 and ρ = 1180 kg/m^3, (c) μ = 43 cP, Re_t = 0.784 and ρ = 1200 kg/m^3.

A computational study of continuous stirred tank by Ansys Fluent has been carried to understand the mixing behavior with tracer injection and the swept volume method. The stirred tank has been simulated with and without impeller and baffles. The simulated results have been compared with the experimental residence time distribution (RTD) data of Burghardt and Lipowska (1972) and Lipowska (1974). A good agreement has been found between them. The hydrodynamics study of stirred tank has also been done to get the insight of flow field in the tank. The effect of rotations of the impeller, tank Reynolds number and viscosity of liquid on the mixing behavior has been evaluated. The mixing behavior has been changed from dispersion to ideal mixing state with increasing the tank Reynolds number and impeller rotations. At higher viscosity of the liquid, the mixing behavior in the tank has been moved towards the ideal mixing state. The mixing characteristic has also been studied in terms of the number of ideal stirred tank in series giving equivalent performance of the actual stirred tank, N_{cstr}, holdback, segregation, mean residence time, τ_m, and second moment, σ. The required values of the flow parameters for ideal mixing state have been identified.

CHAPTER 6

CONCLUSIONS AND FUTURE RECOMMENDATIONS

6.1 CONCLUSIONS

Mixing process is very important aspect in the chemical industries. The performance of mixing process is dependent on many factors like, impeller types, tank size, type of fluids to be mixed, etc. The work reported in this thesis is an attempt to numerically study the characteristics of mixing in stirred tank with the help of Rushton turbine and helical ribbon impellers. A major aspect of the investigation is the study of flow field, mixing time, flow number and power number for varying operating conditions. Also the entropy generation which is one of the parameters for achieving efficient mixing have been numerically predicted for different types of thermal boundary conditions. The predicted entropy generation have been used to determine the optimum operating parameters like inlet Reynolds number, impeller rotations, impeller off bottom clearance, etc. for efficient mixing process. In order to understand the fluid mixing behavior inside the stirred tank, the RTD analyses have been carried out.

The salient accomplishments and major conclusions of this thesis are summarized and recommendations on future directions are made.

In chapter 3, Ansys Fluent turbulent flow models have been used to validate the experimental results of Venneker et al. (2010), and validated models were used further to find the parametric dependency of mixing behavior of stirred tank. The following conclusions are made from this study,

- The computational fluid dynamics study of a stirred tank with Rushton turbine has been carried out to understand the hydrodynamic and thermodynamics behavior.
- The axial, radial and tangential velocities with water and shear thinning fluids have been predicted and validated with literature data (Venneker et al., 2010) and a good agreement was found between them.

- The simulated tangential velocities have been found less dependent on the flow behavior index than the radial and axial component velocities.
- The discharge axial velocity of impeller and the width of the radial and tangential velocity profiles have been predicted successfully and validated with the literature data (Venneker et al., 2010). The computed discharge axial velocities and the width of the discharge radial and tangential velocity profiles have been found independent of flow behavior index, *n*.
- Spearman's rank-order correlation coefficient method has been used to predict the interaction of the theoretically calculated velocity profiles with the impeller Reynolds number and flow behavior index. The interaction of Reynolds number has been found more than the flow behavior index.
- The predicted flow numbers and power numbers of the shear thinning fluids have been found close to flow number and power number of the Newtonian fluid.
- The mixing performance of the batch stirred tank has been studied using tracer injection method. In the transition and turbulent zone, the mixing time has been decreased with increasing impeller rotations, and the nature of the flow inside the stirred tank was mostly simple shear flow.
- The entropy generations has been increased with increase in the impeller rotations, blade width and found independent of the blade thickness, and it was a weak function of impeller clearance and strong function of flow behavior indexes.
- The continuous stirred tank with Rushton turbine has been optimized using entropy generation minimization (EGM) concept where the total entropy generation of the system has been minimized with respect to the inlet Reynolds number, impeller speed, impeller clearance and blade width. The optimized design parameters have been tabulated in Tables 3.6 and 3.7.
- Around the entropy minimization point, the heat transfer irreversibility has been found much higher than the fluid frictional irreversibility. The Bejan number, *Be*, was greater than 0.5 at the entropy minimization point.

- The effect of impeller rotations on the entropy generation has been found less significant as compared to the inlet Reynolds number. The optimal impeller clearance position has been found to be dependent on the wall temperature and independent of wall heat flux. The optimum impeller blade width has been found independent of the magnitude of wall temperature and wall heat flux.

In Chapter 4, the numerical study of power consumption and entropy generation for Newtonian and non-Newtonian fluid has been carried out with helical ribbon and helical ribbon screw impeller in stirred tank. The following conclusions are summarized from this study,

- The predicted power number of Newtonian fluid has been validated with literature data (Brito-De La Fuente et al., 1997).
- The power number of Newtonian fluid for HR and HRS impellers were dependent on the number of pitches and helical impeller blade width, but independent of screw blade width.
- For shear thinning fluids, the power consumptions HRS-2A and HRS-2B impellers were higher than other impeller geometries.
- The power constant for Newtonian fluid (K_p) and non-Newtonian fluid ($K_p(n)$) have been calculated and compared successfully with the literature data (Brito-De La Fuente et al., 1997).
- Four different methods have been adopted for determining the geometry constant K_s. All four methods showed that the computed K_s were dependent on n. Out of four methods; method (II) has been found the best as it predicted the generalized power curve successfully. It has found that the laminar flow could persist up to $Re \approx 100$.
- The laminar zone for shear fluid has been extended to higher impeller number with increasing the flow behavior index.
- In the laminar zone, the flow number of HR and HRS impellers has been increased with impeller Reynolds number and flow behavior index. In the transition zone, the flow number has been decreased gradually or became constant depending on the impeller geometry and flow behavior index.

- The axial velocity of HR impeller has been found more than HRS impellers except very close to the shaft of the impeller.
- The non-dimensional mixing time of HR and HRS impellers has been found varying in scattered manner with impeller Reynolds number. A dispersive flow away from the impeller shaft has been observed for all the close clearance impellers.
- The entropy generation of HR and HRS impellers has been increased with the impeller Reynolds number. An empirical model of entropy generation has been proposed as a function of impeller Reynolds number. The entropy generation has been increased with decrease in the pitch ratio of the impeller.
- The non-isothermal continuous stirred tank with HR and HRS impellers has been optimized employing the entropy generation minimization (EGM) technique. The optimized design parameters have been tabulated in Tables 4.7 to 4.10. The minimum entropy generation has been found almost independent of the impeller geometry.

Based on the numerical study of the residence time distribution (RTD) of liquid in tank with and without impeller and baffles discussed in chapter 5, the following conclusions can be made,

- The simulated internal age distribution function, $I(\theta)$, has been found in excellent agreement with the experimental data available in literature (Burghardt and Lipowska, 1972; Lipowska, 1974).
- The mixing efficiency has been found to be dependent on tank Reynolds number, the rotations of the impeller, and viscosity of the liquid. As the tank Reynolds number and impeller rotations increased, the mixing behavior has been changed from dispersion to ideal mixing state.
- The flow in the tank has been approached to ideal mixing state with increasing the viscosity of the operating liquid.
- The variance and mean residence time have been found equal at higher tank Reynolds number where the ideal mixing condition was confirmed.
- The behavior of mixing of liquid in the stirred tank has been studied successfully with the help of holdback and segregation calculation.

- The number of ideal CSTR in series has been approached to 1.0 with increasing the tank Reynolds number and impeller rotations.

6.2 FUTURE RECOMMENDATIONS

- The study was limited to Newtonian and inelastic shear thinning fluids. It can be extended to shear thickening and viscoelastic fluids.
- The turbulence state of the stirred tank can be predicted by other turbulence models like SST and k-ω as available in Ansys Fluent.
- The geometry constant, K_s was predicted for different helical ribbon and helical ribbon screw impellers. It can also be determined experimentally and theoretically for Rushton turbine to re-examine the Metzner-Otto correlation.
- The RTD study was carried out for the stirred tank with Rushton turbine. The study can be extended to find mixing efficiency of stirred tank with helical ribbon impeller.
- The comparative study between tracer injection and swept volume method can be carried out for the same dimensional system.

BIBLIOGRAPHY

Adham, A.M., Ghazali, N.M., & Ahmad, R., (2014). Optimization of a rectangular microchannel heat sink using entropy generation minimization (EGM) and genetic algorithm (GA). *Arabian Journal for Science and Engineering*, *39*, 7211–7222.

Aghbolaghy, M., & Karimi, A. (2014). Simulation and optimization of enzymatic hydrogen peroxide production in a continuous stirred tank reactor using CFD–RSM combined method. *Journal of the Taiwan Institute of Chemical Engineers*, *45*, 101–107.

Ahmadi, P., Hajabdollahi, H., & Dincer, I. (2011). Cost and entropy generation minimization of a cross-flow plate fin heat exchanger using multi-objective genetic algorithm. *Journal of Heat Transfer*, *133*, 021801-1–10.

Alebrahim, A., & Bejan, A. (1999). Entropy generation minimization in a ram-air cross-flow heat exchanger. *International Journal of Applied Thermodynamics*, *2*(4), 145–157.

Ameur, H., & Bouzit, M. (2012). Mixing in shear thinning fluids. *Brazilian Journal of Chemical Engineering*, *29*(2), 349–358.

Ameur, H., Bouzit, M., & Ghenaim, A. (2012). Hydrodynamics in a vessel stirred by simple and double helical ribbon impellers. *Central European Journal of Engineering*, *3*(1), 87–98.

Ansys Fluent 13: Theory Guide (2011). U.S.A.: Ansys Inc.

Ansys Fluent 13: User's Guide (2011). U.S.A.: Ansys Inc.

Arratia, P.E., Lacombe, J.P., Shinbrot, T., & Muzzio, F.J., (2004). Segregated regions in continuous laminar stirred tank reactors. *Chemical Engineering Science*, *59*, 1481–1490.

Aubin, J., Naude, I., Bertrand, J., & Xuereb, C. (2000). Blending of Newtonian and shear-thinning fluids in a tank stirred with a helical screw agitator. *Chemical Engineering Research and Design*, *78*(8), 1105–1114.

Awad, M.M., & Muzychka, Y.S. (2012). Thermodynamic Optimization, Heat Exchangers - Basics Design Applications, Mitrovic, J. (Ed.), ISBN: 978-953-51-0278-6, InTech, Available from:http://www.intechopen.com/books/heat-exchangers-basics-design applications/thermodynamic-optimization

Balaji, C., Holling, M., & Herwig, H. (2007). Entropy generation minimization in turbulent mixed convection flows. *International Communications in Heat and Mass Transfer*, *34*(5), 544–552.

Bao, Y., Lu, Y., Liang, Q., Li, L., Gao, Z., Huang, X., & Qin, S. (2015). Power demand and mixing performance of coaxial mixers in a stirred tank with CMC solution. *Chinese Journal of Chemical Engineering*, *23*, 623–632.

Bartels, C., Breuer, M., Wechsler, K., & Durst, F. (2002). Computational fluid dynamics applications on parallel-vector computers: Computations of stirred vessel flows. *Computers and Fluids*, *31*(1), 69–97.

Basha, M., Al-Qahtani, M., & Yilbas, B.S. (2007). Entropy generation in a rotating channel. *Proceedings of the Institution of Mechanical Engineers Part A: Journal of Power and Energy*, *221*, 291–299.

Bates, R.L., Fondy, P.L., & Corpstein, R.R. (1963). An examination of some geometrical parameters of impeller power. *Industrial and Engineering Chemistry Process Design and Development*, *2*(4), 310–314.

Bejan, A. (1979). A study of entropy generation in fundamental convective heat transfer. *Journal of Heat Transfer*, *101*(4), 718–725.

Bejan, A. (1995). *Entropy generation minimization*. New York, NY: CRC Press.

Benayad, S., David, R., & Cognet, G. (1985). Measurement of coupled velocity and concentration fluctuations in the discharge flow of a Rushton turbine in a stirred tank. *Chemical Engineering and Processing: Process Intensification*, *19*(3), 157–165.

Bertrand, F., Tanguy, P., Brito-De La Fuente, E., & Carreau, P. (1999). Numerical modeling of the mixing flow of second-order fluids with helical ribbon impellers. *Computer Methods in Applied Mechanics and Engineering*, *180*(3-4), 267–280.

Bombac, A., Zumer, M., & Zun, I. (2007). Power consumption in mixing and aerating of shear thinning fluid in a stirred vessel. *Chemical and Biochemical Engineering Quarterly*, *21*(2), 131–138.

Bonvillani, P., Ferrari, M.P., Ducros, E.M., & Orejas, J.A. (2006). Theorical and experimental study of the effects of scale-up on mixing time for a stirred-tank bioreactor. *Brazilian Journal of Chemical Engineering*, *23*(1), 1–7.

Bourne, J.R., & Butler, H. (1969). Power consumption of helical ribbon impellers in viscous liquids. *Transactions of the Institution of Chemical Engineering*, *47*, 263–270.

Brito-De La Fuente, E., Choplin, L., & Tanguy, P.A. (1997). Mixing with helical ribbon impellers: effect of highly shear thinning behavior and impeller geometry. *Transactions of the Institution of Chemical Engineers*, *75*A, 45–52.

Brito-De La Fuente, E., Leuliet, J.C., & Choplin, L. (1990). Mixing in rheologically complex fluids. *Golden jubilee meeting of the British society of rheology and 3rd European rheology conference*, Edinburgh, United Kingdom, pp. 72–75.

Brito-De La Fuente, E., Leuliet, J.C., Choplin, L., & Tanguy, P.A. (1990). Mixing and circulation times in rheologically complex fluids. Fluid mixing IV, I Chem Eng Symposium Series no. 121, Bradford, England, pp. 75–96.

Brucato, A., Ciofalo, M., Grisafi, F., & Micale, G. (1998). Numerical prediction of flows in baffled stirred vessels: A comparison of alternative modelling approaches. *Chemical Engineering Science*, *53*, 3653–3684.

Bujalski, J., Jaworski, Z., Bujalski, W., & Nienow, A.W. (2002). The influence of the addition position of a tracer on CFD simulated mixing times in a vessel agitated by a Rushton turbine. *Chemical Engineering Research and Design*, *80*(8), 824–831.

Bujalski, W., Nienow, A., Chatwin, S., & Cooke, M. (1987). The dependency on scale of power numbers of Rushton disc turbines. *Chemical Engineering Science*, *42*(2), 317–326.

Burghardt, A., & Lipowska, L. (1972). Mixing phenomena in a continuous flow stirred tank reactor. *Chemical Engineering Science*, *27*, 1783–1795.

Busciglio, A., Grisafi, F., Scargiali, F., & Brucato, A. (2014). Mixing dynamics in uncovered unbaffled stirred tanks. *Chemical Engineering Journal*, *254*, 210–219.

Carreau, P.J. (1972). Rheological equations from molecular network theories. *Transactions of The Society of Rheology*, *16*, 99–127.

Carreau, P.J., Chhabra, R.P., & Cheng, J. (1993). Effect of rhecological properties on power consumption with helical ribbon agitators. *AIChE Journal*, *39*(9), 1421–1430.

Cebeci, T., & Bradshaw, P. (1984). *Physical and computational aspects of convective heat transfer*. New York, NY: Springer.

Chaibakhsh, N., Rahman, M.B.A., Vahabzadeh, F., Abd-Aziz, S., Basri M., & Salleh, A.B. (2010). Optimization of operational conditions for adipate ester synthesis in a stirred tank reactor. *Biotechnology and Bioprocess Engineering*, *15*, 846–853.

Chavan, V.V., & Ulbrecht, J. (1972). Power correlation for helical ribbon impellers in inelastic non-Newtonian fluids. *The Chemical Engineering Journal*, *3*(7), 308–311.

Chavan, V.V., & Ulbrecht, J. (1973). Power correlation for close-clearance helical impellers in non-Newtonian liquids. *Industrial and Engineering Chemistry Process Design and Development*, *12*(4), 472–476.

Chen, M.L., & Wang, F.S. (2010). Optimization of a fed-batch simultaneous saccharification and cofermentation process from lignocellulose to ethanol. *Industrial and Engineering Chemistry Research*, *49*, 5775–5785

Cheng, C.Y., Atkinson, J.F., & Bursik, M.I. (1997). Direct measurement of turbulence structures in mixing jar using PIV. *Journal of Environmental Engineering-ASCE*, *123*, 115–125.

Cheng, J., & Carreau, P.J. (1994). Aerated mixing of viscoelastic fluids with helical ribbons impellers. *Chemical Engineering Science*, *49*(12), 1965–1972.

Chhabra, R.P., & Richardson, J.F. (2008). *Non-Newtonian Flow and Applied Rheology: Engineering Applications* (2nd ed.). Boston: Butterworth-Heinemann/Elsevier.

Chhabra, R.P., Bouvier, L., Delaplace, G., Cuvelier, G., Domenek, S., & Andre, C. (2007). Determination of mixing times with helical ribbon impeller for non-Newtonian viscous fluids using an advanced imaging method. *Chemical Engineering and Technology*, *30*(12), 1686–1691.

Choi, B.S., Wan, B., Philyaw, S., Dhanasekharan, K., & Ring, T.A. (2004). Residence time distributions in a stirred tank: comparison of CFD predictions with experiment. *Industrial and Engineering Chemistry Research*, *43*, 6548–6556

Chowdhury, R., & Tiwari, K.K. (1979). Power consumption studies of helical ribbon-screw mixers. *Industrial Engineering Chemistry, Process Design and Development*, *18*(2), 227–231.

Converti, A., Zilli, M., Arni, S., Felice, R.D., & Borghi, M.D. (1999). Estimation of viscosity of highly viscous fermentation media containing one or more solutes. *Biochemical Engineering Journal*, *4*, 81–85.

Costes, J., & Couderc, J.P. (1988). Influence of the size of the units, I: mean flow and turbulence. *Chemical Engineering Science*, *43*, 2751–2764.

Cozewith, C., & Squire, K.R. (2000). Effect of reactor residence time distribution on polymer functionalization reactions. *Chemical Engineering Science*, *55*, 2019–2029.

Cross, M.M. (1965). Rheology of non-Newtonian fluids: A new flow equation for pseudoplastic systems. *Journal of Colloid Science*, *20*(5), 417–437.

Dagadu, C.P.K., Stegowski, Z., Furman, L., Akaho, E.H.K., & Danso, K.A. (2014). Determination of flow structure in a gold leaching tank by CFD simulation. *Journal of Applied Mathematics and Physics*, *2*, 510-519.

Danckwerts, P.V. (1953). Continuous flow systems: distribution of residence times. *Chemical Engineering Science*, *2*(1), 1–13

De La Villeon, J., Bertrand, F., Tanguy, P.A., Labrie, R., Bousquet, J., & Lebouvier, D. (1998). Numerical investigation of mixing efficiency of helical ribbons. *AIChE Journal*, *44*(4), 972–977.

Deglon, D., & Meyer, C. (2006). CFD modeling of stirred tanks: Numerical considerations. *Minerals Engineering*, *19*(10), 1059–1068.

Delafosse, A., Collignon, M.L., Calvo, S., Delvigne, F., Crine, M., Thonart, P., & Toye, D. (2014). CFD-based compartment model for description of mixing in bioreactors. *Chemical Engineering Science*, *106*, 76–85.

Delaplace, G., Guerin, R., Leuliet, J.C., & Chhabra, R.P. (2006). An analytical model for the prediction of power consumption for shear-thinning fluids with helical ribbon and helical screw ribbon impellers. *Chemical Engineering Science*, *61*, 3250–3259.

Delaplace, G., Leuliet, J. C., & Relandeau, V. (2000). Circulation and mixing times for helical ribbon impellers. Review and Experiments. *Experiments in Fluids*, *28*(2), 170–182.

Delaplace, G., Leuliet, J.C., & Ronse, G. (2000). Power Requirement when mixing a shear-thickening fluid with a helical ribbon impeller type. *Chemical Engineering and Technology*, *23*(4), 329–335.

Denys, S., Pieters, J., & Dewettinck, K. (2007). CFD analysis of thermal processing of eggs. *In Computational fluid dynamics in food processing*, Sun D.W. (Ed.). CRC press, Taylor and Francis group, pp. 347–380.

Dieulot, J.Y., Delaplace, G., Guerin, R., Brienne, J.P., & Leuliet, J.C. (2002). Laminar mixing performances of a stirred tank equipped with helical ribbon agitator subjected to steady and unsteady rotational speed. *Chemical Engineering Research and Design*, *80*(4), 335–344.

Dittrich, C.J., & Mutsersb, S.M.P. (2007). On the residence time distribution in reactors with non-uniform velocity profiles: the horizontal stirred bed reactor for polypropylene production. *Chemical Engineering Science*, *62*, 5777–5793.

Driss, Z., Kaffel, A., Amira, B.B., Bouzgarrou, G., & Abid, M. S. (2014). PIV measurements to study the effect of the Reynolds number on the hydrodynamic structure in a baffled vessel stirred by a Rushton turbine. *American Journal of Energy Research*, *2*(3), 67–73.

Driss, Z., Karray, S., Chtourou, W., Kchaou, H., & Abid, M.S. (2012). A study of mixing structure in stirred tanks equipped with multiple four-blade Rushton impellers. *The Archive of Mechanical Engineering*, *59*(1), 53–72.

Driss, Z., Karray, S., Kchaou, H. & Abid, M.S. (2011). CFD simulation of the laminar flow in stirred tanks generated by double helical ribbons and double helical ribbons screw impellers. *Central European Journal of Engineering*, *1*(4), 413–422.

Dular, M., Bajcar, T., Slemenik-Perse, L., Zumer, M., & Sirok, B. (2006). Numerical simulation and experimental study of non-Newtonian mixing flow with a free surface. *Brazilian Journal of Chemical Engineering*, *23*(4), 473–486.

Dyster, K.N., Koutsakos, E., Jaworski, Z., & Nienow, A.W. (1993). A LDA study of the radial discharge velocities generated by a Rushton turbine: Newtonian fluids. *Chemical Engineering Research and Design*, *71*, 11–23.

El Haj Assad, M., & Oztop, H.F. (2012). Parametric Study of Entropy Generation in a Fluid with Internal Heat Generation between Two Rotating Cylinders Subjected to Convective Cooling at the Surface. *ISRN Chemical Engineering*, 2012, 1–9.

Emin, M.A., & Schuchmann, H.P. (2013). Analysis of the dispersive mixing efficiency in a twin-screw extrusion processing of starch based matrix. *Journal of Food Engineering*, *115*(1), 132–143

Escudie, R., & Line, A. (2003). Experimental analysis of hydrodynamics in a radially agitated tank. *AIChE Journal*, *49*(3), 585–603.

Espinosa-Solares, T., Brito-De La Fuente, E., Tecante, A., & Tanguy, P. (1997). Power consumption of a dual turbine–helical ribbon impeller mixer in ungassed conditions. *Chemical Engineering Journal*, *67*(3), 215–219.

Fogler, H.S. (1999). *Elements of chemical reaction engineering* (3rd ed.). New Jersey: Prentice Hall Inc.

Galanis, N., & Rashidi, M.M. (2012). Entropy generation in non-Newtonian fluids due to heat and mass transfer in the entrance region of ducts. *Heat and Mass Transfer*, *48*, 1647–1662.

Guo, J., Cheng, L., & Xu, M. (2010). The entropy generation minimisation based on the revised entropy generation number. *International Journal of Exergy*, *7*(5), 607–626.

Hall, J. (2005). Study of viscous and viscoelastic flows with reference to laminar stirred vessels. Ph.D. Thesis, Department of Mechanical Engineering, King's College London.

Hall, K.R., & Godfrey, J.C. (1970). Power Consumption by Helical Ribbon Impellers. *Transactions of the Institution of Chemical Engineers*, *48*, 201–208.

Harnby, N., Edwards, M.F., Nienow, A.W. (1992). *Mixing in process industries* (2nd ed.). Oxford: Butterworth-Heinemann.

Harned, H.S., & Nuttall, R.L. (1949). The differential diffusion coefficient of potassium chloride in aqueous solutions. *Journal of the American Chemical Society*, *71*, 1460–1463.

Hassan, M., Sadri, R., Ahmadi, G., Dahari, M., Kazi, S., Safaei, M., & Sadeghinezhad, E. (2013). Numerical study of entropy generation in a flowing nanofluid used in micro- and minichannels. *Entropy*, *15*(1), 144–155.

Herwig, H., & Kock, F. (2007). Direct and indirect methods of calculating entropy generation rates in turbulent convective heat transfer problems. *Heat and Mass Transfer*, *43*, 207–215.

Hocine, S., Pibouleau, L., Azzaro-Pantel, C., & Domenech, S. (2008). Modelling systems defined by RTD curves. *Computers and Chemical Engineering*, *32*, 3112–3120.

Ihejirika, I., & Ein-Mozaffari, F. (2007). Using CFD and ultrasonic velocimetry to study the mixing of pseudoplastic fluids with a helical ribbon impeller. *Chemical Engineering and Technology*, *30*(5), 606–614.

Jahangiri, M. (2005). A laser Doppler anemometry study of the Rushton turbine velocity profile for mixing of polymeric liquids. *Iranian Polymer Journal*, *14*(6), 521–530.

Jankowski, T.A. (2009). Minimizing entropy generation in internal flows by adjusting the shape of the cross-section. *International Journal of Heat and Mass Transfer*, *52*(15-16), 3439–3445.

Javed, K.H., Mahmud, T., & Zhu, J.M. (2006). Numerical simulation of turbulent batch mixing in a vessel agitated by a Rushton turbine. *Chemical Engineering and Processing: Process Intensification*, *45*(2), 99–112.

Kahraman, A., & Yurusoy, M. (2008). Entropy generation due to non-Newtonian fluid flow in annular pipe with relative rotation: constant viscosity case. *Journal of Theoretical and Applied Mecahnics*, *46*(1), 69–83.

Ko, T.H., & Wu, C.P. (2009). A numerical study on entropy generation induced by turbulent forced convection in curved rectangular ducts with various aspect ratios. *International Communications in Heat and Mass Transfer*, *36*(1), 25–31.

Kock, F., & Herwig, H. (2003). Dissipation in turbulent shear flows: A wall function approach for high Reynolds numbers. *International Journal of Computational Fluid Dynamics*, *17*(5), 423–431.

Kock, F., & Herwig, H. (2004). Local entropy production in turbulent shear flows: a high-Reynolds number model with wall functions. *International Journal of Heat and Mass Transfer*, *47*(10-11), 2205–2215.

Kock, F., & Herwig, H. (2005). Entropy production calculation for turbulent shear flows and their implementation in cfd codes. *International Journal of Heat and Fluid Flow*, *26*, 672–680.

Koutsakos, E., & Nienow, A.W. (1990). Effects of rheological properties of simulated fermentation broths on flows in stirred bioreactors: A laser anemometry study. *Rheology of Food, Pharmaceutical and Biological Martials with General Rheology*, Carter, R.E. (Ed.), 284–303.

Kuriyama, M., Arai, K., & Saito, S. (1983). Mechanism of heat transfer to pseudoplastic fluids in an agitated tank with helical ribbon. *Journal of Chemical Engineering Japan*, *16*, 489–494.

Lamberto, D.J., Alvarez, M.M., & Muzzio, F.J. (1999). Experimental and computational investigation of the laminar flow structure in a stirred tank. *Chemical Engineering Science*, *54*(7), 919–942.

Lee, K.C., & Yianneskis, M. (1998). Turbulence properties of the impeller stream of a Rushton turbine. *AIChE Journal*, *44*, 13–24.

Levenspiel, O. (1999). *Chemical Reaction Engineering* (3rd ed.). New York: John Wiley & Sons, Inc.

Levenspiel, O., & Turner, J.C.R. (1970). The interpretation of residence-time experiments. *Chemical Engineering Science*, *25*, 1605–1609.

Levenspiel, O., La1, B.W., & Chatlynne, C.Y. (1970). Tracer curves and the residence time distribution. *Chemical Engineering Science*, *25*, 1611–1613.

Lipowska, L. (1974). The influence of geometric parameters on the ideal mixing range of liquid in a continuous flow stirred tank reactor. *Chemical Engineering Science*, *29*, 1901–1908.

Liu, M. (2012). Age distribution and the degree of mixing in continuous flow stirred tank reactors. *Chemical Engineering Science*, *69*, 382–393.

Lunden, M. (1995). Simulation of three-dimensional flow in stirred vessels: influence of the impeller-modeling and scale-up. *Chemical Engineering Communications*, *139*, 79–114.

Manzi, J., & Carrazzoni, E. (2008). Analysis and optimization of a CSTR by direct entropy minimization. *Journal of Chemical Engineering of Japan*, *41*(3), 194–199.

Manzi, J., Vianna, R., & Bispo, H. (2009). Direct entropy minimization applied to the production of propylene glycol. *Chemical Engineering and Processing: Process Intensification*, *48*(1), 470–475.

McClintock, F.A. (1951). The design of heat exchangers for minimum irreversibility. *1951 ASME Annual Meeting*, Paper No. 51-A-108.

Metzner, A.B., & Otto, R.E. (1957). Agitation of non-Newtonian fluids. *AIChE Journal*, *3*(1), 3–10.

Minge, Z., Luhong, Z., Bin, J., Yuguo, Y., & Xingang, L. (2008). Calculation of metzner constant for double helical ribbon impeller by computational fluid dynamic method. *Chinese Journal of Chemical Engineering*, *16*(5), 686–692.

Mishra, V.P., Dyster, K.N., Jaworski, Z., Nienow, A.W., & Mckemmie, J. (1998). A study of an up and down-pumping wide blade hydrofoil impeller: part I. LDA measurements. *Canadian Journal of Chemical Engineering*, *76*, 577–588.

Molnar, B., Egedy, A., & Varga, T. (2014). Analysis of Mixing Efficiency of Rushton Turbines Based on CFD Models. *Periodica Polytechnica Chemical Engineering*, *58*(2), 93–102.

Montante, G., Bakker, A., Paglianti, A., & Magelli, F. (2006). Effect of the shaft eccentricity on the hydrodynamics of unbaffled stirred tanks. *Chemical Engineering Science*, *61*(9), 2807–2814.

Montante, G., Lee, K., Brucato, A., & Yianneskis, M. (1999). Double to single loop flow pattern transition in stirred vessels. *Canadian Journal of Chemical Engineering*, *77*, 649–659.

Nagata, S. (1975). *Mixing Principles and applications*. New York, NY: John Wiley & Sons, Inc.

Naterer, G.F., & Adeyinka, O.B. (2009). Imaging velocimetry measurements for entropy production in a rotational magnetic stirring tank and parallel channel flow. *Entropy*, *11*, 334–350.

Netusil, J., & Rieger, F. (1993). Power consumption of screw and helical ribbon agitators in highly viscous pseudoplastic fluids. *The Chemical Engineering Journal*, *52*(1), 9–12.

Norris, S.E., Richards, P.J., & Mallinson, G.D. (2011). Improved finite volume discretizations of entropy generation and turbulence production. *Computers and Fluids*, *49*, 302–311.

Nouri, J., & Whitelaw, J. (1990). Flow characteristics of stirred reactors with Newtonian and non-Newtonian fluids. *AIChE Journal*, *36*, 627–629.

Ochieng, A., Onyango, M.S., Kumar, A., Kiriamiti, K., & Musonge, P. (2008). Mixing in a tank stirred by a Rushton turbine at a low clearance. *Chemical Engineering and Processing: Process Intensification*, *47*(5), 842–851.

Pakzad, L., Ein-Mozaffari, F., & Chan, P. (2008). Using computational fluid dynamics modeling to study the mixing of pseudoplastic fluids with a Scaba 6SRGT impeller. *Chemical Engineering and Processing: Process Intensification*, *47*(12), 2218–2227.

Patankar, S.V. (1980). *Numerical heat transfer and fluid flow*, Series in Computational Methods in Mechanics and Thermal Sciences. New York, NY: McGraw-Hill.

Patterson, W.I., Carreau, P.J., & Yap, C.Y. (1979). Mixing with helical ribbon agitators: part II, Newtonian fluids. *AIChE Journal*, *25*(3), 508–516.

Patwardhan, A.W. (2001). Prediction of residence time distribution of stirred reactors. *Industrial and Engineering Chemistry Research*, *40*(24), 5686–5695.

Perse, L.S., & Zumer, M. (2004). Mixing and viscosity determinations with helical ribbon impeller. *Chemical and Biochemical Engineering Quarterly*, *18*(4), 363–371.

Petrov, M., & Tzonkov, St. (2009). Multiple objective optimization of a mass transfer in stirred tank bioreactors. *Bioautomation*, *13*(4), 173–184.

Powell, E.E., & Hill, G.A. (2008). Optimization of continuously stirrer tank bioreactor design for cost minimization: effect of microbial species and operating conditions. *International Journal of Chemical Reactor Engineering*, *6*(1), Article A20, DOI: 10.2202/1542-6580.1642.

Rahimi, M., Kakekhani, A., & Alsairafi, A.A. (2010). Experimental and computational fluid dynamic (CFD) studies on mixing characteristics of a modified helical ribbon impeller. *Korean Journal of Chemical Engineering*, *27*(4), 1150–1158.

Ranade, V., Perrard, M., Le Sauze, N., Xuereb, C., & Bertrand, J. (2001). Trailing vortices of Rushton turbine: PIV measurements and CFD simulations with snapshot approach. *Chemical Engineering Research and Design*, *79*(1), 3–12.

Rieger, F., & Novak, V. (1973). Power consumption of agitators in highly viscous non-Newtonian liquids. *Transactions of the Institution of Chemical Engineers*, *51*, 105–111.

Robinson, B.A., & Tester, J.W. (1986). Characterization of flow maldistribution using inlet-outlet tracer techniques: an application of internal residence time distributions. *Chemical Engineering Science*, *41*, 469–483.

Sahin, A.Z. (2002). Entropy generation and pumping power in a turbulent fluid flow through a smooth pipe subjected to constant heat flux. *Exergy, 2*, 314–321.

Sahin, A.Z. (2014). A simple method of determining entropy generation rate in viscous fluid flow through ducts. *Arabian Journal for Science and Engineering, 39*, 1241–1249.

Sahin, A.Z., & Mansour, B.R. (2003). Entropy generation in laminar fluid flow through a circular pipe. *Entropy, 5*, 404–416.

Sahle-Demessie, E., Bekele, S., & Pillai, U.R. (2003). Residence time distribution of fluids in stirred annular photoreactor. *Catalysis Today*, *88*, 61–72.

Sanjuan-Galindo, R., Heniche, M., Ascanio, G., & Tanguy, P.A. (2011). CFD investigation of new helical ribbon mixers bottom shapes to improve pumping. *Asia-Pacific Journal of Chemical Engineering*, *6*(1), 181–193.

Saravanathamizhan, R., Paranthaman, R., Balasubramanian, N., & Basha, C.A. (2008). Residence time distribution in continuous stirred tank electrochemical reactor. *Chemical Engineering Journal*, *142*(2), 209–216.

Sawinsky, J., Deak, A., & Havas, G. (1976). Power requirement of anchor and helical ribbon impellers for the case of agitating Newtonian and pseudo-plastic liquids. *Chemical Engineering Science*, *31*, 507–509.

Sciubba, E. (2010). Entropy generation minima in different configurations of the branching of a fluid-carrying pipe in laminar isothermal flow. *Entropy, 12*, 1855–1866.

Shamlou, P.A., & Edwards, M. (1985). Power consumption of helical ribbon mixers in viscous Newtonian and non-Newtonian fluids. *Chemical Engineering Science*, *40*(9), 1773–1781.

Shekhar, S.M., & Jayanti, S. (2003). Mixing of power-law fluids using anchors: Metzner-Otto concept revisited. *AIChE Journal*, *49*(1), 30–40.

Shekhar, S.M., & Jayanti, S. (2003). Mixing of pseudoplastic fluids using helical ribbon impellers. *AIChE Journal*, *49*(11), 2768–2772.

Sheskin, D.J., (2004). Handbook of parametric and nonparametric statistical procedures, 3rd ed., CRC Press.

Sivapathasekaran, C., & Sen, R. (2013). Performance evaluation of an ANN–GA aided experimental modeling and optimization procedure for enhanced synthesis of marine biosurfactant in a stirred tank reactor. *Journal of Chemical Technology and Biotechnology, 88*, 794–799.

Solomon, J., Elson, T., & Nienow, A.W. (1981). Cavern sizes in agitated fluids with a yield stress. *Chemical Engineering Communication*, *11*(1-3), 143–164.

Song, X., Zhang, M., Wang, J., Li, P., & Yu, J. (2010). Optimization design for DTB industrial crystallizer of potassium chloride. *Industrial and Engineering Chemistry Research*, *49*, 10297–10302

Sossa-Echeverria, J., & Taghipour, F. (2015). Computational simulation of mixing flow of shear thinning non-Newtonian fluids with various impellers in a stirred tank. *Chemical Engineering and Processing*, *93*, 66–78.

Szoplik, J., & Karcz, J. (2008). Mixing time of a non-Newtonian liquid in an unbaffled agitated vessel with an eccentric propeller. *Chemical Papers*, *62*, 70–77.

Takahashi, K., Yokota, T., & Konno, H. (1984). Power consumption of helical ribbon agitators in highly viscous pseudoplastic liquids. *Journal of Chemical Engineering of Japan*, *17*(6), 657–659.

Tanguy, P.A, Thibault, F., Brito-De La Fuente, E., Espinosa-Solares, T., & Tecante, A. (1997). Mixing performance induced by coaxial flat blade-helical ribbon impellers rotating at different speeds. *Chemical Engineering Science*, *52*(11), 1733–1741.

Tanguy, P.A., Lacroix, R., Bertrand, F., Choplin, L., & Brito-De La Fuente, E. (1992). Finite element analysis of viscous mixing with a helical ribbon-screw impeller. *AIChE Journal*, *38*(6), 939–944.

Tiljander, P., Ronnmark, B., & Theliander, H. (1997). Characterization of 3 different impellers using the LDV technique. *Canadian Journal of Chemical Engineering*, *75*, 787–793.

Torrez, C., & Andre, C. (1999). Simulation of a Rushton turbine mixing yield stress fluids: application of the Metzner-Otto concept. *Chemical Engineering and Technology*, *22*(8), 701–706.

Trivedi, R.N., & Vasudeva, K. (1974). RTD for diffusion free laminar flow in helical coils. *Chemical Engineering Science*, *29*(12), 2291–2295.

Tsui, Y.Y., & Hu, Y.C. (2008). Mixing flow characteristics in a vessel agitated by the screw impeller with a draught tube. *Journal of Fluids Engineering*, *130*(4), 041103-1–10.

Tsui, Y.Y., & Hu, Y.C. (2011). Flow characteristics in mixers agitated by helical ribbon blade impeller. *Engineering Applications of Computational Fluid Mechanics*, *5*(3), 416–429.

Turner, J.C.R. (1982). Perspectives in residence-time distributions. *Chemical Engineering Science*, *38*(1), 1–4.

Van de Vusse, J.G. (1962). A new model for the stirred tank reactor. *Chemical Engineering Science*, *17*(7), 507–521.

Van Der Molen, K., & Van Maanen, H.R.E. (1978). Laser-Doppler measurements of the turbulent flow in stirred vessels to establish scaling rules. *Chemical Engineering Science*, *33*(9), 1161–1168.

Vaneshani, S., & Jazayeri-Rad, H. (2011). Optimized fuzzy control by particle swarm optimization technique for control of CSTR. *World Academy of Science, Engineering and Technology*, *5*(11), 11–26.

Venneker, B., Derksen, J., & Van den Akker, H.E.A. (2010). Turbulent flow of shear-thinning liquids in stirred tanks: the effects of Reynolds number and flow index. *Chemical Engineering Research and Design*, *88*(7A), 827–843.

Vite-Martinez, P., Duran-Valencia, C., Cruz-Maya, J.A., Ramirez-Lopez, A., & Lopez-Ramirez, S. (2014). Optimization of reagents injection in a stirred batch reactor by numerical simulation. *Computers and Chemical Engineering*, *60*, 307–314.

Wang, J.J., Feng, L.F., Gu, X.P., Wang, K., & Hu, C.H. (2000). Power consumption of inner-outer helical ribbon impellers in viscous Newtonian and non-Newtonian fluids. *Chemical Engineering Science*, *55*, 2339–2342.

Wang, S., Wu, J., & Ohmura, N. (2013). Inclined-shaft agitation for improved viscous mixing. *Industrial and Engineering Chemistry Research*, *52*(33), 11741–11751.

Wu, B. (2009). CFD analysis of mechanical mixing in anaerobic digesters. *Transactions of the ASABE*, *52*(4), 1371–1382.

Wu, B. (2010). CFD simulation of mixing in egg-shaped anaerobic digesters. *Water Research*, *44*(5), 1507–1519.

Wu, H., & Patterson, G.K. (1989). Laser-Doppler measurements of turbulent-flow parameters in a stirred mixer. *Chemical Engineering Science*, *44*, 2207–2221.

Xiao-chang, C., Ting-an, Z., & Qiu-yue, Z. (2009). Computational simulation of fluid dynamics in a tubular stirred reactor. *Transactions of Nonferrous Metals Society of China*, *19*, 489–495.

Xie, M.H., Xia, J.Y., Zhou, Z., Zhou, G.Z., Chu, J., Zhuang, Y.P., Zhang, S.L., & Noorman H. (2014). Power consumption, local and average volumetric mass transfer coefficient in multiple-impeller stirred bioreactors for xanthan gum solutions. *Chemical Engineering Science*, *106*, 144–156.

Yablonskya, G.S., Constalesb, D., & Marinc, G.B. (2009). A new approach to diagnostics of ideal and non-ideal flow patterns: I, the concept of reactive-mixing index (REMI) analysis. *Chemical Engineering Science*, *64*, 4875–4883.

Yao, W., Mishima, M., & Takahashi, K. (2001). Numerical investigation on dispersive mixing characteristics of MAXBLEND and double helical ribbons. *Chemical Engineering Journal*, *84*(3), 565–571.

Yap, C.Y., Patterson, W.I., & Carreau, P.J. (1979). Mixing with helical ribbon agitators. *AIChE Journal*, *25*, 516–521.

Yapici, K., Karasozen, B., Schäfer, M., & Uludag, Y. (2008). Numerical investigation of the effect of the Rushton type turbine design factors on agitated tank flow characteristics. *Chemical Engineering and Processing: Process Intensification*, *47*(8), 1340–1349.

Yeoh, S.L., Papadakis, G., & Yianneskis, M. (2005). Determination of mixing time and degree of homogeneity in stirred vessels with large eddy simulation. *Chemical Engineering Science*, *60*(8-9), 2293–2302.

Yianneskis, M., Popiolek, Z., & Whitelaw, J.H. (1987). An experimental study of the steady and unsteady flow characteristics of stirred reactors. *Journal of Fluid Mechanics*, *175*, 537–555.

Yilbas, B.S, Shuja, S., & Budair, M. (1999). Second law analysis of a swirling flow in a circular duct with restriction. *International Journal of Heat and Mass Transfer*, *42*, 4027–4041.

Zadghaffari, R., Moghaddas, J. S., Ahmadlouydarab, M., & Revstedt, J. (2008). A mixing study in a double-Rushton stirred tank. In Hogge, M., Van Keer, R., Noels, L., Stainier, L., Ponthot, J.-P., Remacle, J.-F. & Dick E. (Eds.), *Fourth International Conference on Advanced COmputational Methods in ENgineering (ACOMEN 2008)*, University of Liège, Belgium, pp. 26–28.

Zadghaffari, R., Moghaddas, J., & Revstedt, J. (2008). A study on liquid-liquid mixing in a stirred tank with a 6-blade Rushton turbine. *Iranian Journal of Chemical Engineering*, *5*(4), 12–22.

Zhang, L.P., Zhang, J., Li, C.H., & Bao, J. (2014). Rheological characterization and CFD modeling of corn stover–watermixing system at high solids loading for dilute acid pretreatment. *Biochemical Engineering Journal*, *90*, 324–332.

Zhang, M., Zhang, L., Jiang, B., Yin, Y., & Li, X. (2008). Calculation of Metzner constant for double helical ribbon impeller by computational fluid dynamic method. *Chinese Journal of Chemical Engineering*, *16*(5), 686–692.

Zhou, G., Shi, L., & Yu, P. (2003). CFD study of mixing process in Rushton turbine stirred tanks. In *Third International Conference on CFD in the Minerals and Process Industries*, CSIRO, Melbourne, Australia, pp. 293–298.

Zimparov, V., & Penchev, P. (2003). Entropy generation minimization of tubes with three-dimensional surface roughness for shell-and-tube heat exchangers. In *Proceedings of the First International Exergy, Energy and Environment Symposium*, 13-17 July 2003, Izmir, Turkey.

CURRICULUM VITAE

Akhilesh Prabhakar Khapre
Email: akhilesh_khapre@yahoo.co.in
Phone: +91 7894044869

Educational Qualifications

- **Doctor of Philosophy** in Chemical Engineering, National Institute of Technology, Rourkela, India, Dissertation submitted – May 2015
- **Master of Technology** in Computational Fluid Dynamics, University of Petroleum and Energy Studies, Dehradun, India, July 2009 (CGPA: 3.64 (Scale on 4))
  Partial Coursework towards Master of Technology above (under credit transfer)
  Lomonosov Moscow State University, Moscow, Russia – Mar-June 2008
- **Bachelor of Engineering** in Chemical Engineering, University of Pune, India, July 2007 (First Class with Distinction, 69.2%)

Research Publications:

Refereed Journals:

- Rajavathsavai, D., **Khapre, A.** and Munshi, B., Study of Mixing Behavior of CSTR using CFD, Brazilian Journal of Chemical Engineering, Vol. 31, No. 01, pp. 119–129, 2014.
- **Khapre, A.** and Munshi, B., Numerical investigation of hydrodynamic behavior of shear thinning fluids in stirred tank, Journal of the Taiwan Institute of Chemical Engineers, 2015, http://dx.doi.org/10.1016/j.jtice.2015.04.003.
- **Khapre, A.** and Munshi, B., Computational Study of Entropy Generation Minimization in Continuous Stirred Tank Reactor, International Journal of Exergy, 2015, In Press.
- **Khapre, A.,** Rajavathsavai, D. and Munshi, B., Study on Residence Time Distribution of CSTR using CFD, Indian Journal of Chemical Technology, Accepted.

Books/Books Chapter:

- **Akhilesh Khapre** and Basudeb Munshi, "Study of Mixing in Shear Thinning Fluid Using CFD Simulation," Chapter 16 in Chemical and Bioprocess Engineering: Trends and Developments, Editors: Shirish Sonawane, Y. Pydi Setty, Srinu Naik Sapavatu, Apple Academic Press, 2015, pp. 157–169. ISBN: 978-1-77188-077-0, DOI: 10.1201/b18402-18

Conferences:

- Rajavathsavai, D., **Khapre, A.** and Munshi, B., Study of Hydrodynamic Behavior of a CSTR using CFD, International Conference on Recent Advances in Chemical Engineering and Technology (RACET-2011), Kochi, 2011
- **Khapre, A.** and Munshi, B., CFD Study of Hydrodynamics and Mixing in Stirred Tank at Low impeller Clearance, International Conference on Application of Fluid Engineering (CAFÉ-2012), G.L. Bajaj Institute of Technology & Management, Greater Noida, September 2012
- **Khapre, A.** and Munshi, B., Hydrodynamic Study of non-Newtonian Fluid in a Stirred Tank using CFD, International Conference on Advances in Chemical Engineering (ICACE-2013), NIT Raipur, April 2013
- **Khapre, A.** and Munshi, B., Study of Mixing in Shear Thinning Fluid using CFD Simulation, International Conference on Chemical and Bioprocess Engineering-India (ICCBPE-IN, 2013), NIT Warangal, November 2013
- **Khapre, A.** and Munshi, B., CFD Simulation of Shear Thinning Fluid in Stirred Tank, International Conference on Frontiers in Chemical Engineering (ICFCE-2013), NIT Rourkela, December 2013